TΠ

Environmental stress level − a mathematical modeling framework to investigate the influence of the microenvironment on tumor cell survival

Sabrina Schönfeld

Acknowledgements

Freude am Schauen und Begreifen ist die schönste Gabe der Natur.
– Albert Einstein –

First and foremost, I want to thank Prof. Dr. Christina Kuttler and Dr. Laura Scarabosio for their wonderful supervision, guidance and tireless support over the last few years. You always had an open ear for me and gave me a good feeling about myself – work-related and beyond. I really appreciated all of our conversations and feel greatly thankful for the opportunity to contribute to the exciting and meaningful research field of biomathematics, especially in the medical context.

I am very grateful to Prof. Dr. Helen Byrne for taking her precious time to review and examine this thesis as well as to Prof. Dr. Andreas Wiese for assuming the chair of the examination committee. I want to thank Dr. M. Nichole Rylander and Dr. Alican Ozkan for providing the experimental data, which motivated the modeling ideas and played an essential part in this work, as well as for supporting me with valuable insights and explanations.

I really enjoyed being part of the chair M6 for mathematical modeling. This is thanks to all the thoughtful colleagues who created a very pleasant and friendly working environment. Special thanks goes to Dr. Pirmin Schlicke for helping me getting settled at the beginning of my PhD as well as Dr. Gabriele Witterstein for being my mentor and – together with Prof. Dr. Christina Kuttler – sparking my fascination for mathematical modeling during my bachelor studies. I also want to thank Veronika Hofmann for lending me a helping hand towards the end of my PhD by trying out all of my calibration ideas. Furthermore, I want to thank Dr. Hannes Petermeier, who passed on the excitement and enjoyment for teaching to me.

Finally, the success of my PhD would not have been possible without the loving environment of my family – my parents Precy and Ludwig, my sister Katja and my brother Mario. I am deeply grateful to my parents for planting the seed of excitement about science during our little stargazing sessions when I was a kid, for letting me find my own path in life and inexhaustibly supporting me along the way. Furthermore, I want to give my heartfelt thanks to my husband Ladi for always having my back, no matter what, and finding words of encouragement in every situation, especially towards the end of my PhD. A special thanks goes to all of my friends as well as Günther the cat and everyone who came before him.

Abstract

This thesis presents a novel mathematical modeling approach: the so-called environmental stress level (ESL). It describes the collective influence of the microenvironment on the viability of cells. We apply the ESL approach to different biological experiments. In combination with data-based parameter estimation using Bayesian inference, this allows for investigating the impact of nutrient supply, oxygen concentration, chemotherapeutic drugs and stiffness of the extracellular matrix on particular hepatocellular carcinoma cell lines.

In dieser Arbeit wird ein neuartiger mathematischer Modellierungsansatz vorgestellt: das sogenannte Environmental Stress Level (ESL). Es beschreibt den kollektiven Einfluss der Zellumgebung auf die Lebensfähigkeit von Zellen. Wir wenden den ESL-Ansatz auf verschiedene biologische Experimente an. Die Kombination mit datenbasierter Parameterschätzung mithilfe von Bayesscher Inferenz ermöglicht die Untersuchung des Einflusses von Nährstoffversorgung, Sauerstoffkonzentration, Chemotherapeutika und Steifigkeit der extrazellulären Matrix auf bestimmte hepatozelluläre Karzinom-Zelllinien.

Pubilcation(s) by the author

S. Schönfeld, A. Ozkan, L. Scarabosio, M. N. Rylander and C. Kuttler.
"Environmental stress level to model tumor cell growth and survival".
Mathematical Biosciences and Engineering 19.6 (2022), pp. 5509–5545.
ISSN: 1551-0018. DOI: 10.3934/mbe.2022258.

Contents

1 Introduction

As one of the leading causes of death worldwide, cancerous diseases are a highly relevant field of research in medicine and biology. Up to this day, there is a great demand on advancing the understanding of fundamental dynamics of tumor growth and treatment strategies. For this, gaining empirical data is essential, which can be done by *in vivo* or *in vitro* studies, i.e. assessment of the tumor growth inside the living body (humans or animals) or based on e.g. cell cultures.

Mathematics for biology. Besides the statistical investigation of the acquired data [1], mathematical methods in general provide powerful tools to increase the knowledge gain.

Mathematical modeling. One of such tools is applied mathematical modeling [2, 3], i.e. the mathematical description of processes incorporating biological, physical or chemical background knowledge. In the context of tumor modeling, it can help to understand fundamental biological dynamics or to optimize treatment by adequate quantitative descriptions and predictions. Naming differential equations of all types, stochastic models, phenomenological models as well as more mechanistic ones, there are numerous mathematical models and methods already available (see [4, 5]). For *in vivo* settings, the quantification of realistic tumor growth in terms of parameter values is still challenging without harming a patient or affecting a potential treatment, despite good new experimental techniques [6–8]. Alternatively, *in vitro* approaches allow for observing tumor cells, individually or as populations, under well-controlled conditions to examine at least parts of the underlying processes and how they are potentially influenced by their environment (see e.g. [9, 10]).

There are various starting points for mathematical models to investigate tumor dynamics, depending on which processes should be investigated and which omitted: e.g. describing tumor growth for solid tumors or cell populations [2, 11, 12], potentially in consideration of treatment [13–15] and/or environmental influences like blood supply or mechanical forces [16–20]. Modeling can give insight into unknown causal relations, especially in combination with empirical data. In this work, a novel modeling approach is proposed based on the introduction of an immeasurable auxiliary variable – the so-called *environmental stress level* (ESL) – quantifying the collective effect of environmental factors on the cell growth and death. In particular, we investigate the influence of nutrient supply, oxygenation, tissue stiffness and/or drug treatment on the cells, showcasing the potential of the ESL to provide a flexible and easily adjustable modeling framework for considering an arbitrary number of environmental factors – especially if combined with empirical observations. Using the experimental *in vitro* data from [21, 22], we estimate the involved model parameters to acquire quantities with biological interpretation, eventually providing a deeper understanding of specific environmental influences on the chemoresistance of particular tumor cell lines.

Uncertainty quantification. The reconstruction of model parameters from data is referred to as the inverse problem. This work employs uncertainty quantification with Bayesian inversion [23–25], in particular with Sequential Monte Carlo (SMC) methods [26, 27]. These fall into the category of statistical inversion methods, which allow to quantitatively address uncertainties/inaccuracies in the observations as well as the mathematical model. As a result, we obtain probability distributions for the parameters, giving access to more information, in particular the uncertainty in the parameter estimates, compared to deterministic inversion methods like least-square estimation

(see e.g [28, Ch. 10]) at the cost of increased computational effort. The latter provide only the one set of parameter values which is considered as the "best" (depending on the mathematical assumptions) possible match to the data. Currently, the application of uncertainty quantification in the context of deterministic tumor modeling, especially for parameter inference, is scarce and sometimes limited to synthetic data [29].

There are of course other possibilities besides SMC to approach the Bayesian inverse problem in practice, which have also been partially applied in biological context. While the so-called posterior distribution of the parameters can be constructed deterministically in suitable applications (e.g. quasi-Monte Carlo [30] or sparse grids [31, 32]), sampling-based methods (like SMC) have shown to be more practical for this task and hence are commonly used. In particular, they rely on fewer regularity assumptions of the posterior with reference to the parameters and require less tuning to handle concentrated posteriors. Simple Markov Chain Monte Carlo (MCMC) methods are among the most popular ones [33, Ch. 6-7] as they are simple to implement and well understood theoretically. Using appropriate experimental data, they are applied e.g. for modeling tumor growth [21, 29, 34] or tissue growth [35]. Hence, particle-based methods, like sequential importance sampling and resampling (annealed importance sampling [36] and SMC) and population MCMC [37–39], have gained popularity in the last decade due to their higher efficiency and robustness compared to simple MCMC [40, 41]. Note that SMC based on filtering distributions is especially computationally cheaper for time-resolved data. An alternative approach is the ensemble Kalman filter [42], which is similar to SMC but assumes a Gaussian approximation of the posterior [43]. However, it has been shown in [44] that for nonlinear forward models (which are typically used for tumor modeling), the ensemble Kalman filter is not consistent with the full posterior distribution and can be rather looked at as a derivative-free optimization method to obtain point estimates [43, 45, 46].

Alternatively to sampling-based methods like MCMC or SMC, the posterior distribution could also be constructed via measure transport [47], based on the task of solving an optimization problem over maps, i.e. determining a function transporting a given reference probability density measure to the the posteriors measure. There are also likelihood-free approaches for solving the inverse problem [48], also with applications in experimental biology (see e.g. [49–52]).

Outline   The thesis is structured as follows: The subsequent Chapter 2 provides some background information about the biological processes, which are described by mathematical models in Chapter 3. We present a novel modeling approach to consider the influence of the tumor microenvironment on cancer cells (Section 3.1). This approach is then applied to two different biological settings: tumor cells under nutrient deprivation (Section 3.2) and under chemotherapeutic treatment in varying environments (Section 3.3). Each application is based on respective *in vitro* experiments.

The corresponding measurements are used to estimate the unknown parameters of the models using the methods introduced in Chapter 4. In particular, under consideration of experimental and modeling inaccuracies (Section 4.1) we use Bayesian inversion (Section 4.2) and Sequential Monte Carlo methods (Section 4.3) to calibrate the mathematical models. Chapter 5 explains how the calibration methods are actually applied to the mathematical models. In particular, it gives the problem-specific algorithmic settings (Section 5.1), demonstrates how the available experimental data are utilized (Section 5.2) and how *a priori* knowledge about the parameters is incorporated (Section 5.3).

In Chapter 6 the corresponding calibration results are presented and discussed in the biological context of nutrient deprivation (Section 6.2) and chemoresistance (Section 6.3). Beforehand, we give an overview over the mathematical tools which are employed to investigate the calibra-

tion results (Section 6.1). Eventually, Chapter 7 summarizes the obtained insights (Section 7.1) and observed difficulties/limitations (Section 7.2) while presenting possible solutions. We conclude with an outlook in view of further extensions of the ESL approach and the calibration algorithm (Section 7.3).

The subsequent appendices give additional material to support the comprehensibility of the thesis. In particular, we summarize important notations and terminologies (Appendix A) and outline relevant mathematical basics for mathematical modeling with differential equations (Appendix B). Furthermore, we provide calculations yielding some properties of the mathematical models from Section 3.3 (Appendix C) as well as some supplementary material regarding the model calibration and post processing of the calibration results (Appendix D). Lastly, we give further investigations of the results, complementary to Chapter 6, on both biological applications (Appendix E).

2   Biological and experimental background

This chapter provides a short overview of the biological background of (tumor) cell dynamics and the role of the cells' surroundings. Furthermore, we briefly describe the experimental methods in the studies [21] and [22], from which we utilize data to calibrate the mathematical models.

Cell dynamics.   Cells are basic structural units of every life form. By fulfilling specified functions they play a significant role in developing and maintaining a well-functioning organism [53]. Under healthy conditions, a cell replicates and dies in a highly regulated manner. In particular, cells can *proliferate*, i.e. grow and divide to increase the number of cells (tissue growth). This process is balanced by *programmed cell death* as part of the cells' life cycle. During proliferation, a cell divides and produces a genetically identical copy of itself. It can happen that the genetic information of the new cell shows alternations in comparison to the original one, i.e it *mutates*. Certain mutations can lead to a disturbance of the balance between cell proliferation and death, resulting in cancerous cells [54], which divide in an uncontrolled manner.

Tumor cells and their environment.   When considering cancerous diseases in the body, we can – in simplified terms – distinguish between the tumor cells and the surrounding *tumor microenvironment* (TME). The latter includes, for instance, blood vessels, signaling molecules and the *extracellular matrix* (ECM), a three-dimensional, fibrous structure supporting the surrounding cells. On the one hand, the TME is known to play a significant role in cancer development and progression by biochemically and physically stimulating the cells [55] as well as influencing drug efficacy [56]. On the other hand, the tumor cells can actively modify the TME, e.g. by inducing the growth of blood vessels (so-called angiogenesis) [57] or altering the ECM's mechanical properties [58, 59] to improve their survival conditions.

A sufficient blood supply provides oxygen and essential nutrients, hence is crucial for any cells' survival. Due to the excessive growth of tumor cells, their demand is even higher compared to healthy cells and the tumor can easily outgrow its blood supply. In this situation, tumor cells experience nutrient and/or oxygen deprivation (the latter is called *hypoxia*), which can change the cells' behavior and their interaction with the TME [55, 60]. This also applies to the ECM and especially its stiffness and elasticity, as cells are able to sense and react to the mechanical properties of the ECM. Even under healthy conditions, the ECM plays an important role in the regulation of cell dynamics. However, a stiff ECM can also contribute to tumor progression [55].

Experimental investigation of tumor cell viability under controlled conditions.   In an experimental *in vitro* setting, a way of monitoring cell viability is the so-called CellTiter-Blue® assay [61]. In particular, cell populations are exposed to a certain chemical, which is then metabolized by viable cells: the resulting product emits measurable light. A higher amount of living cells yields an increased metabolization of the chemical. Therefore, measuring the light intensity quantifies the metabolic activity, which is proportional to the population's viability. In practice, we observe a combination of this emitted light and the background fluorescence of the cell-free medium (the latter has to be measured separately and subtracted from the total fluorescence).

The cell population itself is placed in a particular, controlled environment. This allows for investigating the influence of ambient features on the viability. To maintain stable growth conditions, the cells are incubated at an adjustable temperature, humidity and oxygen supply. The culture medium can be supplemented with e.g. a specific nutrient or chemo-therapeutic drug concentration. In the experiments from [21, 22] the cell populations are either seeded directly into the culture medium or into a collagen hydrogel. The latter is used to mimic the ECM with specific mechanical properties [62].

3 Mathematical modeling

In this chapter we present the novel modeling approach of using a so-called *environmental stress level* (ESL) to describe how the viability of tumor cells is influenced by its environment (Section 3.1). This framework is used for two applications. The first one is a simple biological setting to investigate the effect of nutrient deprivation on the tumor cells (Section 3.2). The corresponding model calibration results using the methods of Section 4.3 focus on showing the applicability and reasonableness of the ESL approach. In a second application, we investigate the influence of a more complex environment considering chemotherapeutic drugs, oxygen concentration and tissue stiffness (Section 3.3). In this setting we are interested in getting a deeper understanding of the effect of each individual environmental component as well as their combined influence on the cells.

Preliminaries on conventional techniques and notations regarding mathematical modeling with differential equations can be found as supplementary material in Appendix B. The implementation of all models and the calculation of their solutions is done in Python 3.

3.1 General approach: Environmental stress level (ESL) influencing tumor cells

The TME can influence cell reproduction, viability and movement. We use the term *environmental factors* to denote the features of the TME, which potentially affect the tumor cells' survival in a harmful or beneficial way, e.g. nutrient supply, oxygen saturation, drug concentrations or ECM stiffness.

The following paragraphs explain a novel modeling approach, which was firstly introduced in [63][1] as part of the thesis project. Each environmental factor, which should be considered in the model, is mathematically represented by a time-dependent system variable: $E_1(t), \dots, E_n(t)$, where $n \in \mathbb{N}$ is the number of factors/variables and $t \geq 0$ is the time. These quantities might influence each other as well as be influenced by present tumor cells. Such dynamics can be captured by a respective reaction function g_j $(1 \leq j \leq n)$, leading to an initial value problem for each variable of the form

$$\dot{E}_j = g_j(E_1, \dots, E_n, V, t), \quad E_j(t_0) = E_{j,0}, \tag{3.1}$$

with $V = V(t) \geq 0$ being the density of viable (i.e. alive) tumor cells and t_0 an initial time point.

3.1.1 Influence of the tumor microenvironment on viable cells

The collective influence of all environmental variables on the tumor cells is modeled by an auxiliary time-dependent variable $\eta = \eta(t)$, which we call the *environmental stress level* or *ESL* for short. It is an immeasurable quantity and describes how stressful the conditions, generated by the present environmental factors, are for viable cells. By definition, the ESL is bounded by $0 \leq \eta(t) \leq 1$ $\forall t$, where the bounds $\eta = 0$ resp. $\eta = 1$ mean that cells find optimal resp. most inexpedient survival conditions. Note that "most inexpedient" always has to be seen in the context of the given environmental factors, since the ESL is normalized. This means that there is no point in comparing the ESL for two settings which respectively consider different sets of environmental factors.

---

[1]Note that content and formulations in this section are partly taken from this article.

Optimal growth conditions. For $\eta \equiv 0$, the viable cells V can proliferate with a maximal possible growth rate β, and they only die from programmed cell death with a constant rate λ, i.e.

$$\eta \equiv 0 \quad \Rightarrow \quad \dot{V} = \beta V \left(1 - \left(\frac{V}{V_{\mathrm{cap}}} \right)^b \right) - \lambda V \,.$$

The right hand side of this ordinary differential equation (ODE) is a combination of a generalized logistic growth and an additional exponential death term. In this context, $1/b$ is a dimensionless measure for the strength of contact inhibition and K the corresponding carrying capacity of the biological system. As a feature of the logistic part of the ODE, population growth for very small populations (i.e. $V \ll V_{\mathrm{cap}}$) can be approximated by exponential growth with rate β. It is a reasonable assumption that, independently of the initial population size V_0, the cell population's size actually increases over time under optimal growth conditions, which translates to a parameter relation: $\beta > \lambda$. With this constraint, the ODE can be rewritten as a purely logistic growth term

$$\dot{V} = \underbrace{(\beta - \lambda)}_{= \beta^*} V \left(1 - \left(\frac{V}{\underbrace{V_{\mathrm{cap}} \left(1 - \frac{\lambda}{\beta} \right)^{1/b}}_{= V_{\mathrm{cap}}^*}} \right)^b \right) \,,$$

with "net" growth rate $\beta^* = \beta - \lambda$ and "net" carrying capacity $V_{\mathrm{cap}}^* = V_{\mathrm{cap}} (1 - \frac{\lambda}{\beta})^{1/b}$.

Most inexpedient conditions. For the extreme situation of $\eta \equiv 1$, the cells cannot reproduce anymore and cell death is induced by the poor growth conditions. In this case, the cells' dynamics can be described by

$$\eta \equiv 1 \quad \Rightarrow \quad \dot{V} = -(\lambda + \lambda_{\mathrm{ind}}) V \,,$$

where λ_{ind} is the maximal possible death rate due to the stressful environment.

Varying conditions. In general, the induced death rate λ_{ind} increases whereas the proliferation rate β decreases with rising ESL. Consequently, for arbitrary values of η these rates need to be scaled accordingly. Since $\eta(t) \in [0,1] \; \forall t$, this can be achieved by

$$\dot{V} = (1 - \eta) \cdot \beta V \left(1 - \left(\frac{V}{V_{\mathrm{cap}}} \right)^b \right) - (\lambda + \eta \cdot \lambda_{\mathrm{ind}}) V \,. \tag{3.2}$$

With this modeling approach the tumor population size is only regulated by the ESL η, which itself depends on the present environmental factors $E_1, \ldots, E_n$. They influence the reaction terms of the ODE for η, which will be constructed in the following two Sections 3.1.2 and 3.1.3. Beforehand, we briefly summarize the mathematical features of the solution V; analogous properties for the ESL η are presented in Subsection 3.1.3.

With the boundedness of η, equation (3.2) yields $V = 0 \Rightarrow \dot{V} = 0$, i.e. positivity of the solution V. Hence, its biological reasonableness is preserved given a non-negative initial condition $V(t_0) = V_0 \geq 0$. By generalizing the calculations in our publication [63], we achieve the steady states $\bar{V}$ of V:

$$\dot{V}|_{V = \bar{V}, \eta = \bar{\eta}} = 0 \quad \Rightarrow \quad \bar{V} = 0 \quad \text{or} \quad \bar{V} = V_{\mathrm{cap}} \sqrt[b]{1 - \frac{\lambda + \bar{\eta} \cdot \lambda_{\mathrm{ind}}}{(1 - \bar{\eta}) \cdot \beta}} \,.$$

Since the root has to be well-defined for arbitrary $b \geq 1$, the latter steady state only exists in case of $\frac{\lambda + \bar{\eta} \cdot \lambda_{\mathrm{ind}}}{(1 - \bar{\eta}) \cdot \beta} < 1$, with $\bar{\eta}$ denoting the only steady state of η (see (3.4) in Subsection 3.1.3).

Rewriting this constraint gives $\lambda + \bar{\eta} \cdot \lambda_{\text{ind}} < (1 - \bar{\eta}) \cdot \beta$, which means that the net growth rate has to be larger than the net death rate even under stressful conditions, in order to have a non-trivial steady state of the population size V. The stability of the steady states depends on the given reaction terms of the remaining variables. Similar calculations (for details see [63]) yield the upper bound of V, which is $\max\left\{V_0 \, , \, V_{\text{cap}} \sqrt[b]{1 - \frac{\lambda}{\beta}}\right\}$.

3.1.2   Influence of a specific environmental factor

To describe how exactly these environmental factors influence the ESL, we use *influence functions*, which are respectively defined for each E_j $(1 \leq j \leq n)$ by

$$\delta_j^+ : (E_1, \ldots, E_n) \mapsto \delta_j^+(E_1, \ldots, E_n) \in [0, 1]$$
$$\text{and} \quad \delta_j^- : (E_1, \ldots, E_n) \mapsto \delta_j^-(E_1, \ldots, E_n) \in [0, 1] \, .$$

The superscript "+" resp. "$-$" of δ_j indicates whether the function describes a positive or negative influence of the variable E_j on the cells' survival. Hence, we call them *positive/negative influence function* accordingly. An influence function $\delta_j^{\pm}$ can depend on the other environmental variables E_i $(i \neq j)$, as well: for instance, the influence of a chemotherapeutic drug on the cells' viability might be affected by the presence of another drug. We use $E_{1:n}$ as a short notation for $E_1, \ldots, E_n$ in the following.

We call an environmental factor *beneficial* if increasing its corresponding variable E_j (with fixed E_i, $i \neq j$) increases the value of δ_j^+ and decreases the value of δ_j^- (see Figure 1). We call it *harmful* if it is the other way round. Examples for a beneficial and harmful environmental factor can be nutrient saturation and anti-cancer drug concentration, respectively.
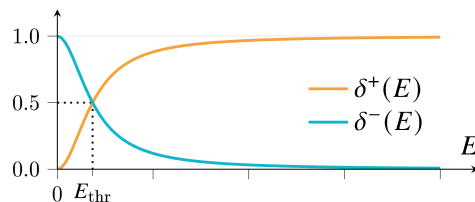
Figure 1: Plots of exemplary influence functions δ^+, δ^- for a system with only one (i.e. $n = 1$) beneficial environmental factor $E_1 = E$, here using $\delta^+(E) = \frac{E^2}{E_{\text{thr}}^2 + E^2}$ and $\delta^-(E) = 1 - \delta^+(E)$.

To model the influence functions for beneficial/harmful environmental variables, we use ideas from so-called ultrasensitive responses [64]. In this context, a response is triggered by a stimulus in a switch-like manner: for low stimulus there is hardly any response; the response amplifies with increasing stimulus, but not before the latter overcomes a specific threshold. This behavior is depicted by a sigmoid stimulus-response curve, which can be mathematically described, for instance, by a Hill-type function

$$\mathcal{H} : \ \mathbb{R}_+ \to [0, 1] \, , \quad E \mapsto \frac{E^m}{E_{\text{thr}}^m + E^m} \, , \quad \text{with } m > 1 \, .$$

Note that, in general, the positive Hill coefficient m can also be smaller than one. However, for $m \in (0, 1]$ the function $\mathcal{H}$ loses the sigmoidal shape, which is not useful for this application. Translating this concept to our setting, E is the variable of a beneficial resp. harmful environmental factor and we use $\delta^+(E) = \mathcal{H}(E)$ resp. $\delta^-(E) = \mathcal{H}(E)$ for the influence functions. The (switch) threshold E_{thr} can be interpreted as the critical value of E, where the cells get influenced

by this environmental factor (see Figure 2, left). The Hill coefficient m regulates how sensitive the cells are to a change in E (see Figure 2, right).
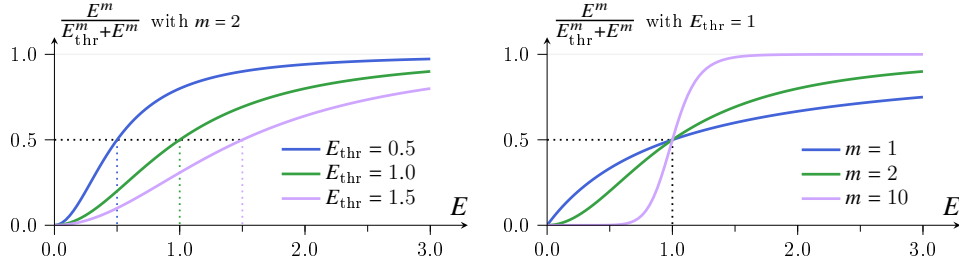
Figure 2: Graphs of the Hill function $E \mapsto \frac{E^m}{E_{\text{thr}}^m + E^m}$ for varying values of E_{thr} (left) resp. m (right).

For such a beneficial/harmful variable E, a relation of the form $\delta^-(E) = 1 - \delta^+(E)$, or equivalently $\delta^+(E) = 1 - \delta^-(E)$, means that the thresholds, for which the cells experience stress and recover from it, are the same, namely E_{thr} (recall Figure 1). This does not necessarily have to be the case: if, for example, E denotes the nutrient supply (beneficial), then the cells might need a larger amount of nutrients to recover from nutrient deprivation compared to the nutrient threshold, at which falling below induces stress – this would be modeled by the influence functions

$$\delta^+(E) = \frac{E^m}{E_{\text{thr},1}^m + E^m} \quad \text{and} \quad \delta^-(E) = 1 - \frac{E^m}{E_{\text{thr},2}^m + E^m}, \quad \text{with } E_{\text{thr},1} > E_{\text{thr},2}.$$

3.1.3   Dynamics of the environmental stress level

With the influence functions introduced in the previous subsection, the collective of positive and negative influences of all environmental factors on the cells' survival can be described by the following ODE for the ESL:

$$\dot{\eta} = \underbrace{\left(\sum_{j=1}^n \alpha_j^- \cdot \delta_j^-(E_{1:n})\right)(1-\eta)}_{\substack{\text{increasing stress level} \\ \text{(stressful conditions)}}} - \underbrace{\left(\sum_{j=1}^n \alpha_j^+ \cdot \delta_j^+(E_{1:n})\right)\eta}_{\substack{\text{recovery from stress} \\ \text{(beneficial conditions)}}}, \quad \text{with } \eta(t_0) = \eta_0 \in [0,1]. \quad (3.3)$$

We call the parameters α_j^- resp. α_j^+ *impact rates*[2]. These variable-specific rates describe how fast the stress level increases (α_j^-) or decreases (α_j^+) if the cells' viability is impacted negatively resp. beneficially by the environmental factor of the associated variable E_j. A distinction between α^- and α^+ per variable takes into consideration that cells can react differently fast to a progressively stressful resp. beneficial environment. All parameters and function codomains in (3.3) are non-negative, resulting in $\eta = 0 \Rightarrow \dot{\eta} \geq 0$, i.e. positivity of the solution η is preserved for $\eta_0 \in [0,1]$. The steady state $\bar{\eta}$ of η is given by

$$\dot{\eta}\big|_{\eta=\bar{\eta},\, E_{1:n}=\bar{E}_{1:n}} = 0 \quad \Rightarrow \quad \bar{\eta} = \frac{\sum_{j=1}^n \alpha_j^- \cdot \delta_j^-(\bar{E}_{1:n})}{\sum_{j=1}^n \left(\alpha_j^- \cdot \delta_j^-(\bar{E}_{1:n}) + \alpha_j^+ \cdot \delta_j^+(\bar{E}_{1:n})\right)} \leq 1, \quad (3.4)$$

where $\bar{E}_{1:n}$ denotes the respective steady states of the variables $E_1, \ldots, E_n$.

---

[2]For our applications, it was sufficient that the impact rates are constants. Note that for other biological processes, it might make sense to consider time-dependent impact rates, for instance, in the context of tumor cells potentially building a resistance to a chemotherapeutic drug, see e.g. [65].

3.2 Application 1: Tumor cells under nutrient deprivation

In a first application, we consider a very simple biological setting, where the nutrient saturation is the only environmental factor. The presented model (using the ESL) will be analyzed and the calibration results will be compared with a corresponding model not using an ESL (see Section 6.2). This application serves as a proof of principle demonstrating that the ESL modeling approach is a feasible alternative way to describe the influence of the environment on a tumor population. The content and formulations of this section are taken from our publication [63] (for consistency within this work, some notations may be altered).

The environmental setting, which should be described by the model, is given by the experiments in [21]. In particular, cell viability is being monitored while the cells are supplemented with a concentration between 0% to 10% of fetal bovine serum (FBS). A supplementation with 0% FBS does not provide the cells with any nutrients, whereas 10% FBS generates optimal growth conditions. The nutrient supply is kept constant throughout the whole duration of each experiment. It serves as an energy source for cell proliferation and strong deprivation thereof inhibits growth and induces cell death. Hence, the nutrient saturation serves as a beneficial environmental factor in our modeling framework and it is the only one to be considered in this model. With $t_0 = 0$ as starting point of the experiments, we denote the dimensionless variable for the nutrient supply by

$$N(t) = N(t_0) = N_0 = \text{const.} \ \forall t \geq 0,$$

i.e. it is bounded and normalized: $N(t) \in [0, 1]$. The bounds represent a complete absence of nutrients ($N = 0$) and an optimal nutrient supply ($N = 1$) with 10% FBS. Following notation (3.1) from the previous section, the environment is described by only one (i.e. $n = 1$) variable:

$$E_1(t) = N(t) = N_0 \quad \Rightarrow \quad \dot{N} = 0 \quad \forall t \geq 0.$$

3.2.1 Environmental stress by nutrient deprivation

For simplicity, we assume that the cells react in the same manner to beneficial and harmful nutrient conditions, that is

$$\alpha_1^- = \alpha_1^+ = \alpha_N, \quad \delta_1^-(E_1) = \delta_N^-(N_0) \quad \text{and} \quad \delta_1^+(E_1) = \delta_N^+(N_0) = 1 - \delta_N^-(N_0),$$

with *nutrient impact rate* α_N and corresponding *nutrient influence functions* $\delta_N^-(N)$ and $\delta_N^+(N)$. Since we do not consider other environmental variables in this application, we omit the subscript "N" for the rest of this section to improve readability. Given an initial ESL $\eta(0) = \eta_0 \in [0, 1]$, we now consider the ODE

$$\dot{\eta} \overset{(3.3)}{=} \alpha_N \delta_N^-(N_0) \cdot (1 - \eta) - \alpha_N \big(1 - \delta_N^-(N_0)\big) \cdot \eta = \alpha_N \big(\delta_N^-(N_0) - \eta\big) \tag{3.5}$$

for the ESL. Since this equation is independent of the variable V, the exact solution can be calculated by separation of variables and, for $t \geq 0$, it is given by

$$\eta(t) = \delta_N^-(N_0) \cdot (1 - e^{-\alpha_N t}) + \eta_0 e^{-\alpha_N t}. \tag{3.6}$$

With N being a beneficial environmental variable, a possible choice for $\delta^\pm(N)$ are Hill type functions (cf. Section 3.1), e.g. with Hill coefficient $m = 2$. The nutrient sensitivity functions can then be defined by

$$\delta^+ : N \mapsto \frac{N^2}{N_{\text{thr}}^2 + N^2} \qquad \text{and} \qquad \delta^- : N \mapsto 1 - \delta_N^+(N) = 1 - \frac{N^2}{N_{\text{thr}}^2 + N^2}, \tag{3.7}$$

where $0 < N_{\text{thr}} < 1$ denotes the *nutrient sensitivity threshold*, for which the cells proliferate/starve with half-maximal rate. This parameter quantifies how tolerant viable cells are to a lack of nutrients. In particular, we can assume $N_{\text{thr}} \ll 1$, since we know from the experiments that the cells can endure a severe shortage of nutrients.

Overall, this results in the following initial value problem:

$$(\mathcal{M}_N^\eta) \begin{cases} \dot{V} \stackrel{(3.2)}{=} \left(1 - \eta(t)\right) \cdot \beta\, V \left(1 - \left(\frac{V}{V_{\text{cap}}}\right)^b\right) - \left(\lambda + \eta(t) \cdot \lambda_{\text{ind}}\right) V\,, \\[2ex] \dot{\eta} = \alpha_N \left(1 - \frac{N_0^2}{N_{\text{thr}}^2 + N_0^2}\right) \cdot (1 - \eta) - \alpha_N \frac{N_0^2}{N_{\text{thr}}^2 + N_0^2} \cdot \eta\,, \\[2ex] V(0) = V_0,\ \eta(0) = \eta_0\,. \end{cases}$$

By inserting the explicit time-dependent analytical solution $\eta(t)$ from (3.6) into the right-hand side of the first ODE of model $\mathcal{M}_N^\eta$, the system reduces to a non-autonomous ODE for V, which is solved numerically. Table 1 summarizes the model variables and parameters as well as their biological interpretation (their units result from the experimental setting).

Table 1: Overview over the variables and parameters of model $\mathcal{M}_N^\eta$.

		Meaning	Scaling
Variables	$V = V(t)$	Density of viable tumor cells	$10^5\,\text{cells/mL}$
	$\eta = \eta(t)$	Environmental stress level	–
	$N = N_0$	Nutrient saturation (constant)	$10\%\,\text{FBS}$
Parameters	V_0	Initial viable cell density	$10^5\,\text{cells/mL}$
	η_0	Initial environmental stress level	–
	β	Maximal possible proliferation rate	$1/\text{day}$
	V_{cap}	Carrying capacity of the biological system	$10^5\,\text{cells/mL}$
	$1/b$	Strength of proliferation contact inhibition	–
	λ	Natural death rate	$1/\text{day}$
	λ_{ind}	Maximal possible induced death rate	$1/\text{day}$
	α_N	Impact rate of nutrient changes on stress level	$1/\text{day}$
	N_{thr}	Nutrient sensitivity threshold	$10\%\,\text{FBS}$

As stated in Section 3.1, the solutions V and η remain bounded and their positivity is preserved. The latter is an important feature for biological reasonableness. Table 2 summarizes the computed bounds as well as the steady states $(\bar{V}, \bar{\eta})^T$ and their stability. These features depend on the relationship between the terms

$$\tilde{\beta} = \delta^+(N_0) \cdot \beta \qquad \text{and} \qquad \tilde{\lambda} = \lambda + \delta_N^-(N_0) \cdot \lambda_{\text{ind}}\,,$$

which are the net growth and death rates while the ESL has reached its equilibrium. The detailed calculations providing these results can be found in the supplementary material of our publication [63] (note that the notation of some variables and parameters might differ).

Table 2: Bounds of the solutions and steady states of model $\mathcal{M}_N^\eta$ for non-negative initial values V_0, η_0.

	Bounds of the solutions $V(t)$, $\eta(t)$	Steady states $(\bar{V}, \bar{\eta})^T$	
		stable	unstable
for all $\tilde{\lambda}, \tilde{\beta}$:	$0 \leq \eta(t) \leq \max\left\{\eta_0, \delta_N^-(N_0)\right\} \leq 1$		
for $\tilde{\lambda} < \tilde{\beta}$:	$0 \leq V(t) \leq \max\left\{V_0, V_{\text{cap}}\sqrt[b]{1 - \tilde{\lambda}/\tilde{\beta}}\right\}$	$\begin{pmatrix} V_{\text{cap}}\sqrt[b]{1 - \tilde{\lambda}/\tilde{\beta}} \\ \delta_N^-(N_0) \end{pmatrix}$	$\begin{pmatrix} 0 \\ \delta_N^-(N_0) \end{pmatrix}$
for $\tilde{\lambda} \geq \tilde{\beta}$:	$0 \leq V(t) \leq V_0$	$\begin{pmatrix} 0 \\ \delta_N^-(N_0) \end{pmatrix}$	

3.2.2   Quasi-steady state: Immediate reaction to nutrient deprivation

Under the assumption that nutrient changes influence the viable cells immediately (i.e. $\alpha_N \to \infty$) the stress level tends to the value of the influence function at N_0:

$$\eta(t) \overset{(3.6)}{=} \delta_N^-(N_0) \cdot (1 - e^{-\alpha_N t}) + \eta_0 e^{-\alpha_N t} \overset{\alpha_N \to \infty}{\longrightarrow} \delta_N^-(N_0) = \text{const}.$$

The same stress level is achieved by a quasi-steady state assumption, stating that changes in the ESL happen on a much faster time scale than changes in the tumor cell density. In this case, the stress level reaches its steady state virtually instantly, which is:

$$\dot{\eta} \overset{(3.5)}{=} \alpha_N\left(\delta_N^-(N_0) - \eta\right) = 0 \;\Rightarrow\; \eta = \delta_N^-(N_0)\,.$$

By using $1 - \delta_N^-(N_0) = \delta^+(N_0)$, insertion of the now constant ESL into model $\mathcal{M}_N^\eta$ reduces the system to the autonomous ODE

$$(\mathcal{M}_N) \quad \begin{cases} \dot{V} = \underbrace{\delta^+(N_0) \cdot \beta}_{=\tilde{\beta}}\, V\left(1 - \left(\frac{V}{V_{\text{cap}}}\right)^b\right) - \underbrace{(\lambda + \delta_N^-(N_0) \cdot \lambda_{\text{ind}})}_{=\tilde{\lambda}} V\,, \\ V(0) = V_0\,, \end{cases}$$

which has the analytical solution

$$V(t) = \begin{cases} V_0 V_{\text{cap}} \cdot \left(\dfrac{\tilde{\beta} - \tilde{\lambda}}{\tilde{\beta}V_0^b + \left(\left(\tilde{\beta} - \tilde{\lambda}\right) V_{\text{cap}}^b - \tilde{\beta}V_0^b\right) e^{-(\tilde{\beta}-\tilde{\lambda})mt}}\right)^{1/b} & \text{if } \tilde{\beta} \neq \tilde{\lambda}, \\[2em] V_0 V_{\text{cap}} \cdot \left(\dfrac{1}{mt\tilde{\beta}V_0^b + V_{\text{cap}}^b}\right)^{1/b} & \text{if } \tilde{\beta} = \tilde{\lambda}, \end{cases} \tag{3.8}$$

for $t \geq 0$. The corresponding calculations can be found in the supplementary material of our publication [63] (note that the notation of some variables and parameters might differ). With $\mathcal{M}_N$ we have an alternative model without using the ESL η, but neglecting the impact rate α_N of the cells to nutrient changes. In Section 6.2, we compare the calibration results of both models $\mathcal{M}_N^\eta$ and $\mathcal{M}_N$ to demonstrate the feasibility of the ESL approach.

3.3   Application 2: Influence of oxygen supply and ECM stiffness on chemotherapeutic effect on tumor cells

In a second application, we consider a more complex environmental setting consisting of the oxygen supply, ECM stiffness and chemotherapeutic drugs. In the corresponding experimental setting from [22], for which we design a suitable mathematical model, the cell population size stays sufficiently smaller than the system's capacity ($V \ll V_{\mathrm{cap}}$) during the whole experiment, which allows to simplify the ODE (3.2) to an initial value problem with a purely exponential, stress- and hence time-dependent rate $\beta_\eta(t)$:

$$\dot{V} \overset{V \ll V_{\mathrm{cap}}}{=} \Big(\big(1 - \eta(t)\big) \cdot \beta - \big(\lambda + \eta(t) \cdot \lambda_{\mathrm{ind}}\big) \Big) V = \Big(\underbrace{\beta - \lambda - \big(\beta + \lambda_{\mathrm{ind}}\big)\eta(t)}_{\beta_\eta(t)} \Big) V \,. \tag{3.9}$$

Depending on its sign, $\beta_\eta(t)$ is the actually observable net growth/death rate. In a stress-free environment (i.e. $\eta(t) \equiv 0$), the population grows with constant rate $\beta_\eta(t) \equiv \beta - \lambda > 0$. The population size starts to decline once the stress level exceeds a certain threshold:

$$\eta(t) > \frac{\beta - \lambda}{\beta + \lambda_{\mathrm{ind}}} \quad \Rightarrow \quad \beta_\eta(t) < 0 \,. \tag{3.10}$$

Environmental factors/variables.   The model should describe the influence of oxygen concentration, ECM stiffness and a combination therapy with two chemotherapeutic drugs on viable tumor cells. In this setting, the nutrient supply is maintained optimal for cell growth. Therefore, it does not influence the stress level and hence it is not necessary as an environmental variable in the model. In total, we need four environmental variables $E_1, \dots, E_4$. The first two variables E_1 resp. E_2 represent the dosage of the drugs doxorubicin (DOX) and sorafenib (SOR), respectively. The oxygen supply varies between normoxic ($21\% \, \mathrm{O_2}$) and hypoxic ($1\% \, \mathrm{O_2}$) conditions. For an easier mathematical description, the corresponding variable $E_3(t) \in [0,1]$ describes the present *hypoxia level*, i.e. $E_3 \equiv 0$ resp. $E_3 \equiv 1$ represent a normoxic resp. hypoxic environment. Similarly, the last variable $E_4(t) \in [0,1]$ models the *cirrhosis level*, as the ECM stiffness ranges between normal ($E_4 \equiv 0$) and cirrhotic ($E_4 \equiv 1$) conditions. For better readability, instead of $E_1, \dots, E_4$ we use more intuitive notations for the environmental variables:

$$\underline{\mathrm{d}}\text{oxorubicin concentration: } D(t) = E_1(t) \,, \qquad \underline{\mathrm{s}}\text{orafenib concentration: } S(t) = E_2(t) \,,$$
$$\underline{\mathrm{h}}\text{ypoxia level: } H(t) = E_3(t) \,, \qquad\qquad \underline{\mathrm{c}}\text{irrhosis level: } C(t) = E_4(t) \,.$$

During all experiments, the cells grow under constant oxygen (either normoxic or hypoxic) and stiffness (either normal or cirrhotic) conditions, i.e.

$$H(t) = H_0 \in \{0,1\} \quad \text{and} \quad C(t) = C_0 \in \{0,1\} \quad \forall\, t \geq 0 \,.$$

Influence on the tumor cells.   Following the definition of the general stress equation (3.3), we now consider an ODE of the form

$$\dot{\eta} = \Big(\alpha_D^- \delta_D^- + \alpha_D^- \delta_S^- + \alpha_H^- \delta_H^- + \alpha_C^- \delta_C^- \Big) \cdot (1 - \eta) - \Big(\alpha_D^+ \delta_D^+ + \alpha_S^+ \delta_S^+ + \alpha_H^+ \delta_H^+ + \alpha_C^+ \delta_C^+ \Big) \cdot \eta \,,$$

with $\eta(0) = 0$. In general, each influence function can depend on all environmental variables, which means $\delta_*^- = \delta_*^-(D, S, H, C)$ and $\delta_*^+ = \delta_*^+(D, S, H, C)$, with $* \in \{D, S, H, C\}$.

To specify these functions, we have to consider the time line of the underlying experiment, which can be divided into three phases (see Figure 3):

1. *Adaption phase*: The tumor cells grow under specific oxygen (normoxic/hypoxic) and stiffness (normal/cirrhotic) conditions for three days to reach native morphology before starting the drug treatment.

2. *Treatment phase*: Chemotherapy is applied for 24 or 48 hours with a certain dosage of DOX, potentially in combination with a normal/high dosage of SOR.

3. *Growth phase*: After treatment, remaining drugs are washed from the cells and the population is grown for further three days. Eventually, viability is measured to investigate the treatment effect.
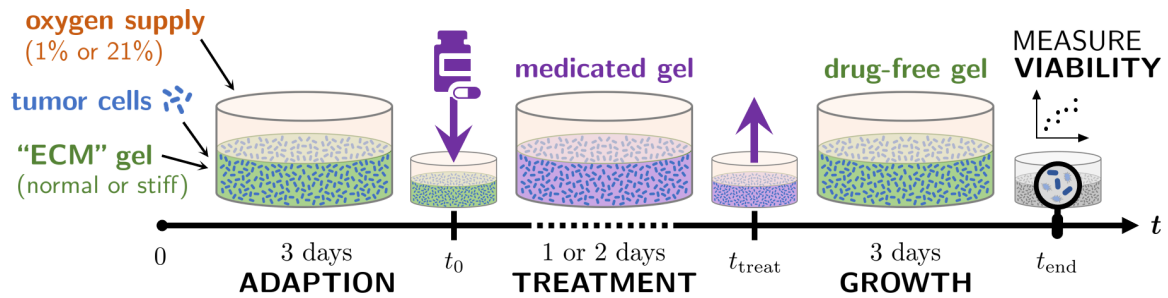
Figure 3: Schematic overview of the phases of the underlying experimental setting.

The mathematical description of the experimental phases is explained in the following Section 3.3.1.

3.3.1 Construction of the mathematical model

The reaction terms for each environmental variable and their influence on the ESL depend on the considered phase and will be summarized in one model in Section 3.3.2 after the following paragraphs.

Adaption phase: $t \in [0, t_0]$. There are no drugs involved in this phase, hence the only environmental variables influencing the ESL are the hypoxia level $H \equiv H_0$ and cirrhosis level $C \equiv C_0$, and the reaction terms of the environmental variables are all zero:

$$\dot{D} \equiv 0, \qquad \dot{S} \equiv 0, \qquad \dot{H} \equiv 0, \qquad \dot{C} \equiv 0.$$

The cells were grown under optimal conditions before starting the experiment, i.e. there is no initial stress at the beginning of the adaption phase. Overall, this leads to the initial value problem

$$\dot{\eta} = \left(\alpha_H^- \cdot \delta_H^- + \alpha_C^- \cdot \delta_C^- \right) \cdot (1 - \eta) - \left(\alpha_H^+ \cdot \delta_H^+ + \alpha_C^+ \cdot \delta_C^+ \right) \cdot \eta, \quad \eta(0) = 0 \quad \text{for } t \in [0, t_0].$$

We assume that the cells' reaction to hypoxia resp. cirrhosis is not influenced by the stiffness resp. oxygen supply, i.e. that the influence functions of H do not depend on C and vice versa:

$$\delta_H^- = \delta_H^-(H), \ \delta_H^+ = \delta_H^+(H), \ \delta_C^- = \delta_C^-(C) \text{ and } \delta_C^+ = \delta_C^+(C).$$

The adaption phase allows the tumor cells to reach native morphology, i.e. to completely adapt to normoxic/hypoxic and normal/cirrhotic conditions before the drug treatment is started. Therefore, it is reasonable to assume that the stress level η has reached its steady state

$$\eta(t_0) \overset{(3.4)}{=} \frac{\alpha_H^- \cdot \delta_H^-(H_0) + \alpha_C^- \cdot \delta_C^-(C_0)}{\alpha_H^- \cdot \delta_H^-(H_0) + \alpha_C^- \cdot \delta_C^-(C_0) + \alpha_H^+ \cdot \delta_H^+(H_0) + \alpha_C^+ \cdot \delta_C^+(C_0)}$$

not later than the end of this phase. If we assume that the cells react with the same sensitivity to stress inducing and reducing oxygen resp. stiffness conditions, i.e. $\alpha_*^- = \alpha_*^+$ (abbreviated α_*) and $\delta_*^- = 1 - \delta_*^+$ for $* \in \{H, C\}$, this steady state simplifies further. This leads to the stress level η_{HC} at the end of the adaption phase:

$$\eta_{HC}(H_0, C_0) = \eta(t_0) = \frac{\alpha_H \cdot \delta_H^-(H_0) + \alpha_C \cdot \delta_C^-(C_0)}{\alpha_H + \alpha_C} \in \left[0, \frac{\beta - \lambda}{\beta + \lambda_{\mathrm{ind}}}\right] \tag{3.11}$$

under the constant environmental conditions $H \equiv H_0$ and $C \equiv C_0$. The upper bound of η_{HC} follows from relation (3.10), since it is reasonable to assume that stress induced solely by hypoxic and/or stiff environment will not lead to a declining population size. We do not have any particular information on how the influence functions δ_H^- and δ_C^- can be defined. Therefore, we will proceed with the more general notation η_{HC}.

Note that in the following we omit the arguments of η_{HC} for better readability. An analogous way of notation is adopted for all upcoming quantities which depend on the constant environmental factors H_0 and C_0, by indicating this with the subscript "HC".

Treatment phase: $t \in [t_0, t_{\mathbf{treat}}]$.   After the cells have adapted to the oxygen and stiffness conditions ($H \equiv H_0$ and $C \equiv C_0$), chemotherapeutic drugs are added to the biological system:

$$D(t_0) = D_0 > 0 \qquad \text{and} \qquad S(t_0) = S_0 \geq 0\,.$$

Both drugs might degrade over time with constant, drug-specific rates. Additionally, liver cells, as they are used in the underlying experiments, can express the so-called CYP3A4 enzyme, which is able to metabolize drugs. In the human body, the half-life of DOX and SOR is approximately 1-2 days, where the metabolization in the liver via CYP3A4 plays a major role [66, 67]. Assuming constant exponential decay of the drugs, this half-life translates to total decay rates in the range of approximately $0.35 - 0.70 \frac{1}{\mathrm{day}}$. Since this decay includes both degradation and metabolization, it is reasonable to assume that the degradation rates are significantly smaller than these total decay rates. Hence, we choose to omit the degradation rates in our model and only focus on the metabolization rates. These are expected to be proportional to the cell-specific CYP expression. We see in [22] that the latter can depend on the environmental factors H_0 and C_0, which is modeled by the following reaction terms for D and S in the treatment phase:

$$\dot{D} = -\gamma_{D,HC} \cdot D \quad \text{and} \quad \dot{S} = -\gamma_{S,HC} \cdot S \qquad \text{for } t \in [t_0, t_{\mathrm{treat}}],$$

with $\gamma_{D,HC}$ and $\gamma_{S,HC}$ being the environment-dependent metabolization rates of DOX and SOR, respectively. For $t \in [t_0, t_{\mathrm{treat}}]$, these ODEs have the analytical solutions

$$D(t) = D_0 \exp\left(-\gamma_{D,HC} \cdot t\right) \qquad \text{and} \qquad S(t) = S_0 \exp\left(-\gamma_{S,HC} \cdot t\right). \tag{3.12}$$

The stress level is now influenced only by the present drugs, since the cells have already adapted to the oxygen and stiffness conditions. Hence, we use the steady state (3.11) from the previous phase as initial condition for the ESL. It is reasonable to assume that the cells do not significantly

recover from the drug treatment during the period of the experiment, i.e. $\alpha_D^+, \alpha_S^+ \approx 0$. Overall, for $t \in [t_0, t_{\text{treat}}]$ we arrive at

$$\dot{\eta} = \left(\alpha_D^- \cdot \delta_D^- + \alpha_D^- \cdot \delta_S^- \right) \cdot (1 - \eta) \quad \text{with} \quad \eta(t_0) = \eta_{0,HC} = \eta_{HC}$$

Both, DOX and SOR can directly induce stress to the cells. As described in Section 3.1, Hill-type functions are a suitable choices for δ_D^- and δ_S^-. In this context, the respective threshold values can be interpreted as a measure for the cells' chemoresistance to the corresponding drug. A large threshold means that the cells tolerate higher drug dosages before their survival is impaired. We know that the chemoresistance can be influenced by other environmental factors. On the one hand, we know that varying SOR dosage, oxygen supply and ECM stiffness can influence the chemoresistance of the tumor cells to DOX. On the other hand, the cytotoxic effect of SOR might be influenced by the present oxygen and stiffness conditions [22]. Overall, this translates to

$$\delta_{D,HC}^-(D, S) = \frac{D^{m_1}}{\left(D_{\text{thr},HC}(S) \right)^{m_1} + D^{m_1}} \qquad \text{and} \qquad \delta_{S,HC}^-(S) = \frac{S^{m_2}}{S_{\text{thr},HC}^{m_2} + S^{m_2}},$$

where the thresholds $D_{\text{thr},HC}(S) = D_{\text{thr},HC}(S, H_0, C_0)$ and $S_{\text{thr},HC} = S_{\text{thr},HC}(H_0, C_0)$ are functions depending on the environmental factors, which influence chemoresistance to the respective drug. In particular, we assume that each variable of the threshold's argument can shift the critical (switch) value of the corresponding Hill function. For DOX, this can be written mathematically as

$$D_{\text{thr},HC}(S) = D_{\text{norm}} \cdot d_S(S) \cdot d_H(H_0) \cdot d_C(C_0), \qquad (3.13)$$

where each d_* is a positive function, describing how the respective variable $* \in \{S, H, C\}$ scales the *unaffected threshold* D_{norm} (i.e. the chemoresistance under normal conditions, unaffected by other environmental influences):

$$\begin{aligned} d_* < 1 \quad &\Rightarrow \quad \text{reduces chemoresistance,} \\ d_* = 1 \quad &\Rightarrow \quad \text{does not influence chemoresistance,} \\ d_* > 1 \quad &\Rightarrow \quad \text{increases chemoresistance.} \end{aligned}$$

Therefore, $d_*(0) = 1$ should hold by definition. Figure 4 visualizes the change of chemoresistance to DOX for an example case of only SOR influencing the threshold.
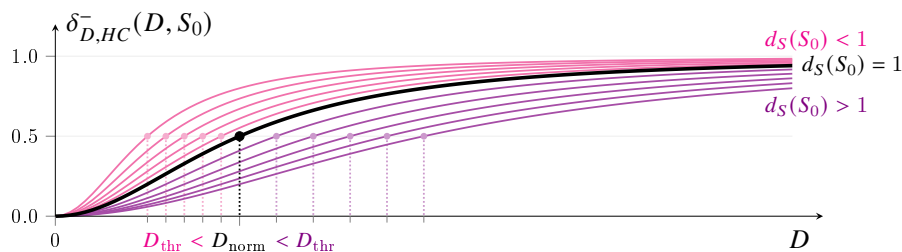
Figure 4: Illustration of how the threshold $D_{\text{thr}} = D_{\text{thr},HC}(S_0)$ of the influence function $\delta_{D,HC}^-$ is shifted compared to D_{norm} by $d_S(S_0)$ for fixed $d_H(H), d_C(C) = 1$.

For defining d_S, we know that a sufficient dosage of SOR can decrease the cells' chemoresistance to DOX, i.e. d_S is a monotonically decreasing function on $[0, 1]$. To implement an appropriate dose-response relation, we can again use a Hill-type function:

$$d_S(S) = 1 - \frac{a_{\max} S^{m_3}}{S_{\text{supp}}^{m_3} + S^{m_3}}, \qquad (m_3 > 0),$$

where S_{supp} is the critical dosage of SOR, after which the chemoresistance to DOX is significantly influenced. The parameter $a_{\max} \in (0,1)$ ensures that d_S does get arbitrarily small for very large S. For the remaining functions d_H and d_C, we do not have enough understanding of how hypoxia and/or high ECM stiffness influence chemoresistance to explicitly define them. Therefore, for better readability, we summarize them in a shorter notation:

$$d_{HC} = d_H(H_0) \cdot d_C(C_0)\,.$$

Analogously to (3.13), for functions $s_H, s_C : [0,1] \to (0,\infty)$ with $s_H(0), s_C(0) = 1$ we define

$$S_{\text{thr},HC} = S_{\text{norm}} \cdot s_H(H_0) \cdot s_C(C_0)$$

as the influenced threshold of the sensitivity function δ_S^- for SOR. Again, we do not have further information to explicitly define the positive functions $s_H(H)$ and $s_C(C)$, so we proceed with the more general notation $S_{\text{thr},HC}$. Altogether, in the treatment phase, i.e. for $t \in [t_0, t_{\text{treat}}]$, we consider the ODE system

$$\begin{cases} \dot{V} = \Big(\beta - \lambda - \big(\beta + \lambda_{\text{ind}}\big)\eta\Big) V\,, \\[2mm] \dot{\eta} = \left(\dfrac{\alpha_D^- D^{m_1}}{\big(D_{\text{thr},HC}(S)\big)^{m_1} + D^{m_1}} + \dfrac{\alpha_S^- S^{m_2}}{S_{\text{thr},HC}^{m_2} + S^{m_2}}\right)(1 - \eta)\,, \end{cases} \tag{3.14}$$

with D and S as given in (3.12) and the initial conditions: $V(t_0) = V_0$ and $\eta(t_0) = \eta_{0,HC} = \eta_{HC}$.

Growth phase: $t \in [t_{\text{treat}}, t_{\text{end}}]$. At the beginning of the experiment's last phase, all drugs are removed from the cells' environment, motivating the initial conditions $D(t_{\text{treat}}), S(t_{\text{treat}}) = 0$. The cell population is left to grow under drug-free conditions for the remaining time of the experiment, meaning the reaction terms of the environmental variables are again all zero:

$$\dot{D} \equiv 0\,, \qquad \dot{S} \equiv 0\,, \qquad \dot{H} \equiv 0\,, \qquad \dot{C} \equiv 0\,.$$

For the other variables, the corresponding solutions $V(t_{\text{treat}})$ and $\eta(t_{\text{treat}})$ from system (3.14) are used as initial conditions. Since the stress level is not influenced by treatment anymore and the cells are still fully adapted to oxygen and stiffness conditions, the ESL stays constant. Hence, we can use a single ODE to model the dynamics of the growth phase, i.e. for $t \in [t_{\text{treat}}, t_{\text{end}}]$:

$$\dot{V} = \Big(\beta - \lambda - \big(\beta + \lambda_{\text{ind}}\big)\eta(t_{\text{treat}})\Big) V\,. \tag{3.15}$$

After numerically solving ODE system (3.14) from the treatment phase, the initial value problem above has the analytical solution

$$V(t) = V(t_{\text{treat}}) \cdot \exp\left(\Big(\beta - \lambda - \eta(t_{\text{treat}}) \cdot \big(\beta + \lambda_{\text{ind}}\big)\Big) \cdot (t - t_{\text{treat}})\right), \quad \text{for } t \in [t_{\text{treat}}, t_{\text{end}}]\,.$$

3.3.2 The complete chemoresistance model for different cell lines

We can collect all results from Section 3.3.1 into one model. Since the dynamics of the adaption phase are covered by the value of $\eta(t_0) = \eta_{0,HC}$, we set the initial time of model $\mathcal{M}_{DS}^{\mathrm{CYP}}$ to $t_0 = 0$. By denoting the treatment phase with $T = [t_0 = 0, t_{\mathrm{treat}}]$ and $\mathbb{1}_T(t)$ the indicator function on T, we achieve the *complete chemoresistance model* for $t \geq 0$:

$$(\mathcal{M}_{DS}^{\mathrm{CYP}}) \begin{cases} \dot{V} = \Big(\beta - \lambda - \eta \cdot \big(\beta + \lambda_{\mathrm{ind}} \big) \Big) V \, , \\[2ex] \dot{\eta} = \left(\dfrac{\alpha_D^- D^{m_1}}{\left(D_{\mathrm{norm}} \left(1 - \dfrac{a_{\mathrm{max}} S^{m_3}}{S_{\mathrm{supp}}^{m_3} + S^{m_3}} \right) d_{HC} \right)^{m_1} + D^{m_1}} + \dfrac{\alpha_S^- S^{m_2}}{S_{\mathrm{thr},HC}^{m_2} + S^{m_2}} \right) (1 - \eta) \, , \\[3ex] D(t) = D_0 \, \exp\big(-\gamma_{D,HC} \cdot t \big) \cdot \mathbb{1}_T(t) \, , \\[1ex] S(t) = S_0 \, \exp\big(-\gamma_{S,HC} \cdot t \big) \cdot \mathbb{1}_T(t) \, , \end{cases}$$

with the initial conditions

$$V(0) = V_0 \qquad \text{and} \qquad \eta(0) = \eta_{HC} \overset{(3.11)}{\leq} \frac{\beta - \lambda}{\beta + \lambda_{\mathrm{ind}}} \, .$$

The following tables summarize the variables (Table 3) and parameters (Table 4) of model $\mathcal{M}_{DS}^{\mathrm{CYP}}$.

Table 3: Variables of model $\mathcal{M}_{DS}^{\mathrm{CYP}}$.

		Meaning	Scaling
General	$V = V(t)$	Density of viable tumor cells	–
	$\eta = \eta(t)$	Environmental stress level	–
Environmental	$D = D(t)$	Doxorubicin (DOX) concentration	$1\,\mu\mathrm{M}$
	$S = S(t)$	Sorafenib (SOR) concentration	$22\,\mu\mathrm{M}$
	$H = H_0$	Hypoxia level (constant), representing oxygen supply: $21\%\,O_2$ ($H \equiv 0$) or $1\%\,O_2$ ($H \equiv 1$)	–
	$C = C_0$	Cirrhosis level (constant), representing ECM stiffness: normal ($C \equiv 0$) or cirrhotic ($C \equiv 1$)	–

Table 4: Parameters of model $\mathcal{M}_{DS}^{\text{CYP}}$.

	Meaning	Scaling
	Time point of	
$t_0 = 0$	the end of adaption phase / beginning of treatment phase	day
t_{treat}	the end of treatment phase / beginning of growth phase	day
t_{end}	the end of growth phase	day
V_0	Number of viable tumor cells at t_0	–
$\eta_{0,HC}$	Environmental stress level at t_0	–
D_0	Doxorubicin (DOX) concentration at t_0	$1\,\mu\text{M}$
S_0	Sorafenib (SOR) concentration at t_0	$22\,\mu\text{M}$
β	Maximal possible growth rate (under optimal growth conditions)	1/day
λ_{ind}	Maximal possible induced death rate (under stressful conditions)	1/day
λ	Natural death rate	1/day
$\gamma_{D,HC}$	Drug metabolization rate of DOX (can be influenced by H and C)	1/day
$\gamma_{S,HC}$	Drug metabolization rate of SOR (can be influenced by H and C)	1/day
	Impact rate of cells reacting to	
α_H, α_C	changes in hypoxia level resp. cirrhosis level	1/day
α_D^-, α_S^-	stressful changes in DOX resp. SOR concentration	1/day
	Sensitivity threshold of cells reacting to stressful changes	
D_{norm}	in DOX concentration, if $S, H, C = 0$	$1\,\mu\text{M}$
$D_{\text{thr},HC}(S)$	in DOX concentration (can be influenced by S, H and C)	$1\,\mu\text{M}$
$S_{\text{thr},HC}$	in SOR concentration (can be influenced by H and C)	$22\,\mu\text{M}$
S_{supp}	SOR concentration threshold to support DOX treatment	$22\,\mu\text{M}$
	Hill-coefficient regarding the	
m_1, m_2	influence function $\delta_{D,HC}^-$ resp. $\delta_{S,HC}^-$	–
m_3	supportive effect of SOR, i.e. function $d_S(S)$	–
a_{max}	Scaling parameter for bounding the supportive effect	–

To clarify their role in the underlying biological setting, we will refer to $D_{\text{thr},HC}$ resp. $S_{\text{thr},HC}$ as *DOX/SOR susceptibility threshold* and to $\delta_{D,HC}^-$ resp. $\delta_{S,HC}^-$ as *DOX/SOR dose-response function*.

Reduced model in CYP-free environment. Measurements quantifying the CYP expression from [22] show that one of the cell lines (Hep3B2), which we want to investigate with the model, did not express CYP for any combination of oxygen and stiffness conditions. Hence, for this cell line the drug concentrations stay constant during the whole treatment phase: $D(t) = D_0$ and $S(t) = S_0$ for $t \in [0, t_{\text{treat}}] = T$. Omitting the ODEs for D and S in $\mathcal{M}_{DS}^{\text{CYP}}$ yields the

following *reduced chemoresistance model* for $t \geq 0$:

$$(\mathcal{M}_{DS}^0) \quad \begin{cases} \dot{V} = \left(\beta - \lambda - (\beta + \lambda_{\text{ind}})\eta \right) V \,, \\[2mm] \dot{\eta} = \left(\dfrac{\alpha_D^- D_0^{m_1}}{\left(D_{\text{thr},HC}(S_0) \right)^{m_1} + D_0^{m_1}} + \dfrac{\alpha_S^- S_0^{m_2}}{S_{\text{thr},HC}^{m_2} + S_0^{m_2}} \right) (1 - \eta)\, \mathbb{1}_T(t) \,, \\[2mm] \text{with } V(0) = V_0 \,, \ \eta(0) = \eta_{0,HC} \,. \end{cases}$$

In contrast, the remaining investigated cell lines (HepG2 and C3Asub28) both show significant CYP expression [22], i.e. it is not possible to simplify the dynamics for D and S and the complete model $\mathcal{M}_{DS}^{\text{CYP}}$ is used to describe their population dynamics.

Mathematical properties of the models. For both models $\mathcal{M}_{DS}^{\text{CYP}}$ and $\mathcal{M}_{DS}^0$ positivity and hence biological meaningfulness can be concluded. Except for the cell density V, all variables are bounded from above. However, unboundedness of V is acceptable in the time-limited setting $(t \leq t_{\text{end}})$ of both models, which motivated the simplification of the logistic growth to an exponential one (recall (3.9)). The only relevant steady state $(\bar{V}, \bar{\eta})$ of the models is the situation of a dying cell population up to the point of extinction: $\bar{V} = 0$. Since all drugs are manually removed from the system by the end of the modeled experiment, their steady states are not of interest. As mentioned at the beginning of Section 3.3, the cell population can only decline if a sufficiently large stress level η is reached during the treatment phase, which gives $\bar{\eta} = \eta(t_{\text{treat}}) > \frac{\beta - \lambda}{\beta + \lambda_{\text{ind}}}$, recall equation (3.10). Due to this condition, the steady state $(\bar{V}, \bar{\eta})$ is stable. If the stress threshold $\frac{\beta - \lambda}{\beta + \lambda_{\text{ind}}}$ is not exceeded, there exists no realistic steady state. All calculations and further details yielding the described boundedness and steady states can be found in Appendix C.

3.3.3 Solving the cell line-specific models

Depending on the coupling of the ODEs, it may not be possible to solve each model analytically. Nevertheless, doing some calculations towards solving the initial value problems $\mathcal{M}_{DS}^{\text{CYP}}$ and $\mathcal{M}_{DS}^0$ are still useful to understand the mathematical structure of the solutions, especially after the treatment phase (for details on the calculations see Appendix C).

Towards solving the general model $\mathcal{M}_{DS}^{\text{CYP}}$. For model calibrations the model $\mathcal{M}_{DS}^{\text{CYP}}$ is solved numerically using the Python function `scipy.integrate.odeint`[3]. Applying separation of variables on each ODE yields, for a time point $t \geq t_{\text{treat}}$ after finishing the treatment:

$$V(t) = V_0 \exp\left((\beta - \lambda)t - (\beta + \lambda_{\text{ind}}) \left(\eta(t_{\text{treat}})(t - t_{\text{treat}}) + \int_0^{t_{\text{treat}}} \eta(\tau)\, \mathrm{d}\tau \right) \right), \qquad (3.16)$$

$$\eta(t) = 1 - (1 - \underbrace{\eta_{0,HC}}_{\leq \frac{\beta - \lambda}{\beta + \lambda_{\text{ind}}}}) \exp\left(-\int_0^t \alpha_D^- \delta_{D,HC}^-\big(D(\tau), S(\tau)\big) + \alpha_S^- \delta_{S,HC}^-\big(S(\tau)\big)\, \mathrm{d}\tau \right) \qquad (3.17)$$

with $D(t) = D_0 \exp\big(-\gamma_{D,HC} \cdot t \big) \cdot \mathbb{1}_T(t)$ and $S(t) = S_0 \exp\big(-\gamma_{S,HC} \cdot t \big) \cdot \mathbb{1}_T(t)$.

---

[3] Depending on the stiffness of the problem, this function switches automatically between Adams methods (nonstiff) resp. backward differentiation formula methods (stiff) by using the LSODA algorithm [68, 69]. All methods use adaptive time stepping.

The model calibrations in this biological context consider the so-called *percentage viability*, i.e. the ratio between the viability of a treated population V^{treat} and a corresponding[4] control population V^{ctrl} without treatment $(D_0, S_0 = 0)$. Equation (3.16) gives for $t \geq t_{\text{treat}}$:

$$\frac{V^{\text{treat}}}{V^{\text{ctrl}}}(t) = \exp\left(-(\beta + \lambda_{\text{ind}})\left(\eta(t_{\text{treat}})(t - t_{\text{treat}}) - \eta_{0,HC} \cdot t + \int_0^{t_{\text{treat}}} \eta(\tau)\,\mathrm{d}\tau\right)\right). \qquad (3.18)$$

We conclude two observations: First, in (3.16), (3.17) and (3.18) the growth and death rates show up solely in the form of $(\beta - \lambda)$ and $(\beta + \lambda_{\text{ind}})$. For model calibrations, this means that instead of β, λ and λ_{ind} we can only estimate $(\beta - \lambda)$ and $(\beta + \lambda_{\text{ind}})$. Second, the term $(\beta - \lambda)$ does not show up explicitly in (3.18) and it is also not implicitly involved, since the stress level (3.17) does not depend on V. This means $(\beta - \lambda)$ has no influence on the percentage viability (the quantity of interest, for which we have measurements) and thus cannot be reconstructed by model calibration. For the same reason, the relation $\eta_{0,HC} \leq \frac{\beta - \lambda}{\beta + \lambda_{\text{ind}}}$ cannot be incorporated in the prior information for estimating $\eta_{0,HC}$ in Section 5.3.

Analytical solution of the reduced model $\mathcal{M}_{DS}^0$. Due to the absence of CYP in the system, the present drug concentrations stay constant during the whole treatment phase, i.e. $D(t) = D_0$ and $S(t) = S_0 \ \forall t \in T$. Therefore, using (3.17), we get

$$\eta(t) = 1 - (1 - \eta_{0,HC})\exp\left(-\left(\alpha_D^- \cdot \delta_{D,HC}^-(D_0, S_0) + \alpha_S^- \cdot \delta_{S,HC}^-(S_0)\right)t\right)$$

as solution for the ESL. This term is independent from all other variables, especially from V, and easy to integrate. By insertion into (3.16), we achieve the explicit solution of V. Hence, model $\mathcal{M}_{DS}^0$ is analytically solvable and the percentage viability (3.18) can be calculated explicitly.

---

[4]This means that except for the drug supply the remaining environmental conditions (oxygen concentration and stiffness) and hence all terms not depending on D and S are the comparable for both populations.

4 Model calibration: estimating unknown parameters with data

It not possible to obtain a quantitative model solution without having values for the involved model parameters. Unknown parameters can be estimated on the basis of data. We distinguish between deterministic and probabilistic approaches to do so. The first ones aim on obtaining parameter values, which analytically minimize the distance between the experimental data and the model solution. The second ones allow to additionally quantify uncertainties such as measurement inaccuracy or model imperfection by the so-called *Bayesian inversion* method, which we realize numerically by using a *Sequential Monte Carlo* (SMC) algorithm.

In Section 4.1 we introduce uncertainty into our mathematical setting by considering inaccuracies and variation in measurements and modeling. The mathematical details about the idea of Bayesian inversion and SMC methods are presented in Section 4.2 resp. 4.3. Note that the majority of the content and formulations in this chapter are taken and adopted from [63] (for consistency within this work, some notations may be altered). For basic mathematical background on probability theory see e.g. [70–72].

4.1 Uncertainties in measurements and modeling

We use data from the experiments described in [21] resp. [22] to calibrate the unknown parameters from for models $\mathcal{M}_N^\eta$ and $\mathcal{M}_N$ resp. $\mathcal{M}_{DS}^0$ and $\mathcal{M}_{DS}^{\mathrm{CYP}}$. In both studies a CellTiter-Blue$^\circledR$ assay was used to monitor the viability of tumor cells as described in Chapter 2. Let I^{total} be an intensity measurement of a specific cell line at time point $\tilde{t}$. Excluding the corresponding measured background intensity I^{BG} (constant) of the cell-free medium, the fluorescence intensity produced by viable cells I^V at time $\tilde{t}$ is assumed to be directly proportional to the density of viable tumor cells $V(\tilde{t})$, which leads to the relation

$$I^V = I^{\mathrm{total}} - I^{\mathrm{BG}} \propto V(\tilde{t}) \qquad \Rightarrow \qquad n_{I/V} = \frac{I^V}{V(\tilde{t})}\,, \tag{4.1}$$

where $n_{I/V}$ denotes the *proportionality constant* translating fluorescence intensity to cell density. Whenever we refer to *intensity measurements* in the following, we mean the fluorescence produced by the cells I^V and neglect the superscript "V" for better readability. For the same reason, we will omit the subscript "I/V" of $n_{I/V}$ if its meaning is clear from the context.

4.1.1 Cell viability data/modeling

In reality, the equation $n = I/V(\tilde{t})$ is not rigorously fulfilled. Possible reasons are model inadequacy, measurement noise and biological fluctuations of the cells' metabolism, which again can affect measurement accuracy. From a mathematical perspective, it makes sense to distinguish the source (model or data) of discrepancies between the observations and the simulation.

Uncertainty in the observations.   To capture the biological and measurement uncertainty, we assume a multiplicative noise for each element of a set of $M \in \mathbb{N}$ measurements $\{I_i\}_{i=1}^M$ and a set of corresponding model solutions $\{V_i\}_{i=1}^M$. In the Bayesian framework that we adopt (see Section 4.3), we model this to be a random variable $\varepsilon_{V,i}$, which we call *uncertainty factor*, such that

$$I_i = n\,V_i \cdot \varepsilon_{V,i} \qquad \text{for } i = 1,\dots,M\,. \tag{4.2}$$

The reason for considering a multiplicative (and, for instance, not additive) noise term is twofold. From a mathematical perspective, it allows to preserve positivity of the data. A more practical motivation is the reasonable assumption that the fluorescence noise of the intensity measurements is proportional to the density of viable cells. This is also supported by the observation of a larger variance for experiments with larger cell numbers in the data from [21]. Furthermore, multiplicative noise has demonstrated to be better suited for fluorescence than additive noise in other experimental settings [73].

Let $\varepsilon_{V,i}$ be i.i.d. and have the unimodal and continuous distribution of a random variable ε with probability density function (PDF) f_ε. Then, the following properties should hold:

$$[\text{P1}]: \quad \text{supp}(f_\varepsilon) \subseteq \mathbb{R}^+ \,, \text{i.e. all measurements are positive;}$$
$$[\text{P2}]: \quad \mathbb{E}(\varepsilon) = 1 \,, \text{i.e. measurements are accurate on average;}$$
$$[\text{P3}]: \quad f_\varepsilon(x) \xrightarrow{x \to \infty} 0 \text{ and } f_\varepsilon(x) \xrightarrow{x \to 0} 0 \,, \text{i.e. outliers are possible but not likely.}$$

Different distributions are possible to accomplish these properties. A small number of shape parameters and an easy calculation to ensure property [P2] are desirable. Therefore, we choose a Gamma distribution $\varepsilon \sim \Gamma(a, b)$, $a, b > 0$ with a few restrictions. This is a plausible choice for multiplicative noise and often used in imaging theory (see e.g. [74–76]). The corresponding expected value is $\mathbb{E}(\varepsilon) = \frac{a}{b}$ and the PDF is given by $f_\varepsilon^{a,b}(x) = \frac{b^a}{\Gamma(a)} x^{a-1} e^{-bx}$, where $\Gamma(\cdot)$ denotes the Gamma function. Property [P1] and the desired behavior near infinity of [P3] are satisfied by definition. The remaining properties can be achieved with the constraint $b = a > 1$:

$$\mathbb{E}(\varepsilon) = \frac{a}{a} = 1 \;\Rightarrow [\text{P2}] \qquad \text{and} \qquad \lim_{x \to 0} f_\varepsilon^{a,a}(x) = \lim_{x \to 0} \left(\frac{a^a}{\Gamma(a)} x^{a-1} e^{-ax} \right) \stackrel{a \geq 1}{=} 0 \;\Rightarrow [\text{P3}].$$

Note that by constraining $b = a > 1$ the shape of the distribution depends only on the parameter a. In fact, a is directly related to the standard deviation σ and hence the variance of the distribution: $\sigma^2 = \text{Var}(\varepsilon) = \frac{a}{a^2} = \frac{1}{a} \Rightarrow a = \frac{1}{\sigma^2}$. Therefore, for $i = 1, \dots, M$ the uncertainty factor $\varepsilon_{V,i}$ for a particular measurement I_i can be modeled by

$$\varepsilon_{V,i} = \frac{I_i}{n \cdot V_i} \sim \Gamma\left(\frac{1}{\sigma^2}, \frac{1}{\sigma^2} \right) \text{ with } \sigma^2 \in (0, 1) \,. \tag{4.3}$$

Model inadequacy.   Aside from fluctuations in the observations, it is reasonable to assume that a corresponding mathematical model from Chapter 3 can only give a simplified description of the complete underlying biological processes due to their high complexity. This can be captured by incorporating *model inadequacy*, e.g. by including an additive random term in (4.2):

$$I_i = (n\, V_i + \chi_i) \cdot \varepsilon_{V,i} \,.$$

The modeling error χ_i could for example be defined as a random variable with a zero-centered truncated (from below) normal distribution to preserve positivity. The latter could also be obtained by a multiplicative error like in [77]. Since the variance of the error's distribution is unknown, it needs to be estimated as a hyper-parameter with the modeling calibrations. This increases the dimension of the parameter space as well as requires appropriate prior assumptions. While the consideration of modeling inadequacy in combination with suitable prior information can be important for obtaining good calibration results [78], we choose to omit it for the applications in this thesis.

On the one hand, this reduces the number of unknown parameters for the model calibrations, i.e. potentially demands less computational effort as well as increases the chance that the

informational content of the data is sufficient to retrieve all parameters. On the other hand, we expect the considerable variation observable in the viability data of [21] to dominate and basically "absorb" the modeling error. In fact, even without considering the modeling error, the calibration results of the first application achieved comparable parameter estimates (see later Section 6.2) as a similar approach in [21], where the error was included.

4.1.2   Percentage viability data/modeling

While in [21] a time series of intensity measurements is available, viability was only measured once in the chemoresistance experiments of [22]. In this context, the so-called *percentage viability* is constructed from the viability measurements to monitor the treatment efficacy. It is given by the ratio between the population sizes of a treated and a corresponding[5] untreated (control) cell population, denoted by V^{treat} and V^{ctrl} respectively. Therefore, the *percentage viability data* has the form

$$I^{\%} = \frac{I^{\mathrm{treat}}}{I^{\mathrm{ctrl}}} \stackrel{(4.2)}{=} \frac{n\, V^{\mathrm{treat}} \cdot \varepsilon_1}{n\, V^{\mathrm{ctrl}} \cdot \varepsilon_2} = \frac{V^{\mathrm{treat}}}{V^{\mathrm{ctrl}}} \cdot \frac{\varepsilon_1}{\varepsilon_2}\,,$$

where the uncertainty factors are respectively Gamma distributed according to (4.3):

$$\varepsilon_1 \sim \Gamma\left(\frac{1}{\sigma_1^2}, \frac{1}{\sigma_1^2}\right) \quad \text{and} \quad \varepsilon_2 \sim \Gamma\left(\frac{1}{\sigma_2^2}, \frac{1}{\sigma_2^2}\right) \qquad \text{with } \sigma_1^2, \sigma_2^2 \in (0,1)\,.$$

The ratio between two such independent random variables is distributed according to a generalized Beta prime distribution via

$$\frac{\varepsilon_1}{\varepsilon_2} \sim \beta'\left(\frac{1}{\sigma_1^2}, \frac{1}{\sigma_2^2}, 1, \frac{\sigma_1^2}{\sigma_2^2}\right),$$

which is shown in Appendix D.I. Under the assumption that the uncertainty variance is not influenced by the treatment of the cells, i.e. $\sigma_1 = \sigma_2$, this distribution simplifies to a standard Beta prime distribution. In particular, the uncertainty factor $\varepsilon_{\%} = \varepsilon_1/\varepsilon_2$ for a percentage viability data point is given by

$$\varepsilon_{\%} = \frac{I^{\mathrm{treat}}/I^{\mathrm{ctrl}}}{V^{\mathrm{treat}}/V^{\mathrm{ctrl}}} \sim \beta'\left(\frac{1}{\sigma^2}, \frac{1}{\sigma^2}\right) \text{ with } \sigma^2 \in (0, 0.5)\,. \tag{4.4}$$

Note that in this context we need $\frac{1}{\sigma^2} > 2 \Rightarrow \sigma^2 < 0.5$ to have a well-defined variance.

4.1.3   Range of uncertainty

We can use the percentiles $\mathcal{P}_{0.05}$ and $\mathcal{P}_{0.95}$ of an (Γ- or β'-distributed) uncertainty factor ε to define the

> *90% (uncertainty) range* around the solution V : $\left[V \cdot \mathcal{P}_{0.05}\,, V \cdot \mathcal{P}_{0.95}\right].$ 　　　(4.5)

In particular, given a specific uncertainty variance, the model expects 90% of the data within this interval, whereas respectively 5% are expected below and above it. The left side of Figure 5 depicts exemplary plots of the PDF f_ε of a Gamma distributed ε for different values of σ^2. It also shows the positive skewness of the distribution. Under consideration of the measurement method, this is a reasonable feature for the uncertainty factors, assuming the cells might not

---

[5]treated and untreated populations are exposed to the same environmental conditions, with exception of the drug concentration

metabolize the assay to their full potential. On the right side of Figure 5 we see an example of a 90% uncertainty range around a solution.
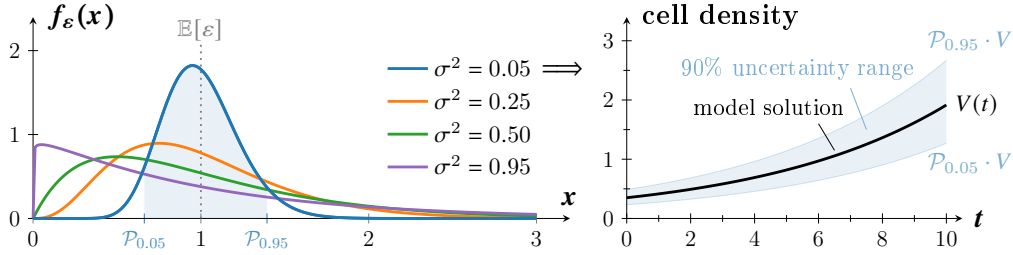

Figure 5: Left: Probability density function f_ε of $\varepsilon \sim \Gamma\left(1/\sigma^2, 1/\sigma^2\right)$ for varying variances σ^2. The percentiles $\mathcal{P}_{0.05}$ and $\mathcal{P}_{0.95}$ are illustrated for $\sigma^2 = 0.05$.
Right: Resulting 90% uncertainty range (shaded area) around an exemplary model solution.

4.2   Bayesian inversion

The task to identify the unknown true parameters from given data is called the *inverse problem*. We solve it using a Bayesian approach, which leads, under mild assumptions, to a naturally well-posed inverse problem [25]. Furthermore, this approach allows to quantify the uncertainty in the estimated parameters and hence it brings more information than a deterministic inversion method, at the price of a higher computational cost.

4.2.1   Data likelihood

Assuming we want to estimate $d \in \mathbb{N}$ parameters by using a set of $M \in \mathbb{N}$ intensity measurements (excluding background intensity), we collect them respectively in a vector:

$$\theta \in \Theta \subseteq \mathbb{R}^d \qquad \text{and} \qquad \left(I_1, \dots, I_M\right)^T = \left(I_i\right)_{i=1}^M \in \mathbb{R}_+^M \,,$$

where Θ denotes the parameter space. The *forward operator*

$$\mathcal{G}_I^{\mathcal{M}} : \begin{cases} \Theta \to \mathbb{R}^M \,, \\ \theta \mapsto \left(\mathcal{G}_{I,i}^{\mathcal{M}}(\theta)\right)_{i=1}^M \,, & \text{with } \mathcal{G}_{I,i}^{\mathcal{M}}(\theta) = n\, V_i \,, \end{cases} \qquad (4.6)$$

maps parameter values to intensities. In particular, it calculates the scaled cell density V_i obtained as the solution of model $\mathcal{M}$ using the parameter values of θ. Similarly, we can define

$$\mathcal{G}_\%^{\mathcal{M}} : \begin{cases} \Theta \to [0,1]^M \,, \\ \theta \mapsto \left(\mathcal{G}_{\%,i}^{\mathcal{M}}(\theta)\right)_{i=1}^M \,, & \text{with } \mathcal{G}_{\%,i}^{\mathcal{M}}(\theta) = \dfrac{V_i^{\text{treat}}}{V_i^{\text{ctrl}}} \,, \end{cases} \qquad (4.7)$$

as the forward operator calculating percentage viability with equation (3.18) using the parameter values in θ. Since the choice of the particular model does not matter for the following paragraphs, we omit the superscript $\mathcal{M}$ for better readability.

Likelihood of viability data.   If a measurement I_i was received under the same environmental conditions as $\mathcal{G}_{I,i}(\theta)$, we can rewrite I_i with

$$I_i \overset{(4.3)}{=} \underbrace{\mathcal{G}_{I,i}(\theta)}_{=\,n\,V_i} \cdot\, \varepsilon_{V,i} \quad \Rightarrow \quad \frac{I_i}{\mathcal{G}_{I,i}(\theta)} = \varepsilon_{V,i} \sim \Gamma\left(\frac{1}{\sigma^2}, \frac{1}{\sigma^2}\right) \text{ with } \sigma^2 \in (0,1)\,.$$

Therefore, the likelihood associated to an observation I_i ($i = 1, \ldots, M$) is defined by

$$L_i(I_i \,|\, \theta) = \frac{1}{Z_i} \left(\frac{I_i}{\mathcal{G}_{I,i}(\theta)} \right)^{1/\sigma^2 - 1} \exp \left(-\frac{1}{\sigma^2} \frac{I_i}{\mathcal{G}_{I,i}(\theta)} \right),$$

with a normalization constant Z_i. This gives the *data likelihood*

$$L(\mathcal{I} \,|\, \theta) \propto \prod_{i=1}^{M} \left(\frac{I_i}{\mathcal{G}_{I,i}(\theta)} \right)^{1/\sigma^2 - 1} \exp \left(-\frac{1}{\sigma^2} \frac{I_i}{\mathcal{G}_{I,i}(\theta)} \right) \qquad (\mathfrak{L}_I)$$

for a set of viability measurements $\mathcal{I} = \left\{ I_i \right\}_{i=1}^{M}$.

Likelihood of percentage viability data.   Analogously, we obtain

$$\frac{I_i^{\text{treat}}}{I_i^{\text{crtl}}} \overset{(4.4)}{=} \frac{V_i^{\text{treat}}}{V_i^{\text{ctrl}}} \cdot \varepsilon_{\%,i} = \mathcal{G}_{\%,i}(\theta) \cdot \varepsilon_{\%,i} \qquad \text{with} \quad \varepsilon_{\%} \sim \beta' \left(\frac{1}{\sigma^2}, \frac{1}{\sigma^2} \right), \; \sigma^2 \in (0, 0.5).$$

With a normalization constant $\tilde{Z}_i$ this leads to the likelihood

$$L_i \left(I_i^{\%} \,\middle|\, \theta \right) = \frac{1}{\tilde{Z}_i} \left(\frac{I_i^{\%}}{\mathcal{G}_{\%,i}(\theta)} \right)^{1/\sigma^2 - 1} \left(1 + \frac{I_i^{\%}}{\mathcal{G}_{\%,i}(\theta)} \right)^{-2/\sigma^2}$$

for an observed percentage viability $I_i^{\%} = I_i^{\text{treat}} / I_i^{\text{crtl}}$. Given a set $\mathcal{I}^{\%} = \left\{ I_i^{\%} \right\}_{i=1}^{M}$ of such data, the corresponding data likelihood is then:

$$L \left(\mathcal{I}^{\%} \,\middle|\, \theta \right) \propto \prod_{i=1}^{M} \left(\frac{I_i^{\%}}{\mathcal{G}_{\%,i}(\theta)} \right)^{1/\sigma^2 - 1} \left(1 + \frac{I_i^{\%}}{\mathcal{G}_{\%,i}(\theta)} \right)^{-2/\sigma^2}. \qquad (\mathfrak{L}_{\%})$$

4.2.2   Bayesian inference

Given a set of data $\mathcal{I} \in \mathbb{R}^M$, we now want to use the data likelihood $L(\mathcal{I} \,|\, \theta)$ to reconstruct the unknown parameter values of the underlying model. Note that for the rest of this chapter we use the general notation $\mathcal{I}$. In practice, $\mathcal{I}$ can refer to a set of intensity measurements or percentage viability data, depending on the application. Hence, $L(\mathcal{I} \,|\, \theta)$ has to be chosen accordingly to formula ($\mathfrak{L}_I$) resp. ($\mathfrak{L}_{\%}$).

The parameter vector θ and the uncertainties $\left(\varepsilon_{V,i} \right)_{i=1}^{M}$, $\left(\varepsilon_{\%,i} \right)_{i=1}^{M}$ are modeled as multi-dimensional random variables taking values in Θ and $\mathbb{R}^M$, respectively. The Bayesian formulation of the problem is the following: Given a prior (measure) μ_0 on Θ, compute the posterior (measure) $\mu^{\mathcal{I}}$ given the data $\mathcal{I}$. The prior in the Bayesian setting is the correspondent of a regularization in deterministic inverse problems [25]. It reflects the knowledge about the parameters before including any information given by the data, whereas the posterior describes the knowledge after seeing the data. With π_0 resp. $\pi^{\mathcal{I}}$ denoting the probability densities of μ_0 resp. $\mu^{\mathcal{I}}$, the Bayes' formula yields the following relation between prior and posterior:

$$\pi^{\mathcal{I}}(\theta) = \frac{L(\mathcal{I} \,|\, \theta) \cdot \pi_0(\theta)}{\int_{\Theta} L(\mathcal{I} \,|\, \theta) \cdot \pi_0(\theta) \, \mathrm{d}\theta} \propto L(\mathcal{I} \,|\, \theta) \, \pi_0(\theta). \qquad (4.8)$$

The proportionality constant of this relation depends only on $\mathcal{I}$. It is called *model evidence* and it can be used to quantitatively compare two models (more details will be provided in Section 6.1.1).

In order to make predictions about the parameter values, we want to sample from the given posterior distribution (4.8). While we can choose the prior, such that we can sample exactly from it with a random number generator, this cannot be done for the posterior, which has a complicated, concentrated density. So-called Monte Carlo methods are a class of algorithms based on repeated random sampling and provide several approaches to draw from a probability distribution like $\mu^{\mathcal{I}}$. The following Section 4.3 presents a selection of such methods, which we use to calibrate the models from Sections 3.2 and 3.3.

4.3   Sequential Monte Carlo (SMC) algorithm

To approximate the posterior measure $\mu^{\mathcal{I}}$, we use the *Sequential Monte Carlo* (SMC) method[6], which we explain in this section based on [26, 40, 79]. In SMC, one considers a sequence of $K \in \mathbb{N}$ intermediate distributions $(\mu_k)_{k=0}^{K}$, such that μ_0 is the prior and $\mu_K = \mu^{\mathcal{I}}$ coincides with the posterior distribution. In particular, over the course of K so-called *SMC steps* we approximate the respective intermediate distribution μ_k at the k-th step ($k = 1, \dots, K$).

The SMC method sequentially draws from the intermediate measures μ_k using a swarm of samples, so-called *particles* $\{\theta_p\}_{p=1}^{P}$ with associated *weights* $\{W_p^k\}_{p=1}^{P}$, where $P \in \mathbb{N}$ is the *sample size* (i.e. the number of particles). This particle approximation gives the probability density of μ_k ($k = 1, \dots, K$) by

$$\pi_k(\theta) \approx \sum_{p=1}^{P} W_p^k \delta_{\theta_p}(\theta) \propto \mathcal{L}_k \cdot \pi_0(\theta) \,, \tag{4.9}$$

where $\mathcal{L}_k = \mathcal{L}_k(\,\cdot\,|\,\theta)$ is an appropriate *intermediate data likelihood* (its explicit argument depends on the method to construct π_k: more details will be provided in the subsequent Subsection 4.3.1) and the proportionality assumption is reasoned analogously to (4.8). There are different possibilities to obtain such particle approximations of π_k. In general, the intermediate distributions μ_k should transition between the prior μ_0 and posterior distribution $\mu_K = \mu^{\mathcal{I}}$ as "smoothly" as possible. This is obtained by sequentially updating the weights $W_p^{k-1} \rightsquigarrow W_p^k$ and filtering for particles in the high-probability region by resampling according to these weights. Therefore, SMC is also known as *Sequential Importance Resampling* (SIR) or sometimes just called *particle filtering* [80].

Each SMC iteration consists of three steps, to which the respective details are explained in the following Sections 4.3.1–4.3.3. We start with the *reweighting step*, in which the particle weights are updated as mentioned previously. There are different approaches to do this (Section 4.3.1). Since this step incorporates the "data knowledge" into the particle representation of the distribution, it can be seen as the centerpiece of each SMC iteration. It is followed by the *resampling step* (Section 4.3.2) and *mutation step* (Section 4.3.3). Both independently contribute to improve the numerical stability and ensure practicability of the algorithm.

4.3.1   Reweighting step – construction of intermediate distributions

In the following paragraphs we describe two methods to perform the reweighting of the particles: *data splitting*[7] [26] and *likelihood tempering* [40]. Data splitting divides up the available data set $\mathcal{I}$, such that the intermediate likelihoods $\mathcal{L}_k$ in (4.9) consider the respective chunks over the

---

[6]Another frequently used method is Markov Chain Monte Carlo (MCMC) [33, Ch. 6-7]. However, SMC is more efficient in the context of time-series data [40, 41], and it allows an easier computation of the so-called model evidence for model comparison [41].

[7]Note that, as there is no commonly used distinctive name, the term *data splitting* is introduced within this thesis for the purpose of being able to terminologically distinguish between the reweighting methods.

course of the SMC steps until the full data set $\mathcal{I}$ is taken into account. In contrast, likelihood tempering makes use of $L(\mathcal{I}\,|\,\theta)^{\nu=0}\,\pi_0(\theta) = \pi_0(\theta)$ and $L(\mathcal{I}\,|\,\theta)^{\nu=1}\,\pi_0(\theta) \propto \pi^{\mathcal{I}}(\theta)$ from (4.8) to tune the data likelihood $L(\mathcal{I}\,|\,\theta)$ by step-wisely increasing the exponent $\nu \in [0,1]$ over the course of the SMC steps. Figure 6 schematically compares and summarizes the idea of both approaches.
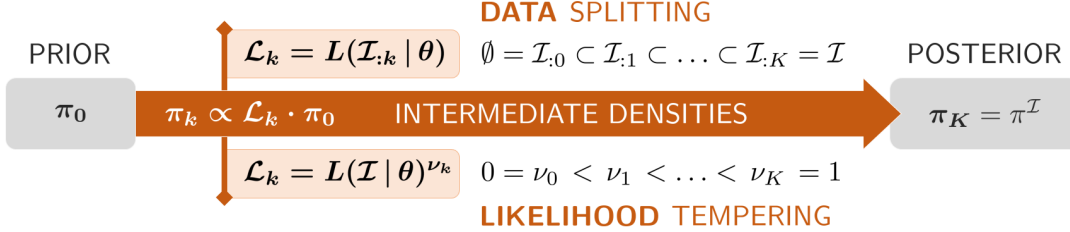

Figure 6: Schematic description of the idea behind SMC with data splitting or likelihood tempering: Sequential construction of intermediate distributions with densities π_k $(k = 1, \ldots, K)$ to bridge from the prior, from which we can sample directly, to the posterior, from which we want to obtain samples.

Note that in general the reweighting solely changes the weights and not the position of the particles.

Data splitting.   As mentioned previously, the idea of data splitting is based on splitting the set of all available measurements $\mathcal{I}$ into progressively increasing data sets:

$$\emptyset = \mathcal{I}_{:0} \subset \mathcal{I}_{:1} \subset \mathcal{I}_{:2} \subset \ldots \subset \underbrace{\mathcal{I}_{:k}}_{\substack{\text{calibration data} \\ \text{at the } k\text{-th SMC step}}} \subset \ldots \subset \mathcal{I}_{:K} = \mathcal{I}\,.$$

Then, the intermediate distribution μ_k $(k = 1, \ldots, K)$ is approximated at the k-th SMC step using the data likelihood of $\mathcal{I}_{:k}$. In particular, analogously to (4.8), Bayesian rule gives

$$\pi_k(\theta) \propto L\big(\mathcal{I}_{:k}\,|\,\theta\big) \cdot \pi_0(\theta)\,,$$

which relates the prior and the k-th intermediate distribution. However, for a sequential construction of the intermediate distributions, we want to have a relation between two consecutive densities π_{k-1} and π_k. Hence, we consider the *increment data* $\mathcal{I}_{k-1:k} = \mathcal{I}_{:k} \backslash \mathcal{I}_{:k-1}$ at the k-th SMC step. This yields the disjoint data sets $\{\mathcal{I}_{k-1:k}\}_{k=1}^K$. Therefore, with $\mathcal{I}_{:k} = \mathcal{I}_{0:1} \,\dot\cup\, \mathcal{I}_{1:2} \,\dot\cup\, \ldots \,,\dot\cup\, \mathcal{I}_{k-1:k}$ we can follow

$$\pi_k(\theta) = \frac{\prod_{s=1}^k L\big(\mathcal{I}_{s-1:s}\,|\,\theta\big)}{Z_k} \cdot \pi_0(\theta) \;\;\text{or, equivalently,}\;\; \pi_k(\theta) = \frac{L\big(\mathcal{I}_{k-1:k}\,|\,\theta\big)}{Z_k^*} \cdot \pi_{k-1}(\theta)\,, \quad (4.10)$$

where the denominators Z_k resp. Z_k^* are normalizing constants and $L(\mathcal{I}_{k-1:k}\,|\,\theta)$ is the *incremental data likelihood* as defined in $(\mathfrak{L}_I)$ or $(\mathfrak{L}_\%)$. We recall (4.9), i.e the representation of the intermediate distribution at the k-th SMC step by a collection of weighted particles: $\pi_k(\theta) \approx \sum_{p=1}^P W_p^k \delta_{\theta_p}(\theta)$. With (4.10), we now have a relation between two consecutive intermediate densities π_k and π_{k-1}, which is used to construct the weight W_p^k of each particle θ_p by updating its previous weight W_p^{k-1} with importance sampling:

$$W_p^k = \frac{w_p^k}{\sum_{p=1}^P w_p^k}\,, \quad \text{with} \quad w_p^k \overset{(4.10)}{=} L(\mathcal{I}_{k-1:k}\,|\,\theta_p)\,W_p^{k-1} \quad \text{for } p = 1, \ldots, P\,. \tag{RW$_\mathcal{I}$}$$

We see that W_p^k is normalized to ensure that $\sum_{p=1}^P W_p^k = 1$, i.e. having a probability distribution, without the need to compute the normalization constant Z_k^* explicitly.

Likelihood tempering. With data splitting we basically start from "nothing" ($\mathcal{I}_{:0} = \emptyset$) at the prior and incrementally incorporate the information of the whole data ($\mathcal{I}_{:K} = \mathcal{I}$) to reach the posterior. One could say that the approach of likelihood tempering somehow "thinks" the other way around. The following explanations are based on [40].

We recall from (4.9) that $\pi_k(\theta) \propto \mathcal{L}_k(\,\cdot\,|\,\theta) \cdot \pi_0(\theta)$, i.e. an intermediate distribution μ_k is determined by an appropriate data likelihood $\mathcal{L}_k$ (besides the prior). This means, two consecutive distributions μ_k and μ_{k+1} are sufficiently similar, if their respective likelihoods $\mathcal{L}_k$ and $\mathcal{L}_{k+1}$ are similar as well. Since the posterior is given by the last intermediate density $\pi_K(\theta) \propto L(\mathcal{I}\,|\,\theta)\,\pi_0(\theta)$, a reasonable choice of the previous one can be $\pi_{K-1}(\theta) \propto L\big(\mathcal{I}\,|\,\theta\big)^\nu \pi_0(\theta)$ for an exponent $\nu \in [0, 1]$ sufficiently close to one. Repeatedly carrying on this idea to the precedent densities $\pi_{N-2}, \ldots, \pi_0$ results in the following approach to construct a "smooth" sequence of intermediate distributions μ_k ($k = 1, \ldots, K$):

$$\pi_k(\theta) = \frac{L\big(\mathcal{I}\,|\,\theta\big)^{\nu_k}}{\tilde{Z}_k} \cdot \pi_0(\theta) = \frac{L\big(\mathcal{I}\,|\,\theta\big)^{\nu_k - \nu_{k-1}}}{\tilde{Z}_k^*} \cdot \pi_{k-1}(\theta)\,, \qquad (4.11)$$

with *temperatures* $0 = \nu_0 < \nu_1 < \ldots < \nu_K = 1$ and normalizing constants $\tilde{Z}_k$ resp. $\tilde{Z}_k^*$. Analogously to (RW$_\mathcal{I}$), the reweighting of each particles θ_p is now achieved by

$$W_p^k = \frac{w_p^k}{\sum_{p=1}^P w_p^k}\,, \quad \text{with} \quad w_p^k \overset{(4.11)}{=} L(\mathcal{I}\,|\,\theta_p)^{\nu_k - \nu_{k-1}} \cdot W_p^{k-1} \quad \text{for } p = 1, \ldots, P\,. \qquad (\text{RW}_\nu)$$

However, we still need to define an appropriate sequence of temperatures $\{\nu_k\}_{k=1}^K$. To do so, we introduce the concept of the so-called *effective sample size* (ESS), which we use for selecting the temperature adaptively [40].

Unless two consecutive intermediate distributions are very similar to each other in terms of their low/high probability area, reweighting (independently of the applied method) will eventually associate a low weight to a significant amount of particles over the course of the SMC steps. Particles with vanishing weights barely contribute to the sample representation of the distribution, i.e. they are in a sense "ineffective". Therefore, we use the ESS P_{eff} to access the depletion of the particle representation of μ_k. It is given by [41]:

$$P_{\text{eff}}\Big(\{W_p^k\}_{p=1}^P\Big) \approx \frac{\Big(\sum_{p=1}^P W_p^k\Big)^2}{\sum_{p=1}^P \big(W_p^k\big)^2} \in [0, P]\,.$$

If there are many particles with low weights, i.e. $P_{\text{eff}} \ll P$, the estimation is only as accurate as a Monte Carlo approximation with a very small number of particles [81]. Since this is not desirable, it is reasonable the choose the temperatures ν_k to maintain a sufficient ESS over the course of the SMC iterations. Hence, given the previous exponent ν_{k-1} we select ν_k to make the according to (RW$_\nu$) updated weights W_p^k fulfill

$$P_{\text{eff}} = P^*\,,$$

with a user-set threshold $P^* = \tau \cdot P$, $\tau \in (0, 1)$. In practice, this can be done e.g. by the bisection method.

4.3.2   Resampling step – improving the particle representation

Independently from the reweighting method, it is reasonable to discard particles with low weight to focus the computational effort on the high portability region [80]. This can be done by *resampling*, which replaces particles according to their weights. Whether resampling is necessary, can be decided with the ESS:

$$P_{\text{eff}} \begin{cases} < P^* & \Rightarrow \text{resample } \{\theta_p\}_{p=1}^P \text{ according to } \{W_p^k\}_{p=1}^P \text{ and uniformly weigh new particles,} \\ \geq P^* & \Rightarrow \text{do not resample.} \end{cases}$$

The appropriate selection of P^* as well as of the resampling method depends on the underlying inverse problem (see Section 5.1 for the particular choices in our calibrations).

We make use of two different resampling schemes[8]. The first approach, which we refer to as *random resampling* (RR), is given in [81] and basically draws P i.i.d. samples with replacement from the set of indices $\{p\}_{p=1}^P$, where p has the probability W_p^k. Alternatively, we apply *systematic resampling* (SR) as described in [80], see Appendix D.II for the algorithmic details. This method has the advantage that it returns the same collection of input samples, if they all have the same weight, i.e. no samples get lost [84]. Recalling that $P_{\text{eff}} \approx P$ indicates almost uniformly weighted particles, we observed this feature to be especially useful for a relatively large ESS P_{eff} at the moment of resampling. Then, SR tends to generate less duplicates (i.e. particles with the same values) compared to RR. This can be beneficial for the algorithmic stability, since duplication reduces the sample diversity, i.e. the coverage of the parameter space. Figure 7 illustrates this observation by comparing the two resampling methods for different ESS in terms of the resulting sample diversity. We see that SR generates less duplicates in total compared to RR (plots in second column), while also resulting in a lower count of the most replicated sample (third column).
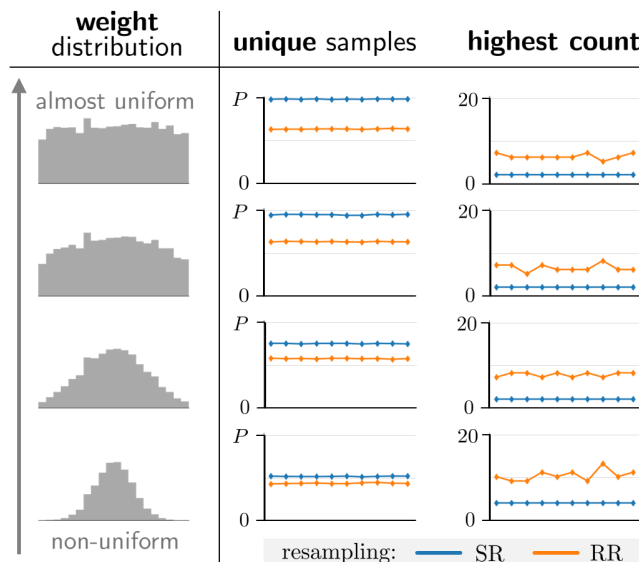
Figure 7: Illustrative comparison of the sample diversity after systematic or random resampling (SR/RR). The horizontal axis of all line plots shows ten different draws (markers).
Column 1: Exemplary histograms of sample weights with different ESS
(from top to bottom: $P_{\text{eff}} \approx P$, $0.98P$, $0.76P$, $0.45P$).
Column 2: Sample size after resampling and removing duplicates.
Column 3: Highest count of a sample after resampling.

---

[8]others are possible, see e.g. [80, 82, 83]

4.3.3   Mutation step – exploring the parameter space

Performing only importance sampling (known as Sequential Importance Sampling, or SIS for short, see e.g. [80]) will eventually lead to degeneracy in the diversity of the particle population, since resampling will discard more and more low-weighted particles in the course of the algorithm. To prevent this we scatter the particles by applying a *Markov kernel* $\kappa_k(\,\cdot\,,\,\cdot\,)$. Such a kernel is μ_k-invariant, i.e. it preserves the particle distribution. A large variety of possible choices for κ_k can be found in the literature on so-called Markov Chain Monte Carlo (MCMC) methods (see e.g. [33, 85]).

For our applications, we adopt the adaptive strategy developed in [40] to construct an appropriate Markov kernel. A random walk Metropolis-Hastings (RWMH) proposal is used on each univariate component, conditionally independently. More precisely, remembering from Section 4.2.1 that each particle is a vector $\theta_p \in \mathbb{R}^d$, RWMH proposes another set of samples $\{q_p\}_{p=1}^P$ with $q_p \in \mathbb{R}^d$ by computing its j-th component via

$$(q_p)_j = (\theta_p)_j + \xi_j \quad \text{with random walk step size } \xi_j \sim \mathcal{N}(0, \epsilon_j^2)\,. \tag{4.12}$$

Eventually, the positions of the current particles are adapted by randomly accepting the proposed samples, i.e.

$$\text{set } \theta_p = q_p \quad \text{with probability} \quad \min\left\{ \frac{\pi_k(q_p)}{\pi_k(\theta_p)}, 1 \right\}.$$

To further improve the particle diversity, this process can be repeated more than once by applying κ_k again on the moved particles. We refer to each application of κ_k as an *MCMC update*. For $H \in \mathbb{N}$ such updates, we can define the *average acceptance ratio*

$$a_k = \frac{1}{H} \sum_{h=1}^H \frac{A_h}{P}\,, \tag{4.13}$$

with $A_h \in \{1, \dots, P\}$ being the number of accepted samples in the h-th MCMC update. The step size ξ_j of (4.12) as well as the number of MCMC updates H affect to which extent the proposed particles are able to explore the parameter space [40].

Role of the acceptance ratio.   A small/large value of a_k from (4.13) means that the majority of the proposed particles lie in the low/high probability region of the current density π_k. For a sufficient ESS P_{eff}, the particles $\{\theta_p\}_{p=1}^P$ are mostly located in the high probability area. Hence, if a_k is small/large, $\{q_p\}_{p=1}^P$ were potentially proposed close/far from the the current particles. A balanced acceptance ratio finds a compromise between sufficiently exploring the parameter space while moving enough particles. To achieve that, it is reasonable to take the variance of the current distribution μ_k as a basis for the random walk's variance [40], which determines the step size. In particular, the variance ϵ_j^2 from (4.12) is given by the tuned empirical marginal variance $\widehat{\text{Var}}_k$ of the j-th component of all current particles $\underline{\theta}_j = \{(\theta_1)_j, \dots, (\theta_P)_j\}$ via

$$\epsilon_j^2 = \rho^2 \cdot \widehat{\text{Var}}_k\big(\underline{\theta}_j\big)\,, \tag{4.14}$$

with a *scaling factor* $\rho > 0$. Eventually, we want to choose ρ in such a way that an appropriate acceptance ratio a_k is reached. Depending on the underlying application, we use two approaches to select ρ, which are explained in the following paragraph. Note that it is also possible to adapt the proposal using empirical covariances instead [86]. However, this would be computationally more expensive in view of possible extensions to parameters which are random fields and therefore very high dimensional.

Adaptive step size tuning. We want to choose the factor ρ in (4.14) to achieve a balanced acceptance ratio. According to [87], it is reasonable to aim for $a_k \approx 0.23$ (for more than two scalar parameters). We present two approaches in the following paragraphs. The choice of the adaptive scheme for our model calibrations depends on the underlying inverse problem (details can be found in Section 5.1).

<u>Scheme 1</u>. One possibility is introduced in [40] as checking the acceptance ratio a_{k-1} of the previous SMC step to judge, whether the step sizes ξ_j $(j = 1, \ldots, d)$ need to be increased or decreased. In particular, we adaptively set the random walk variance at the k-th SMC step to

$$\epsilon_j^2 = \rho_{k-1}^2 \cdot \widehat{\mathrm{Var}}_k(\underline{\theta}_j)$$

with recursively defined scaling factor

$$\rho_0 = 1 \quad \text{and} \quad \rho_s = \begin{cases} \rho_{s-1} \cdot 2 & \text{if } a_{k-1} > 0.30, \\ \rho_{s-1}/2 & \text{if } a_{k-1} < 0.15, \\ \rho_{s-1} & \text{otherwise,} \end{cases} \quad \text{for } s = 1, \ldots, K-1. \qquad (\mathrm{MH}_{k-1})$$

One drawback of this approach is that the readjustment of ϵ_j^2 can only be done once per SMC step. If this is not enough to reach an appropriate acceptance ratio, this can only be noticed and counteracted with a delay of one SMC step. Depending on the evolution of the marginal variances, it might not be possible to reach a reasonable acceptance ratio over the course of several SMC steps.

<u>Scheme 2</u>. We extend the idea of [40] by the possibility to readjust the step size of the random walk between consecutive MCMC updates. Let $H^* \in \{1, \ldots, H\}$ be the number of MCMC updates, after which we want to check the acceptance ratio and potentially adapt the step size. Then, we can split the H MCMC steps into $\lceil H/H^* \rceil$ compartments, which we denote by $\mathfrak{H}_l$, $l = 1, \ldots, \lceil H/H^* \rceil$. For example, suppose we want to do $H = 10$ MCMC updates and check the acceptance ratio after every $H^* = 4$-th step to potentially update the scaling factor. Then, we get $\lceil H/H^* \rceil = 3$ compartments of MCMC steps after which the scaling factor is updated, respectively:

$$\{1, \ldots, 10\} = \underbrace{\{1, 2, 3, 4\}}_{\mathfrak{H}_1} \,\dot\cup\, \underbrace{\{5, 6, 7, 8\}}_{\mathfrak{H}_2} \,\dot\cup\, \underbrace{\{9, 10\}}_{\mathfrak{H}_3}.$$

Analogously to (4.13), we define the *partial acceptance ratio* for the l-th compartment as

$$a_{k,l}^* = \frac{1}{|\mathfrak{H}_l|} \sum_{h \in \mathfrak{H}_l} \frac{A_h^*}{P},$$

where $A_h^* \in \{1, \ldots, P\}$ is the number of accepted proposals in the h-th MCMC update. We check this acceptance ratio analogously to scheme (MH_{k-1}): we set the variance of the random walk for the h-th MCMC update at the k-th SMC step as

$$\epsilon_j^2 = \rho_{k,h}^2 \cdot \widehat{\mathrm{Var}}_k(\underline{\theta}_j), \qquad (4.15)$$

where the scaling factor $\rho_{k,h}$ is defined recursively as follows. After each compartment $\mathfrak{H}_l$ of MCMC updates is done, we adapt the scaling $\rho_{k,h}$ according to the partial acceptance ratio of the recently completed compartment of steps. For the first MCMC update of a SMC step, we

adapt the scaling factor according to the partial acceptance ratio of the last compartment of the previous SMC step. The mathematical description of this recursive scheme is given by:

$$
\rho_{k,s+1} = \begin{cases} \rho_{k,s} \cdot 2 & \text{if } s = lH^* \text{ and } a^*_{k,l} > 0.30, \\ \rho_{k,s} / 2 & \text{if } s = lH^* \text{ and } a^*_{k,l} < 0.15, \\ \rho_{k,s} & \text{otherwise,} \end{cases}
$$

$$
\rho_{k+1,1} = \begin{cases} \rho_{k,H} \cdot 2 & \text{if } a^*_{k,\lceil H/H^* \rceil} > 0.30, \\ \rho_{k,H} / 2 & \text{if } a^*_{k,\lceil H/H^* \rceil} < 0.15, \\ \rho_{k,H} & \text{otherwise,} \end{cases}
$$

for $k = 1, \ldots, K - 1$,
$s = 1, \ldots, H - 1$ (MH*)
and $l = 1, \ldots, \lceil H/H^* \rceil - 1$.

Table 5 demonstrates the described scheme for exemplary MCMC updates with $H^* = 4$ and $H = 10$.

Table 5: Application of the adaptive scheme (MH*) for the k-th SMC step and h-th MCMC update, given exemplary acceptance ratios A^*_h/P. It splits the $H = 10$ MCMC steps into compartments $\mathfrak{H}_l$ of maximal size $H^* = 4$ and checks the respective partial acceptance ratios $a^*_{k,l}$ to readjust the scaling factor $\rho_{k,h}$ in between MCMC steps.

	$k = 1$										$k = 2$	
h	1	2	3	4	5	6	7	8	9	10	1	$\cdots$
		$\mathfrak{H}_{l=1}$				$\mathfrak{H}_{l=2}$				$\mathfrak{H}_{l=3}$		
A^*_h/P	0.10	0.12	0.09	0.10	0.35	0.36	0.33	0.30	0.22	0.21	$\cdots\cdots$	
		$a^*_{k,l=1} < 0.15$				$a^*_{k,l=2} > 0.30$			$0.15 < a^*_{k,l=3} < 0.30$			
$\rho_{k,h}$	1.0	1.0	1.0	1.0	0.5	0.5	0.5	0.5	1.0	1.0	1.0	$\cdots$
					$\cdot 1/2 \Uparrow$				$\cdot 2 \Uparrow$	keep $\Uparrow$		

Note that Table 5 is just a demonstration example. In practice, the acceptance ratios in the last compartment $\mathfrak{H}_3$ will not lie in the range $[0.15, 0.30]$ after rescaling $\rho_{1,8} \rightsquigarrow \rho_{1,9}$. Instead, we expect them to be similar to the ones of $\mathfrak{H}_1$, since the scaling factor has the same value. In such situations, where consecutive partial acceptance ratios $a^*_{k,l} \rightsquigarrow a^*_{k,l+1}$ switch from being too small (< 0.15) to being too large (> 0.30), or vice versa, the scaling factor will jump back and forth between two values due to alternating division and multiplication with the factor 2 (e.g. Table 5: $1.0 \rightsquigarrow 0.5 \rightsquigarrow 1.0$ for $\mathfrak{H}_1 \rightsquigarrow \mathfrak{H}_2 \rightsquigarrow \mathfrak{H}_3$). This indicates that by picking a scaling factor between the two alternating values, we could achieve an acceptance ratio in the desired range $[0.15, 0.30]$. We make use of this observation by enhancing (MH*), resulting in the following adaptive scheme to set the variance (4.15) of the random walk:

$$
\rho_{k,s+1} = \begin{cases} \rho_{k,s} \cdot 2 & \text{if } s = lH^* \text{ and } a^*_{k,l} > 0.30, \\ \rho_{k,s} / 2 & \text{if } s = lH^* \text{ and } a^*_{k,l} < 0.15, \\ \rho_{k,s} & \text{otherwise,} \end{cases}
$$

$$
\tilde{\rho}_{k+1,1} = \begin{cases} \rho_{k,H} \cdot 2 & \text{if } a^*_{k,\lceil H/H^* \rceil} > 0.30, \\ \rho_{k,H} / 2 & \text{if } a^*_{k,\lceil H/H^* \rceil} < 0.15, \\ \rho_{k,H} & \text{otherwise,} \end{cases}
$$

$$
\rho_{k+1,1} = \begin{cases} \frac{1}{2}\big(\rho_{k,H} + \tilde{\rho}_{k+1,H}\big) & \text{if } \bar{a}^*_k \in [0.15, 0.30], \\ \tilde{\rho}_{k+1,1} & \text{otherwise,} \end{cases}
$$

for $k = 1, \ldots, K - 1$,
$s = 1, \ldots, H - 1$ (MH$^*_{k,h}$)
and $l = 1, \ldots, \lceil H/H^* \rceil - 1$,

where $\bar{a}_k^* = \frac{1}{2}\left(a_{k,\lceil H/H^*\rceil-1}^* + a_{k,\lceil H/H^*\rceil}^*\right)$ is the mean of the last two partial acceptance ratios of the k-th SMC step and $\rho_{1,1} = 1$.

Appropriate number of MCMC updates. So far, we have considered the number of MCMC updates H to be constant for the whole SMC algorithm. However, the more often the Markov kernel is applied, the further we can reach to explore the parameter space. This becomes especially relevant if the selected variance ϵ_j^2 and hence the step size ξ_j of the random walk are small. Therefore, it can be reasonable to adaptively choose the number of MCMC updates in dependence of the scaling factor $\rho_{k,h}$ for $h = 1, \ldots, H$. Based on [40] we can use for example

$$H_{k,h} = \min\left\{\max\left\{\left\lfloor\frac{\zeta}{\rho_{k,h}^2}\right\rfloor, H_{\min}\right\}, H_{\max}\right\}, \qquad \text{(MH}_H)$$

where $\zeta > 0$ is a global parameter and $H_{\min}$ resp. $H_{\max}$ are lower/upper bounds. The latter should enable a minimum extent of particle movement (lower bound) as well as avoid an exploding number of MCMC updates (upper bound). Note that, while this adaptive approach improves the exploration of the parameter space, it can significantly increase the computational cost of the algorithm, since the forward model has to be solved for each MCMC update. Hence, we make it dependent on the underlying model calibration, whether we employ $H = \text{const.}$ or $H_{k,h}(\rho_{k,s})$, see upcoming Section 5.1.

5   Applied model calibration frameworks

As described in Section 4.3, we use the SMC method to calibrate the models of Chapter 3 and investigate the underlying biological processes. This chapter explains how we choose the algorithmic features of the SMC method. We discuss which aspects have to be considered to make appropriate decisions and how these are implemented in the model calibrations. First, we have to choose the reweighting, resampling and MCMC methods for the SMC algorithm (Section 5.1). Second, if data splitting is applied, we need to determine how to utilize the available data in the course of the SMC steps (Section 5.2). Eventually, we construct reasonable prior distributions for the unknown parameters (Section 5.3).

Parameter estimation is performed in Python 3 adapting the code structure from [81]. Note that some content and formulations of Sections 5.2.1 and 5.3.1 are taken from our publication [63]. For consistency within this work, some notations may be altered – this concerns especially the notation for the data sets in Section 5.2.1.

5.1   Application of SMC on the model calibrations

Recalling from the previous sections, we have several choices for the methods to do the reweighting step (data splitting or likelihood tempering), resampling (random or selective resampling) and MCMC updates (adaptive scheme (MH_{k-1}) or $(\mathrm{MH}_{k,h}^*)$). The particular selection of those is motivated and justified in the following.

5.1.1   Selection of the reweighting method

As introduced in Section 4.3.1, we can use data splitting or likelihood tempering to construct the intermediate distributions. However, data splitting is computationally more efficient if the model solution has to be calculated numerically and the available measurements are given as a time-series[9]. This is applicable for calibrating the models $\mathcal{M}_N^\eta$ and $\mathcal{M}_N$ using the corresponding data from [21]. Hence, data splitting is used for these applications, as it showed to be effective in combination with a large sample size ($P = 50\,000$).

For the calibration of models $\mathcal{M}_{DS}^0$ and $\mathcal{M}_{DS}^{\mathrm{CYP}}$ with data from [22], we observed difficulties to construct the intermediate distributions using only data splitting. Recalling that the corresponding measurements are given in terms of percentage viability data for a particular selection of drug dosages, the change of viability between two consecutive data sets $\mathcal{I}_{:k-1}$ and $\mathcal{I}_{:k}$ can be drastic. This causes a large information gain between two the respective SMC steps, which translates mathematically to a large discrepancy between the respective data likelihoods. In this case, the majority of particles are in the low-probability region and are sorted out by resampling. Eventually, if the sample size P is not sufficiently large, the remaining particles are not enough to appropriately represent the intermediate distribution μ_k. Increasing P would allow for compensating this issue. However, this also significantly increases the computational cost of the algorithm as the forward operator $\mathcal{G}$ has to be calculated for each particle and each time

---

[9]In particular, for $0 \le t_1 < t_2 < \ldots < t_k$, suppose $\mathcal{I}_{t_k}$ being the data increment for the k-th SMC step, consisting of measurement(s) at a time point t_k, and $\{\mathcal{I}_{t_1}, \ldots, \mathcal{I}_{t_{k-1}}\}$ being the calibration data set of the previous SMC step. Then, to get the respective data likelihoods, we actually do not need to call the numerical solver for each time point t_i ($i = 1, \ldots, k$) separately, but only once on the interval $[t_0, t_k]$ (where $t_0 \in [0, t_1]$ is the initial time point of the model) and specify that the time discretization should include all time points $\{t_1, \ldots, t_k\}$. In contrast, if the calibration data set is not a time-series, we need to call the solver for each data increment, respectively.

the algorithm uses the data likelihoods, recall ($\mathfrak{L}_I$) and ($\mathfrak{L}_\%$). Due to the model complexity of $\mathcal{M}_{DS}^0$ and $\mathcal{M}_{DS}^{\mathrm{CYP}}$, it is not practical to increase the sample size P up to the point where this issue is resolved. Therefore, for these models we choose to do a "nested" approach [79]: while still using data splitting to construct the intermediate distributions to get from the prior to the posterior, we additionally perform likelihood tempering to bridge between two consecutive intermediate distributions, if necessary. The algorithmic details can be found in Algorithms 2 and 3 in Section 5.1.3.

5.1.2 Selection of the resampling method and MCMC scheme

After the reweighting step, the particle approximation of the respective intermediate distribution is improved by resampling and subsequent mixing of the particles (recall Sections 4.3.2 and 4.3.3). In general, we try to keep the calibration algorithms as simple as possible to maintain a manageable computation time. For models $\mathcal{M}_N^\eta$ and $\mathcal{M}_N$ applying random resampling and the basic adaptive MCMC scheme (MH_{k-1}) over the course of $H = 5$ MCMC steps showed to be sufficient to get robust results. Resampling is performed if the effective sample size P_{eff} is below the threshold $P^* = 0.75 \cdot P$. The choices of H and P^* are adopted from [81].

However, for models $\mathcal{M}_{DS}^0$ and $\mathcal{M}_{DS}^{\mathrm{CYP}}$ the effectiveness of the calibration turned out to be dependent on the underlying data set/cell line. We started with investigating the data of cell line Hep3B2 (with no significant CYP expression). For this purpose, we found random resampling and scheme (MH_{k-1}) with $H = 5$ to be still expedient, but not optimal. In particular, the algorithm occasionally shows difficulties to sufficiently mix the particles if resampling generates a large number of duplicates. Hence, for the investigation of cell lines HepG2 and C3Asub28 we switch to systematic resampling and the extended adaptive MCMC scheme ($\mathrm{MH}_{k,h}^*$) to reduce the generation of duplicates and improve the mixing. The method of likelihood tempering is designed to keep the ESS P_{eff} from dropping below the threshold P^*. Unless we have reached the the last tempering step (i.e. a temperature $\nu = 1$), the ESS after reweighting will be $P_{\mathrm{eff}} \approx P^*$ by construction. Therefore, we resample at each tempering step with $\nu < 1$ [41].

5.1.3 Summary of the applied calibration algorithms

Concluding the methodological choices made in Sections 5.1.1–5.1.2, we get three different algorithms depending on the underlying inverse problem. The general structure of all algorithms is the same: we achieve appropriately weighted particles to approximate $\mu_K = \mu^{\mathcal{I}}$ by starting with uniformly weighted particles distributed according to the prior μ_0 and iteratively move the samples to the next measure μ_{k+1} ($k = 0, \ldots, K$) in a resampling and a mutation step [27, Ch. 5]. Additional information on the appropriate choice of the particular sample size P for both applications will be provided in Section 5.3.

For the nutrient deprivation models $\mathcal{M}_N^\eta$ and $\mathcal{M}_N$ a basic version of the SMC method in combination with a large sample size $P = 50\,000$ was sufficient to get reasonable results, see Algorithm 1. In particular, we use data splitting over the course of K SMC steps with random resampling and a fixed number of MCMC updates using scheme (MH_{k-1}).

Algorithm 1 – SMC with data splitting (for models $\mathcal{M}_N^\eta$ and $\mathcal{M}_N$)

Sampling settings: sample size $P = 50\,000$ (particle index $p = 1, \ldots, P$), threshold $P^* = 0.75 \cdot P$

1: $k = 0:$ sample $\theta_p \sim \mu_0$ and set $W_p^0 = 1/P$

2: **for** $k = 1, \ldots, K$ **do**   ▷ **data splitting**

3:     $w_p^k = L(\mathcal{I}_{k-1:k} \,|\, \theta_p)\, W_p^{k-1} \;\Rightarrow\; W_p^k = w_p^k / \big(\sum_{p=1}^P w_p^k\big)$ ▷ reweighting with (RW$_\mathcal{I}$) and ($\mathfrak{L}_I$)

4:     **if** $P_{\text{eff}} < P^* = 0.75 \cdot P$ **then** resample: ▷ random resampling

5:         (i): sample indices ι_p acc. to distribution $\mathcal{R}$ of particle indices,
                 i.e. $(\iota_1, \ldots, \iota_P) \sim \mathcal{R}(W_1^k, \ldots, W_P^k)$

6:         (ii): set $\theta_p = \theta_{\iota_p}$ and $W_p^k = 1/P$

7:     **end if**

8:     **for** $h = 1, \ldots, H = 5$ **do**   ▷ MCMC updates with (MH$_{k-1}$)

9:         move $\theta_p \sim \kappa_k(\theta_p \,, \cdot)$ with MCMC scheme (MH$_{k-1}$)

10:    **end for**

11: **end for**

For the chemoresistance models $\mathcal{M}_{DS}^0$ and $\mathcal{M}_{DS}^{\text{CYP}}$, sole data splitting was not sufficient to achieve reasonable posteriors with a practical sample size. Hence, we use a nested approach of performing likelihood tempering within an external data splitting scheme to calibrate these models with a sample size of $P = 10\,000$. The choice of the resampling and MCMC methods depends on the investigated data/cell line. For Hep3B2 (no CYP expression) we use Algorithm 2 with random resampling and MCMC scheme (MH$_{k-1}$), while for HepG2/C3Asub28 (relevant CYP expression) we apply Algorithm 3 with selective resampling and MCMC scheme (MH$_{k,h}^*$).

Algorithm 2 – SMC with nested reweighting (for cell line Hep3B2)

Sampling settings: sample size $P = 10\,000$ (particle index $p = 1, \ldots, P$), threshold $P^* = 0.75 \cdot P$;
MCMC settings: $H_{\min} = 8$, $H_{\max} = 64$, $\zeta = 1$

1: $k = 0:$ sample $\theta_p \sim \mu_0$ and set $W_p^0 = 1/P$, $H_{0,H} = H_{\min}$

2: **for** $k = 1, \ldots, K$ **do**   ▷ **external: data splitting**

3:     $s = 0:$ set $\tilde{\mathcal{I}} = \mathcal{I}_{k-1:k}$, $\tilde{W}_p^0 = W_p^{k-1}$, $\nu_s = 0$ ▷ **internal: likelihood tempering**

4:     **while** $\nu_s < 1$ **do**   ▷ reweighting with (RW$_\nu$) and ($\mathfrak{L}_\%$)

5:         determine $\nu_{s+1} \in (\nu_s, 1]$ such that $P_{\text{eff}}\big(\{\tilde{W}_p^{s+1}\}_{p=1}^P\big) = P^*$
                for $\tilde{W}_p^{s+1} = \tilde{w}_p^{s+1} / \big(\sum_{p=1}^P \tilde{w}_p^{s+1}\big)$ with $\tilde{w}_p^{s+1} = L(\tilde{\mathcal{I}} \,|\, \theta_p)^{\nu_{s+1} - \nu_s} \tilde{W}_p^s$

6:         resample particles: ▷ random resampling

7:         (i): sample indices ι_p acc. to distribution $\mathcal{R}$ of particle indices,
                 i.e. $(\iota_1, \ldots, \iota_P) \sim \mathcal{R}(W_1^k, \ldots, W_P^k)$

8:         (ii): set $\theta_p = \theta_{\iota_p}$ and $W_p^k = 1/P$

9:         $h = 1:$ set $H = H_{k-1,H}$ acc. to MH$_H$ ▷ MCMC updates with (MH$_{k-1}$)

10:        **while** $h \leq H$ **do**

11:            move $\theta_p \sim \kappa_k(\theta_p \,, \cdot)$ with MCMC scheme (MH$_{k-1}$) while updating $H = H_{k,h}$

12:            $h = h + 1$

13:        **end while**

14:        $s = s + 1$

15:    **end while**

16:    set $W_p^k = \tilde{W}_p^s$

17: **end for**

Algorithm 3 – SMC with nested reweighting (for cell lines HepG2 and C3Asub28)

Sampling settings: sample size $P = 10\,000$ (particle index $p = 1, \dots, P$), threshold $P^* = 0.75 \cdot P$;
MCMC settings: $H_{\min} = 8$, $H_{\max} = 64$, $\zeta = 1$

1: $k = 0$: sample $\theta_p \sim \mu_0$ and set $W_p^0 = 1/P$, $H_{0,H} = H_{\min}$
2: **for** $k = 1, \dots, K$ **do**   ▷ **external: data splitting**
3:      $s = 0$: set $\tilde{\mathcal{I}} = \mathcal{I}_{k-1:k}$, $\tilde{W}_p^0 = W_p^{k-1}$, $\nu_s = 0$ ▷ **internal: likelihood tempering**
4:      **while** $\nu_s < 1$ **do**   ▷ reweighting with (RW_ν) and $(\mathcal{L}_\%)$
5:          determine $\nu_{s+1} \in (\nu_s, 1]$ such that $P_{\mathrm{eff}}\big(\{\tilde{W}_p^{s+1}\}_{p=1}^P\big) = P^*$
            for $\tilde{W}_p^{s+1} = \tilde{w}_p^{s+1}/\big(\sum_{p=1}^P \tilde{w}_p^{s+1}\big)$ with $\tilde{w}_p^{s+1} = L(\tilde{\mathcal{I}} \mid \theta_p)^{\nu_{s+1} - \nu_s}\, \tilde{W}_p^s$
6:          resample particles acc. to weights $\{\tilde{W}_p^{s+1}\}_{p=1}^P$ ▷ systematic resampling
7:          $h = 1$: set $H = H_{k-1,H}$ acc. to MH_H ▷ MCMC updates with $(\mathrm{MH}_{k,h}^*)$
8:          **while** $h \leq H$ **do**
9:              move $\theta_p \sim \kappa_k(\theta_p, \cdot)$ with MCMC scheme $(\mathrm{MH}_{k,h}^*)$ while updating $H = H_{k,h}$
10:             $h = h + 1$
11:         **end while**
12:         $s = s + 1$
13:     **end while**
14:     set $W_p^k = \tilde{W}_p^s$
15: **end for**

Note that, in general, the calibration of the Hep3B2 data with model $\mathcal{M}_{DS}^0$ did work well with Algorithm 2. However, for two out of altogether sixteen calibrations the posteriors showed unwanted artifacts due to a large amount of duplicates in the particles. These calibrations were repeated using Algorithm 3, which improved the robustness of the calibration results for Hep3B2.

5.2   Fragmentation of the full calibration data for data splitting

Besides deciding on particular algorithmic methods, we need to appropriately split the set of available measurements $\mathcal{I}$ into the calibration data sets $\mathcal{I}_{:1} \subset \mathcal{I}_{:2} \subset \dots \subset \mathcal{I}_{:K} = \mathcal{I}$ to use them for the data splitting over K SMC steps. In this matter, we need to consider that a data point has a particular informative content on specific parameters. For example, given an exemplary viability measurement $\tilde{V}$, this data point contains the information that the parameter V_{cap} for the maximal possible population size, has to be larger than this value: $V_{\mathrm{cap}} \geq \tilde{V}$ (up to measurement/model inaccuracy). Therefore, the informative gain between two consecutive calibration data sets $\mathcal{I}_{:k}$ and $\mathcal{I}_{:k+1}$ has a significant influence on the data likelihood of a particle and hence on the reweighting process, which we explain in more detail in the following paragraphs. Subsequently, we give the particular calibration data sets for the calibration of models $\mathcal{M}_N^\eta$, $\mathcal{M}_N$ (Section 5.2.1) and $\mathcal{M}_{DS}^0$, $\mathcal{M}_{DS}^{\mathrm{CYP}}$ (Section 5.2.2).

Omitting uninformative data.   If we have no significant information gain between two consecutive data sets $\mathcal{I}_{:k}$ and $\mathcal{I}_{:k+1}$, the weights of the particles will barely change from W^k to W^{k+1}. This means that considering the data increment $\mathcal{I}_{k:k+1} = \mathcal{I}_{:k+1} \setminus \mathcal{I}_{:k}$ does not contribute to the approximation the posterior. Therefore, we can omit $\mathcal{I}_{k:k+1}$ to save computational time, since we need a smaller number of SMC steps to eventually cover the whole set of calibration data.

Avoiding "information jumps".   In contrast, if the information gain from $\mathcal{I}_{:k}$ to $\mathcal{I}_{:k+1}$ is very large, the consideration of the corresponding data increment can significantly alter the high probability region in the parameter space. As a result, very small weights might be associated

to the majority of the parameter samples in the reweighting step. This yields an ineffective particle representation of the intermediate distribution and triggers resampling, which discards the low-weighted samples. We end up with a small number of distinct samples, i.e. the variance of the particle distribution tends to zero and the intermediate distribution degenerates. At this point the calculations possibly fail due to numerical issues. If the algorithm proceeds, the MCMC updates might reintroduce sample diversity in the course of the subsequent SMC steps. This could suffice for reaching the correct posterior distribution, however it is not guaranteed, since the reach of the random walk is proportional to the (vanishing) variance of the intermediate distributions.

Note that reweighting by likelihood tempering can counteract this issue, since it preserves a sufficient ESS. This is the reason why for some model calibrations sole data splitting is not sufficient and we switch to the nested SMC approach. However, in this context large information jumps between two consecutive data sets $\mathcal{I}_{:k}$ and $\mathcal{I}_{:k+1}$ will result in the execution of many internal tempering steps to appropriately bridge between the respective intermediate distributions μ_k and μ_{k+1}. This can significantly increase the computation time of the algorithm. Hence, in summary it is desirable to avoid excessive information jumps while deciding on the fragmentation of the data.

5.2.1   Calibration with the nutrient deprivation data

As described in Section 4.1.1, the experiments in [21] modeled by $\mathcal{M}_N^\eta$ and $\mathcal{M}_N$ monitor the dependence between cell viability $V(t)$ and nutrient supply $N(t)$ over time t.

Structure of the available viability data.   The tumor cells grow under constant nutrient conditions N_0 and viability is measured daily over a period of seven days (at $t \approx 0, 1, \ldots, 7$). Nutrients are supplied with a particular concentration between 0% to 10% of fetal bovine serum (FBS). A concentration of $N_0 = 0 \propto 0\%\,\text{FBS}$ does not provide any nutrients, whereas $N_0 = 1 \propto 10\%\,\text{FBS}$ generates optimal growth conditions. All experiments are started with several populations of different initial size $V_0 \propto 10^5\,\text{cells/mL}$. There are four biological replicates to estimate statistical significance and repeatability of the measurements, i.e. in total we have four data points for each combination of t, V_0 and N_0. We collect all viability measurements corresponding to a specific nutrient concentration N_0 in a data set. These are denoted by "D0", "D1", $\ldots$, "D4" respectively for a concentration of $0/2.5/5/7.5/10\%$ FBS and are employed for model calibrations. There is another experiment in [21], which particularly investigates cell viability under optimal growth conditions over a period of 21 days. The corresponding data set is not considered for the model calibrations, but used in addition to D0–D4 to validate the calibration results. We denote it with "DV" ("V"alidation data set). Table 6 summarizes the available data sets.

Table 6: Overview over the nutrient deprivation data and the corresponding initial values. D0–D4 are used to calibrate the models $\mathcal{M}_N^\eta$ and $\mathcal{M}_N$ and DV to validate the calibration results. The initial values η_0 are only needed for model $\mathcal{M}_N^\eta$.

Data set	Nutrition (in % FBS)	Duration (in days)	Initial values in the models V_0	N_0	η_0
D0	0.0	7	$1.00, 0.50, 0.25$	0.00	0.00
D1	2.5	7	$1.00, 0.50, 0.25$	0.25	0.00
D2	5.0	7	$1.00, 0.50, 0.25$	0.50	0.00
D3	7.5	7	$1.00, 0.50, 0.25$	0.75	0.00
D4	10.0	7	$1.00, 0.50, 0.25$	1.00	0.00
DV	10.0	21	$1.00, 0.50, 0.25, 0.10, 0.05$	1.00	0.00

Order and segmentation of the calibration data.   As depicted in Figure 8, we use the measurements of D0–D4 over the course of $K = 8 \cdot 3 = 24$ SMC steps. In particular, at the k-th step we include $4 \cdot 5 = 20$ measurements (four biological samples per N_0) to the data of the previous step while iterating over the eight points in time (inner loop) and over the three seeding densities (outer loop). In total, we use $M_K = 24 \cdot 20 = 480$ measurements. For $k = 1, \dots, K$, the data collections $\mathcal{I}_{:k}$ with $\mathcal{I}_{:1} \subset \mathcal{I}_{:2} \subset \dots \subset \mathcal{I}_{:K}$ can be schematically outlined by:

- calibration data at k-th SMC step: $\mathcal{I}_{:k} = \{I_{k,i}\}_{i=1}^{M_k}$ with $|\mathcal{I}_{:k}| = M_k = k \cdot 20$,

- $\mathcal{I}_{:1} = \{I_{1,1}, \dots, I_{1,20}\}$ contains all measurements for $t = 0$, $V_0 = 1$,

- $\mathcal{I}_{:2} = \mathcal{I}_{:1} \cup \{\text{all measurements for } t \approx 1, V_0 = 1\}$,

- analogously: $\mathcal{I}_{:3}, \dots, \mathcal{I}_{:8}$ respectively add measurements for $t \approx 2, \dots, 7$ and $V_0 = 1$,

- $\mathcal{I}_{:9}, \dots, \mathcal{I}_{:16}$ resp. $\mathcal{I}_{:17}, \dots, \mathcal{I}_{:24}$ add data for $t \approx 0, \dots, 7$ and $V_0 = 0.5$ resp. $V_0 = 0$.
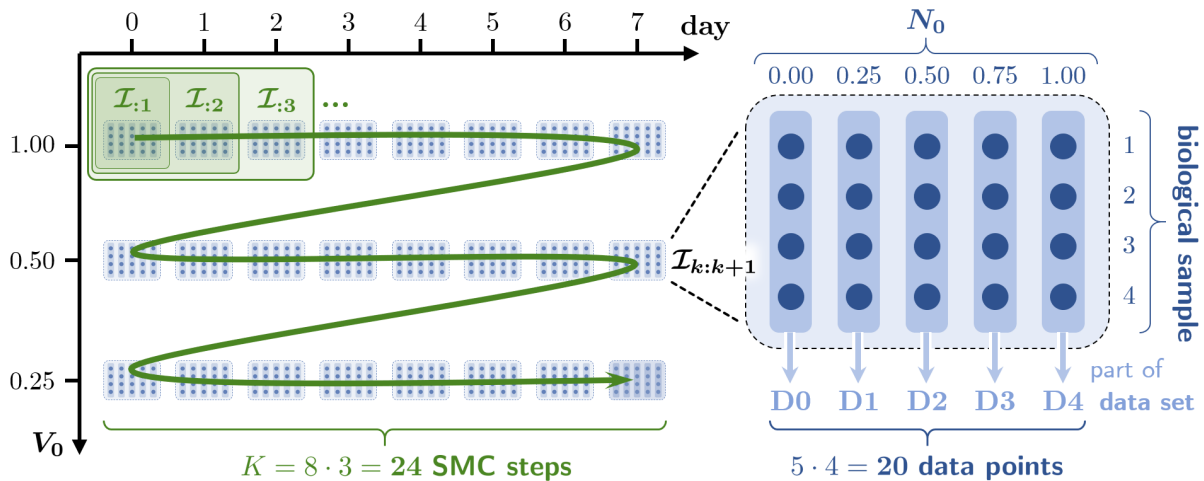

Figure 8: Schematic description of the data utilization to calibrate the models $\mathcal{M}_N^\eta$ and $\mathcal{M}_N$: The data splitting steps $k = 1, \dots, K$ iterate over the observations on day $t \in \{0, \dots, 7\}$ (inner loop) and initial cell density $V_0 \in \{1.00, 0.50, 0.25\}$ (outer loop).

By considering parts of all data sets D0–D4 at each SMC step, we aim to maximize the information about the effect of varying nutrients on the cells. Apparently, although considering a notable amount of data with high informative content per step, this does not lead to degenerating intermediate distributions as discussed at the beginning of Section 5.2.

5.2.2   Calibration with the chemoresistance data

The models $\mathcal{M}_{DS}^0$ and $\mathcal{M}_{DS}^{\mathrm{CYP}}$ describe the experiments from [22]. In particular, that study analyzes the effect of chemotherapy on different hepatocellular carcinoma cell lines under various oxygen (normoxic/hypoxic) and ECM stiffness (normal/cirrhotic) conditions. In our investigations we are particularly interested in the behavior of the cell lines Hep3B2, HepG2 and C3Asub28, which especially differ in their CYP expression, i.e. their drug metabolization activity. In particular, we want to calibrate model $\mathcal{M}_{DS}^0$ with the CYP-free Hep3B2 data and $\mathcal{M}_{DS}^{\mathrm{CYP}}$ with HepG2 resp. C3Asub28. All experiments start with the same initial cell density V_0.

Structure of the available percentage viability data.   We briefly recall the experimental design from Section 3.3. After allowing the tumor cells of a specific cell line to adapt to the present oxygen and stiffness conditions, combination therapy with DOX and SOR is applied; subsequently, the cell population is grown in the absence of drugs for further three days and, eventually, viability is examined by an intensity measurement (at time point $t_{\text{end}} = t_{\text{treat}} + 3$, given in days). Control populations are grown under the same experimental setting but without adding drugs to the system to investigate the treatment efficacy. The latter is quantified by the ratio between $I_{D_0}^{\text{treat}}$ and I^{ctrl}, i.e. the measured viability of a treated population (with dosage D_0) and a corresponding control population. This yields an observation for the percentage viability:

$$I_{D_0}^{\%} = \frac{I_{D_0}^{\text{treat}}(t_{\text{end}})}{I^{\text{ctrl}}(t_{\text{end}})} \,. \tag{5.1}$$

By performing the described experiment for various DOX dosages, we get a discrete reversed[10] representation of a dose-response relationship. Figure 9 illustrates the experimental design and the resulting percentage viability data, which is used for model calibrations.
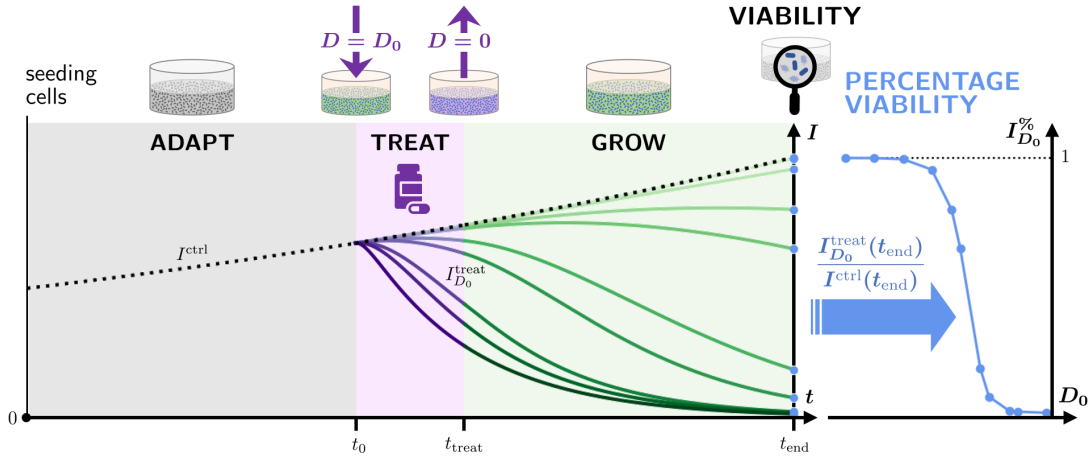

Figure 9: Outline of the experimental design yielding the calibration data for models $\mathcal{M}_{DS}^0$ and $\mathcal{M}_{DS}^{\text{CYP}}$.
Left plot: Exemplary time evolution of the cell density over the course of the experiment (adaption/treatment/growth phase), showing the untreated growth of a control population (black dotted curve) compared to populations exposed to different DOX dosages D_0 in the treatment phase $T = [t_0, t_{\text{treat}}]$ (colored solid curves, where a darker shade indicates a higher dosage). Viability is measured once at t_{end}.
Right plot: Resulting percentage viability data in form of a dose-response relationship.

Repeating this procedure for different conditions (treatment duration, oxygen supply, ECM stiffness and supportive drug dosage) allows to investigate the environment's influence on the treatment efficacy. Per cell line, this results in measurements $I_{D_0}^{\%}$ for each combination of

- $D_0 \in \{0.0001, 0.001, 0.01, 0.1, 0.5, 1, 5, 10, 50, 100, 1000\}$ (µM) DOX dosage,
- $t_{\text{treat}} \in \{1, 2\} \propto 24/48$ hours treatment duration,
- $S_0 \in \{0, 0.5, 1\} \propto 0/11/22$ µM SOR dosage (supportive drug),
- $H_0 \in \{0, 1\} \propto$ normoxic/hypoxic oxygen supply,
- $C_0 \in \{0, 1\} \propto$ normal/cirrhotic ECM stiffness,

i.e. in total we have data for $11 \cdot 2 \cdot 3 \cdot 2 \cdot 2 = 264$ different environmental settings.

---

[10]Usually a "dose-response" is given by a term like $(1 - I_{D_0}^{\%}) \in [0,1]$, i.e. in our context $I_{D_0}^{\%} \equiv 0$ represents the maximal response to the drug, while $I_{D_0}^{\%} \equiv 1$ means no response.

Deliberate utilization of the data. For each combination of the above quantities, there are three biological replicates. Due to the complexity of the chemoresistance models, we want to minimize the effect of biological variation and potential outliers on the model calibrations. Hence, we consider the median over the corresponding replicates instead of the separate measurements $I_{D_0,i}^{\mathrm{treat}}$ and I_i^{crtl} (i-th replicate) to construct the percentage viability $I_{D_0}^{\%}$ of (5.1). Consequently, for given t_{treat}, D_0, S_0, H_0 and C_0, the uncertainty factor $\varepsilon_{\%}$ determining the data likelihood ($\mathfrak{L}_{\%}$) is:

$$I_{D_0}^{\%} = \frac{\mathrm{median}\big\{I_{D_0,1}^{\mathrm{treat}}, I_{D_0,2}^{\mathrm{treat}}, I_{D_0,3}^{\mathrm{treat}}\big\}}{\mathrm{median}\big\{I_{D_0,1}^{\mathrm{ctrl}}, I_{D_0,2}^{\mathrm{ctrl}}, I_{D_0,3}^{\mathrm{ctrl}}\big\}} \quad \Rightarrow \quad \varepsilon_{\%} = \frac{I_{D_0}^{\%}}{V^{\%}(D_0)} \overset{(4.4)}{\sim} \beta'\left(\frac{1}{\sigma^2}, \frac{1}{\sigma^2}\right),$$

where $V^{\%}$ is the percentage viability derived by the mathematical model $\mathcal{M}_{DS}^{0}$ or $\mathcal{M}_{DS}^{\mathrm{CYP}}$.

Due to biological variation and measurement inaccuracies some (median) data points appear outside of the range of $0 - 100\%$. However, both models can only give percentage viabilities within this range by construction, i.e. we clip these data points to the interval $[0.001, 1]$. Note that we cannot choose the lower bound of the data arbitrarily small without excessively increasing the uncertainty variance of $\varepsilon_{\%}$, since the high probability area of the multiplicative noise gets more narrow for measurements closer to zero. This could lead to numerical issues during the reweighting steps of the SMC algorithm.

As the data points $I_{D_0}^{\%}$ represent a (noisy but smooth) dose-response relationship, it is reasonable to iterate over the measurements along the D_0-axis for the data splitting steps. As mentioned at the beginning of Section 5.2, there are situations where particular data points do not contribute to significantly improve the estimation of the posterior distribution. In this context, we can make the following observation (illustrated in Figure 10). If the calibration has already incorporated the information "no response for dosages $D_{0,1}$ and $D_{0,2}$" with $D_{0,1} < D_{0,2}$, then a data point $D_0 \in (D_{0,1}, D_{0,2})$ will not provide additional information to that statement, since the cells will show no response for this dosage either. An analogous observation can be made for dosages, which trigger a maximal response. Hence, such data points are feasible candidates to be omitted for the calibration process.
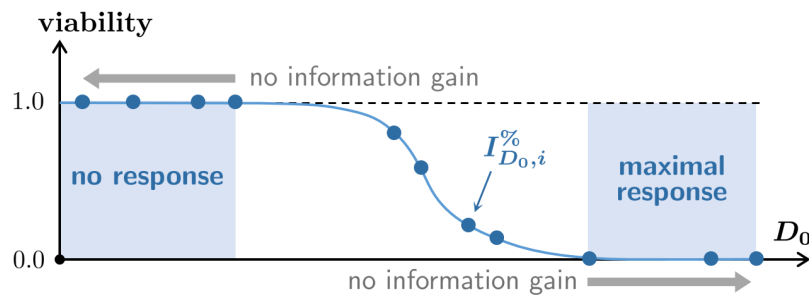

Figure 10: Illustration of the informative content of exemplary (undisturbed) dose-response data $\big\{I_{D_0,i}^{\%}\big\}_i$. Once the measurements suggest no resp. maximal response to the applied dosage D_0 (i.e. $I_{D_0}^{\%} = 1$ resp. $I_{D_0}^{\%} = 0$), there is no significant information gain from considering data for smaller resp. larger dosages in the calibration.

The particular omitted measurements for each data set are mentioned while discussing the respective calibration results in Sections 6.3.1 and 6.3.2.

Order and segmentation of the calibration data. Instead of time-resolved measurements (like in the calibrations of models $\mathcal{M}_N^{\eta}$ and $\mathcal{M}_N$), we now have measurements describing the dose-response over D_0 for a given combination of t_{treat}, S_0, H_0 and C_0. We have to consider that

tumor cells of distinct cell lines can react differently to the treatment, especially depending on the present oxygen supply and ECM stiffness. Hence, we calibrate the corresponding model separately to the measurements for each combination of $H_0 \in \{0, 1\}$ and $C_0 \in \{0, 1\}$, i.e. four individual calibrations are performed per cell line.

Figure 11 illustrates how the measurements are used for each calibration to construct the consecutive data sets $\{\mathcal{I}_{:k}\}_{k=1}^K$. Over the course of the K data splitting steps, we iterate over the drug dosages S_0 and D_0, where a data increment $\mathcal{I}_{k:k+1}$ consists of the two respective measurements for $t_{\text{treat}} \in \{1, 2\}$ (right side of Figure 11). The algorithm starts with data for $S_0 = 0$ and iterates over the relevant values of D_0 in ascending order, which is repeated for $S_0 = 0.5$ and eventually $S_0 = 1$ (left side of Figure 11).
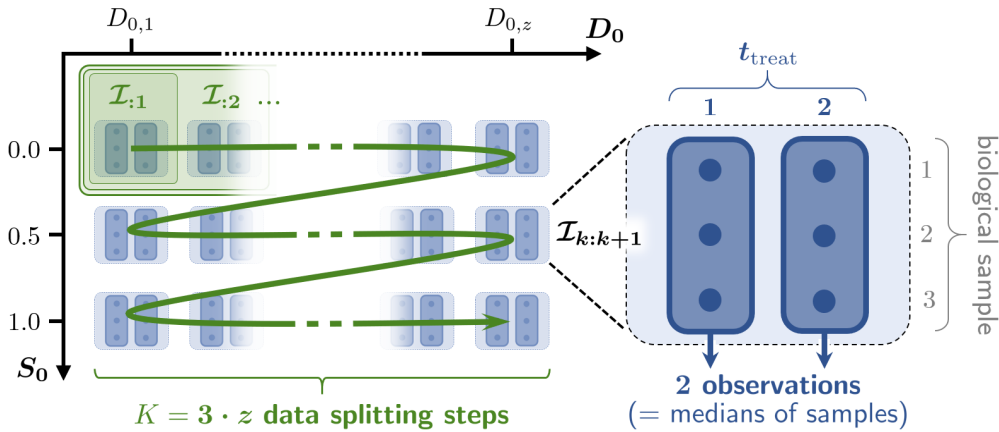
Figure 11: Schematic description of the data utilization to calibrate the models $\mathcal{M}_{DS}^0$ and $\mathcal{M}_{DS}^{\text{CYP}}$. The data splitting steps $k = 1, \ldots, K$ iterate over the observations for a selection of DOX dosages $D_{0,1}, \ldots, D_{0,z}$, $z \in \{1, \ldots, 11\}$ (inner loop) and all SOR dosages $S_0 \in \{0.0, 0.5, 1.0\}$ (outer loop).

This order has the advantage that the data of the first third of SMC steps ($S_0 = 0$) contains no information about any SOR-related parameter. Hence, before considering the first measurements with $S_0 > 0$ we can reset the values of these parameters to their prior samples without changing the current intermediate distribution. This improves the sample diversity of the particle approximation.

5.3   Prior distributions of the parameters

The prior distribution represents the knowledge about the parameters' values without having seen the associated data. Depending on the parameter, we can use biological or experimental background information to get a feeling for its magnitude. There can also be mathematical restrictions, which give actual bounds for feasible parameter values. This mostly applies to the lower bound, e.g. if a parameter is per definition non-negative. However, often the biological and mathematical *a priori* information is not enough to distinctively give an upper bound. This can complicate the choice of the prior distribution, since it affects the decision on an appropriate sample size P.

Prior support vs. sample size.   The support of the prior distribution ideally covers all biologically reasonable parameter values. If we want to use prior distributions with bounded supports, the supports of their marginals need to be large enough to cover the actual parameter values.

However, it is not practical to choose the support arbitrarily large, as this means a large variance for the prior, which can, for a given sample size P, reduce the coverage of the high probability region of the parameter space. With basic algorithmic methods, e.g. sole data splitting or a fixed number of mixing steps, this can lead to numerical issues, if the majority of particles is associated with a low weight. For a given P, likelihood tempering and an adaptive number of mixing steps can counteract this problem at the cost of computational effort. In general, a scarce prior coverage of the high probability region can be compensated by increasing the sample size. However, this will also increase the computational cost, since the ODE model has to be solved for each parameter sample several times in the course of the SMC algorithm. Hence, we need to find a tradeoff of sufficiently large prior support and sample size P to perform the calibration within a practical time frame.

The models $\mathcal{M}_N^\eta$ and $\mathcal{M}_N$ were calibrated with a very large sample size: $P = 50\,000$. This improved the comparability of the two models, as a large sample size reduces the numerical variations in the calibration results. Note that using a smaller sample size might have been enough for this application, but the computational time was still manageable due to the simplicity of the models and the time-resolved data.

For calibrating the chemoresistance models $\mathcal{M}_{DS}^0$ and $\mathcal{M}_{DS}^{\mathrm{CYP}}$ finding the balance between sample size and prior support is more challenging for two reasons. First, the ODE systems have a higher number of unknown parameters compared to the previous models. Hence, a sufficiently large sample size is necessary to generate enough qualitatively different and biologically reasonable parameter combinations when sampling from the prior distribution. Second, we need to perform several, consecutive calibrations (one for each combination of H_0 and C_0 and cell line), which increases the total computation time significantly – additionally to more costly solving procedures. Therefore, special attention is directed to selecting the prior support and sample size only as large as necessary (for more details see Section 5.3.2). Eventually, this led to using the sample size $P = 10\,000$ together with the nested reweighting approach and adaptive number of mixing steps as described in Algorithms 2 and 3.

Mathematical implementation of prior knowledge[11].   Information about the parameters' magnitude can be described by using an appropriate uniform distribution $\mathcal{U}(a, b)$ on an interval $[a, b]$. If we can additionally assume that the neighborhood of a parameter value h has a high probability, a triangular distribution $\mathrm{Triang}(a, h, b)$ on $[a, b]$ is used, where $h \in [a, b]$ is the mode of the distribution, i.e. the value that is most likely to be sampled. Note that the mode can also lie on the interval bounds, if low/large values within the interval are assumed to have high probability. We set $h = (a + b)/2$ to the center of the interval, if we expect the borders a, b to have a low probability but there is no particular tendency to a value within the interval.

5.3.1   Prior information to calibrate the nutrient deprivation models

For calibrating $\mathcal{M}_N^\eta$ and $\mathcal{M}_N$, the set of unknown parameters can be distinguished between model parameters (part of the ODE systems) and hyperparameters. The latter include the uncertainty variance σ^2 and the proportionality constant n (their definitions will be recalled in the corresponding following paragraphs). A summary of all prior distributions from the following paragraphs can be found in Table D.1 in Appendix D.III.

Most of the content and formulations of the following paragraphs are taken from our publication [63]. Note that some prior distributions will differ from the published ones: We observed that instead of triangular distributions, all calibrations of models $\mathcal{M}_N^\eta$ and $\mathcal{M}_N$ actually started

---

[11]Remark: Content and formulations of this paragraph are taken from our publication [63].

with uniform prior samples on the corresponding support (due to a minor coding error). However, this would not alter the calibration results significantly, as using a uniform prior is more conservative (i.e. less informative) than using a triangular one.

Prior distributions for the model parameters.   We recall the models from Section 3.2:

$$(\mathcal{M}_N): \quad \dot{V} = \delta^+(N_0) \cdot \beta \, V \left(1 - \left(\frac{V}{V_{\text{cap}}}\right)^b\right) - (\lambda + \delta_N^-(N_0) \cdot \lambda_{\text{ind}})V \quad \text{with } V(0) = V_0 \,,$$

$$(\mathcal{M}_N^\eta): \quad \begin{cases} \dot{V} = (1 - \eta) \cdot \beta \, V \left(1 - \left(\frac{V}{V_{\text{cap}}}\right)^b\right) - (\lambda + \eta \cdot \lambda_{\text{ind}})V \quad \text{with } V(0) = V_0 \,, \\[2ex] \dot{\eta} = \frac{\alpha_N \cdot N^2}{N_{\text{thr}}^2 + N^2} \cdot (1 - \eta) - \alpha_N \cdot \left(1 - \frac{N^2}{N_{\text{thr}}^2 + N^2}\right) \cdot \eta \quad \text{with } \eta(0) = \eta_0 \,. \end{cases}$$

We want to utilize biological and experimental knowledge to construct appropriate prior distributions for all involved model parameters. If possible, we try to find a bounded interval which covers all reasonable values of the respective parameter. For better readability, in the following we omit units of variables and parameters where not necessary.

The doubling time τ of the used cell type is larger than one day while in exponential growth [88, 89], i.e. $\tau > 1$. We can estimate an upper bound for the growth rate β:

$$2V_0 = V(\tau) = V_0 e^{\beta\tau} \quad \Rightarrow \quad \beta = \frac{\ln(2)}{\tau} \overset{\tau>1}{<} \ln(2) < 1 \,.$$

Therefore, it is reasonable to expect $\beta \in (0, 1)$. Under optimal nutrient conditions, we know that the cell population size increases. This translates to the parameter relation $\beta > \lambda$, which can also be written as

$$\lambda = c_\beta \cdot \beta \quad \text{with} \quad c_\beta \in (0, 1) \,.$$

With c_β we have found a bounded parameter, which we can calibrate instead of λ. A similar reparametrization can be given for the induced death rate λ_{ind}: it is reasonable to assume that cells in a nutrient-free environment die faster from starvation than from natural causes, which leads to

$$\lambda_{\text{ind}} > \lambda \qquad \Rightarrow \quad \lambda_{\text{ind}} = \frac{\lambda}{c_\lambda} = \frac{c_\beta}{c_\lambda}\beta \quad \text{with} \quad c_\lambda \in (0, 1) \,.$$

The underlying experimental setting in [21] implies that the populations do not exceed a density of $3 \cdot 10^5$ cells/mL. Furthermore, all experiments start with initial densities which are smaller than the carrying capacity. Since $V_0 = 1$ (corresponding to 10^5 cells/mL) is the largest seeding density, we can eventually assume $V_{\text{cap}} \in (1, 3)$. The restrictions $b > 1$ and $N_{\text{thr}} \in (0, 1)$ are motivated by the modeling framework. Utilizing all this information, we adopt the following prior distributions for the model parameters of $\mathcal{M}_N$:

$$\beta \sim \mathcal{U}(0, 1) \,, \qquad c_\beta \sim \mathcal{U}(0, 1) \,, \qquad c_\lambda \sim \mathcal{U}(0, 1) \,,$$
$$V_{\text{cap}} \sim \mathcal{U}(1, 3) \,, \qquad b \sim \mathcal{U}(1, 12) \,, \quad N_{\text{thr}} \sim \mathcal{U}(0, 1) \,.$$

The same prior distributions are used for the common parameters in model $\mathcal{M}_N^\eta$. Additionally, the impact rate α_N needs to be calibrated for that model. However, since we do not have any particular information about this parameter, we set its prior distribution to

$$\alpha_N \sim \mathcal{U}(0, 12) \,.$$

For better comparability between the models, we start the respective calibrations from the same prior particle sample. In particular, the SMC algorithm is performed for model $\mathcal{M}_N^\eta$ and the generated initial sample, but without the component regarding to parameter α_N, is used to start the calibration of model $\mathcal{M}_N$.

Prior distributions for the hyperparameters. Additionally to the model parameters, the uncertainty variance σ^2 as well as the proportionality constant n need to be estimated – recall from relation (4.3):

$$\varepsilon = \frac{I}{n \cdot V} \sim \Gamma\left(\frac{1}{\sigma^2}, \frac{1}{\sigma^2}\right) \text{ with } \sigma^2 \in (0, 1).$$

To consider a certain degree of confidence in the measurements, we assume a smaller upper bound for the uncertainty variance: $\sigma^2 \in (0, 1/2)$. All experiments are started with cells from a batch with optimal nutrient conditions. If they are put into a nutrient-free environment without going through a weaning process beforehand, they can undergo a starvation shock. This might disturb or decrease the cells' ability to metabolize the chemical for the fluorescence measurements. To consider this in the hyperparameters, we allow the data sets to have different uncertainty variances and proportionality constants: σ_0^2 and n_0 for $N_0 = 0$ resp. σ_N^2 and n_N for $N_0 > 0$, where potentially $n_N \geq n_0$. Using the latter for the reparametrization

$$n_0 = c_n \cdot n_N \quad \text{with} \quad c_n \in (0, 1)$$

leads to the prior distributions

$$\sigma_0^2, \, \sigma_N^2 \sim \mathcal{U}(0, 1/2), \quad n_N \sim \mathcal{U}(0, 1/2), \quad \text{and} \quad c_n \sim \mathcal{U}(0, 1).$$

The upper bound for n_N is motivated by the known magnitude of the intensity measurements. A large value for the uncertainty variance σ^2 allows a larger deviation of the model solution from the data. For the purpose of model comparison, using the same uncertainty variance for both models is desirable to increase comparability. Hence, we first calibrate each model separately to get estimates for the variances σ_0^2 and σ_N^2. Then, we respectively take the average over both models, in particular:

$$\bar{\sigma}_0^2 = \frac{\mathbb{E}\left(\sigma_0^2 \,|\, \mathcal{M}_N^\eta\right) + \mathbb{E}\left(\sigma_0^2 \,|\, \mathcal{M}_N\right)}{2} \quad \text{and} \quad \bar{\sigma}_N^2 = \frac{\mathbb{E}\left(\sigma_N^2 \,|\, \mathcal{M}_N^\eta\right) + \mathbb{E}\left(\sigma_N^2 \,|\, \mathcal{M}_N\right)}{2}, \qquad (5.2)$$

with $\mathbb{E}(\,\cdot\,|\,\mathcal{M})$ denoting the expected value of the marginal posterior distribution of σ_0^2 resp. σ_N^2 from calibrating model $\mathcal{M} \in \{\mathcal{M}_N^\eta, \mathcal{M}_N\}$. Eventually, these average values $\bar{\sigma}_0^2$ and $\bar{\sigma}_N^2$ are used deterministically and are especially not estimated anymore in further calibrations.

5.3.2 Prior information to calibrate the chemoresistance models

We recall the definition of percentage viability data from Section 4.1.2. By taking the ratio of two intensity measurements $I^{\text{treat}}/I^{\text{ctrl}}$, the proportionality constant n, which scales the observed light intensity to the present viable cell density via $I = n \cdot V$, cancels. Hence, it is not necessary to consider n in the calibrations and the only unknown hyperparameter is the variance of the uncertainty factor $\varepsilon_\%$ in the context of percentage viability:

$$\varepsilon_\% = \frac{I^{\text{treat}}/I^{\text{ctrl}}}{V^{\text{treat}}/V^{\text{ctrl}}} \sim \beta'\left(\frac{1}{\sigma^2}, \frac{1}{\sigma^2}\right) \quad \Rightarrow \quad \text{Var}(\varepsilon_\%) = \frac{\sigma^2(2 - \sigma^2)}{(1 - 2\sigma^2)(1 - \sigma^2)^2} \text{ for } \sigma^2 \in (0, 1/2),$$

where σ^2 is the variance of the uncertainty factor $\varepsilon = \frac{I}{n \cdot V} \sim \Gamma\left(\frac{1}{\sigma^2}, \frac{1}{\sigma^2}\right)$ for cell viability. The variance $\text{Var}(\varepsilon_\%)$ can be tuned by the value of σ^2. To ensure comparability of the calibration

results for all cell lines and environmental conditions, the parameter σ^2 is used deterministically. As a rough benchmark, we orient ourselves by the magnitude of the estimated values of $\bar{\sigma}_o^2$ and $\bar{\sigma}_N^2$ from equation (5.2), which were obtained by pre-calibrations of the nutrient deprivation models $\mathcal{M}_N^\eta$ and $\mathcal{M}_N$. Anticipating the corresponding calibration results from Section 6.2.1, we found $\sigma^2 = 0.10$ resp. $\sigma^2 = 0.15$ to be suitable choices for the calibrations to the data of cell lines Hep3B2 resp. HepG2/C3Asub28, achieving a balance between numerical stability of the algorithm and sufficient concentration of the distributions. This results in uncertainty variances of $\mathrm{Var}(\varepsilon_\%) \approx 0.29$ resp. $\mathrm{Var}(\varepsilon_\%) \approx 0.55$.

Before proceeding with constructing the prior distributions in the following paragraphs, we note: If we do not give a biological/mathematical criterion to set a distinctive upper bound for a parameter, we choose the corresponding prior support as small as possible without being too restrictive. This allows to initialize the SMC algorithm with a computationally manageable sample size. A summary over the prior distributions to calibrate model $\mathcal{M}_{DS}^0$ resp. $\mathcal{M}_{DS}^{\mathrm{CYP}}$ can be found in Tables D.2a resp. D.2b in Appendix D.III.

Recall from Section 5.2.2 that we calibrate a particular model separately to the measurements for each combination of $H_0 \in \{0,1\}$ and $C_0 \in \{0,1\}$, i.e. we perform four individual calibrations per cell line/model. In particular, we start with the case $H_0, C_0 = 0$. For the remaining thesis we will use the following terms and abbreviations to denote the underlying environmental conditions:

$$
\begin{aligned}
\text{"normal conditions"}: \quad & H_0, C_0 = 0 \overset{\mathrm{abbr.}}{\rightsquigarrow} \text{HC0}, \\
\text{"sole hypoxia"}: \quad & H_0 = 1, C_0 = 0 \rightsquigarrow \text{H1}, \\
\text{"sole cirrhosis"}: \quad & H_0 = 0, C_0 = 1 \rightsquigarrow \text{C1}, \\
\text{"cirrhosis and hypoxia"}: \quad & H_0, C_0 = 1 \rightsquigarrow \text{HC1}.
\end{aligned}
$$

To minimize numerical deviations between the separate calibrations within a SMC run, we start each of the four calibrations from the same prior particle sample (regarding common parameters).

Prior distributions for model $\mathcal{M}_{DS}^0$. Given the treatment phase $T = [0, t_{\mathrm{treat}}]$, we consider the unknown parameters of system

$$
\mathcal{M}_{DS}^0 : \begin{cases} \dot{V} = \Big(\beta - \lambda - \big(\beta + \lambda_{\mathrm{ind}}\big)\eta\Big) \cdot V, \\[2mm] \dot{\eta} = \left(\underbrace{\dfrac{\alpha_D^- D_0^{m_1}}{\left(D_{\mathrm{norm}}\left(1 - \dfrac{a_{\max} S_0^{m_3}}{S_{\mathrm{supp}}^{m_3} + S_0^{m_3}}\right)d_{HC}\right)^{m_1} + D_0^{m_1}}}_{\delta_{D,HC}^-(D_0, S_0)} + \underbrace{\dfrac{\alpha_S^- S_0^{m_2}}{S_{\mathrm{thr},HC}^{m_2} + S_0^{m_2}}}_{\delta_{S,HC}^-(S_0)} \right) (1 - \eta)\, \mathbb{1}_T(t), \\[2mm] \text{with } V(0) = V_0 \ \text{ and } \ \eta(0) = \eta_{0,HC} \le \dfrac{\beta - \lambda}{\beta + \lambda_{\mathrm{ind}}} \in (0,1). \end{cases}
$$

While the values of t_{treat}, H_0, C_0, D_0, S_0 and V_0 are given from the experiment, the remaining parameters need to be calibrated. Recall two observations from Section 3.3.3. First, the parameters β, λ and λ_{ind} can only be estimated in combination as the terms $(\beta - \lambda)$ and $(\beta + \lambda_{\mathrm{ind}})$. Second, the percentage viability (measurements) are modeled by (3.18) as

$$
\frac{V^{\mathrm{treat}}}{V^{\mathrm{ctrl}}}(t) = \exp\left(-(\beta + \lambda_{\mathrm{ind}})\left(\eta(t_{\mathrm{treat}})\big(t - t_{\mathrm{treat}}\big) - \eta_{0,HC} \cdot t + \int_0^{t_{\mathrm{treat}}} \eta(\tau)\,\mathrm{d}\tau\right)\right).
$$

Since this equation is independent from $(\beta - \lambda)$, it is neither necessary nor possible to estimate this term. Consequently, we cannot incorporate the particular upper bound $\frac{\beta - \lambda}{\beta + \lambda_{\mathrm{ind}}} < 1$ in the

prior information for $\eta_{0,HC}$. Summarizing these observations yields the prior distributions

$$\eta_{0,HC} \sim \text{Triang}(0, 0, 1) \qquad \text{and} \qquad (\beta + \lambda_{\text{ind}}) \sim \mathcal{U}(0, 3) \,.$$

Note that by definition $\eta_{0,HC} = 0$ for $H_0, C_0 = 0$ (HC0), i.e. $\eta_{0,HC}$ only needs to be estimated for data with hypoxic and/or cirrhotic conditions (H1/C1/HC1). Furthermore, we know that the parameter $(\beta + \lambda_{\text{ind}})$ is uninfluenced by H_0 and C_0. Hence, we can use the estimate[12] for $(\beta + \lambda_{\text{ind}})$ resulting from the first calibration (HC0) to set the parameter fixed for the remaining calibrations (H1/C1/HC1).

Next, we take a closer look at the cells' stress response to DOX and SOR. The sensitivity function $\delta_{D,HC}^{-}$ is determined by (among others) the unaffected sensitivity threshold D_{norm} and its shifting terms

$$d_S(S_0) = 1 - \frac{a_{\max} S_0^{m_3}}{S_{\text{supp}}^{m_3} + S_0^{m_3}} \qquad \text{and} \qquad d_{HC} \,.$$

Since we do not have an explicit definition of d_{HC}, we can only estimate it with the combined term $(D_{\text{norm}} \cdot d_{HC})$, which we denote by $D_{\text{norm},HC}$. Based on the experimental design, it is reasonable to assume that significant changes of cytotoxicity of DOX occur in a logarithmic scale in the magnitude of the applied dosages $0.0001 - 1000 \,\mu\text{M}$ [22]. We do not expect the threshold $D_{\text{norm},HC}$ to be very close to the bounds of this range, i.e. we assume

$$D_{\text{norm},HC} \in \left[10^{-4}, 10^{4}\right] \quad \text{and define} \quad \log_{10}(D_{\text{norm},HC}) = \widehat{D}_{\text{norm},HC} \sim \text{Triang}(-4, 0, 4) \,.$$

The Hill coefficient m_1 tunes the slope of $\delta_{D,HC}^{-}$. If m_1 is in a high magnitude, large variations are necessary to significantly change the slope. Therefore, we use a logarithmic scale to obtain useful prior samples and set

$$m_1 \in [1, 50] \approx \left[10^{0}, 10^{1.7}\right] \quad \Rightarrow \quad \log_{10}(m_1) = \widehat{m}_1 \sim \mathcal{U}(0, 1.7) \,.$$

For the DOX impact rate we assume

$$\alpha_D^{-} \sim \mathcal{U}(0, 20) \,,$$

where the upper bound can be interpreted as an immediate reaction to the DOX treatment.

The supportive influence of SOR is given by $d_S(S_0)$. For this Hill-type function we do not know an upper bound for the threshold S_{supp}. In particular, it is possible that its value is significantly larger than the investigated dosages $S_0 \in \{0, 0.5, 1\}$, i.e. potentially $S_{\text{supp}} > 1$. For large values of S_{supp}, especially in combination with a large Hill coefficient m_3 (i.e. a steep switch), the function values of $d_S(S)$ can be very similar in the range of $S \in [0, 1]$. As Figure 12 illustrates, the exact shape of d_S and hence the values of $a_{\max}$, S_{supp} and m_3 are difficult to reconstruct from the available data in such a situation. To be precise, it might even be not possible to distinctively reconstruct the three unknowns, i.e. three degrees of freedom, with the information for only two non-zero dosages S_0.

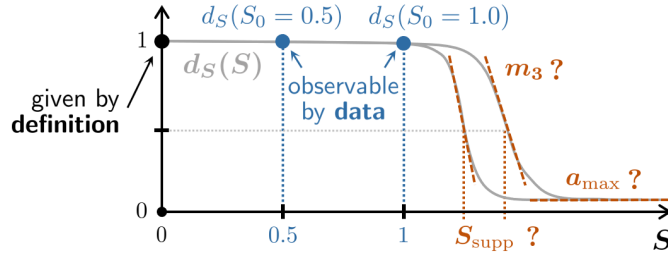[12]We use its so-called marginal MAP estimate, which will be introduced in the upcoming Section 6.1.2.

Figure 12: Schematic plots of the supportive function $d_S(S) = 1 - a_{\max} S^{m_3} / \left(S_{\text{supp}}^{m_3} + S^{m_3} \right)$. The available data provides just enough information to estimate $d_S(S_0)$ for $S_0 \in \{0.5, 1\}$ (blue markers). Especially for $d_S(0.5), d_S(1) \approx 1$, the parameters $a_{\max}$, S_{supp} and m_3 are not distinctively reconstructable.

To counteract this issue, we make use of the fact that in the reduced model $\mathcal{M}_{DS}^0$ the SOR concentration remains constant during treatment. Then, instead of estimating the continuous shape of d_S with the parameters $a_{\max}$, S_{supp} and m_3, we only consider the discrete values $d_S(S_0)$ for $S_0 \in \{0, 0.5, 1\}$. Knowing that by definition $d_S(S_0 = 0) = 1$, we calibrate the unknown values of $d_S(0.5)$ and $d_S(1)$ (blue markers in Figure 12). Since $d_S : \mathbb{R}_+ \to [0, 1]$ is strictly monotonically declining with $0 < d_S(1) < d_S(0.5) < 1$, we define

$$d_S(0.5) \sim \mathcal{U}(0, 1) \qquad \text{and} \qquad d_S(1) = c_d \cdot d_S(0.5) \text{ with } c_d \sim \mathcal{U}(0, 1) \,.$$

If the estimated values for $d_S(0.5)$ and $d_S(1)$ are significantly distinguishable, we could reconstruct some information about the values of S_{supp} and m_3.

While for d_S the constant SOR dosage improves the traceability of the involved unknowns and simplifies an appropriate choice for their priors, we observe difficulties in the context of the cells' reaction to SOR. Their corresponding stress response is given by

$$\alpha_S^- \delta_{S,HC}^-(S_0) = \frac{\alpha_S^- \cdot S_0^{m_2}}{S_{\text{thr},HC}^{m_2} + S_0^{m_2}} \,,$$

i.e. it has three unknowns and hence three degrees of freedom. However, since $\alpha_S^- \delta_{S,HC}^-(0) = 0$ is given by definition, the data do only provide information for two dosages $S_0 = 0.5$ and $S_0 = 1$. This means we do not have enough data to distinctively trace back the shape of $\alpha_S^- \delta_S^-$ and hence the involved parameters (see Figure 13).
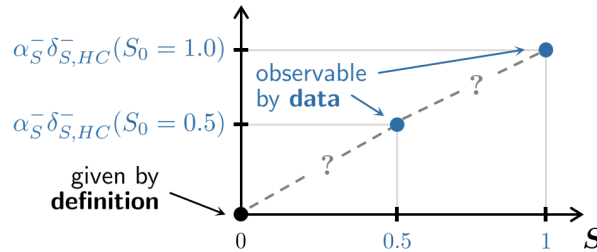

Figure 13: The available two data points provide just enough information to estimate $\alpha_S^- \delta_{S,HC}^-(S_0)$ for $S_0 \in \{0.5, 1\}$ (blue markers). Since the function $\alpha_S^- \delta_{S,HC}^-$ has three free parameters, this data is not enough to reconstruct the curve of the function.

In summary, with the available data we can only reconstruct the values of $\alpha_S^- \delta_{S,HC}^-(S_0)$ for dosages $S_0 \in \{0.5, 1\}$. Keeping in mind that $\delta_{S,HC}^- \in [0, 1] \Rightarrow \alpha_S^- \delta_{S,HC}^- \leq \alpha_S^-$, we can use a similar

approach as for d_S to reparametrize $\alpha_S^- \delta_{S,HC}^-$. Since δ_S^- is strictly monotonically increasing, we define

$$\alpha_S^- \delta_{S,HC}^-(1) \sim \mathcal{U}(0,2) \quad \text{and} \quad \alpha_S^- \delta_{S,HC}^-(0.5) = c_\delta \cdot \alpha_S^- \delta_{S,HC}^-(1) \quad \text{with } c_\delta \sim \text{Triang}(0,0,1).$$

The choice of the upper bound of $\alpha_S^- \delta_{S,HC}^-(1)$ follows the assumption that the tumor cells are more sensitive to treatment with DOX than with SOR, as the latter mainly serves as a supportive drug. According to [90], even high dosages of SOR show relatively low cytotoxicity compared to DOX. Furthermore, the cells show no obvious reaction to the treatment with a standard SOR dosage ($S_0 = 0.5$) for low D_0, motivating the triangular prior for c_δ. For a summary of the above derived prior distributions, see Table D.2a in the appendix.

Prior distributions for the general model $\mathcal{M}_{DS}^{\mathbf{CYP}}$. For the priors of the full model

$$\mathcal{M}_{DS}^{\text{CYP}} : \begin{cases} \dot{V} = \left(\beta - \lambda - (\beta + \lambda_{\text{ind}})\eta \right) \cdot V, \\[2ex] \dot{\eta} = \left(\dfrac{\alpha_D^- D^{m_1}}{\left(D_{\text{norm},HC} \cdot \left(1 - \dfrac{a_{\max} S^{m_3}}{S_{\text{supp}}^{m_3} + S^{m_3}} \right) \right)^{m_1} + D^{m_1}} + \dfrac{\alpha_S^- S^{m_2}}{S_{\text{thr},HC}^{m_2} + S^{m_2}} \right) (1 - \eta), \\[3ex] D(t) = D_0 \exp\left(-\gamma_{D,HC} \cdot t \right) \cdot \mathbb{1}_T(t), \\[1ex] S(t) = S_0 \exp\left(-\gamma_{S,HC} \cdot t \right) \cdot \mathbb{1}_T(t), \\[1ex] \quad \text{with } V(0) = V_0 \text{ and } \eta(0) = \eta_{0,HC} \leq \dfrac{\beta - \lambda}{\beta + \lambda_{\text{ind}}} \in (0,1), \end{cases}$$

we take the prior distributions of the previous model $\mathcal{M}_{DS}^0$ as an orientation. In particular, while it is still not possible to estimate $(\beta - \lambda)$, we adopt the priors

$$\eta_{0,HC} \sim \text{Triang}(0,0,1) \qquad \text{and} \qquad (\beta + \lambda_{\text{ind}}) \sim \mathcal{U}(0,3).$$

Again, $\eta_{0,HC}$ resp. $(\beta + \lambda_{\text{ind}})$ are only calibrated under hypoxia and/or cirrhosis (H1,C1,HC1) resp. under normal environmental conditions (HC0).

Furthermore, as $S = S(t)$ is now explicitly time-dependent, we cannot employ a discrete approach for estimating the SOR-related dynamics anymore. Hence, for the stress reaction parameters we set

$$\begin{aligned} \widehat{D}_{\text{norm},HC} &\sim \text{Triang}(-4,0,4), & m_1 &\sim \mathcal{U}(0,6), & \alpha_D^- &\sim \mathcal{U}(0,20), \\ S_{\text{thr},HC} &\sim \mathcal{U}(0,3), & \widehat{m}_2 &\sim \mathcal{U}(0,1.7), & \alpha_S^- &\sim \mathcal{U}(0,10), \\ S_{\text{supp}} &\sim \mathcal{U}(0,1), & \widehat{m}_3 &\sim \mathcal{U}(0,1.7), \end{aligned}$$

where $\widehat{D}_{\text{norm},HC} = \log_{10}(D_{\text{norm},HC})$ and $\widehat{m}_i = \log_{10}(m_i)$, $i \in \{2,3\}$. For the DOX-related parameters $\widehat{D}_{\text{norm},HC}$, α_D^- and m_1, we adopt the priors from $\mathcal{M}_{DS}^0$, except that we choose a smaller prior support for the Hill coefficient m_1. This was found to be sufficient, especially after seeing the calibration results from model $\mathcal{M}_{DS}^0$ using the Hep3B2 data (details will follow in Section 6.3.1). For the SOR impact rate α_S^-, we enlarged the prior support of $\alpha_S^- \delta_{S,HC}^-(1)$ from model $\mathcal{M}_{DS}^0$, since by definition it holds $\alpha_S^- \delta_{S,HC}^-(1) \leq \alpha_S^-$. The supports of the thresholds $S_{\text{thr},HC}$ and S_{supp} are based on experimental observations from [22]. Additionally to these parameters, model $\mathcal{M}_{DS}^{\text{CYP}}$ considers the drug metabolization rates, for which we set

$$\gamma_D \sim \mathcal{U}(0,20) \qquad \text{and} \qquad \gamma_S \sim \mathcal{U}(0,20).$$

All prior distributions to calibrate model $\mathcal{M}_{DS}^{\text{CYP}}$ are summarized in Table D.2b in the appendix.

6   Calibration results and biological interpretation

The results from calibrating the models $\mathcal{M}_N^\eta$, $\mathcal{M}_N$ and $\mathcal{M}_{DS}^{\mathrm{CYP}}$, $\mathcal{M}_{DS}^0$ are presented in this chapter in Sections 6.2 resp. 6.3. Beforehand, Section 6.1 provides an overview over the methods which are used to analyze the calibration results. The implementation is done in Python 3. The main results of Sections 6.2 and 6.3 will be summarized and concluded in Section 7.1 at the beginning of the subsequent chapter.

6.1   Mathematical investigation of the calibration results

Once a model calibration has finished, we can mathematically post process the resulting approximation of the posterior distribution to obtain insight into the modeling and the biological interpretation. The following sections explain how we extract useful information from the particle approximation for further investigation. In particular, we can quantify the quality of fit between estimated model solution and the data (Section 6.1.1), get estimates for the unknown parameters values (Section 6.1.2), and check for correlations between them (Section 6.1.4). For the following explanations, we assume that the SMC algorithm was performed with a sample size P to calibrate d parameters over the course of K steps ($P, d, K \in \mathbb{N}$).

6.1.1   Quality of fit between model and data

The SMC algorithm provides direct access to measures for the quality of fit of the model calibrations to the underlying data, which will be presented in the following paragraphs[13].

Validation metric – comparing model solution with data.   The *validation metric* proposed in [91] quantitatively compares the model prediction with the corresponding set of measurements. Their mismatch is measured as the area between the data distribution F^{data} and the prediction distribution $F_{\mathcal{M}}^{\mathrm{sol}}$ using the calibration results of a model $\mathcal{M}$. Mathematically, this is defined by the metric

$$d_{\mathrm{valid}}\big(F^{\mathrm{data}}, F_{\mathcal{M}}^{\mathrm{sol}}\big) = \int_0^\infty \big| F^{\mathrm{data}}(O) - F_{\mathcal{M}}^{\mathrm{sol}}(O) \big| \; \mathrm{d}O \,. \tag{6.1}$$

We consider a set of observations $\{O_i\}_{i=1}^M$ of a quantity of interest given the same circumstances, e.g. cell viability measurements of several biological samples at a specific time point and grown under the same environmental conditions. For our applications, these observations are either intensity measurements $O_i = I_i$ or percentage viability measurements $O_i = I_i^{\mathrm{treat}}/I_i^{\mathrm{crtl}}$ (recall Sections 4.1.1 resp. 4.1.2). The data distribution function is then given by

$$F^{\mathrm{data}}(O) = \sum_{i=1}^M \mathbb{I}\big(O_i, O\big) \quad \text{with} \quad \mathbb{I}\big(O_i, O\big) = \begin{cases} 1/M & \text{for } O_i \leq O \,, \\ 0 & \text{for } O_i > O \,. \end{cases}$$

The prediction distribution function $F_{\mathcal{M}}^{\mathrm{sol}}$ is estimated using the particle approximation: with all weighted particle θ_p of the posterior, we calculate the empirical cumulative distribution function from the solution of model $\mathcal{M}$. By applying the problem-specific forward operator $\mathcal{G}^{\mathcal{M}}$ from

---

[13]Note that most of the content and formulations of the paragraphs regarding the validation metric and Bayes factor are taken from our publication [63].

equations (4.6) resp. (4.7) on all parameter samples θ_p, we get a set $\{\mathcal{G}^{\mathcal{M}}(\theta_p)\}_{p=1}^{P}$ which then approximates the prediction distribution by

$$F_{\mathcal{M}}^{\mathrm{sol}}(O) \approx \sum_{p=1}^{P} \mathbb{I}_W\big(\mathcal{G}^{\mathcal{M}}(\theta_p),\, O\big) \quad \text{with} \quad \mathbb{I}_W\big(\mathcal{G}^{\mathcal{M}}(\theta_p),\, O\big) = \begin{cases} W_p^K & \text{for } \mathcal{G}^{\mathcal{M}}(\theta_p) \leq O\,, \\ 0 & \text{for } \mathcal{G}^{\mathcal{M}}(\theta_p) > O\,, \end{cases}$$

where W_p^K is the final weight of the p-th particle after the SMC algorithm has finished. Figure 14 illustrates the above distribution functions and the resulting validation metric for a set of four exemplary observations.
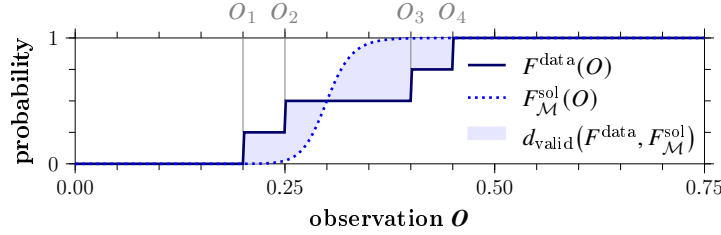
Figure 14: Plots of the data distribution function F^{data} given by four exemplary observations $O_1, \ldots, O_4$ and an approximate prediction distribution function $F_{\mathcal{M}}^{\mathrm{sol}}$. The corresponding validation metric $d_{\mathrm{valid}}\big(F^{\mathrm{data}}, F_{\mathcal{M}}^{\mathrm{sol}}\big)$ is the enclosed area between the two functions.

Bayes factor – comparing how well different models describe the same data.   The so-called Bayes factor [92] can be used for a quantitative comparison of two models based on the same set of data $\mathcal{I}$. It gives the ratio between the respective model evidences, which describe the posterior probability of the data given the model in consideration of the parameter distribution. As mentioned at the end of Section 4.2.2, the model evidence is the proportionality constant in the relation $\pi^{\mathcal{I}}(\theta) \propto L(\mathcal{I}\,|\,\theta)\,\pi_0(\theta)$ between the parameter distribution $\pi^{\mathcal{I}}$ and the prior π_0. In particular, the *evidence* of a model $\mathcal{M}$ is defined by the marginal data likelihood of $\mathcal{I}$:

$$L(\mathcal{I}\,|\,\mathcal{M}) = \int_{\Theta} \underbrace{\pi_0(\theta\,|\,\mathcal{M})}_{\substack{\text{prior on } \theta \\ \text{using } \mathcal{M}}} \cdot \underbrace{L(\mathcal{I}\,|\,\theta, \mathcal{M})}_{\substack{\text{likelihood of } \mathcal{I} \\ \text{given } \theta \text{ and } \mathcal{M}}} \,\mathrm{d}\theta\,.$$

Following [41], the evidence $Z_k^{\mathcal{M}}$ of model $\mathcal{M}$ at the k-th SMC step can be approximated with the weighted particle collection $\{\theta_p\}_{p=1}^{P}$ by

$$Z_k^{\mathcal{M}} \approx Z_0^{\mathcal{M}} \cdot \prod_{s=1}^{k} \sum_{p=1}^{P} L\big(\mathcal{I}_{s-1:s}\,\big|\,\theta_p\,, \mathcal{M}\big) \cdot W_p^{s-1} \qquad \text{for } k = 1, \ldots, K\,,$$

where $L\big(\mathcal{I}_{s-1:s}\,\big|\,\theta_p\,, \mathcal{M}\big)$ is the likelihood of the data increment $\mathcal{I}_{s-1:s} = \mathcal{I}_{:s} \setminus \mathcal{I}_{:s-1}$ at the s-th SMC step given the parameter sample θ_p with model $\mathcal{M}$, and W_p^{s-1} denotes the normalized weight of θ_p before reweighting. Since we start the calibrations with priors, from which we can sample directly, the initial evidence is $Z_0 = 1$. The *Bayes factor* of two models $\mathcal{M}_1$ and $\mathcal{M}_2$ regarding the whole calibration data set $\mathcal{I}_{:K} = \mathcal{I}$ is then given as

$$\mathcal{Z}_{\mathcal{I}}(\mathcal{M}_1, \mathcal{M}_2) = \frac{L(\mathcal{I}\,|\,\mathcal{M}_1)}{L(\mathcal{I}\,|\,\mathcal{M}_2)} \approx \frac{Z_K^{\mathcal{M}_1}}{Z_K^{\mathcal{M}_2}}\,.$$

For $\mathcal{Z}_{\mathcal{I}}(\mathcal{M}_1, \mathcal{M}_2) > 1 = 10^0$, i.e. $L(\mathcal{I} \,|\, \mathcal{M}_1) > L(\mathcal{I} \,|\, \mathcal{M}_2)$, the strength of evidence can be described by the following scale [41]:

$$\log_{10}\left(\mathcal{Z}_{\mathcal{I}}(\mathcal{M}_1, \mathcal{M}_2)\right) \in \begin{cases} \left(0, \frac{1}{2}\right] & \text{barely worth mentioning}, \\ \left(\frac{1}{2}, 1\right] & \text{substantial support for } \mathcal{M}_1, \\ \left(1, 2\right] & \text{strong support for } \mathcal{M}_1, \\ \left(2, \infty\right) & \text{decisive support for } \mathcal{M}_1. \end{cases} \tag{6.2}$$

6.1.2   Estimated parameters values

There are several quantities to characterize the estimates of the parameter values resulting from the obtained posterior approximation. Recalling the definition of the particle approximation of the posterior $\pi_K = \pi^{\mathcal{I}}$, the marginal distribution $\pi_j^{\mathcal{I}}$ of the j-th parameter $(j = 1, \dots, d)$ is obtained by

$$\pi_K(\theta) \approx \sum_{p=1}^P W_p \cdot \delta_{\theta_p}(\theta) \quad \Rightarrow \quad \pi_j^{\mathcal{I}}\big((\theta)_j\big) \approx \sum_{p=1}^P W_p \cdot \delta_{(\theta_p)_j}\big((\theta)_j\big),$$

where $W_p = W_p^K$ is the posterior weight of particle θ_p and $(\theta_p)_j$ resp. $(\theta)_j$ is the j-th component of a particle θ_p resp. of an element θ of the parameter space Θ. Due to the discrete nature of the particle approximation, the statistics of the marginal distributions tend to be more robust than the ones of the global distribution. Hence, it is reasonable to access the parameter estimates by the marginals.

We take a look at the most interesting moments of the distributions. The marginal mean resp. variance of the j-th parameter $(j = 1, \dots, d)$ can be calculated directly from the particle approximation:

$$\mathbb{E}\big((\theta)_j\big) = \sum_{p=1}^P (\theta_p)_j \cdot W_p \qquad \text{and} \qquad \text{Var}\big((\theta)_j\big) = \sum_{p=1}^P \left((\theta_p)_j - \mathbb{E}\big((\theta)_j\big)\right)^2 \cdot W_p. \tag{6.3}$$

These quantities can give first insight into the parameter estimates and their uncertainty. If the corresponding marginal distribution is unimodal and symmetric (not skewed), the marginal mean is a good approximate for the mode of the distribution, i.e. the maximum of the probability density function. Otherwise, the mode of the posterior has to be accessed differently. It was found that some kind of smoothing of the particle approximation is necessary to get a robust estimate of the mode. We obtain the corresponding probability density function by a *kernel density estimation* (KDE) on $\{(\theta_p)_j\}_{p=1}^P$ with Gaussian kernels and Scott's bandwidth selection method[14] [93]. Evaluating this function on the marginalized particle population and selecting the $\arg\max$ gives an estimate of the marginal mode. In the context of Bayesian statistics, this quantity is also called marginal *maximum a posteriori probability (MAP) estimate*. Note that we adapted the KDE, if needed, to ensure that the support of the obtained density function lies within the bounds of the prior support – we will refer to this adjusted routine as *truncated KDE* or *trKDE* for short (details can be found in Appendix D.IV). By combining the marginal means resp. MAPs of all calibrated parameters, we can calculate a corresponding model solution and investigate the underlying biological processes.

---

[14]executed with Python function `scipy.stats.gaussian_kde` with $\{W_p\}_{p=1}^P$ as the `weights` argument

6.1.3   Variation of the estimates and statistical significance

The SMC algorithm is performed several times for each application to investigate dispersion of the results. For biological and numerical investigation we want to compare different estimates of the same quantity (e.g. a parameter) and judge whether an observed difference is systematic or a result of sampling noise (biological, numerical or experimental variation). We can assess the statistical significance of such observations by the so-called p-value p_{sig}. We consider a value smaller than 0.05 as significant and classify the significance level with the widely used "star notation": $p_{\text{sig}} < 0.05 / p_{\text{sig}} < 0.01 / p_{\text{sig}} < 0.001$ which are respectively denoted by $*/**/***$. It is important to note that $p_{\text{sig}} \geq 0.05$ does not lead to the conclusion that there is actually no difference between two estimates. It merely states that if there is a difference, it cannot be distinctively distinguished from the sample noise.

Nutrient deprivation models.   The simplicity of the models $\mathcal{M}_N^{\eta}$ and $\mathcal{M}_N$ allowed to perform many repetitions of the model calibrations within a manageable calculation time. Hence, for each quantity of interest (e.g. a marginal mean of a particular parameter) we achieve statistically independent samples $x_1, \dots, x_{12}$, where $q = 12$ is the number of performed SMC runs. Motivated by the central limit theorem, we assume that these samples are normally distributed via $\mathcal{N}(\mu, \sigma^2)$. As the exact values for μ and σ are unknown, they are estimated by the sample mean $\bar{x} = (\sum_{i=1}^{q} x_i)/q$ resp. sample standard deviation $\sigma_x = \sqrt{\sum (x_i - \bar{x})^2/(1-q)}$. We can use the associated standard error $\sigma_x q^{-1/2}$ to state numerical deviations of the quantity of interest in terms of the corresponding 95% confidence interval: $\bar{x} \pm 1.96 \cdot \sigma_x q^{-1/2}$. This notation will be used in Section 6.2.1 to present the dispersion of the calibration results, especially for the marginal means and variances of the posteriors.

Furthermore, we want to compare the two models $\mathcal{M}_N^{\eta}$ and $\mathcal{M}_N$ based on the respective calibration results obtained by considering the same data. As mentioned before, given a particular model, we can construct an average estimate $\bar{x}$ for a quantity of interest by summarizing all SMC runs. By doing so for each model, we obtain two estimates of the same quantity $\bar{x}_1$ and $\bar{x}_2$. In order to judge the statistical significance of the difference between $\bar{x}_1$ and $\bar{x}_2$, we use the Python function `scipy.stats.ttest_ind(..., equal_var=False)` to do a two-tailed Welch's t-test [94] which allows for unequal variances $\sigma_{x,1}^2 \neq \sigma_{x,2}^2$.

Chemoresistance models.   Due to the increased model complexity and hence computational effort it is not practical to do a large number of SMC runs for calibrating the models $\mathcal{M}_{DS}^{0}$ and $\mathcal{M}_{DS}^{\text{CYP}}$. We did $q = 4$ repetitions of the SMC algorithm for each cell line and environmental setting. However, for this limited number of SMC runs, an analysis of numerical deviation and significance analogously to the nutrient deprivation models is less useful/reliable. Therefore, we collect all the weighted particles from the individual runs in one set of samples. As their weights are normalized on the run-specific particle sets, we have to make the collected particles comparable by updating their weights appropriately. We do this by removing the duplicates and recalculating the posterior densities of the remaining particles with equation (4.8): $\pi^{\mathcal{I}}(\theta) = L(\mathcal{I} \,|\, \theta) \, \pi_0(\theta)$. After normalizing these calculated densities and associating them as weights to the respective particles, we get a new particle approximation of the posterior with a larger sample size. The model parameters are then investigated based on the estimates of this posterior.

We can do a cross-validation to check the robustness of the results obtained by collecting the particles of all SMC runs. Numerical variation is assessed by applying the same reweighting approach as described above on a set of particles obtained by collecting all except one run. This yields four different "extended" particle representations of the posterior. Suppose we want to investigate the numerical variation of a quantity x (e.g. the marginal mean of a parameter),

each of these posteriors gives an estimate x_i ($i = 1, \ldots, q$ and $q = 4$) and we can state the *cross-validated 95% confidence interval*: $\bar{x} \pm 1.96\sigma_x q^{-1/2}$ with $\bar{x}$ being the average over $x_1, \ldots, x_4$ and σ_x the corresponding standard deviation. This notation will be used in Section 6.3 to depict the dispersion of the calibration results in the context of marginal MAPs.

In this application, we want to compare the estimates of the same quantity (e.g. a particular parameter) obtained in different environmental settings. Such an estimate is given by the particle representation of the respective marginal posterior distribution. There are several possibilities (e.g. Student's [95] or Welch's [94] *t*-test, Mann–Whitney U-test [96, 97], Brunner-Munzel test [98]) to compare two distributions given by samples which are each based on different assumptions[15]. A visualization of the calibrated marginal distributions implies that we cannot consistently assume normal-distributed samples or equal variances. Hence, we use the Brunner-Munzel test in Python (`scipy.stats.brunnermunzel`) to compare marginal distributions. However, this test (as well as the others) is not designed for very large samples sizes. From a mathematical perspective, it is nearly impossible to achieve analytically equal marginal distributions due to the approximative and non-deterministic nature of the calibration. Hence, in our setting we will always encounter mathematically different marginal posteriors. The more accurate the approximation of these distributions, i.e. the larger the sample size, the more obvious the differences between them show up for the statistical tests. In fact, trying to use the whole particle sets as samples for statistical testing appeared to be ineffective since this yields vanishing p-values. Therefore, we need to compare the distributions based on a considerably smaller sample size (note that before testing we resample the particles for uniform weights). To get an impression of the role of the sample size on the significance results, we perform the test with different sample sizes which should work well for this testing method [98]: 500, 100, 50 and 30. Furthermore, we repeat each test 1000 times to consider numerical variation of the test results. Eventually, we can visualize the obtained p-values to finally judge statistical significance (illustrated in Figure 15). This testing approach will be referred to as *significance check* for the rest of the thesis. We use this method in Section 6.3 to compare particular marginal posteriors as well as for comparing obtained fitted[16] estimates with the given uncertainty of the fit. Note that the latter is given by a confidence interval of a normal distribution. Hence, we use the two-tailed Welch's test (Python: `scipy.stats.ttest_ind(..., equal_var=False)`) for checking the significance of observed differences between fitted estimates.
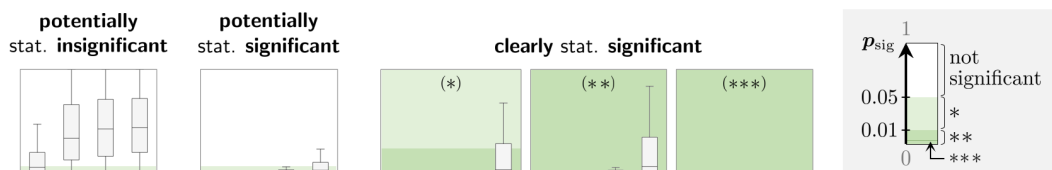

Figure 15: Different scenarios for the boxplots (box: first to third quartile; horizontal line: median) of the 1000 p-values obtained by significance checks with sample sizes 500, 100, 50 and 30 (from left to right per subplot, i.e. horizontal axis). The shaded background gives the significance level and determines the upper limit of the vertical axis (the lower limit is always zero): mainly white (upper limit: 1), two-shaded green marked with (∗) (upper limit: 0.05), dark green marked with (∗∗) or (∗∗∗) (upper limit: 0.01 resp. 0.001). Note that some boxplots might not be visible due to vanishing p-values.

---

[15]Student's resp. Welch's: normal distributed samples with equal resp. unequal variances; Mann–Whitney resp. Brunner-Munzel: non-normally distributed samples with equal resp. unequal variances

[16]More details on the context of fitting are given in Section 6.3 where the method is applied.

However, note that this approach can only discern clear statistical significance or provide an overview over the degree of similarity between distributions. As mentioned previously, it does especially not imply irrelevance or non-existence of differences between estimates if we do not see obvious statistical significance.

6.1.4   Parameter correlations

Knowing significant correlation between different parameters can give useful insight into their interplay in the mathematical model. The particle approximation directly gives a weighted sample representation of the parameter distribution. We resample the particles $\{\theta_p\}_{p=1}^P$ to obtain equally weighted samples $\{\tilde{\theta}_p\}_{p=1}^P$. These can be used to calculate the *Pearson's correlation coefficient* [99] of each pair of parameters $(j, l = 1, \ldots, d)$:

$$r_{j,l} = \frac{\overbrace{\sum_{p=1}^P \left((\tilde{\theta}_p)_j - (\tilde{\theta})_j^{\mathrm{mean}} \right) \left((\tilde{\theta}_p)_l - (\tilde{\theta})_l^{\mathrm{mean}} \right)}^{\text{sample covariance of } j\text{-th and } l\text{-th parameter}}}{\underbrace{\sqrt{\sum_{p=1}^P \left((\tilde{\theta}_p)_j - (\tilde{\theta})_j^{\mathrm{mean}} \right)^2}}_{\substack{\text{sample standard deviation} \\ \text{of } j\text{-th parameter}}} \cdot \underbrace{\sqrt{\sum_{p=1}^P \left((\tilde{\theta}_p)_l - (\tilde{\theta})_l^{\mathrm{mean}} \right)^2}}_{\substack{\text{sample standard deviation} \\ \text{of } l\text{-th parameter}}}}$$

with respective sample mean $(\tilde{\theta})_s^{\mathrm{mean}} = \sum_{p=1}^P (\tilde{\theta}_p)_s / P$ for $s \in \{j, l\}$. This coefficient measures the strength of the linear relationship between the j-th and l-th parameter. Accepted guidelines for interpreting the correlation coefficient (see e.g. [100, 101]) are:

$$|r_{j,l}| \in \begin{cases} (0.0, 0.3] & \text{weak correlation,} \\ (0.3, 0.7] & \text{moderate correlation,} \\ (0.7, 1.0] & \text{strong correlation.} \end{cases} \tag{6.4}$$

In practice, we calculate this coefficient by applying the Python function `scipy.stats.pearsonr` on the samples $\{\tilde{\theta}_p\}_{p=1}^P$. This function also gives access to the p-value of each coefficient to judge the statistical significance of the correlation. To visualize the correlation between two parameters, we can do a 2D scatter diagram of the corresponding sample components (see Figure 16). The strength of correlation shows itself by the degree of accumulation of the points along a straight non-vertical/non-horizontal line, whereas samples of uncorrelated parameters are rather widespread.
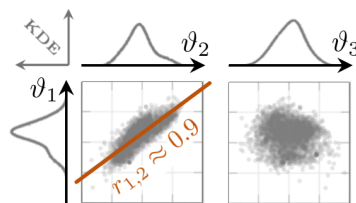

Figure 16: Illustration of how point clouds of samples from the 2D-marginalized posterior distribution can show pairwise correlation. The line plots in the first row/column show KDEs of the respective 1D marginal distributions for exemplary parameters ϑ_1, ϑ_2 and ϑ_3. The axis labels for the parameter value correspond to the ones of the scatter plots in the respective column/row. The first scatter plot indicates that parameters ϑ_1 and ϑ_2 are strongly positively correlated with $r_{1,2} \approx 0.9$, while the second one shows no obvious correlation for parameters ϑ_1 and ϑ_3.

The above visualization can also help the find non-linear correlations, for which the Pearson's correlation coefficient is not optimal. They might only be captured by a relatively small value of $r_{j,l}$ or remain completely undetected by the coefficient. There are other correlation measures which are better suited to find non-linear correlations, see e.g. [102, 103]. However, we found the coefficient $r_{j,l}$ to be sufficient for our investigations.

6.2   Cell viability under nutrient deprivation

We consider the simple biological setting of the nutrient saturation being the only environmental factor to influence the tumor cells. Model $\mathcal{M}_N^\eta$ uses the ESL approach to implement the cells' reaction on nutrient deprivation. In contrast, model $\mathcal{M}_N$ assumes a quasi-steady state for the stress level η, i.e. the cells react immediately and the impact rate α_N is not considered. The calibration results of both models are presented and compared in this section. They serve as a proof of principle for using the ESL approach to describe the influence of the TME on tumor cells. In particular, we investigate estimated parameter values and their biological interpretation (Sections 6.2.1) and compare the models in terms of quality of fit to the available data (Section 6.2.2).

Note that content and formulations (some notations may be altered) of this section are taken from our publication [63], in which we used the sample standard deviation σ_x instead of the standard error $\sigma_x q^{-1/2}$ to quantify numerical deviations. To maintain consistency within this work, the respective values from that article were adapted accordingly.

6.2.1   Calibration results for models $\mathcal{M}_N^\eta$ and $\mathcal{M}_N$

A pre-calibration of the models (recall equation (5.2) from Section 5.3.1) yields the average uncertainty variances

$$\bar{\sigma}_0^2 \approx 0.2410 \quad \text{(for } N_0 = 0\text{, i.e. data set D0)}$$
$$\text{and} \quad \bar{\sigma}_N^2 \approx 0.0355 \quad \text{(for } N_0 > 0\text{, i.e. data sets D1–D4).}$$

These values are used deterministically for further calibrations to estimate the remaining unknown parameters of the models.

We see that, in the absence of nutrients, the variance is considerably larger ($\bar{\sigma}_0^2 > \bar{\sigma}_N^2$), which is in general a reasonable observation. From a biological perspective, this could be the consequence of a starvation shock disturbing the cells' metabolism. Furthermore, the measurement accuracy of small data points, which make the majority of data set D0, might be decreased due to weak fluorescence. Additionally, such small data points play a special role for our modeling approach of using a multiplicative uncertainty factor. Due to the multiplicativity, the range of the high probability region is proportional to the magnitude of the observations. In particular, the region is more narrow the smaller the data, which might be necessary to compensate with a lager uncertainty variance.

Estimated model parameters.   Since all calibrations yield sufficiently unimodal and symmetric posterior distributions, we use the marginal means and variances (6.3) to present the parameter estimates (see Table 7). Comparing both models, the estimations appear to be very similar and observed differences are found to be statistically insignificant ($p_{\text{sig}} > 0.05$). Numerical deviations from performing the SMC algorithm $q = 12$ times are given as 95% confidence interval.

Table 7: Comparison of the estimated model parameters of models $\mathcal{M}_N^\eta$ and $\mathcal{M}_N$.

(a) Posterior's marginal means $\mathbb{E}(\cdot)$ for each model parameter.

	$\boldsymbol{\beta}$	$\boldsymbol{\lambda}$	$\boldsymbol{\lambda}_{\text{ind}}$	$\boldsymbol{\alpha_N}$
$\mathcal{M}_N^\eta$	0.437 ± 0.007	0.106 ± 0.007	0.196 ± 0.005	6.930 ± 0.739
$\mathcal{M}_N$	0.435 ± 0.012	0.103 ± 0.012	0.186 ± 0.009	
	$\boldsymbol{V}_{\text{cap}}$	$\boldsymbol{b}$	$\boldsymbol{N}_{\text{thr}}$	
$\mathcal{M}_N^\eta$	1.731 ± 0.028	5.315 ± 0.856	0.106 ± 0.002	
$\mathcal{M}_N$	1.740 ± 0.038	4.731 ± 0.685	0.104 ± 0.003	

(b) Posterior's marginal variances $\text{Var}(\cdot)$ for each model parameter.

	$\boldsymbol{\beta}$	$\boldsymbol{\lambda}$	$\boldsymbol{\lambda}_{\text{ind}}$	$\boldsymbol{\alpha_N}$
$\mathcal{M}_N^\eta$	0.010 ± 0.006	0.009 ± 0.006	0.012 ± 0.007	3.211 ± 0.870
$\mathcal{M}_N$	0.007 ± 0.005	0.006 ± 0.004	0.010 ± 0.006	
	$\boldsymbol{V}_{\text{cap}}$	$\boldsymbol{b}$	$\boldsymbol{N}_{\text{thr}}$	
$\mathcal{M}_N^\eta$	0.033 ± 0.019	1.071 ± 0.515	0.004 ± 0.002	
$\mathcal{M}_N$	0.028 ± 0.018	0.751 ± 0.224	0.004 ± 0.002	

The obtained parameter values can be concluded as biologically reasonable, since we chose respective prior distributions ensuring this (recall Section 5.3.1). Up to some adaptions regarding units and reparametrization, their meaningfulness is also supported by comparing the estimated values to the calibration results of [21], where a set of similar models is used together with parts of the same data.

Cells' reaction to nutrient changes. Both models use the same influence functions from (3.7)

$$\delta_N^+(N) = \frac{N^2}{N_{\text{thr}}^2 + N^2} \qquad \text{and} \qquad \delta_N^-(N) = 1 - \frac{N^2}{N_{\text{thr}}^2 + N^2}$$

for the effect of the nutrients on the cell dynamics. In model $\mathcal{M}_N$ these functions scale the rates β (growth) and λ_{ind} (induced death) directly, whereas in model $\mathcal{M}_N^\eta$ they scale them indirectly via the stress level $\eta(t)$. Therefore, the value of the nutrient sensitivity threshold N_{thr} should not depend on the choice of the model, which actually holds true in the results: $\mathbb{E}(N_{\text{thr}}) \approx 0.1$ (see Table 7a).

Next, we take a closer look at the cells' reaction owing to an ESL η. For the following investigations, we fix $N_{\text{thr}} = 0.106$ to its estimate from model $\mathcal{M}_N^\eta$, since we already observed sufficiently small variations of this parameter. The nutrient impact rate α_N shows a large average variance of its marginal posterior (Table 7b: $\text{Var}(\alpha_N) \approx 3.211$) as well as relatively large numerical deviations between the SMC runs. This could be explained by the fact that only a minority of the measurements contain meaningful information to estimate α_N. In particular, if the provided nutrient supply is sufficiently large ($N_0 \gg N_{\text{thr}} = 0.106$), the corresponding value of the influence function $\delta_N^-(N_0)$ is virtually zero and

$$\eta(t) = \delta_N^-(N_0) \cdot (1 - e^{-\alpha_N t}) + \underbrace{\eta_0}_{=0} e^{-\alpha_N t}$$

from (3.6) barely changes from its initial value $\eta_0 = 0$. The stress level is the only quantity of the system coupling the parameter α_N with the cell viability (i.e. the data), hence $\eta(t) \approx 0$ provides little information to estimate α_N. In fact, due to the small value of $N_{\mathrm{thr}} = 0.106$, the relation $N_0 \gg N_{\mathrm{thr}}$ holds true for most of the calibration data, recall $N_0 \in \{0.00, 0.25, 0.50, 0.75, 1.00\}$. Nevertheless, we can argue that the observed variance of α_N does not have a big influence on the estimated average solution of model $\mathcal{M}_N^\eta$. We calculate the ESL $\eta(t)$ with $N_{\mathrm{thr}} = 0.106$ and varying α_N. In particular, we assume α_N to be normally distributed with sample mean and standard deviation as given in Table 7a. The resulting time evolution is depicted in the first two plots of Figure 17. The left one shows $\eta(t)$ for varying α_N, while in the middle one we also fix α_N to its estimated marginal mean. The third plot shows the corresponding influence functions δ_N^+ and δ_N^-.
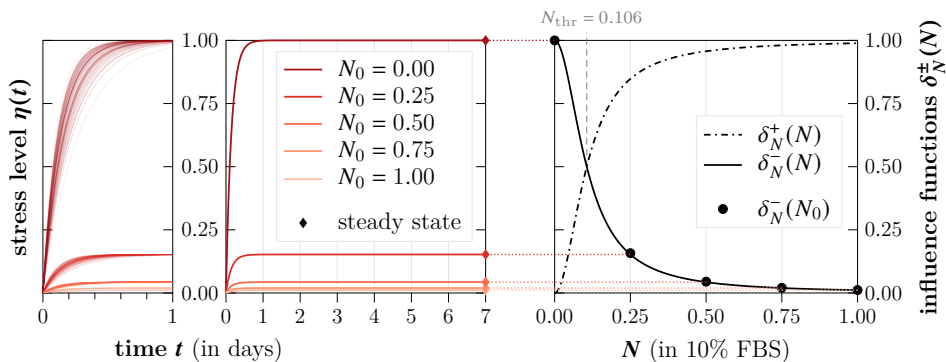
Figure 17: Left: Time evolution of $\eta(t)$ on the first day for different nutrient conditions N_0 with $N_{\mathrm{thr}} = 0.106$ and varying $\alpha_N \sim \mathcal{N}(\bar{x}, \sigma_x)$, where $\bar{x} = 6.930$ and $\sigma_x = 1.707$ are the sample mean resp. standard deviation of the different SMC runs.
Middle: Corresponding time evolution of $\eta(t)$ over seven day and fixed $\alpha_N = 6.930$.
Right: Illustration of how the values $\delta_N^-(N_0)$ of the influence functions coincide with the steady states of η.

Figure 17 shows that the steady state of η is already reached after approximately one day (see middle plot). This means the cells react quickly to nutrient changes due to the large estimated value for α_N (Table 7a: $\mathbb{E}(\alpha_N) \approx 6.930$). This behavior remains unchanged even for the large deviations in the estimate of α_N (see left plot). Therefore, variation of α_N within the calibrated scale does not significantly alter $\eta(t)$ and hence the solution of model $\mathcal{M}_N^\eta$.

The right plot demonstrates how the steady state of $\eta(t)$ actually coincides with the function value $\delta_N^-(N_0)$ of the influence function (which was stated in Table 2 in Section 3.2). Therefore, the high nutrient sensitivity explains why the remaining parameters estimates turn out to be very similar for both models, as model $\mathcal{M}_N$ was achieved from $\mathcal{M}_N^\eta$ by assuming a very fast reaction to nutrient changes.

Parameter correlation in the models. To identify parameter correlations resulting from the modeling, we investigate the estimated posterior from a single run of the SMC algorithm. We choose a run whose resulting expected values of the parameters' marginal distributions approximately match the ones in Table 7a. Figure 18 shows the KDEs of the corresponding marginal posteriors (line plots in first row/column) for each model (red/blue) and samples drawn from the 2D posterior distributions of pairwise parameter combinations (scatter diagrams). As explained in Section 6.1.4, the shape of the point clouds can give an impression regarding the pairwise correlations between parameters.
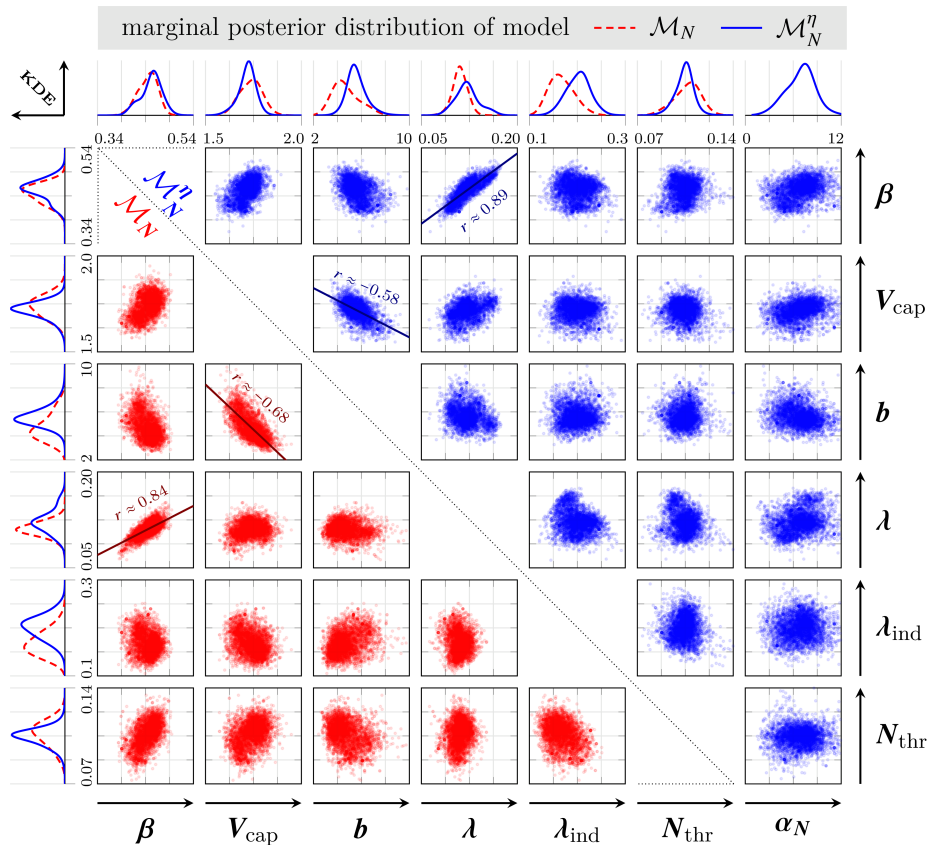
Figure 18: Figure structure: Each subplot regards to the parameter combination of the respective horizontal and vertical axis label on the bottom resp. right side – in particular:
Line plots in first row/column: KDEs of marginal posterior distributions of the model parameters (note: KDE axes have different scale).
Scatter plots: 5000 samples drawn from the 2D distributions of pairwise parameter combinations (red, below diagonal: $\mathcal{M}_N$; blue, above diagonal: $\mathcal{M}_N^\eta$). A regression line and correlation coefficient r is depicted if a considerable linear correlation is observable.

We see that the SMC algorithm leads to unimodal marginal distributions. For the majority of parameters, the scatter plots indicate no correlation, especially between the stress-related parameter α_N and other parameters (last column of blue scatter diagrams). For both models, a significant ($p_{\text{sig}} < 0.001$) linear correlation can be observed between β and λ ($\mathcal{M}_N^\eta$: $r \approx 0.89$; $\mathcal{M}_N$: $r \approx 0.84$) as well as between V_{cap} and b ($\mathcal{M}_N^\eta$: $r \approx -0.58$; $\mathcal{M}_N$: $r \approx -0.68$).

Both correlations can be reasoned by the design of the models. Recall from Section 3.1 that the ratio between the cells' maximal growth rate β and the natural death rate λ is crucial for the behavior of the population: it determines the "net" growth rate $\beta^* = \beta - \lambda$ and the "net" capacity $V_{\text{cap}}^* = V_{\text{cap}}(1 - \lambda/\beta)^{1/b}$ and requires the relation $\beta > \lambda$. This motivates the observed strong positive correlation ($r > 0.7$). For the carrying capacity V_{cap} and the parameter b, we see a moderate negative correlation ($-0.7 < r < -0.5$). These parameters regulate the proliferation contact inhibition with the term $(V/V_{\text{cap}})^b$ in the logistic part of the models' ODE for V. This term is smaller, the larger V_{cap} or b are. Hence, these parameters need to be negatively correlated to mathematically describe a certain level of contact inhibition.

6.2.2   Comparison of the models $\mathcal{M}_N^\eta$ and $\mathcal{M}_N$ with data

In this section we compare the estimated solutions of the respective models with each other as well as with the available data from [21].

Estimated model solution compared to the data.   We use the marginal means of the model parameters in Table 7a to calculate the corresponding estimated model solution V. Following relation (4.1): $I = n \cdot V$, the intensity measurements I are scaled with the calibrated marginal means of n_0 and n_N (see Table E.3 in the appendix) – in particular for model $\mathcal{M}_N^\eta$ resp. $\mathcal{M}_N$:

$$\mathbb{E}(n_0) = 0.182 \quad \text{resp.} \quad \mathbb{E}(n_0) = 0.190 \quad \text{(for } N_0 = 0\text{, i.e. data set D0)},$$
$$\mathbb{E}(n_N) = 0.243 \quad \text{resp.} \quad \mathbb{E}(n_N) = 0.244 \quad \text{(for } N_0 > 0\text{, i.e. data sets D1–D4)}.$$

Figure 19 shows the resulting time evolution of $V(t)$ compared to the calibration data sets D0–D4.
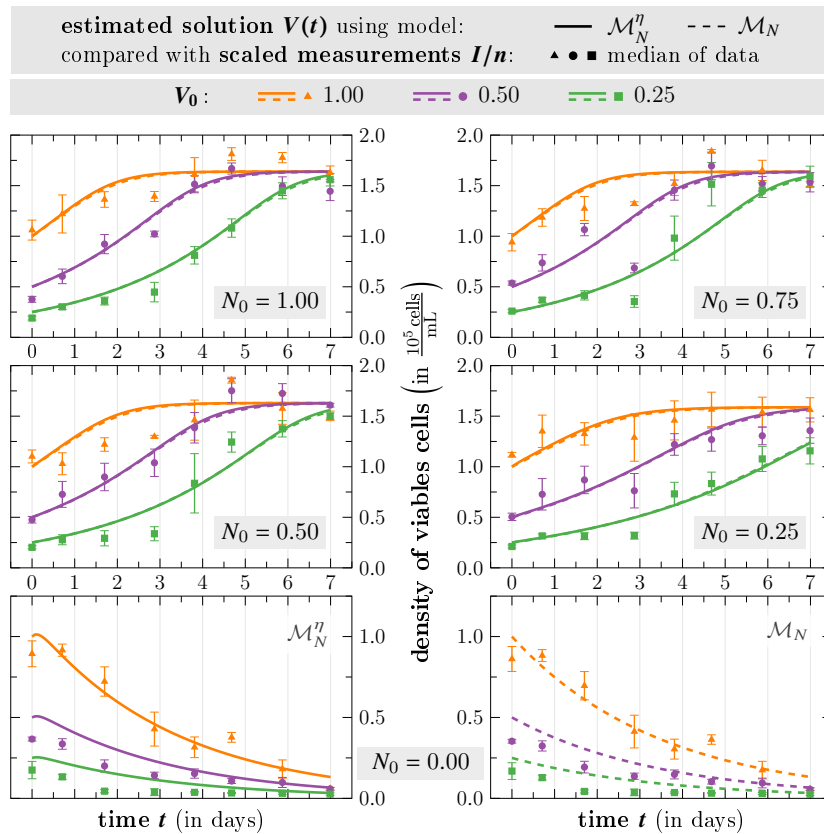
Figure 19: Time evolution of the estimated model solution V of model $\mathcal{M}_N^\eta$ resp. $\mathcal{M}_N$ for different V_0 and N_0 compared to the corresponding median of the scaled viability measurements I/n with $n = n_0$ resp. $n = n_N$ for $N_0 = 0$ resp. $N_0 > 0$ as estimated with the corresponding model (error bars: median absolute deviation considering the four biological replicates).

In general, we observe a good fit for both models. As expected, the similar model parameter values in Table 7a result in nearly the same solution for each model – at least for all cases of $N_0 > 0$ (first two rows of plots in Figure 19). In these cases, the estimated proportionality constant is $n_N \approx 0.24$ for both models, whereas for $N_0 = 0$ they are slight differences: $n_0 \approx 0.18$ resp. $n_0 \approx 0.19$ ($\mathcal{M}_N^\eta$ resp. $\mathcal{M}_N$). This results in different scaling of data set D0 (markers of

bottom row plots of Figure 19). However, the difference of the estimates of n_0 between the models is found to be statistically insignificant ($p_{\text{sig}} > 0.05$), see Appendix E.I.1 for more details.

Taking a closer look into the measurements in Figure 19, we see that the population size drops at the third day of the experiment ($t \approx 3$) for almost all seeding densities V_0 and nutrient saturations $N_0 > 0$, most obviously visible for $N_0 = 0.75$ (top right plot). However, there is no obvious biological reason for this as long as there are nutrients available. Hence, it is reasonable to assume that the discrepancy between the corresponding data and model solution results from an unknown experimental bias rather than modeling inaccuracy or biological variation. The hypothesis that these measurements might be outliers can be supported by checking the amount of data which is actually situated in the 90% uncertainty range of the solution (i.e. the neighborhood in which we would expect 90% of the data points to be, recall Section 4.1.3). In fact, for the measurements on the third day, we see an extraordinarily large amount of data (up to 78%) is below the uncertainty range, where only 5% would be expected. The detailed analysis can be found in Appendix E.I.2.

Quality of fit to the data.   We calculate the Bayes factor as well as the validation metric as described in Section 6.1.1. The resulting values of the latter do not show any preference of a particular model (see Appendix E.I.3) – in contrast to the Bayes factor

$$\log_{10}\left(\mathcal{Z}_\mathcal{I}(\mathcal{M}_N^\eta, \mathcal{M}_N)\right) = \log_{10}\left(\frac{L(\mathcal{I}\,|\,\mathcal{M}_N^\eta)}{L(\mathcal{I}\,|\,\mathcal{M}_N)}\right).$$

Figure 20 shows and interprets its average trend over the course of the SMC steps according to the scale given in (6.2). Additionally to the averaged trend, the plot shows the evolution of the Bayes factor for one particular run of the algorithm (dashed line)[17]. For this run, the estimated marginal means of the parameters match approximately with the ones in Table 7a.
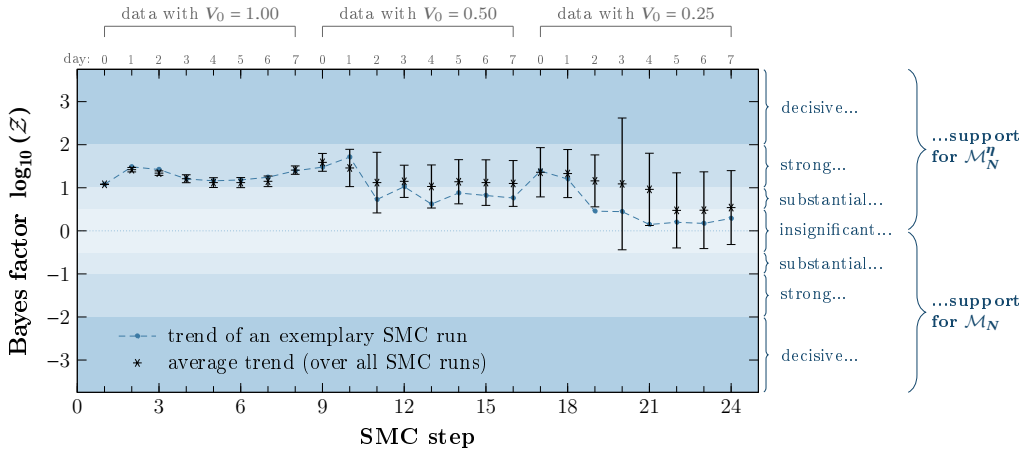
Figure 20: Logarithm of the Bayes factor $\mathcal{Z} = \mathcal{Z}_\mathcal{I}(\mathcal{M}_N^\eta, \mathcal{M}_N)$ over the course of the SMC steps (error bars: 95% confidence interval from 12 runs of the SMC algorithm). The dashed trendline shows the evolution for a single run, which estimated the model parameters close to the average values of all runs. The gray labels on top of the plot give the data increments of each step.

Overall, the average trend of the Bayes factor indicates support for model $\mathcal{M}_N^\eta$, despite needing an additional variable and parameter. In particular, for the first eight SMC steps, the Bayes factor indicates strong evidence to prefer model $\mathcal{M}_N^\eta$ over $\mathcal{M}_N$. Until this point, only data

---

[17]this is the same run for which we investigated the parameter correlations in Section 6.2.1

regarding $V_0 = 1.00$ are considered. Incremental inclusion of the next data set (day 0, $V_0 = 0.50$) weakens the weight of the support for model $\mathcal{M}_N^\eta$, but still allows to conclude a tendency of the evidence towards this model. This can be observed further until SMC step 19. At step 20 (i.e. with inclusion of data for day 3 and $V_0 = 0.25$) the uncertainty increases significantly, which does not allow a clear interpretation of the Bayes factor anymore. The 95% confidence interval reaches from areas of decisive support for model $\mathcal{M}_N^\eta$ to almost substantial support for model $\mathcal{M}_N$. After this step, the uncertainty decreases again but stays on a high level, still not allowing a distinct interpretation of the Bayes factor.

The large deviations in the Bayes factor at SMC step 20 could be explained by our previous finding that the measurements on the third day show characteristics of an outlier. Further investigation of the 90% uncertainty range yields another observation: For small values of V_0, more data points, within the measurements of a particular day, tend to be below the 90% range (see Table E.4 in Appendix E.I.2). This might be the reason for the high deviations of the Bayes factor in Figure 20 when including data with $V_0 \leq 0.50$ in the SMC calibration.

Validation of the model calibration.   For additional validation of the calibration results we consider another data set DV (see Table 6), which was not used for calibrations. In the corresponding experiment from [21] tumor cells were seeded in five different initial densities V_0 and supplied with 10% FBS ($N_0 = 1$) for the duration of 21 days. Since the scaling factor n_N for $N_0 > 0$ showed to be sufficiently similar for both models $\mathcal{M}_N^\eta$ and $\mathcal{M}_N$, we use their estimate $n_N = 0.24$ to scale the measurements of this data set. The density of viable cells is calculated as the solution of a population model under optimal growth conditions. In particular, we solve

$$\dot{V} = \beta\, V \left(1 - \left(\frac{V}{V_{\mathrm{cap}}} \right)^b \right) - \lambda\, V \qquad \text{with } V(0) = V_0 \qquad (\mathcal{M}_{\mathrm{opt}})$$

using the estimated marginal means of the model parameters β, V_{cap}, b and λ from Table 7a. This model can be solved analytically (for details see [63]). Figure 21 compares the corresponding scaled viability data I/n_N with the modeled time course of $V(t)$.
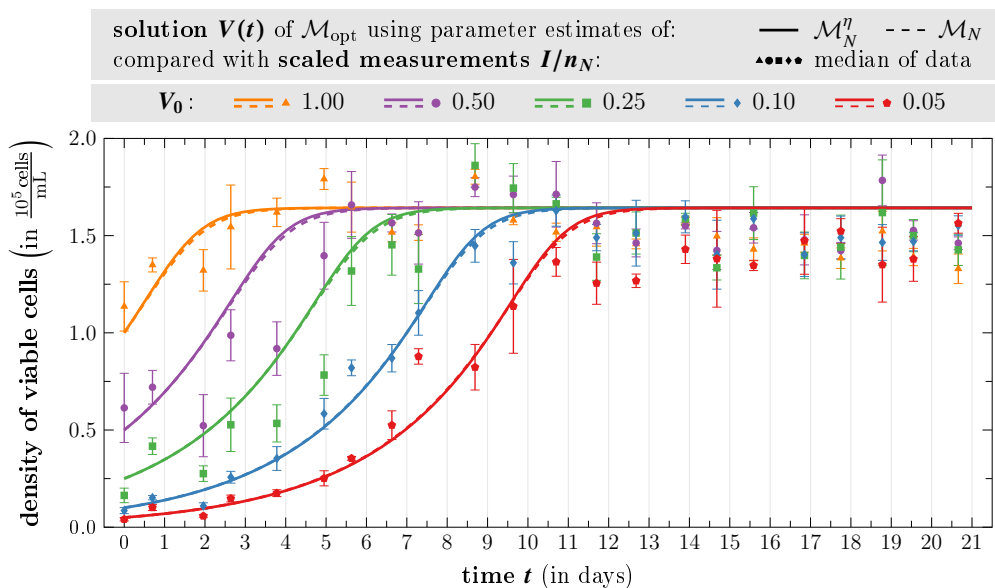
Figure 21: Time evolution of the average model solution $V(t)$ under optimal growth conditions for different V_0 using the parameter estimates from the calibration of model $\mathcal{M}_N^\eta$ resp. $\mathcal{M}_N$ compared to the corresponding median of the scaled measurements I/n_N (error bars: median absolute deviation considering the four biological replicates).

As expected, both solutions are very similar as the parameters β, V_{cap}, b and λ showed almost the same estimates for $\mathcal{M}_N^\eta$ and $\mathcal{M}_N$. In general, we see a good fit to the data (see also ratios of validation metrics in Table E.5 in the appendix).

It is observable that the model solutions tend to overestimate the data after the steady state is reached. In reality, population growth often follows the concept of "overshoot": this describes the observation that a population might exceed its carrying capacity and drop back down afterwards [104, Ch. 4]. Reasons can be a lag in sensing the available resources in the environment or the time interval between birth and death. The measurements starting with $V_0 \in \{1.00, 0.50, 0.25\}$ (orange/triangle, purple/diamond and green/square markers in Figure 21) suggest an observable overshoot effect, but the model solutions cannot reproduce this phenomenon due to the limited structure of the logistic growth model. This could explain the discrepancy between solution and data close to the carrying capacity.

6.3 Chemoresistance of tumor cells under hypoxia and high tissue stiffness

We now move on to the more complex application of the ESL approach. We calibrated the models $\mathcal{M}_{DS}^0$ and $\mathcal{M}_{DS}^{\text{CYP}}$ with the experimental data in [22] to investigate the effect of oxygen and stiffness conditions on the chemoresistance of different hepatocellular carcinoma cell lines (Hep3B2, HepG2, C3Asub28). These cells, among others, differ in the extent of CYP3A (CYP) enzyme expression, which metabolizes the chemotherapeutic drugs doxorubicin (DOX, D) and sorafenib (SOR, S). This dynamic is incorporated in the complete model $\mathcal{M}_{DS}^{\text{CYP}}$ by the metabolization rates γ_D, γ_S and omitted in the reduced model $\mathcal{M}_{DS}^0$, where the drug concentrations to stay constant ($D = D_0$, $S = S_0$) during treatment.

In the following Subsections 6.3.1 resp. 6.3.2, the calibration results will be investigated according to the explanations in Subsection 6.1.3 and subsequently summarized in Subsection 6.3.3. In particular, the parameter estimates are given by the marginal MAPs, as the marginal posteriors partially showed strong skewness, and we present numerical variations with the cross-validated 95% confidence interval, visualized by error bars. In general, the cross-validation showed high robustness and only small numerical variations of the calibration results. Therefore, it is reasonable to base our investigations on the estimates of the posterior obtained by collecting the particles of all four runs and do the significance check as proposed in Subsection 6.1.3 and Figure 15. Before we go into detail with the calibration results, we discuss the fact that it was not possible to calibrate all models and data sets.

Applicability of the models. Recall that only cell line Hep3B2 exhibits no significant CYP expression [22], i.e. for these data we use the reduced model $\mathcal{M}_{DS}^0$. However, attempts to calibrate the remaining data sets for HepG2 and C3Asub28 with model $\mathcal{M}_{DS}^{\text{CYP}}$ did not give reasonable posterior distributions to calculate an appropriate model solution reproducing the measurements. In particular, the algorithm shows difficulties to estimate the drug impact rates α_D^- and α_S^- as well as the metabolization rates γ_D and γ_S. A possible reason is the sparse time resolution of the available data: Viability was measured only once, three days after a one- or two-day treatment. Hence, the only time-related information is given by the variation in viability for different treatment durations. It appears that this information is not sufficient to properly estimate the rates. This conjecture is supported by trying to calibrate the Hep3B2 data with the complete model $\mathcal{M}_{DS}^{\text{CYP}}$, which did not result in vanishing metabolization rates as we would expect knowing that the cells express almost no CYP. As an alternative, we calibrate the data for HepG2 and C3Asub28 with the reduced model $\mathcal{M}_{DS}^0$ instead and focus our investigations on potential correlations between parameters and the available measurements of CYP expression from [22].

Applicability of the data.   Recall the investigated treatments with combined drug dosages of

DOX (main drug): $D_0 \in \{0.0001, 0.001, 0.01, 0.1, 0.5, 1, 5, 10, 50, 100, 1000\}$ (in µM),

SOR (supportive drug): $S_0 \in \{0.0, 0.5, 1.0\}$ (in $22\,\mu M$),

as well as the terms and abbreviations for the underlying environmental settings:

$$\text{"normal conditions" :} \qquad H_0\,, C_0 = 0 \;\overset{\text{abbr.}}{\rightsquigarrow}\; \text{HC0}\,,$$
$$\text{"sole hypoxia" :} \quad H_0 = 1\,, C_0 = 0 \;\rightsquigarrow\; \text{H1}\,,$$
$$\text{"sole cirrhosis" :} \quad H_0 = 0\,, C_0 = 1 \;\rightsquigarrow\; \text{C1}\,,$$
$$\text{"cirrhosis and hypoxia" :} \qquad H_0\,, C_0 = 1 \;\rightsquigarrow\; \text{HC1}\,.$$

As explained in Section 5.2.2, the percentage viability data was clipped to the interval $[0.001, 1]$ to accommodate the models' limited co-domain $(0, 1]$. Clipping the measurements to this upper bound should omit characteristics of enhanced growth which was observed in some data sets, where the percentage viability was strongly overshooting the mark of 100%. In particular, such characteristics can be seen for the cell lines HepG2 (C1, HC1) and C3Asub28 (all). However, attempting model calibrations with these data sets resulted in degenerating variances of the intermediate distributions and unreasonable posteriors. We found that the issues are caused by the inclusion of specific data points. A closer analysis of the respective measurements suggests that obvious growth enhancement only occurs in combined chemotherapy, i.e. in the presence of SOR. This leads to situations where for a particular DOX dosage the viability of cells which underwent combined treatment is significantly higher than for cell exposed to sole DOX treatment. Since the models assume that SOR can only decrease the cell viability, such measurements appeared to be impossible to reproduce without disproportionately increasing the noise variance. Therefore, it is not possible to reasonably investigate the concerned data sets (HepG2: C1, HC1 and C3Asub28: all) with our models. In the following Subsections 6.3.1 resp. 6.3.2 we present and discuss the calibration results of the remaining data sets Hep3B2 (all) and HepG2 (HC0, H1).

6.3.1   Chemoresistance for cell line Hep3B2 without drug metabolization

We investigate the calibration results of model $\mathcal{M}_{DS}^0$ using the data of Hep3B2, i.e. a cell line with negligible CYP expression and hence drug metabolization. Complementary material will be provided in Appendix E.II and referenced in the following where relevant.

Treatment response.   Figure 22 shows the data (markers) with the corresponding model solution (line plots) based on the estimated marginal MAPs of the parameters[18]. For a easier comparison, the small plots in the upper right corners illustrate the trend of the data. Note that, following the approach mentioned in Subsection 5.2.2 (recall also Figure 10), we omitted the measurements for $D_0 \geq 10$ for the calibration data set of this cell line.

---

[18]Note that using the MAP of the joint posterior to calculate the corresponding model solution would be more appropriate. However, its derivation is highly non-trivial due to the high dimensionality. As we need it for visualization purposes only, we use the marginal MAPs which are much easier to compute.
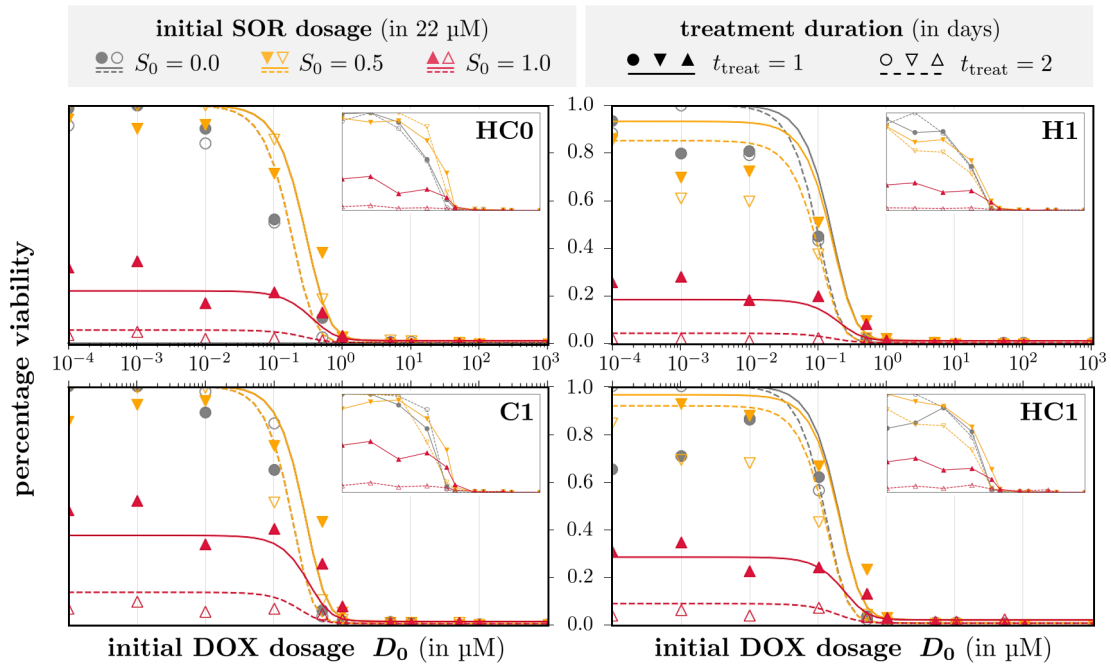
Figure 22: Comparison of the measured percentage viability for cell line Hep3B2 with the corresponding estimated model solutions using model $\mathcal{M}_{DS}^0$ for different environmental settings. Note that some of the gray line plots might not be visible, as they overlap with the yellow ones.

In general, we see reasonable fits of the model solutions to the measurements. For H1 and HC1 the model tends to overestimate the corresponding data for small DOX dosages $D_0 \leq 10^{-2}$ and SOR dosages of $S_0 \in \{0.0, 0.5\}$ (gray and yellow). This could be a result of the uncertainty modeling. On the one hand, the assumed Beta prime distribution of the uncertainty factor from (4.4) is

$$\varepsilon_\% = \overbrace{\frac{\overbrace{I^{\mathrm{treat}}/I^{\mathrm{ctrl}}}^{\mathrm{measured}}}{\underbrace{V^{\mathrm{treat}}/V^{\mathrm{ctrl}}}_{\mathrm{modeled}}}} \sim \beta'\left(\frac{1}{\sigma^2}, \frac{1}{\sigma^2}\right) \text{ with } \sigma^2 = 0.1\,,$$

which is positively skewed with a mode (maximum of the density function) of approximately 0.82. Hence, a modeled percentage viability of

$$\frac{V^{\mathrm{treat}}}{V^{\mathrm{ctrl}}} = \frac{1}{0.82} \cdot \frac{I^{\mathrm{treat}}}{I^{\mathrm{ctrl}}} \approx 1.22 \cdot \frac{I^{\mathrm{treat}}}{I^{\mathrm{ctrl}}}\,,$$

i.e. larger than the corresponding measurement, maximizes the data likelihood function. On the other hand, the multiplicativity of the uncertainty allows larger deviations between solution and data for larger measurements. Therefore, the calibration algorithm might to some extent "prioritize" a closer fit to small data. Another reason could be the modeling of the DOX stress response $\alpha_D^- \cdot \delta_D^-$ by a symmetric Hill function δ_D^-. The line plots of the solutions in Figure 22 show that this leads to a symmetric viability-dose relationship as well. However, the measurements of H1 and HC1 indicate a less steep slope for smaller DOX dosages, which the model cannot reproduce. In summary, the model fit could be further improved by reconsideration of the modeling assumptions for the uncertainty and the DOX dose-response function (more details will be provided in Section 7.2). In the following paragraphs we present more details on the estimated model parameters and discuss them in the biological context of the underlying experiments.

Stress induction by hypoxia and/or cirrhosis.   The direct influence of hypoxia and ECM stiffness on the tumor growth is modeled by the initial ESL $\eta_{0,HC} = \eta_0(H,C) \in [0,1]$. Its marginal MAP estimates are given by

$$\text{(by definition – HC0: 0.000)}, \qquad \text{H1: } 0.2 \cdot 10^{-6}, \qquad \text{C1: } 4.5 \cdot 10^{-6}, \qquad \text{HC1: } 0.119$$

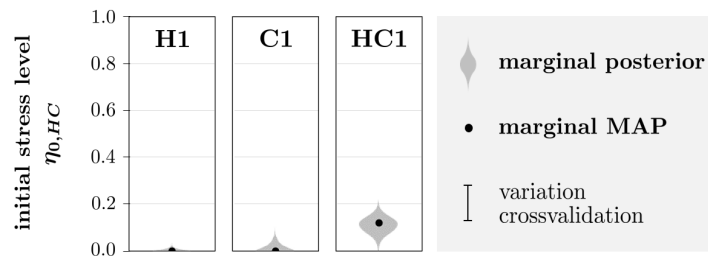and Figure 23 shows the corresponding marginal posteriors as violin plots[19].

Figure 23: Comparison of marginal posteriors (violin plots) and corresponding MAPs of $\eta_{0,HC}$ for Hep3B2. Due to minor numerical variations, the cross-validated 95% confidence intervals (error bars) are not visible.

The distributions indicate that sole hypoxia or cirrhosis (H1/C1) does not induce a significant level of stress on the tumor cells, while a combination of both (HC1) does ($***$, see appended Figure E.6). This suggests a synergistic effect of those environmental factors, since the estimates of $\eta_{0,HC}$ for H1 and C1 clearly do not add up to the one of HC1. Mathematically, this means our modeling assumption in (3.11), i.e.

$$\eta_0(H_0, C_0) = \underbrace{\frac{\alpha_H \cdot \delta_H^-(H_0)}{\alpha_H + \alpha_C}}_{\eta_0(H_0,\,0)} + \underbrace{\frac{\alpha_C \cdot \delta_C^-(C_0)}{\alpha_H + \alpha_C}}_{\eta_0(0,\,C_0)},$$

has to be reconsidered, and we should allow both influence functions δ_H^- and δ_C^- to respectively depend on both variables H and C. Since we do not have any suitable data to estimate these functions or the impact rates α_H and α_C, we cannot make any further conclusions about the influence of hypoxia and high ECM stiffness on the tumor growth.

Cell growth and death.   Due to the context of percentage viability, we were not able to directly estimate the growth/death rates β, λ_{ind} and λ (recall Subsection 3.3.3). In particular, we could only estimate the term $\beta + \lambda_{\text{ind}}$, which was done just for the setting HC0 and fixed to its marginal MAP for the remaining calibrations (H1/C1/HC1). Figure 24 shows the estimates of this term for each SMC run in comparison with the respective estimation resulting from the particle approximation collecting all runs. While the run-specific MAPs were used to perform further calibrations, the MAP considering all runs was used to calculate the new weights of the posterior approximation collecting the particles of all runs.

---

[19]A violin plot is basically a shaded representation of the (truncated) KDE, additionally flipped on a mirror axis (here: vertical), i.e. the width of each "violin" gives the density (or the twice of it to be more precise). Note that the scaling of the width is not the same when comparing different violin plots, as this is not the focus of the investigations.
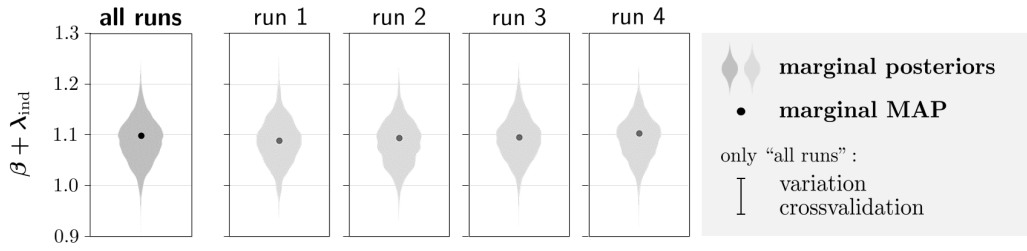
Figure 24: Estimations of $\beta + \lambda_{\text{ind}}$ for Hep3B2 in the setting HC0: Marginal posteriors as violin plot and corresponding MAPs (used deterministically in each run for calibrating the remaining settings H1/C1/HC1). Due to minor numerical variations, the cross-validated 95% confidence interval (error bar) is not visible.

We see that the estimation of $\beta + \lambda_{\text{ind}}$ is very consistent and all calibrations of H1/C1/HC1 suppose virtually the same value for each run. Using the MAP $\beta + \lambda_{\text{ind}} \approx 1.099$ from the particle approximation combining all SMC runs, we can conclude

$$\beta + \lambda_{\text{ind}} > \beta - \lambda \quad \Rightarrow \quad \beta\,,\lambda_{\text{ind}}\,,\lambda < 1.099\,.$$

Furthermore, we know that $\eta_{0,HC} \leq \frac{\beta - \lambda}{\beta + \lambda_{\text{ind}}}$ holds for all environmental conditions (recall bounds in (3.11)). By using the largest observed estimate of $\eta_{0,HC}$, we obtain a lower bound for $\beta - \lambda$:

$$0.119 \overset{\text{HC1}}{\approx} \eta_{0,HC} \leq \frac{\beta - \lambda}{\underbrace{\beta + \lambda_{\text{ind}}}_{\approx\,1.099}} \quad \Rightarrow \quad \beta - \lambda \gtrsim \frac{0.119}{1.099} \approx 0.108\,.$$

Cytotoxic efficacy of SOR. Besides its supportive effect, SOR can be directly cytotoxic for the tumor cells. Given our modeling approach, this would show in significantly non-zero values of the stress response function

$$\alpha_S^- \delta_{S,HC}^-(S) = \alpha_S^- \delta_S^-(S, H, C) = \frac{\alpha_S^- \cdot S^{m_2}}{S_{\text{thr}}(H, C)^{m_2} + S^{m_2}}$$

for $S = S_0 > 0$. Recall from Figure 13 in Subsection 5.3.2 that for the reduced model $\mathcal{M}_{DS}^0$ we could only estimate the function values of $\alpha_S^- \delta_{S,HC}^-$ pointwise for $S_0 \in \{0.5, 1.0\}$ due to the limited number of experimentally investigated SOR dosages. This means that we cannot isolate quantitative information on how fast the cells are impacted by the SOR treatment (α_S^-) or the dose-response ($\delta_{S,HC}^-$) for continuous S. Figure 25 shows the marginal posteriors of the stress response as violin plots as well as the estimated marginal MAPs.
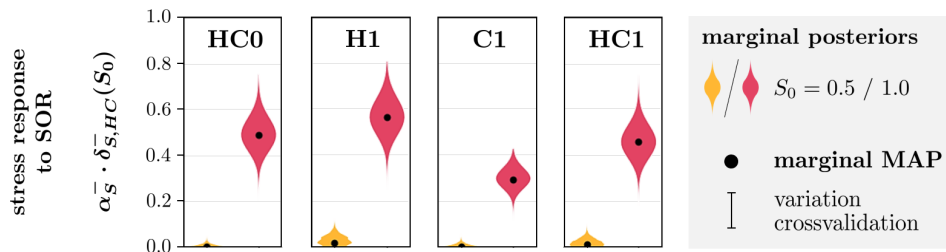
Figure 25: Comparison of marginal posteriors (violin plots) and corresponding MAP estimates of $\alpha_S^- \delta_{S,HC}^-(S_0)$ for Hep3B2. Note that for $S_0 = 1.0$ it was directly calibrated, while for $S_0 = 0.5$ the estimates are obtained by calibration of $c_\delta = \alpha_S^- \delta_{S,HC}^-(0.5) \,/\, \alpha_S^- \delta_{S,HC}^-(1.0)$. Due to minor numerical variations, the cross-validated 95% confidence intervals (error bars) are not visible.

Although we cannot reconstruct the parameters of $\alpha_S^- \delta_{S,HC}^-$ from the estimates in Figure 25, we still get a feeling for the rough shape of the sigmoid function. First, the fact that a standard dosage of SOR ($S_0 = 0.5$) barely shows any stress response compared to a high dosage ($S_0 = 1.0$) in all environments indicates a SOR susceptibility threshold with

$$S_{\mathrm{thr}}(H, C) > 0.5 \qquad \forall H, C \in \{0, 1\} \,.$$

Second, due to $0 \leq \delta_{S,HC}^-(S) < 1 \ \forall S \geq 0$, the response for a high dosage $\alpha_S^- \delta_{S,HC}^-(S_0 = 1.0)$ yields a lower bound for the respective SOR impact rate

$$\alpha_S^- \geq \alpha_S^- \delta_{S,HC}^-(S_0 = 1.0) \,,$$

for given H and C and up to variations in the magnitude of the corresponding marginal variance. We proceed with a closer investigation of the individual estimates of Figure 25, where all mentioned significance results are derived from Figure E.7 in the appendix.

<u>High SOR dosage</u>. We see a clear stress response for $S_0 = 1.0$ under all environmental conditions where the introduction of cirrhosis and hypoxia has a significant influence on the drug efficacy. In particular, oxygen deprivation increases the response to SOR ($***$), while stiffening of the ECM decreases it ($***$):

$$
\begin{aligned}
\text{sole hypoxia (HC0} \rightsquigarrow \text{H1):} &\quad 0.489 \nearrow 0.566 \ (+15.7\%) \,, \\
\text{hypoxia in cirrhosis (C1} \rightsquigarrow \text{HC1):} &\quad 0.294 \nearrow 0.458 \ (+55.8\%) \,, \\
\text{sole cirrhosis (HC0} \rightsquigarrow \text{C1):} &\quad 0.489 \searrow 0.294 \ (-39.9\%) \,, \\
\text{cirrhosis in hypoxia (H1} \rightsquigarrow \text{HC1):} &\quad 0.566 \searrow 0.458 \ (-19.1\%) \,.
\end{aligned}
$$

We see that the degree of the increase/decrease of the response to SOR is different for sole cirrhosis/hypoxia compared to a combination of both, which hints on a synergistic effect of those environmental factors. Furthermore, the combination of high ECM stiffness and hypoxia appears to slightly diminish the response compared to normal conditions:

$$\text{HC0} \rightsquigarrow \text{HC1}: \quad 0.489 \searrow 0.458 \ (-6.3\%) \,.$$

However, we see no statistical significance of latter observation, i.e. its relevance is unclear.

<u>Standard SOR dosage</u>.   For $S_0 = 0.5$ we overall get relatively small marginal MAP estimates for $\alpha_S^- \delta_{S,HC}^-(S_0)$ and a non-zero stress response is only visible if hypoxia involved (H1/HC1):

$$\text{HC0: } 4.4 \cdot 10^{-9} \,, \qquad \text{H1: } 0.019 \,, \qquad \text{C1: } 5.0 \cdot 10^{-7} \,, \qquad \text{HC1: } 0.011 \,.$$

We again see an increasing ($***$) resp. decreasing (unclear significance) influence of hypoxia resp. cirrhosis on the treatment response. The fact that we only see a reaction under hypoxic conditions, even in combination with a stiff ECM (HC1), indicates a dominating increase of SOR efficacy due to hypoxia compared to the decrease by tissue stiffening ($***$).

Cytotoxic efficacy of DOX.   Next, we analyze the estimated stress response to DOX given by

$$\alpha_D^- \cdot \underbrace{\delta_D^-(D_0, S_0, H_0, C_0)}_{\delta_{D,HC}^-(D_0, S_0)} = \alpha_D^- \cdot \frac{D_0^{m_1}}{\left(\underbrace{D_{\mathrm{norm}} \cdot d_H(H_0) \cdot d_C(C_0)}_{D_{\mathrm{norm},HC}} \cdot d_S(S_0) \right)^{m_1} + D_0^{m_1}}$$

for varying DOX and SOR dosages D_0 resp. S_0 and different environmental conditions H_0, C_0. Recall that the functions d_H, d_C (environmental effects) and d_S (supportive effect of SOR)

shift the DOX susceptibility threshold D_{norm}. As expected, the particle approximation indicates relevant correlations of the DOX susceptibility threshold $D_{norm,HC}$ and the remaining parameters of $\alpha_D^- \cdot \delta_D^-$ (see Figure E.4 in the appendix). To consider these, we calculate $\alpha_D^- \delta_{D,HC}^-(D_0, S_0)$ for each particle and each combination of D_0 and S_0. Figure 26 depicts the resulting distributions (gray violin plots) for particular DOX dosages D_0 and without the support of SOR ($S_0 = 0$). Furthermore, it shows a weighted least square fit of $\alpha_D^- \delta_{D,HC}^-$ (dotted black line) to the MAPs of these distributions under consideration of the respective variances[20]. The resulting fitted values of $D_{norm,HC}$ are illustrated (dotted blue line) in comparison with the marginalized posterior distribution of $D_{norm,HC}$ (blue shaded truncated KDE plots on the top/bottom).
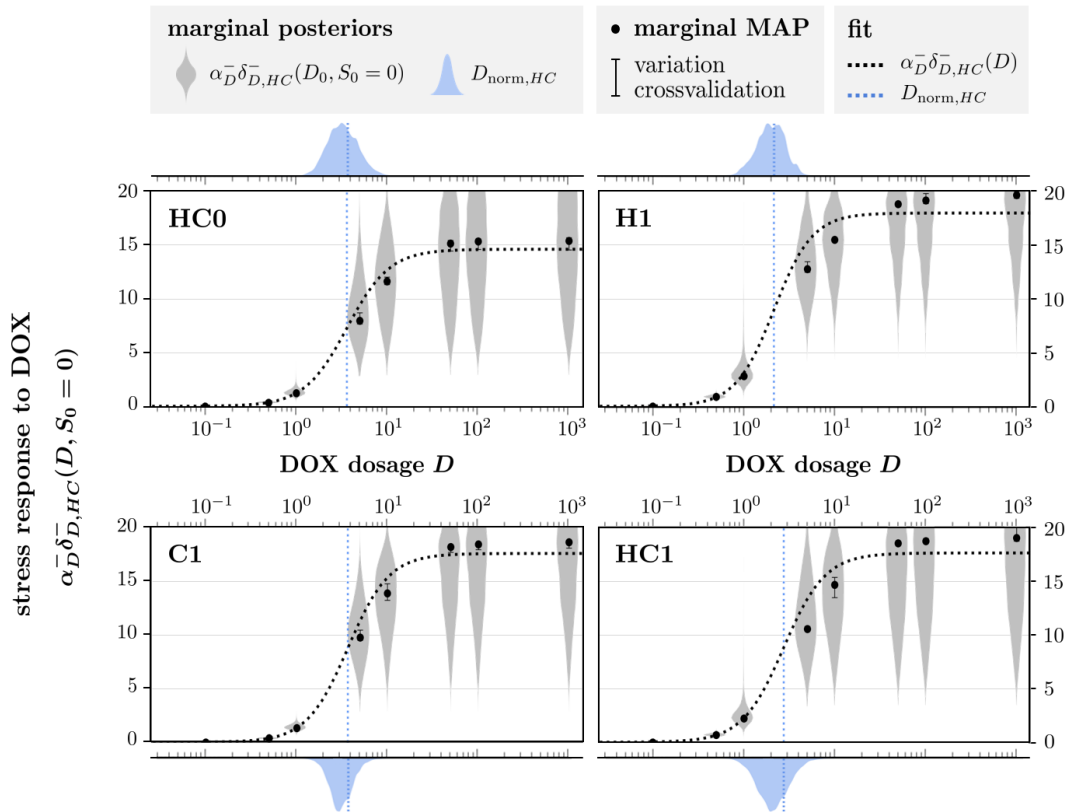
Figure 26: Comparison of marginal posteriors (violin plots) and corresponding MAP estimates of the unsupported DOX efficacy $\alpha_D^- \delta_{D,HC}^-(D_0, 0)$ for Hep3B2. The sigmoidal line is the corresponding least square fit. Note the only measurements for DOX dosages up to $D_0 = 5$ were actually used for the model calibration, hence the marginals for larger D_0 are extrapolated to reach the horizontal asymptote for reasonable fitting. Due to minor numerical variations, some cross-validated 95% confidence intervals (error bars) are not visible.

In general, we achieve good[21] and reasonable fits where the resulting values for the susceptibility threshold $D_{norm,HC}$ are in the high probability region of the respective marginal posteriors, i.e. close to the global modes of the truncated KDEs. Furthermore, the estimated sensitivity parameter m_1 (steepness of the stress response) shows no obvious differences for all environmental

---

[20]We use the Python function `scipy.optimize.curve_fit(..., sigma=stdev, absolute_sigma=True)`, where `stdev` are the standard deviations obtained from the respective marginal variances.

[21]A possible measure to judge the quality of the fit is the so-called *coefficient of determination* $R^2 (\leq 1)$, where $R^2 = 1$ indicates a perfect fit (see e.g. [105] for details). In particular, we get the values:
$R^2 \approx 0.991, 0.982, 0.990, 0.981$ for HC0/H1/C1/HC1.

conditions:

$$\text{HC0:}\ \ 1.858\ (\text{fit}),\ 1.772\ (\text{MAP})\,, \qquad \text{H1:}\ \ 2.059\ (\text{fit}),\ 1.807\ (\text{MAP})\,,$$
$$\text{C1:}\ \ 1.992\ (\text{fit}),\ 1.898\ (\text{MAP})\,, \qquad \text{HC1:}\ \ 1.907\ (\text{fit}),\ 1.857\ (\text{MAP})\,.$$

For such small variations, a closer biological interpretation of the differences is of minor interest. Hence, we focus the following investigations on the susceptibility threshold $D_{\text{norm},HC}$ and the impact rate α_D^-.

<u>DOX susceptibility threshold</u>.   We analyze the fitted estimates of $D_{\text{norm},HC}$ as they are obtained in consideration of the parameter correlations. However, they do not provide a sample representation of the estimates and hence we cannot judge the statistical significance of our observations in contrast to the approach of investigating the marginal distributions (without considering correlations) of $D_{\text{norm},HC}$ instead. The latter is done for comparison in Appendix E.II.3 and will be referred to as *marginalized investigation* for the rest of this paragraph. The significance checks for both fitted and marginal estimates can be found in Appendix E.II.3, as well.

The fitted values of $D_{\text{norm},HC}$ are:

$$\text{sole hypoxia (HC0} \rightsquigarrow \text{H1):}\ \ 3.646\ \searrow\ 2.161\ \ (-40.7\%)\,,$$
$$\text{hypoxia in cirrhosis (C1} \rightsquigarrow \text{HC1):}\ \ 3.689\ \searrow\ 2.762\ \ (-25.1\%)\,,$$
$$\text{sole cirrhosis (HC0} \rightsquigarrow \text{C1):}\ \ 3.646\ \nearrow\ 3.689\ \ (+\ 1.2\%)\,,$$
$$\text{cirrhosis in hypoxia (H1} \rightsquigarrow \text{HC1):}\ \ 2.161\ \nearrow\ 2.762\ \ (+27.8\%)\,.$$

The smaller $D_{\text{norm},HC}$, the more susceptible the cells' are to DOX. Hence, the above estimates show an increase/decrease of the cells' susceptibility to DOX due to hypoxia/cirrhosis. Qualitatively, the same result is obtained by the marginalized investigation. The degree of increase/decreases of $D_{\text{norm},HC}$ appears to be different for sole and combined environmental factors, indicating a synergistic effect between hypoxia and cirrhosis. This is not observable by the marginalized investigation. However, this does not necessarily imply contradicting results, as the marginals of $D_{\text{norm},HC}$ neglect the parameter correlations. Since incorporation of the correlations gives a more holistic approach, it is reasonable to assume a higher validity for the observations obtained with fitting. Furthermore, comparing the fitted values

$$\text{HC0} \rightsquigarrow \text{HC1}:\ \ \ 3.646\ \searrow\ 2.762\ \ (-24.2\%)$$

suggests that the increase of susceptibility due to hypoxia prevails the decreasing effect of high ECM stiffness, which is consistent with the marginalized investigations.

<u>DOX impact</u>.   Figure 26 shows that the MAPs as well as the fit of the stress response $\alpha_D^- \delta_{D,HC}^-$ tend to a horizontal asymptote for large DOX dosages. Mathematically, this asymptote is given by the DOX impact rate α_D^- scaling the sigmoid function $\delta_{D,HC}^- \in [0,1)$. Due to the observable asymptotic behavior, it is reasonable to assume that $\delta_{D,HC}^- \approx 1$ for the largest applied dosage $D_0 = 10^3$. Hence, the estimates of $\alpha_D^- \delta_{D,HC}^-(10^3, 0)$ can be seen as estimates for α_D^- (i.e. the rightmost gray marginals in each subplot in Figure 26).

In general, we see relatively large estimates for α_D^-, i.e. a fast reaction to the DOX treatment. The corresponding MAPs as well as the fitted value of α_D^- appear to be smaller for HC0 than for the other environmental conditions:

$$\text{HC0:}\ \ 14.564\ (\text{fit}),\ 15.365\ (\text{MAP})\,, \qquad \text{H1:}\ \ 17.919\ (\text{fit}),\ 19.619\ (\text{MAP})\,,$$
$$\text{C1:}\ \ 17.507\ (\text{fit}),\ 18.553\ (\text{MAP})\,, \qquad \text{HC1:}\ \ 17.551\ (\text{fit}),\ 18.978\ (\text{MAP})\,,$$

which suggests a faster reaction to the DOX treatment if hypoxia and/or cirrhosis is involved. Comparing the marginal distributions does not imply statistical significance of this observation, see Figure E.10 in the appendix. However, recall that this does not necessarily indicate that the impact rate is actually the same in all environments, i.e. that there is no environmental effect.

The distributions for α_D^- show relatively high variances, which might play a role for the unclear statistical significance. A possible reason for the large variances is the sparse time resolution of the data. Recalling that viability was measured once at t_{end} (three days after a one- or two-day treatment), the only time resolution of the data is given by the variation in viability for different treatment durations. For large DOX dosages, the percentage viability is generally close to zero, i.e. the correspondingly small variation might be hardly distinguishable from measurement inaccuracy. Furthermore, if the cells' reaction to the DOX treatment is considerably fast (and for a sufficiently large induced death rate λ_{ind}), the cell population might go extinct at some time point before viability is measured. Then, the single measurement at t_{end} has no information about when in particular the cells have ceased.

<u>Supportive effect of SOR</u>.   Additionally to direct cytotoxicity, SOR can have a supportive effect on the DOX treatment. This is modeled by the quantity $d_S(S) \in [0, 1]$, which potentially shifts the DOX susceptibility threshold of the dose-response function $\delta_{D,HC}^-$ via

$$D_{\mathrm{thr}}(S, H, C) \overset{(3.13)}{=} \underbrace{D_{\mathrm{norm}} \cdot d_H(H) \cdot d_C(C)}_{D_{\mathrm{norm},HC}} \cdot \underbrace{\left(1 - \frac{a_{\max} \cdot S^{m_3}}{S_{\mathrm{supp}}^{m_3} + S^{m_3}}\right)}_{d_S(S)} .$$

Again, due to the limited number of experimentally investigated SOR dosages we could only estimate the values of $d_S(S)$ for $S \in \{0.5, 1.0\}$ instead of the separate parameters $a_{\max}$, m_3 and S_{supp} (recall Figure 12 in Subsection 5.3.2). The smaller the value of $d_S(S)$, the stronger the supportive influence of SOR. Therefore, we can take the term $1 - d_S(S) \in [0, 1]$ as a measure for the supportive effect.

In order to judge if the obtained estimates for $1 - d_S(S_0)$ actually result in considerable support of the DOX treatment, we set them into relation with the estimates of the unsupported stress response $\alpha_D^- \delta_{D,HC}^-(D_0, S_0 = 0)$. More precisely, we calculate $\alpha_D^- \delta_{D,HC}^-(D_0, S_0)$ for each particle and each combination of H_0, C_0, D_0 and $S_0 \in \{0.5, 1.0\}$ for comparison. This way we also consider the observed correlations between d_S and D_{norm} (see Figure E.4 in the appendix). Analogously to the fits of the unsupported stress response in Figure 26, we can now fit $\alpha_D^- \delta_{D,HC}^-(D, S_0)$ for $S_0 \in \{0.5, 1.0\}$ to the respective MAP estimates at $D = D_0$. For better comparability, we fix the parameters α_D^- and m_1 to the calculated values from the fit of $\alpha_D^- \delta_{D,HC}^-(D, 0)$. Eventually, the resulting fits as well as the MAPs do not show an obvious supportive effect of SOR on the DOX treatment, which is illustrated in Figure 27.
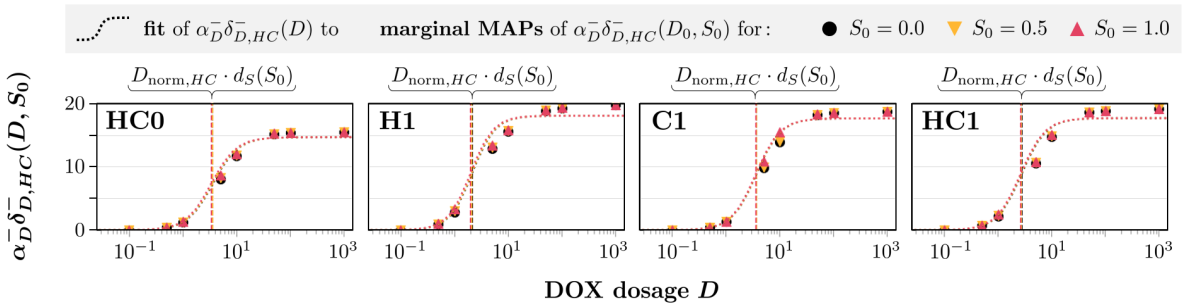

Figure 27: Comparison of the fitted DOX efficacy $\alpha_D^- \delta_{D,HC}^-(D, S_0)$ (sigmoidal lines) for Hep3B2 and the resulting shifted DOX susceptibility threshold $D_{\mathrm{norm},HC} \cdot d_S(S_0)$ (vertical line) for varying SOR dosages $S_0 \in \{0.0, 0.5, 1.0\}$ to support the DOX treatment.

Although the estimates for $1 - d_S(S_0)$ do not yield a noticeable treatment support, it might be interesting to take a closer look at its marginals. Figure 28 shows the corresponding marginal posteriors and the estimated marginal MAPs.
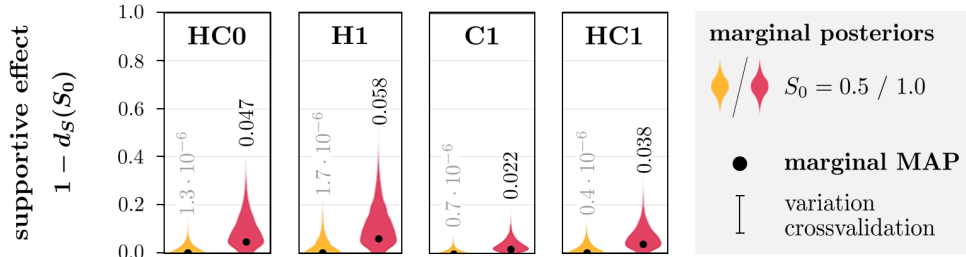

Figure 28: Comparison of marginal posteriors (violin plots) and corresponding MAPs of $1 - d_S(S_0)$ for Hep3B2. Note that for $S_0 = 0.5$ we directly calibrated $d_S(S_0)$, while for $S_0 = 1.0$ the estimates are obtained by calibration of $c_d = d_S(1.0) \, / \, d_S(0.5)$. Due to minor numerical variations, the cross-validated 95% confidence intervals (error bars) are not visible.

As expected, the MAPs for a standard SOR dosage ($S_0 = 0.5$) show no significant support on the DOX treatment under all environmental conditions. For a high dosage ($S_0 = 1.0$) we see non-zero MAPs indicating that hypoxia (HC0 $\rightsquigarrow$ H1 and C1 $\rightsquigarrow$ HC1) resp. high ECM stiffness (HC0 $\rightsquigarrow$ C1 and H1 $\rightsquigarrow$ HC1) might increase resp. decrease the supportive effect of SOR, if there is any. When comparing the marginal distributions in different environmental settings for given S_0, clear statistically significant differences are only visible for a high SOR dosage: HC0 vs. C1, H1 vs. HC1 (influence of stiffness) and C1 vs. HC1 (influence of hypoxia in stiff environment), see Figure E.11 in the appendix. However, it is hard to judge whether these are relevant observations in the context of the negligible support that we observed.

6.3.2   Chemoresistance for CYP-expressing cell line HepG2

Next, we analyze the calibration results using data (HC0, H1) of cell line HepG2, which exhibits a considerable CYP expression. Although this means that the drugs are potentially metabolized during treatment, it was not possible to reasonably estimate the parameters of the respective model $\mathcal{M}_{DS}^{\mathrm{CYP}}$ to this data (recall the explanations at the beginning of Section 6.3). Attempts to calibrate the reduced model $\mathcal{M}_{DS}^0$ instead (which neglects drug metabolization) cause algorithmic issues. Hence, we had to refine $\mathcal{M}_{DS}^0$, which will be denoted by $\mathcal{M}_{DS}^{0,\star}$. The reason for the adjustment, the construction of model $\mathcal{M}_{DS}^{0,\star}$ and the resulting adapted calibration setting will be explained respectively in the following three paragraphs. Subsequently, we investigate the calibration results. Corresponding complementary material can be found in Appendix E.III and will be referenced where relevant. Recall that the analysis of the calibration results follows Subsection 6.1.3 and numerical variations will be presented with the cross-validated 95% confidence interval and visualized by error bars.

<u>Algorithmic issues</u>.   We performed calibrations of the reduced model $\mathcal{M}_{DS}^0$ with the same prior assumptions as for the calibration of the Hep3B2 data (see Table D.2a). However, this repeatedly lead to numerical difficulties with degenerating marginal variances for both HC0 and H1 when the algorithm reaches a specific SMC step, i.e. when certain measurements are added to the calibration data set. A closer investigation of the respective data points suggests that the modeling approach for the supportive effect of SOR in model $\mathcal{M}_{DS}^0$ might be too restrictive to appropriately replicate the measured cell behavior for HepG2. The observed discrepancy is illustrated in Figure 29.
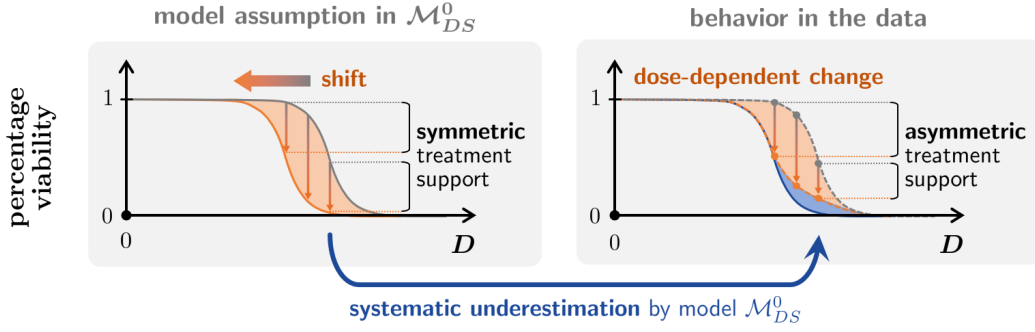
Figure 29: Schematic description of how model $\mathcal{M}_{DS}^0$ fails to appropriately describe the trend of the HepG2 data in terms of the supportive effect of SOR. The approach of shifting the DOX susceptibility threshold by $d_S(S)$ leads to a systematic underestimation of the measurements by the model solution for high DOX dosages.

In particular, by shifting the DOX susceptibility threshold $D_{\text{norm},HC}$ of the dose-response function $\delta_{D,HC}^-(D, S_0)$ with $d_S(S_0) \in (0, 1]$, the treatment support shows itself by an analogous shift of the percentage viability. This means, except for the horizontal shift, the shape of the unsupported (gray graph) and supported (orange graph) percentage viability function is the same, which results in a "symmetric" supportive effect (left side of Figure 29). By contrast, the measurements indicate an asymmetric supportive influence which can be weaker for larger DOX dosages (right side of Figure 29).

Although this discrepancy appears not to be very drastic, it can cause algorithmic difficulties by concerning mainly data points of low percentage viability. As discussed in the beginning of Subsection 6.3.1, the applied uncertainty modeling results in two observations. First, to some extent overestimation of the data is preferred over an exact fit and even more over an underestimation. Second, smaller measurements allow for less deviation between data and model solution, since we only consider a multiplicative noise without an additive modeling error (recall Subsection 4.1.1). In combination, this means that particles yielding a solution which considerably underestimates small measurements can be associated to very small weight. Hence, once the SMC algorithm includes such critical data points in the reweighting process, the systematic underestimation by model $\mathcal{M}_{DS}^0$ (see Figure 29) results in vanishing weights for the majority of the particle sample, i.e. degenerating variances.

<u>Model adaption</u>. As a consequence, we change the modeling of the supportive effect of SOR appropriately. In particular, we introduce a DOX dose-dependent damping factor by

$$d_S(S) = 1 - \frac{a_{\max} \cdot S^{m_3}}{S_{\text{supp}}^{m_3} + S^{m_3}}$$

$$\xrightarrow{\text{adapt}} \quad d_S^\star(S, D) = 1 - \underbrace{\frac{a_{\max} \cdot S^{m_3}}{S_{\text{supp}}^{m_3} + S^{m_3}}}_{\substack{\text{supportive effect} \\ 1 - d_S(S)}} \cdot \underbrace{\left(1 - \frac{D}{D_{\text{damp}} + D}\right)}_{\substack{\text{damping factor} \\ \in (0,1]}}, \quad \text{with } D_{\text{damp}} \in (0, D_{\text{norm},HC}] \,,$$

and propose the adjusted model

$$(\mathcal{M}_{DS}^{0,\star}) \quad \begin{cases} \dot{V} = \left(\beta - \lambda - \eta \cdot \left(\beta + \lambda_{\text{ind}}\right)\right) \cdot V \,, \\[2mm] \dot{\eta} = \left(\dfrac{\alpha_D^- \cdot D_0^{m_1}}{\left(D_{\text{norm},HC} \cdot d_S^\star(S_0, D_0)\right)^{m_1} + D_0^{m_1}} + \dfrac{\alpha_S^- \cdot S_0^{m_2}}{S_{\text{thr},HC}^{m_2} + S_0^{m_2}}\right) \cdot (1 - \eta) \cdot \mathbb{1}_T(t) \,, \\[2mm] \text{with } V(0) = V_0 \,, \; \eta(0) = \eta_{0,HC} \,. \end{cases}$$

Figure 30 visually compares the supportive effect as described by both models $\mathcal{M}_{DS}^0$ and $\mathcal{M}_{DS}^{0,\star}$ as well as shows the role of the term $1 - d_S(S_0)$ and the damping threshold reparameterized by

$$D_{\mathrm{damp}} = D_{\mathrm{norm},HC} \cdot c_{\mathrm{damp}} , \qquad \text{with } c_{\mathrm{damp}} \in (0,1] . \tag{6.5}$$
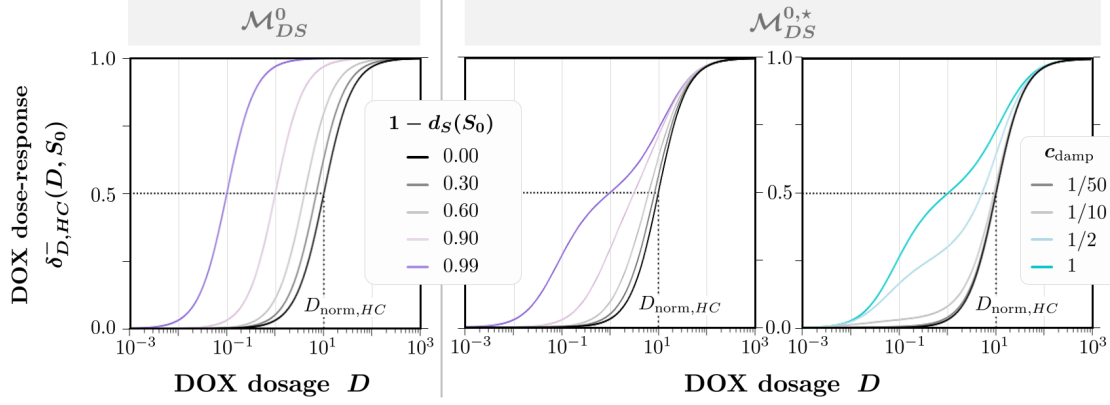
Figure 30: Comparison of the different approaches of models $\mathcal{M}_{DS}^0$ (left) and $\mathcal{M}_{DS}^{0,\star}$ (middle and right) to describe the supported DOX dose-response. Each plot illustrates the influence of the terms $1 - d_S(S_0)$ resp. c_{damp} on the dose-response curve (for all plots: $D_{\mathrm{norm},HC} = 1$, middle plot: $c_{\mathrm{damp}} = 1$, right plot: $1 - d_S(S_0) = 0.99$).

For both models, the term $1 - d_S(S_0)$ is a measure for the strength of the supportive effect. Furthermore, we see that, the smaller D_{damp} in comparison to $D_{\mathrm{norm},HC}$ (i.e. the smaller c_{damp}), the stronger the damping. Note that the constraint $D_{\mathrm{damp}} \leq D_{\mathrm{norm},HC}$, which basically assumes a base degree of damping, is not necessary from a mathematical perspective. For larger values of D_{damp}, the shape of $d_S^\star$ progressively approaches the one of the undamped one d_S. However, pre-calibrations gave no indication that $D_{\mathrm{damp}} \leq D_{\mathrm{norm},HC}$ too restrictive. Hence, we use the reparametrization (6.5) to construct a reasonably bounded prior (see subsequent paragraph).

<u>Adapted calibration settings</u>. We want to calibrate the data of cell line HepG2 with model $\mathcal{M}_{DS}^{0,\star}$ instead. To do so, we again use the same prior assumptions as for calibrating the Hep3B2 data (from Table D.2a) except for the following adaptions:

$$\log_{10}(m_1) = \widehat{m}_1 \sim \mathcal{U}(0,1.7) \quad \xrightarrow{\text{instead}} \quad m_1 \sim \mathcal{U}(0,6) ,$$

$$d_S(0.5) \sim \mathcal{U}(0,1) \quad \xrightarrow{\text{instead}} \quad 1 - d_S(1.0) \sim \mathcal{U}(0,1) ,$$

$$\frac{d_S(1.0)}{d_S(0.5)} = c_d \sim \mathcal{U}(0,1) \quad \xrightarrow{\text{instead}} \quad \frac{1 - d_S(0.5)}{1 - d_S(1.0)} = \tilde{c}_d \sim \mathcal{U}(0,1) .$$

The adjusted prior for the Hill coefficient m_1 is motivated by the estimated marginal posteriors of this parameter from the calibration of cell line Hep3B2 (see Figure E.3 in the appendix). The remaining adaptions result from the fact that the damping factor is applied to the supportive effect term $1 - d_S(S)$ and that $1 - d_S(0.5) \leq 1 - d_S(1.0)$. With the damping factor comes along another parameter: the damping threshold $D_{\mathrm{damp}} \leq D_{\mathrm{norm},HC}$. By using the reparametrization (6.5) in log scale, i.e.

$$(0,1] \ni c_{\mathrm{damp}} = 10^{\widehat{c}_{\mathrm{damp}}} \quad \Rightarrow \quad \log_{10}(c_{\mathrm{damp}}) = \widehat{c}_{\mathrm{damp}} \leq 0 ,$$

we can assume the prior distribution

$$\widehat{c}_{\mathrm{damp}} \sim \mathcal{U}(-3,0) .$$

The support of this uniform distribution translates to $c_{\mathrm{damp}} \in (0.001, 1]$ and is motivated by the observation that even smaller values for c_{damp} would only marginally change the damping effect (see right subplot of Figure 30, where $c_{\mathrm{damp}} = 1/50$ already almost completely damped the supportive effect of SOR). In the remaining parts of this section we will present the results obtained by calibrating model $\mathcal{M}_{DS}^{0,\star}$ to the HepG2 data with these prior assumptions.

Treatment response. Figure 31 shows the data (markers) with the corresponding model solution (line plots) given the estimated marginal MAPs of the parameters. The small plots in the upper right corners illustrate the trend of the data for a easier visual comparison. Following the approach described in Subsection 5.2.2 and Figure 10, we omitted the measurements for $D_0 \in \{10^{-3}, 10^{-2}\}$ for the calibration data set of this cell line.
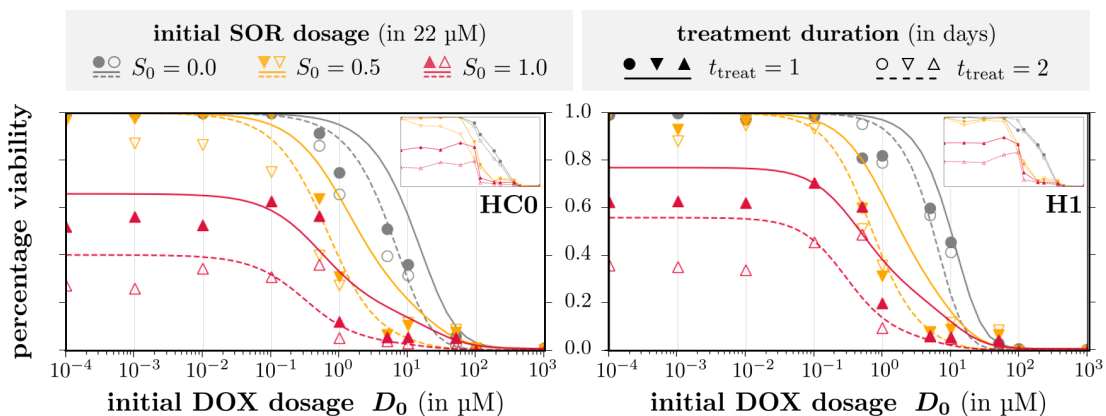
Figure 31: Comparison of the measured percentage viability for cell line HepG2 with the corresponding estimated model solutions using model $\mathcal{M}_{DS}^{0,\star}$ for different environmental settings.

In general, we get reasonable fits of the model solutions to the measurements. We see tendencies to overestimate the data as well as observe more asymmetry in the viability-dose relationship of the measurements in contrast to the solution. The latter is only clearly visible for the gray markers/lines, i.e. without the treatment support of SOR. Overall, these are similar observations as for cell line Hep3B2 (Subsection 6.3.1). Likewise, this suggests the potential to improve the model by reconsidering the symmetry assumption for the DOX dose-response function δ_D^- and the uncertainty modeling (more details will be provided in Section 7.2).

The following paragraphs respectively present the estimated model parameters and discuss them in the underlying biological context. An overview over all marginal distributions, MAPs and corresponding numerical deviations from cross-validation can be found in Figure E.12 in the appendix.

Drug-independent dynamics. The marginal MAP estimate of the initial ESL $\eta_{0,HC}$ is

$$(\text{by definition} - \text{HC0: } 0.000), \qquad \text{H1: } 1.2 \cdot 10^{-6},$$

i.e. we see no significant stress induction by sole hypoxia. This result is comparable to the observation from cell line Hep3B2. As for the cell dynamics, Figure 32 shows the estimates of $\beta + \lambda_{\mathrm{ind}}$ for each SMC run in comparison with the respective estimation resulting from the particle approximation collecting all runs.
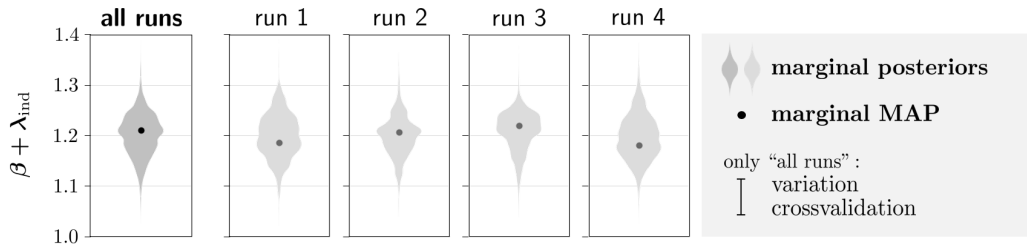
Figure 32: Estimations of $\beta + \lambda_{\text{ind}}$ for HepG2 in the setting HC0: Marginal posteriors as violin plots and corresponding MAPs, which were used deterministically in each run for calibrating the setting H1. Due to minor numerical variations, the cross-validated 95% confidence interval (error bar) is not visible.

Again, the estimation of $\beta + \lambda_{\text{ind}}$ is consistent and all calibrations of H1 assumed a sufficiently similar value. In particular, the estimated MAP using all SMC runs gives $\beta + \lambda_{\text{ind}} \approx 1.210$. Hence, an analogous approach as for cell line Hep3B2 (Subsection 6.3.1) yields

$$\beta\,, \lambda_{\text{ind}}\,, \lambda < 1.210\,.$$

Since we do not have a sufficiently non-zero estimate of $\eta_{0,HC}$ for HepG2, we cannot use its mathematical upper bound of $(\beta - \lambda)/(\beta + \lambda_{\text{ind}})$, recall (3.11), to derive a numeric lower bound for $\beta - \lambda$.

Cytotoxic efficacy of SOR. The marginal estimates of the stress response $\alpha_S^- \delta_{S,HC}^-(S_0)$ to SOR for a standard resp. high dosage $S_0 \in \{0.5, 1.0\}$ are shown in Figure 33.
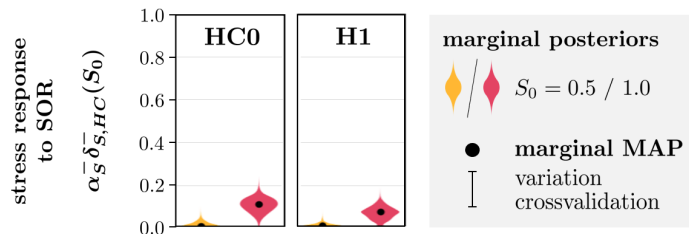
Figure 33: Comparison of marginal posteriors (violin plots) and corresponding MAP estimates of $\alpha_S^- \delta_{S,HC}^-(S_0)$ for HepG2. Note that for $S_0 = 1.0$ it was directly calibrated, while for $S_0 = 0.5$ the estimates are obtained by calibration of $c_\delta = \alpha_S^- \delta_{S,HC}^-(0.5)\,/\,\alpha_S^- \delta_{S,HC}^-(1.0)$. Due to minor numerical variations, the cross-validated 95% confidence intervals (error bars) are not visible.

Similarly to cell line Hep3B2 (Subsection 6.3.1), we can follow the parameter bounds

$$S_{\text{thr}}(H, 0) > 0.5 \text{ for } H \in \{0, 1\} \qquad \text{and} \qquad \alpha_S^- \geq \alpha_S^- \delta_{S,HC}^-(S_0 = 1.0)$$

for given H and $C = 0$ and up to variations in the magnitude of the corresponding marginal variance. While observing almost no stress response for a standard SOR dosage, we see considerably non-zero MAP estimates for a high SOR dosage:

$$\begin{aligned}\alpha_S^- \delta_{S,HC}^-(S_0 = 0.5): &\quad 1.6 \cdot 10^{-6} \text{ (HC0)}, \quad 0.9 \cdot 10^{-6} \text{ (H1)}, \\ \alpha_S^- \delta_{S,HC}^-(S_0 = 1.0): &\quad 0.103 \text{ (HC0)}, \quad 0.063 \text{ (H1)}.\end{aligned}$$

The cytotoxic efficacy of a high SOR dosage appears to be weaker for cell line HepG2 compared to Hep3B2 (recall HC0/H1: 0.489, 0.566). Furthermore, a statistical comparison of the corresponding marginal distributions (Figure E.14 in the appendix) shows a significant (∗∗∗) reduction

of the stress response to SOR for $S_0 = 1.0$ due to hypoxia. For $S_0 = 0.5$ the estimates indicate the same tendency, but with unclear significance.

Interestingly, a decreasing effect of hypoxia on the stress response is just the opposite influence as observed for cell line Hep3B2. However, one should keep in mind that there is a difference between the stress response $\alpha_S^- \delta_{S,HC}^-(S)$ and the cells' susceptibility threshold $S_{\mathrm{thr},HC}$. While the first describes the treatment response for a particular dosage $S = S_0$, the latter gives a more general measure independent from S. Therefore, the apparently contrary influence of hypoxia observed for $\alpha_S^- \delta_{S,HC}^-(S_0)$ does not necessarily imply that the cells react oppositely to the SOR treatment in general.

Cytotoxic efficacy of DOX. We proceed with analyzing the estimated stress response to DOX:

$$\alpha_D^- \delta_{D,HC}^-(D_0, S_0) = \frac{\alpha_D^- \cdot D_0^{m_1}}{\left(D_{\mathrm{norm},HC} \cdot \left(1 - \left(1 - d_S(S_0)\right) \cdot \left(1 - \frac{D}{D_{\mathrm{damp}}+D}\right)\right)\right)^{m_1} + D_0^{m_1}} .$$

Like for Hep3B2 (Subsection 6.3.1), we calculate $\alpha_D^- \delta_{D,HC}^-(D_0, S_0)$ for each particle and each combination of D_0 and S_0 to consider the correlations (see Figure E.17a in the appendix) of the involved parameters. Figure 34 shows the weighted least square fits (dotted curves) of $\alpha_D^- \delta_{D,HC}^-(D, S_0)$ to the MAPs (markers) of the resulting distributions. Note that the marginals of $D_0 > 10^3$ are extrapolated to reach the horizontal asymptote for reasonable fitting.
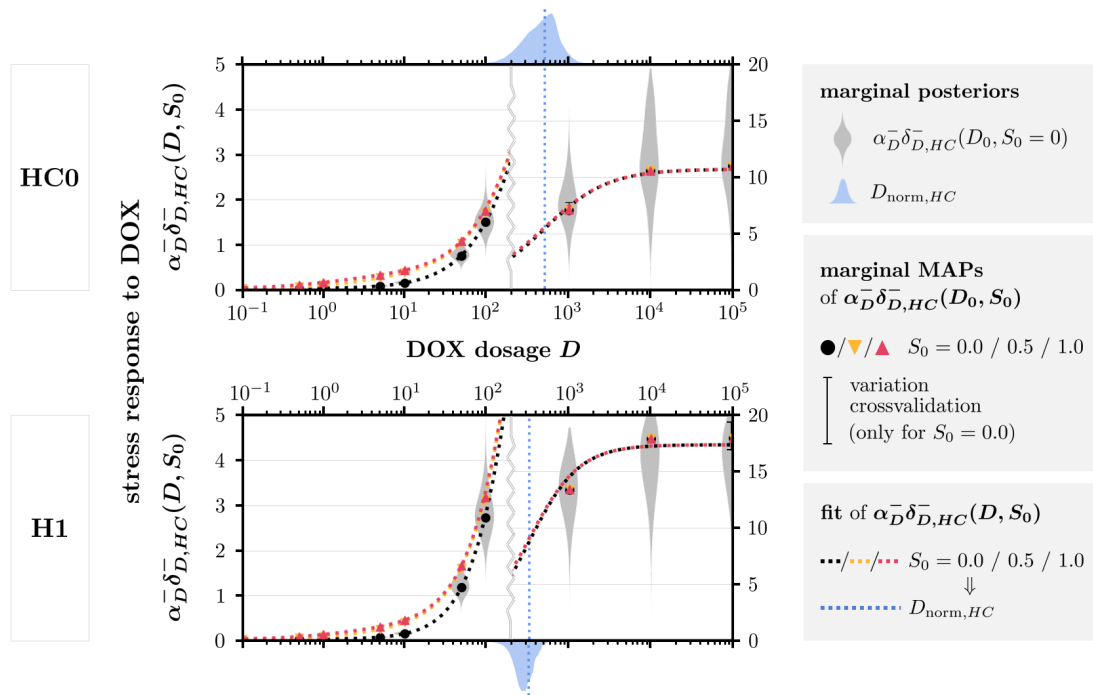

Figure 34: Comparison of distributions (violin plots) and corresponding MAP estimates (black markers) of the unsupported DOX efficacy $\alpha_D^- \delta_{D,HC}^-(D_0, 0)$ for HepG2 for particular dosages D_0. Note the respectively different scaling of the vertical axis for the left and right part of the plot (separated by the vertical light gray wavy line). The non-black markers are the MAPs for combination therapy (corresponding violin plots are not shown; they do not bring more clarity as they have a similar shape to the gray ones). The dotted curves are the least square fits to the respective MAPs and the fitted values of $D_{\mathrm{norm},HC}$ are illustrated as light blue dotted lines in comparison with the marginalized posterior distribution of $D_{\mathrm{norm},HC}$ (light blue shaded truncated KDE plots on the top/bottom). Due to minor numerical variations, some cross-validated 95% confidence intervals (error bars) are barely visible.

We achieve good and reasonable fits[22] with a susceptibility threshold $D_{\mathrm{norm},HC}$ (blue dotted line) close to the global modes of the corresponding marginal truncated KDEs (blue distributions). Table 8 summarizes the fitted values of the parameters involved in the stress response in comparison with their marginal MAPs and shows a high consistency.

Table 8: Comparison of the parameter estimates regarding the stress response to DOX for HepG2 in normal (HC0) and sole hypoxic (H1) environment. The 95% confidence intervals of the fitted values can be found in Table E.6 in the appendix.

(a) Parameters of the unsupported ($S_0 = 0$) stress response. The statistical significance of differences between HC0 an H1 is checked with Figure E.15 in the appendix.

		HC0	⤳	H1	significant?
α_D^-	**fitted**	10.694	↗	17.413	***
	MAP	11.043		17.997	***
$D_{\mathrm{norm},HC}$	**fitted**	501.122	↘	318.290	***
	MAP	574.812		272.357	***
m_1	**fitted**	1.128	↗	1.433	***
	MAP	1.074		1.405	***

(b) Parameters of the supportive influence of SOR on the stress response for $S_0 \in \{0.5, 1.0\}$, where $1 - d_S(S_0) \in [0, 1)$ shows the undamped supportive effect and $1/c_{\mathrm{damp}}$ the strength of damping. For $1/c_{\mathrm{damp}}$ we have two different fits for $S_0 = 0.5$ (top value) and $S_0 = 1.0$ (bottom value). The statistical significance of differences between HC0 an H1 is checked with Figure E.14 in the appendix.

		HC0	⤳	H1	significant?
$1 - d_S(0.5)$	**fitted**	0.879	≈	0.873	potentially insignificant
	MAP	0.903		0.910	potentially insignificant
$1 - d_S(1.0)$	**fitted**	0.948	≈	0.942	potentially insignificant
	MAP	0.960		0.963	potentially insignificant
$\dfrac{1}{c_{\mathrm{damp}}}$	**fitted**	22.542 22.467	↘	18.864 19.128	potentially significant *
	MAP	20.532		16.742	potentially significant

When comparing the parameter values for HC0 and H1, Table 8a shows an increase of α_D^- and a decrease of $D_{\mathrm{norm},HC}$, which both indicate an enhanced cytotoxic efficacy of DOX due to hypoxia. This is similar to the observations for cell line Hep3B2 (Subsection 6.3.1). We also see a slight increase of m_1, i.e. a steeper dose-response relationship.

The estimated values of $1 - d_S(S_0)$ in Table 8b as well as the left side of Figure 34 exhibit a considerable supportive effect for both a standard and high SOR dosage (in contrast to cell line Hep3B2). The effect is respectively similar under normal and hypoxic conditions. Furthermore, we see $1/c_{\mathrm{damp}} \gg 1$ for both HC0 and H1, which yields a considerable DOX dose-dependency of the supportive effect. This is also visible on the right side of Figure 34, where the supportive effect vanishes for large DOX dosages.

---

[22]HC0/H1: $R^2 \approx 0.999, 0.996 \ \ \forall S_0$

Drug metabolization and CYP expression.   Recall that by calibrating model $\mathcal{M}_{DS}^{0,\star}$ instead of $\mathcal{M}_{DS}^{\mathrm{CYP}}$, we omitted the influence of the drug metabolizing enzyme CYP3A4 (CYP) and assumed constant drug concentrations $D(t) = D_0$ and $S(t) = S_0$ during treatment. However, according to [22], the cell line HepG2 actually exhibits a considerable CYP expression. In model $\mathcal{M}_{DS}^{\mathrm{CYP}}$ the resulting drug metabolization would have been incorporated via exponential decay, i.e.

$$D(t) = D_0 \cdot e^{-\gamma_D t} \qquad \text{and} \qquad S(t) = S_0 \cdot e^{-\gamma_S t}$$

with the drug-specific metabolization rates $\gamma_D, \gamma_S \geq 0$. Without loss of generality, let $\phi \in \{D, S\}$ be the dosage of DOX or SOR and γ_ϕ its respective metabolization rate. Then, if we consider a Hill function in ϕ with threshold $\phi_{\mathrm{thr}} > 0$ and Hill coefficient $m > 0$, drug metabolization would show as

$$\frac{\phi(t)^m}{\phi_{\mathrm{thr}}^m + \phi(t)^m} = \frac{\phi_0^m \cdot e^{-m\gamma_\phi t}}{\phi_{\mathrm{thr}}^m + \phi_0^m \cdot e^{-m\gamma_\phi t}} = \frac{\phi_0^m}{(e^{\gamma_\phi t} \cdot \phi_{\mathrm{thr}})^m + \phi_0^m} \,.$$

This corresponds to a Hill function in ϕ assuming a constant dosage $\phi(t) = \phi_0$, but with an adapted threshold

$$\phi_{\mathrm{thr}}^{\mathrm{CYP}}(t) = e^{\gamma_\phi t} \cdot \phi_{\mathrm{thr}}$$

which increases exponentially over time, where ϕ_{thr} is the threshold at the beginning of the treatment ($t = 0$).

<u>Constant approximation of drug metabolization</u>.   Obviously, such a time-dependent dynamic is not considered by model $\mathcal{M}_{DS}^{0,\star}$. Instead, it basically approximates $\phi_{\mathrm{thr}}^{\mathrm{CYP}}$ by a constant. As t will progress from 0 to $t_{\mathrm{treat}} \in \{1, 2\}$ during the treatment phase and $\mathcal{M}_{DS}^{0,\star}$ does not differentiate $\phi_{\mathrm{thr}}^{\mathrm{CYP}}$ for varying treatment durations, it is reasonable to assume that the calibrations approximate t with a positive constant smaller than two. Hence, we propose

$$\phi_{\mathrm{thr}}^{\mathrm{CYP}} \approx e^{\gamma_\phi} \cdot \phi_{\mathrm{thr}} = \omega_\phi \cdot \phi_{\mathrm{thr}} \qquad \Rightarrow \qquad \gamma_\phi \approx \ln(\omega_\phi) \ \ \text{with } \omega_\phi \geq 1 \,. \qquad (6.6)$$

As the variables D and S do not occur outside from Hill functions in $\mathcal{M}_{DS}^{0,\star}$, the simplified consideration of the drug metabolization with this model can be summarized by

$$D_{\mathrm{norm},HC}^{\mathrm{CYP}} \approx \omega_D \cdot D_{\mathrm{norm},HC} \,, \qquad S_{\mathrm{thr},HC}^{\mathrm{CYP}} \approx \omega_S \cdot S_{\mathrm{thr},HC} \,,$$
$$D_{\mathrm{damp}}^{\mathrm{CYP}} \approx \omega_D \cdot D_{\mathrm{damp}} \,, \qquad S_{\mathrm{supp}}^{\mathrm{CYP}} \approx \omega_S \cdot S_{\mathrm{supp}} \,,$$

with $\omega_D, \omega_S \geq 1$ quantifying the drug metabolization, where a value of one represents no metabolic activity. We expect ω_D and ω_S to be positively correlated to the CYP expression, i.e. more CYP yields a stronger effect of drug metabolization. In particular, let both

$$\omega_D = \omega_D(\varrho_{HC}) \qquad \text{and} \qquad \omega_S = \omega_S(\varrho_{HC})$$

be monotonically increasing functions $[0, \infty) \to [1, \infty)$ in the CYP concentration $\varrho_{HC} \geq 0$ which we suppose to be constant but potentially dependent on H and C. We will use the short notations $\omega_{D,HC} = \omega_D(\varrho_{HC})$ and $\omega_{S,HC} = \omega_S(\varrho_{HC})$.

<u>Estimated drug metabolization</u>.   For the SOR-related thresholds, we cannot reconstruct $\omega_{S,HC}$ as we do not have estimates for $S_{\mathrm{thr},HC}$ and S_{supp}. Hence, it is not possible to investigate the role of SOR metabolization with the calibration results. For the DOX-related thresholds, it is reasonable to assume that we actually estimated $D_{\mathrm{norm},HC}^{\mathrm{CYP}}$ and $D_{\mathrm{damp}}^{\mathrm{CYP}}$ instead of $D_{\mathrm{norm},HC}$ resp. D_{damp}. Therefore, the estimates of these parameters from Table 8 could be used to reconstruct $\omega_{D,HC}$. However, we have only sufficient information to do so if we take two modeling assumptions as a starting point. Both suppose that cell lines Hep3B2 and HepG2 respond comparably to the DOX

treatment. According to [106], it is reasonable to assume some degree of similarity between those two cell lines although we have to keep in mind that there are also several differences. Hence, the following investigations only make sense under the premise that these differences are not relevant in our modeling context, which we cannot validate yet with the available data.

First assumption: The environmental factors have the same effect on the stress response to DOX for cell lines Hep3B2 and HepG2. In sole hypoxic conditions (H1: $H = 1, C = 0$) this means that we let the value of $d_H(H = 1)$ from the relation $D_{\mathrm{norm},HC} = D_{\mathrm{norm}} \cdot d_H(H = 1) \cdot d_C(C = 0)$ be the same for both cell lines. Second assumption: Except for the influences of drug metabolization and the environment (in particular hypoxia), Hep3B2 and HepG2 have the same DOX susceptibility threshold D_{norm}. Then, combining the calibration results from both cell lines yields

$$
\begin{aligned}
\text{HC0:} \quad D_{\mathrm{norm},HC}^{\mathrm{CYP}} &= \underbrace{\omega_{D,HC}}_{\substack{\text{unknown} \\ \text{(HepG2)}}} \cdot \underbrace{\overbrace{D_{\mathrm{norm}} \cdot d_H(H = 0)}^{D_{\mathrm{norm},HC}} \cdot \overbrace{d_C(C = 0)}^{= 1}}_{} \,, \\[2pt]
\text{H1:} \quad D_{\mathrm{norm},HC}^{\mathrm{CYP}} &= \omega_{D,HC} \cdot \underbrace{D_{\mathrm{norm}} \cdot d_H(H = 1)}_{\substack{D_{\mathrm{norm},HC} \\ \text{estimated} \\ \text{with Hep3B2}}} \cdot \underbrace{d_C(C = 0)}_{\substack{= 1 \\ \text{by definition}}} \,.
\end{aligned}
\tag{6.7}
$$

where the first factor $\underbrace{\ }_{\substack{\text{estimated} \\ \text{with HepG2}}}$.

Solving each of the above equations for $\ln(\omega_{D,HC})$ eventually provides environment-specific estimates for the involved DOX metabolization $\gamma_{D,HC}$ based on the approximating assumption (6.6). Using the fitted values of $D_{\mathrm{norm},HC}^{\mathrm{CYP}}$ (Table 8a) and of $D_{\mathrm{norm},HC}$ (Subsection 6.3.1), we get[23]

$$
\begin{aligned}
\text{HC0:} \quad & \gamma_{D,HC} = \gamma_D(\varrho_{HC}) \approx 4.904 \pm 0.930 \,, \\
\text{H1:} \quad & \gamma_{D,HC} = \gamma_D(\varrho_{HC}) \approx 5.022 \pm 0.705 \,.
\end{aligned}
$$

On the one hand, we see a considerable DOX metabolization ($\gamma_{D,HC} \gg 0$) for HepG2. On the other hand, the metabolic activity appears to be stronger under sole hypoxic conditions (potentially statistically insignificant, see Figure E.16 in the appendix). It might be interesting to note that calibration attempts with the complete model $\mathcal{M}_{DS}^{\mathrm{CYP}}$ resulted in fairly concentrated marginal distributions for $\gamma_{D,HC}$ (in contrast to other parameters) and the corresponding estimates are actually in a magnitude of $\gamma_{D,HC} \approx 5$ (see Figure E.13 in the appendix). Hence, there could indeed be potential in calibrating $\mathcal{M}_{DS}^{\mathrm{CYP}}$ to gain deeper understanding of the drug metabolization.

We could now proceed with using the estimates of $\omega_{D,HC}$ to reconstruct the threshold D_{damp} from $D_{\mathrm{damp}}^{\mathrm{CYP}} = \omega_{D,HC} \cdot D_{\mathrm{damp}}$. However, there are indications that in this context the cell lines Hep3B2 and HepG2 are not sufficiently comparable as we observe a clear supportive effect for HepG2 in contrast to Hep3B2. Intuitively, we would expect the opposite due to potentially lower SOR concentrations in the presence of CYP, which suggests that the support of SOR might occur differently for the respective cell lines.

<u>Measured CYP expression</u>.   Since $\gamma_{D,HC} = \gamma_D(\varrho_{HC})$ is defined as a function of the CYP expression ϱ_{HC}, we can compare those quantities using the corresponding CYP data[24] from [22]. Figure 35 visualizes the relation between the derived estimates of $\gamma_{D,HC}$ (for Hep3B2 we assume $\gamma_{D,HC} = 0$, i.e. no DOX metabolization) with the measured CYP expression.

---

[23]In particular, we draw 10^7 samples of $D_{\mathrm{norm},HC}^{\mathrm{CYP}}$ and $D_{\mathrm{norm},HC}$ respectively according to a normal distribution (truncated to $\mathbb{R}_+$) which is centered at their fit and using the corresponding standard deviation. Then, the presented 95% confidence interval of $\gamma_{D,HC}$ is obtained by calculating its value for each sample.

[24]The data is given in the form of luminescence measurements which are (similarly to the intensity measurements for cell viability) assumed to be directly proportional to the CYP expression [107]. Since the proportionality constant has no qualitative influence on the results, we treat the measurements as direct quantities for ϱ_{HC}.
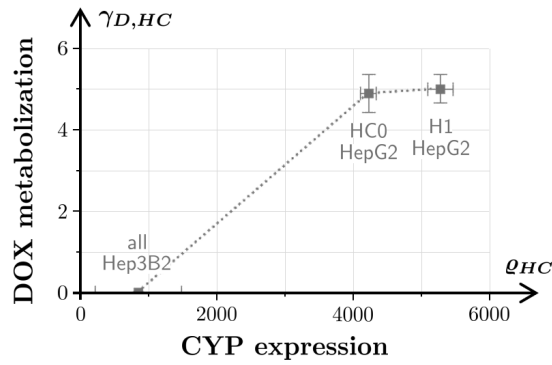
Figure 35: Relation between the estimated DOX metabolization $\gamma_{D,HC}$ and corresponding measured CYP expression ϱ_{HC} (dotted line: trendline). The error bars show the 95% confidence interval of the CYP data (horizontal) and of the estimated values of $\gamma_{D,HC}$ (vertical).

The observed relation suggests a positive and potentially non-linear correlation between $\gamma_{D,HC}$ and ϱ_{HC}, which fits to γ_D actually being a monotonically increasing function in ϱ_{HC}. This implies that the two assumptions for approach (6.7) can make sense from an experimental perspective. Obviously, the validity is quite limited by being based on only three observations. With this small number of points, it is not expedient to fit and compare different possibilities for the monotonic function $\gamma_D(\varrho_{HC})$. However, we can conjecture the rough shape of the function (dotted trendline). Due to the monotonicity and the considerable distance of the left-most marker (Hep3B2) from the origin, it appears that γ_D stays close to zero for sufficiently small values, i.e. approx. $\varrho_{HC} \in [0, 1000]$. Furthermore, the markers for HepG2 indicate the function's slope to be relatively flat in the range of $\varrho_{HC} \in [4000, 5000]$, especially in comparison to the increase between the Hep3B2 and HepG2 markers. Combining these observations to a smooth, monotonically increasing function suggests e.g. a Hill-type function

$$\gamma_D(\varrho_{HC}) = \frac{\tilde{\gamma}_D \cdot \varrho_{HC}^m}{\varrho_{\text{thr}}^m + \varrho_{HC}^m},$$

with a threshold $\varrho_{\text{thr}} \in [1000, 4000]$, a horizontal asymptote $\tilde{\gamma}_D \gtrsim 5$ and a Hill coefficient $m \geq 2$ for sigmoidal shape (supposing the non-zero CYP data for Hep3B2 is not an effect of sole measurement inaccuracy). On the one hand, this would mean that there needs to be a sufficient amount of CYP present to achieve considerable DOX metabolization. On the other hand, the metabolic activity appears to not increase unlimitedly the higher the CYP expression.

In general, this shape of the function $\gamma_D(\varrho_{HC})$ seems reasonable considering the experimentally observed treatment effect for Hep3B2 and HepG2 (see Figure 4 in [22]). In particular, the experiments show a considerable shift of the DOX effect if we compare Hep3B2 and HepG2, which fits to γ_D being significantly larger for HepG2 (HC0, H1) compared to Hep3B2. However, the treatment effect for HepG2 in different environments (i.e. comparing HC0/H1/C1/HC1 with each other) appears to be less drastic, although the cells exhibit nearly double the amount under cirrhotic conditions ($\varrho_{HC} \approx 9000$ resp. 10600 for C1/HC1). This supports the indication of an upper bound for $\gamma_D(\varrho_{HC})$ and that it is almost reached by the CYP expression for HC0 and H1.

6.3.3 Summary and comparison of the treatment response for Hep3B2 and HepG2

We conclude with a brief overview over the obtained calibration results for cell lines Hep3B2 (Subsection 6.3.1) and HepG2 (Subsection 6.3.2) regarding the treatment response. In general, both cell lines show a qualitatively similar behavior, except for the supportive influence of SOR. The

latter appears to be cell line-specific, as we only observe a considerable effect for HepG2. Table 9 summarizes the observed influences of hypoxia (for both cell lines) and high ECM stiffness (for Hep3B2).

Table 9: Influence of introducing hypoxia (H), tissue stiffening (C) or a combination of both (HC) on the treatment response of the investigated cell lines. Recall that for HepG2 we could not apply model calibrations on any data considering high stiffness.

		Hep3B2	HepG2
DOX impact rate α_D^-	**H**	faster reaction	faster reaction
	C	faster reaction	$\begin{bmatrix} \text{N/A} \end{bmatrix}$
	HC	faster reaction, synergism	
DOX susceptibility $D_{\mathrm{norm},HC}$	**H**	higher susceptibility	higher susceptibility
	C	lower susceptibility	$\begin{bmatrix} \text{N/A} \end{bmatrix}$
	HC	hypoxia prevails, synergism	
SOR support $d_S(S_0)$ resp. $d_S^\star(S_0, D)$	**H**	$\begin{bmatrix} \text{unclear due to} \\ \text{inconsiderable} \\ \text{support} \end{bmatrix}$	similar support
	C		$\begin{bmatrix} \text{N/A} \end{bmatrix}$
	HC		
SOR stress response $\alpha_S^- \delta_{S,HC}^-(S_0)$	**H**	increased response	decreased response
	C	decreased response	$\begin{bmatrix} \text{N/A} \end{bmatrix}$
	HC	hypoxia prevails for $S_0 = 0.5$, synergism	

Overall, the calibration results consistently show an enhancing effect of hypoxia on the treatment efficacy of both drugs, whereas tissue stiffening increases the chemoresistance (for Hep3B2). The only apparent discrepancy appears for the stress response to SOR under hypoxia. As mentioned in Subsection 6.3.2, this does not necessarily imply a generally opposite reaction to the SOR treatment. For comparison, we check the unsupported stress response $\alpha_D^- \delta_{D,HC}^-(D_0, 0)$ to DOX in Table 10.

Table 10: Comparison (HC0 $\rightsquigarrow$ H1) of the MAP estimates of $\alpha_D^- \delta_{D,HC}^-(D_0, 0)$ given particular D_0.

D_0	Hep3B2	HepG2
0.5	0.368 $\nearrow$ 0.889	0.005 $\searrow$ 0.001
1.0	1.223 $\nearrow$ 2.804	0.010 $\searrow$ 0.004
5.0	7.971 $\nearrow$ 12.761	0.060 $\searrow$ 0.047
10.0	11.607 $\nearrow$ 15.463	0.130 $\searrow$ 0.127

In fact, analogously to the stress response to SOR, we also observe an increasing resp. decreasing effect of hypoxia on the response to DOX for Hep3B2 resp. HepG2. Nevertheless, the impact rate α_D^- and susceptibility threshold $D_{\mathrm{norm},HC}$ in Table 9 both indicate consistency regarding the DOX treatment response for both cell lines. Hence, the alleged discrepancy does not imply a different influence of hypoxia on the SOR dose-response.

7 Conclusions and perspectives

In this thesis, we have introduced and applied the modeling approach of an *environmental stress level* (ESL) to describe and biologically investigate the collective influence of different environmental factors on tumor viability. In summary, we see that the ESL can feasibly model various environmental influences on the cells. It provides a modular framework which can be easily extended to a large number of environmental factors and allows a biological interpretation of the parameters. With this approach, we are able to reproduce and investigate the cell behavior observed in the experiments [21] (response to nutrient deprivation) and [22] (effect of hypoxia and cirrhosis, i.e. high ECM stiffness, on chemoresistance) by parameter estimation with SMC methods. This last chapter concludes the main results of the model calibrations (Section 7.1) and discusses the observed challenges while presenting possibilities for improvement (Section 7.2). Finally, Section 7.3 provides an outlook over the further potential of the ESL approach from the perspective of mathematical modeling as well as in view of algorithmic improvements of the model calibration. In general, future work with more refined mathematical approaches and additional data could allow to further enhance the biological understanding, while this thesis already provides a good basis.

7.1 Main results

In general, we observe reasonable parameter estimates for the calibration of each model to its respective data. The estimated model solutions show good agreement with the measurements and allow for a closer investigation of the underlying biological processes with the ESL approach, see subsequent paragraphs.

ESL as an efficient modeling framework. With the first application, we calibrated two models – one based on the ESL approach ($\mathcal{M}_N^\eta$) and one without ($\mathcal{M}_N$) – to data from [21] describing how tumor cells react to nutrient deprivation. While obtaining a good fit to the measurements with both models, their comparison via the Bayes factor shows a preference for using the ESL approach, despite needing an additional variable and parameter, which is implicitly penalized by the Bayes factor itself [92]. However, as the investigated biological system is very simplistic and considers only one environmental factor (nutrients), there would be no strong need from a quantitative perspective to use the more complex ESL model.

The usefulness of the general modular ESL framework (3.3) becomes more evident for the second application, in which we investigate the influence of several environmental factors on the cell dynamics of two cell lines Hep3B2 and HepG2 with data from [22]. In particular, the calibration of models $\mathcal{M}_{DS}^0$ and $\mathcal{M}_{DS}^{0,\star}$ (for Hep3B2 resp. HepG2) gives insight into the effect of hypoxia and/or cirrhosis on the chemoresistance to a combination therapy with the drugs doxorubicin (DOX) and sorafenib (SOR), see the following paragraph.

Insights into chemotherapeutic efficacy. While the first application mainly served to test and validate the ESL approach in a simple setting, the second one actually provides insightful information about the underlying biological processes. The calibration results imply that hypoxia enhances the treatment efficacy. In contrast, a cirrhotic environment increases the cells' chemoresistance. There appears to be a synergistic influence of hypoxia and stiffness on the treatment response as well as directly on the cell growth. The effect of hypoxia is observable

for both investigated cell lines Hep3B2 and HepG2, whereas the influence of cirrhosis could only be investigated for Hep3B2 with the current state of the models (for details see Section 7.2). We generally see an increased drug susceptibility for Hep3B2 compared to HepG2. There are indications that the cell-specific expression of the drug metabolizing enzyme CYP3A4 (which is higher for HepG2) can be a reason for this. However, further investigations with additional data would be needed to validate this assumption.

7.2   Challenges and opportunities

For the first application, we did not observe any challenges coming from the modeling assumptions and algorithmic choices. Some limitations became more obvious when performing the model calibrations in the chemoresistance setting (second application), which will be discussed in the following paragraphs.

Structure of the data.   We noticed two limitations of the explanatory power of the calibration results due to the structure of the corresponding data from [22]. First, the experiments only examine two dosages of SOR in contrast to eleven dosages for DOX. While the latter provide enough information to reasonably reconstruct the corresponding continuous stress response function $\alpha_D^- \delta_{D,HC}^-$, this was not the case for the stress response to SOR. Therefore, it was not possible to estimate the involved parameters and properly investigate the influence of hypoxia and/or cirrhosis on the treatment response to SOR. Second, percentage viability is measured only once in the course of the whole experiment, which results in a sparse time resolution of the data. As the differential equations in this context are designed to describe the change of quantities over time, this can diminish the informational content for parameter estimation. In our application, the experimental investigation of two different treatment durations provided sufficient information to apply model calibrations, despite having only viability measurements of one time point. However, we achieved only rough estimates for the impact rate α_D^- of the DOX treatment. Furthermore, having time-resolved data over the course of the treatment and subsequent growth phase could be interesting in (future) scenarios, as it might allow for explicitly distinguishing between the negative and positive impact rate (i.e. the reaction to stressful conditions and the recovery thereof).

   We suspect a combination of both observations to be the main reason why we are not able to adequately calibrate the full chemoresistance model $\mathcal{M}_{DS}^{\mathrm{CYP}}$ to the available data. It may not be practical to acquire additional data for improving the model calibrations of this use case. Nevertheless, we can use the above observations to state general guidelines for future applications of mathematical modeling and parameter estimation with differential equations (if circumstances allow for adjusting the experimental design accordingly). On the one hand, the measurements should provide information about the state of relevant parts (e.g. cell viability) of the biological system for at least two points in time. On the other hand, if we want to reconstruct the continuous relationship between an environmental factor and the cells' response with the current modeling approach, the experiments need to examine at least three different states of that environmental factor (e.g. three different drug dosages). These are minimum requirements from a mathematical point of view. However, in practice more time points resp. environmental states might be necessary if the corresponding cell behavior is not sufficiently different.

Mathematical model. From a modeling perspective, the most restricting feature of the current chemoresistance models is the omission of growth enhancing influences, which appears to play a dominant role for parts of the available data in [22]. As a result, we had to exclude all measurements for cell line C3Asub28 and half of the ones for HepG2 from the investigations, which limits the possibilities for gaining biological insights. The incorporation of growth enhancement itself into the model equations could be done easily by adding a term which upscales of the growth rate β. However, we do not have any biological information on the potential cause of the observed growth enhancement to explicitly define the upscaling term in dependence of the environmental factors. Furthermore, it is not clear whether the available data structure is suitable to appropriately reconstruct the growth enhancement with model calibrations.

For the data which we could investigate with the current modeling assumptions, we saw a potentially systematic overestimation of percentage viability measurements regarding DOX dosages below the respective susceptibility threshold $D_{\mathrm{norm},HC}$. The fit to the data might be improved by assuming an asymmetric dose-response function $\delta_{D,HC}^-$. This allows to model a stronger stress response for these dosages without affecting the ones for which we already obtained a decent fit. Note that this introduces an additional unknown parameter for the model calibration, i.e. the benefit of this model adaption is unclear.

Uncertainty modeling. Lastly, the calibration results of the second application indicated some drawbacks of the current uncertainty modeling. Due to considerable variation in the viability data, which we suppose to be a combination of measuring inaccuracy and biological variation, we assumed the measurement uncertainty to dominate over the modeling error. Therefore, the latter was omitted and the multiplicative uncertainty factor ε was supposed to cover all effects of randomness and inaccuracy (recall Section 4.1.1).

While we generally achieved reasonable and fitting results with this approach, the calibrations failed in situations where the model becomes too inaccurate. However, this issue is not caused by the estimations actually exhibiting very large deviations from the data, but rather by the range of acceptable discrepancy (determined by the variance of ε), as it decreases proportionally with the magnitude of the measurements due to the multiplicativity. Hence, for very small measurements, even a relatively small deviation between the estimated model solution and the corresponding data is considered as "too inaccurate" by the calibration algorithm. In the worst case, this applies to the majority of the particle sample, which eventually leads to degenerating variances and the calibration to fail. Except for the data sets exhibiting growth enhancement (recall previous paragraphs), these issues could be compensated with increasing the model accuracy by adjusting the modeling assumptions for the supportive effect of SOR and appropriately choosing a larger uncertainty variance where necessary.

Nevertheless, for future applications, it might be worth to actually consider an additive modeling error supplementary to the multiplicative measurement noise as mentioned in Section 4.1.1. This can resolve the difficulties of allowing some degree of discrepancy between estimation and data also for very small measurements without having to unreasonably increase the variance of the multiplicative noise. Moreover, it might even be possible to choose a smaller value for latter variance and overall improve the accuracy of the estimation. With the current approach, the calibrations might be slightly biased in favor of fitting small measurements at the cost of allowing more discrepancies for large ones.

7.3   Outlook: Potential of the ESL approach and particle filtering

This section provides a short outlook on how the ESL approach could be used to describe cell movement influenced by the stress level (Subsection 7.3.1) as well as on how we could improve the process of parameter estimation with artificial intelligence (Subsection 7.3.2).

7.3.1   ESL approach in a spatially inhomogeneous setting

At some point, we might want to mathematically investigate the interactions between the cells and the tumor microenvironment in a spatially inhomogeneous setting. The general ESL approach can be easily extended by a spatial component, see the following example[25].

Without loss of generality, suppose a two-dimensional point in space $\vec{x} = (x_1, x_2)^T \in \mathbb{R}_+^2$. Then, by adding a space dependency to a variable $A(t) \rightsquigarrow A(t, \vec{x})$, we can adapt its ODE to achieve a corresponding *partial differential equation* (PDE):

$$\frac{\mathrm{d}}{\mathrm{d}t} A = \dot{A} = \boxed{\text{reaction terms}} \qquad \rightsquigarrow \qquad \partial_t A = \boxed{\text{reaction terms}} + \boxed{\text{spatial dynamics}} .$$

A common term for such spatial dynamics is the classical *diffusion*

$$\nabla \cdot (D_A \nabla A) ,$$

which describes an omnidirectional movement to achieve even spreading of A. This movement is proportional to the (concentration) gradient of A, i.e. ∇A, with the diffusion coefficient D_A which we suppose to be constant. In practice, it might depend on the state of the environment (e.g. temperature, pressure, porosity or viscosity – depending on the application).

Furthermore, there might also be active or passive (depending on the application) directed movement of A motivated by the presence of another quantity $B = B(t, \vec{x})$, which can similarly be given as

$$\pm \nabla \cdot \big(A \, M_A(B) \, \nabla B \big) ,$$

describing a repulsive (+) resp. attractive (−) effect of B proportional to its gradient ∇B with coefficient M_A. The latter potentially depends (among others) on B, e.g. if the movement is faster the higher B. In the context of A denoting the density of an organism like cells and B being the concentration of a substance, this phenomenon is called *chemotaxis*.

We can apply the above principles to construct a PDE for the viable tumor cell density V by assuming some kind of survival strategy to migrate towards regions with beneficial growth conditions, i.e.

$$\partial_t V = \underbrace{(1-\eta)\beta V \left(1 - \left(\frac{V}{V_{\mathrm{cap}}}\right)^b\right) - (\lambda + \eta\,\lambda_{\mathrm{ind}})V}_{\text{reaction term from ODE (3.2)}} + \underbrace{\nabla \cdot (D_V \nabla V)}_{\substack{\text{random} \\ \text{migration}}} + \underbrace{\nabla \cdot \big(V \, M_V(\eta) \, \nabla \eta \big)}_{\substack{\text{stress-motivated} \\ \text{movement}}} ,$$

with coefficients D_V and $M_V(\eta)$ denoting the undirected resp. stress-motivated cell motility. Regarding the ESL, there is no need add spatial dynamics to its ODE (3.3), as it is an artificial quantity with no physical/biological counterpart. Then, for a system of $n \in \mathbb{N}$ environmental

---

[25]We keep the explanations more on a superficial level to demonstrate how the ESL approach could work in a spatially inhomogeneous (one/two/three-dimensional) setting. For the mathematical details of the biological application of partial differential equations, like reaction-diffusion equations and chemotaxis, see e.g. [108].

factors $E_1, \dots, E_n$, we can define a basic general system of PDEs via

$$
\begin{cases}
\partial_t E_1 = \tilde{g}_1(E_1, \dots, E_n, V, t)\,, \\
\qquad \vdots \\
\partial_t E_n = \tilde{g}_n(E_1, \dots, E_n, V, t)\,, \\[4pt]
\partial_t \eta = \left(\sum_{j=1}^n \alpha_j^- \delta_j^- (E_j) \right) (1 - \eta) - \left(\sum_{j=1}^n \alpha_j^+ \delta_j^+ (E_j) \right) \eta\,, \\[4pt]
\partial_t V = (1 - \eta)\beta\, V \left(1 - \left(\dfrac{V}{V_{\text{cap}}} \right)^b \right) - \left(\lambda + \eta\, \lambda_{\text{ind}} \right) V + \nabla \cdot (D_V \nabla V) + \nabla \cdot \left(V\, M_V(\eta)\, \nabla \eta \right),
\end{cases}
$$

where each right hand side $\tilde{g}_j$ $(1 \le j \le n)$ contains both the reaction term and the potential spatial dynamics of the respective environmental variable E_j. We want to showcase exemplary simulation results of such a system in the simplistic $(n = 1)$ biological setting of the nutrient deprivation model $\mathcal{M}_N^\eta$ but with non-constant nutrient supply $E_1(t) = N(t)$, i.e.

$$
\partial_t N = -\gamma_N V N + N_{\text{ext}}(t, \vec{x}) + \nabla \cdot (D_N \nabla N)\,,
$$

where the terms respectively describe (from left to right): the nutrient consumption by the cells with constant rate $\gamma_N \ge 0$, a local and time-dependent external nutrient source $N_{\text{ext}} \ge 0$ and nutrient diffusion with a constant coefficient $D_N \ge 0$. In particular, Figure 36 shows the following behavior for this system starting from the initial conditions as illustrated for $t = 0$:

- **day 5:** cells grow and consume nutrients,

- **day 10:** increasing ESL due to nutrients running low,

- **day 15:** cells start to die due to stress from nutrient deprivation,

- **days 20–45:** cells migrate to regions with low ESL, i.e. sufficient nutrient supply, while consuming nutrients on their way and enlarging the region with high ESL,

- **day 50:** adding a constant nutrient source to the system (bottom left corner),

- **day 55:** ESL starts to decrease around the nutrient source,

- **day 75:** nutrient conditions and hence ESL are most beneficial around the nutrients source,

- **days 90–160:** cells move towards the nutrient source by migrating to the region with the most beneficial growth conditions (lowest ESL).
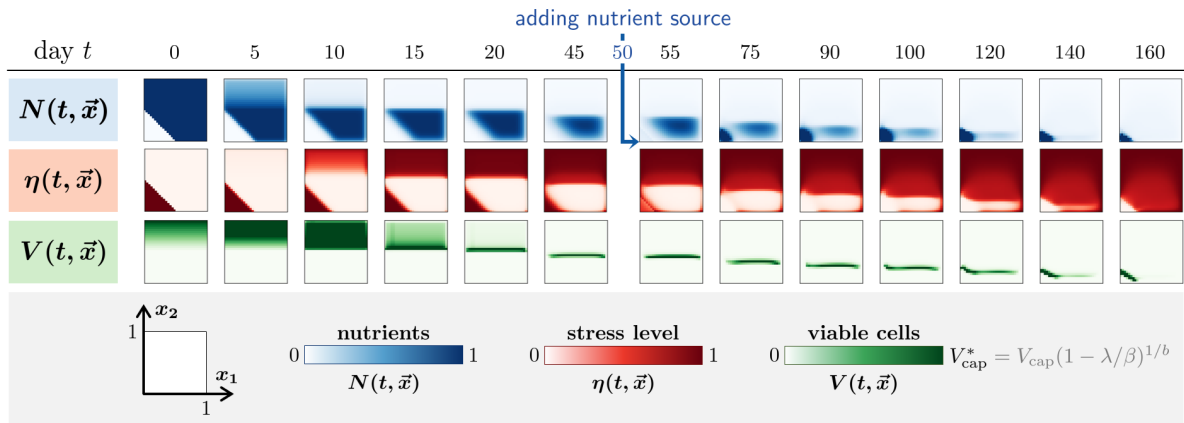
Figure 36: Exemplary simulation results demonstrating a conceivable survival strategy of tumor cells (green, bottom) migrating towards regions with beneficial growth conditions, i.e. low ESL (red, middle), due to sufficient nutrient supply (blue, top). The parameter values are chosen appropriately to make this effect visible (but are roughly based on the calibration results of the ODE model $\mathcal{M}_N^\eta$): $D_N = 0.00015$, $\gamma_N = 0.3$, $\alpha_N = 7$, $\beta = 0.45$, $\lambda = 0.1$, $\lambda_{\mathrm{ind}} = 0.2$, $b = 4$, $V_{\mathrm{cap}} = 1.6$, $N_{\mathrm{thr}} = 0.1$. Cells do only move stress-motivated to demonstrate the principle: $D_V = 0$, $M_V = 0.00015$. External nutrient source: $N_{\mathrm{ext}}(t < 50, \vec{x}) = 0$ resp. $N_{\mathrm{ext}}(t \geq 50, \vec{x}) = 0.1$ (for $\vec{x}$ located in a small triangular area in the bottom left corner). We assume closed boundaries.

7.3.2   Utilizing artificial neural networks

All mathematical models presented in this thesis fall into the category of *physical/biological models*, which describe processes based on knowledge of the underlying physical dynamics and relationships between involved quantities. An almost completely contrary approach are computing systems like *artificial neural networks* (for details see e.g. [109, 110]), which are commonly used for pattern recognition (e.g. images or speech) and natural language processing. They are based on translating a collection of input values to an output value through a network of mathematical functions. Given a sufficient amount of inputs with known respective outputs, the neural network can be trained to recognize the relation between input and corresponding output without needing any specific preknowledge thereof. In the ideal case, an appropriately trained network can give the correct output for arbitrary new, previously unseen inputs (this is called *generalization*). In practice, this is obviously connected with numerous non-trivial challenges, which can be highly problem-specific. In general, the processing through the network happens in a black box nature, i.e. eventually we cannot reconstruct an explicit function connecting the inputs with the output.

In the context of biological processes, neural networks could be used to learn about the relation between a quantity of interest (output) and a collection of system features (inputs) without needing any preknowledge of the underlying processes themselves. However, without the incorporation of any modeling assumptions, such networks will not provide quantities with a physical/biological meaning to gain a deeper understanding of the underlying real-world processes due to the network's black box nature. Furthermore, we have to keep in mind that such a neural network has to be trained with a sufficient amount of reliable data (inputs and output), whose acquisition can be a challenge in biological applications. Nevertheless, there might be potential in applying neural networks in the context of the model calibration itself instead of using it as a complementary approach to the biological models. The subsequent paragraph briefly outlines

the idea of how a neural network could act as a surrogate to the model calibrations. Note that there are also other surrogates which could be considered, naming e.g. Gaussian process regression [111, Ch. 2], stochastic collocation [112–114], polynomial chaos [115][116, Ch. 2] (if the model is sufficiently linear), and reduced basis [117]. The latter is an example of a method for model order reduction while the remaining ones build approximations of model solutions in the parameter space. Neural networks can be used in the context of both approaches (see e.g. [118, 119] resp. [120–122]). In general, the feasibility of the mentioned methods might be more restricted compared to neural networks in our highly non-linear setting and hence should be checked, especially in terms of robustness with reference to the dimension of the parameter space as well as of necessary smoothness assumptions for the dependence of the approximated quantity on the parameters.

The details on how to construct an appropriate neural network and how to feasibly incorporate it in the calibration process are highly non-trivial and would be subject of future work. In particular, we suggest to apply the neural network to potentially improve the total calculation time of the SMC algorithm by using it as an alternative way to numerically solve the biological model, especially in a spatially inhomogeneous setting (there is no need to improve the calculation time for sufficiently simple ODE models or if the analytical solution is available). For neural networks the most time-consuming aspect is the training process itself, whereas its application on new, unseen inputs afterwards can be relatively fast. During the calibration process, we solve the corresponding model for each particle in order to reweight them according to their data likelihood at each SMC step. If we calibrate a model based on P particles over the course of K SMC steps, we solve the system at least $P \cdot K$ times (in practice even more often due to mutation and potential tempering steps). Hence, we collect a considerable amount of known relations between inputs (parameter vector) and an output (model solution) while constructing the posterior distribution. This fact could be utilized by letting a neural network learn the numerical solution in parallel to the parameter estimation. Then, e.g. by tracking the output error of the neural network and checking it against a user-set upper threshold, the forward solving could be switched (partially/gradually) from the numerical solver to the neural network. After switching, it might make sense to occasionally check the output error to keep track of accuracy. Note that the choice of the "switching point" would be not trivial. It is possible to overfit the neural network by training on too much data. This can lead to poor generalization ability of the network [123] and has to be taken into account when defining the details of the learning process. There are several other aspects to consider for good generalization, e.g. an appropriate and unbiased representation of the complete input space by the training data. It is actually desirable to tune the surrogate to the posterior and not to the prior, see e.g [32, 124, 125].

Appendices

Appendix A   Notations and symbols

This section briefly summarizes the most important notations introduced in this thesis.

Mathematical modeling.   In Section 3.1, the general ESL modeling approach defines:

V	Density of viable tumor cells
η	Environmental stress level (ESL)
n	Number of environmental variables/factors
E_j	Specific environmental variable ($j = 1, \ldots, n$)
g_j	Reaction function for E_j defining the right hand side of $\dot{E}_j = \ldots$
$\delta_j^+ \,/\, \delta_j^-$	Positive/negative influence function regarding the stress response to E_j
$\alpha_j^+ \,/\, \alpha_j^-$	Positive/negative impact rate regarding the stress response to E_j

Similar notations are used for each application of the ESL approach in Sections 3.2 resp. 3.3, given by the following models:

$\mathcal{M}_N^\eta$	Nutrient deprivation model using the ESL approach
$\mathcal{M}_N$	Nutrient deprivation model without the ESL approach
$\mathcal{M}_{DS}^{\mathrm{CYP}}$	Complete chemoresistance model
$\mathcal{M}_{DS}^0$	Reduced chemoresistance model
$\mathcal{M}_{DS}^{0,\star}$	Adapted reduced chemoresistance model

The corresponding variables and parameters can be found in Table 1 (for $\mathcal{M}_N^\eta$, $\mathcal{M}_N$) resp. Tables 3 and 4 (for $\mathcal{M}_{DS}^{\mathrm{CYP}}$, $\mathcal{M}_{DS}^0$). Furthermore, we construct the adapted model $\mathcal{M}_{DS}^{0,\star}$ in Subsection 6.3.2, which introduces additional parameters compared to $\mathcal{M}_{DS}^0$:

$d_S^\star(S, D)$	Adapted function to model the supportive effect of SOR on the DOX treatment
D_{damp}	Threshold of the damping factor of $d_S^\star(S, D)$
c_{damp}	Reparametrization parameter for calibrating D_{damp}

Model calibration with SMC.   Section 4.1 explains the structure of the measurements as well as the role of uncertainty for model calibrations with the following notations:

I	Intensity measurement (proportional to density of viable cells V)
$n_{I/V}$	Proportionality constant for intensity measurements
$\varepsilon_V \,/\, \varepsilon_\%$	Uncertainty factor for viability data/percentage viability data
σ^2	Uncertainty variance of ε_V

Section 4.2 introduces the concept of Bayesian inversion for parameter estimation via:

d	Number of estimated parameters
Θ	d-dimensional parameter space
θ	Parameter vector in Θ

$\mathcal{G}^{\mathcal{M}}$	Forward operator for a model $\mathcal{M}$ mapping parameter values to intensities
$\mathcal{I}$	Set of intensity measurements
M	Number of measurements considered for model calibration
$L_i(\, I_i \,|\, \theta\,)$	Likelihood of observation I_i $(i = 1, \ldots, M)$
$L(\, \mathcal{I} \,|\, \theta\,)$	Data likelihood of $\mathcal{I}$
$\mu_0 \,/\, \mu^{\mathcal{I}}$	Prior/posterior (measure) given calibration data $\mathcal{I}$
$\pi_0 \,/\, \pi^{\mathcal{I}}$	Probability density of $\mu_0 \,/\, \mu^{\mathcal{I}}$

Section 4.3 elaborates the Sequential Monte Carlo (SMC) method for model calibrations, using:

K	Number of SMC steps
μ_k	Intermediate distribution at k th SMC step $(k = 1, \ldots, K)$
π_k	Approximation of probability density of μ_k
P	Sample size
θ_p	Particle $(p = 1, \ldots, P)$
W_p^k	Weight associated to p-th particle at k-th SMC step
$\mathcal{L}_k$	Intermediate data likelihood
$\mathcal{I}_{:k}$	Calibration data at k-th SMC step
$\mathcal{I}_{k-1:k}$	Increment data at k-th SMC step, i.e. $\mathcal{I}_{:k} \setminus \mathcal{I}_{:k-1}$
ν_k	Temperature at k-th SMC step if reweighting with likelihood tempering
P_{eff}	Effective sample size (ESS)
P^*	Threshold for resampling or tempering

Subsection 4.3.3 describes how Markov Chain Monte Carlo (MCMC) updates are used for mixing the particles during the SMC algorithm – we introduce:

κ_k	Markov kernel for MCMC updates at k-th SMC step $(k = 1, \ldots, K)$
q_p	Proposed sample $(p = 1, \ldots, P)$
ξ_j	Random walk step size for j-th parameter $(j = 1, \ldots, d)$
ϵ_j^2	Variance of $\xi_j \sim \mathcal{N}(0, \epsilon_j^2)$
ρ	Scaling factor for adapting step size variance
H	Number of MCMC updates
A_h	Number of accepted samples at h-th MCMC update $(h = 1, \ldots, H)$
a_k	Average acceptance ratio of proposed samples at k-th SMC step
H^*	Number of MCMC updates after which the acceptance ratio is checked for adjusting ρ

Post processing of the calibration results. Further notations to investigate the quality of fit and the statistical significance of the calibration results are introduced in Subsection 6.1 as:

d_{valid}	Validation metric comparing the model prediction with corresponding data
$L(\, \mathcal{I} \,|\, \mathcal{M}\,)$	Model evidence of a model $\mathcal{M}$
$\mathcal{Z}_{\mathcal{I}}(\mathcal{M}_1, \mathcal{M}_2)$	Bayes factor comparing two models $\mathcal{M}_1, \mathcal{M}_2$ by their evidence
p_{sig}	p-value for judging statistical significance
$* \,/\, {**} \,/\, {***}$	Star notation to denote the significance level $p_{\text{sig}} < 0.05 \,/\, 0.01 \,/\, 0.001$

Appendix B Mathematical preliminaries: Modeling with differential equations

This chapter explains the idea behind mathematical modeling with differential equations, especially for biological applications, as well as important concepts in this context. In particular, after a basic introduction to differential equations (Appendix B.I), we outline how to obtain solutions and their mathematical features (Appendix B.II). Eventually, we provide a simple example to illustrate the previous explanations (Appendix B.III).

B.I Differential equations

Mathematically, a *differential equation* sets an unknown function f in relation with its derivative(s). In practice, such equations can be used to describe the dynamics of a physical or biological quantity f (e.g. the size of a population). Then, the derivative(s) of f represent its change (e.g. over time) and the equation itself incorporates the known information about the particular dynamics (e.g. reproduction rate, death rate, ...). The following paragraphs provide the mathematical fundamentals to get a basic understanding of differential equations and their application, esp. in the context of this thesis. Note, within this section we always assume sufficient differentiability of the involved functions. For further reading see e.g. [108, 126, 127].

Ordinary differential equation (ODE). We consider a scalar function and its j-th derivative:

$$f : \begin{cases} \mathcal{T} \to \mathbb{R} \,, \\ t \mapsto f(t) \,, \end{cases} \qquad \text{and} \qquad f^{(j)} : \begin{cases} \mathcal{T} \to \mathbb{R} \,, \\ t \mapsto \left(\dfrac{\mathrm{d}}{\mathrm{d}t}\right)^j f(t) \,, \end{cases} \qquad \text{with } \mathcal{T} \in \mathbb{R} \,, \; j \in \mathbb{N}.$$

In this case, a differential equation of k-th order ($k \in \mathbb{N}$) can be defined via

$$G\big(f(t), f'(t), f''(t), \dots, f^{(k)}(t), t \big) = 0 \,, \tag{B.1}$$

where G is a function $\mathbb{R}^k \times \mathcal{T} \to \mathbb{R}$, which describes the relationship between f, its derivatives up to order k and the independent function variable t. In applications, the latter often represents the time dimension, i.e. $f(t) \in \mathbb{R}$ gives the state of a quantity of interest at a specific time point $t \geq 0$. An equation like (B.1) is called *ordinary differential equation* (ODE) and can be distinguished from a *partial differential equations* (PDE), which involves a function f depending on more than one variable. They can be analogously defined, but consider the partial derivatives instead. In practice, such equations are often used for describing the dynamics of a quantity $f = f(t, x)$, where t denotes the time and x a point in space (in up to three dimensions).

Depending on the definition of G, several terminologies are used for characterizing a differential equation. We write G in the form of

$$G\big(f(t), f'(t), f''(t), \dots, f^{(k)}(t), t \big) = h(t) + g\big(f(t), \dots, f^{(k)}(t), t\big) \,,$$

where $h : \mathcal{T} \to \mathbb{R}$ collects all terms which do not depend explicitly on f or its derivatives, and $g : \mathbb{R}^k \times \mathcal{T} \to \mathbb{R}$ the remaining ones. Then, a differential equation is called:

- *linear*, if $g(\dots) = \sum_{j=0}^{k} a_j \cdot f^{(j)}(t)$ with $a_j \in \mathbb{R}$ – *nonlinear* otherwise;
- *homogeneous*, if the so-called inhomogeneity h is $h(t) \equiv 0$ – *inhomogeneous* otherwise;
- *autonomous*, if the variable t only occurs implicitly via f and its derivatives, i.e. $h = \text{const.}$ and $g = g\big(f(t), \dots, f^{(k)}(t)\big)$ – *non-autonomous* otherwise.

These characteristics influence how easy it is to determine the solution f from the equation, or if it is even possible in an analytical way. In Section B.II we present a selection of solving strategies.

System of (first order) ODEs. By using a set of differential equations we can model a physical/biological system, considering the interplay between multiple quantities of interest $f_1, \ldots, f_n$. For the sake of simplicity and relevance for this thesis, we focus on ODE systems of first order, which can be given in the form of

$$\begin{cases} \dot{f}_1(t) = r_1\big(f_1(t), \ldots, f_n(t), t\big), \\ \qquad\qquad \vdots \\ \dot{f}_n(t) = r_n\big(f_1(t), \ldots, f_n(t), t\big), \end{cases} \tag{B.2}$$

where $r_i : \mathbb{R}^n \times \mathcal{T} \to \mathbb{R}$ $(i = 1, \ldots, n)$ is the *reaction function* for the respective *system variable* f_i. Note that the notation $\dot{f}$ is equivalent to f' and often used in the context of time-dependent ODEs. Since the reaction functions r_i can also depend on variables $f_{j \neq i}$, this is a coupled system of ODEs. If additionally to (B.2) *initial conditions*

$$f_1(t_0) = f_{0,1}, \quad \ldots \quad, f_n(t_0) = f_{0,n} \tag{B.3}$$

are given with $t_0 \in \mathcal{T}$ and $f_{0,i}$ $(i = 1, \ldots, n)$, we have a so-called *initial value problem* (IVP).

B.II Model solutions and their mathematical features

A *(model) solution* of an IVP like (B.2) is a collection $\{f_1(t), \ldots, f_n(t)\}$ which fulfills all equations of the system as well as the initial conditions (B.3). If the characteristics of the ODEs allow it and the degree of coupling is not too complex (e.g. for linear, autonomous ODEs), the system could be solved analytically, i.e. we derive explicit formulas for all $f_i(t)$. Otherwise, numerical methods are needed to approximately calculate a model solution by discretization of the system. So-called *Runge-Kutta* methods (see e.g. [128, Ch. 2]), and within them the *explicit/implicit Euler* methods, are among the most popular ones.

Analytical solver: Separation of variables. If a model is analytically solvable, there are different approaches to obtain the solution, depending on the characterization of the system (see e.g. [126]). Often, several methods are feasible to the same system. For the models within this thesis, we focus on a method called *separation of variables* [126, Ch. 1.3]. It is applicable for a *separable* ODE which has the form

$$\dot{f}_i(t) = u(t) \cdot v(f_i), \quad \text{with } f_i(t_0) = f_{i,0},$$

i.e. it can be written by a product of two terms which only depend on t or f_i, respectively (for an example, see Subsection B.III). Then, the solution can be derived by solving

$$\int_{f_{i,0}}^{f_i(t)} \frac{1}{v(\zeta)} \, \mathrm{d}\zeta = \int_{t_0}^{t} u(\tau) \, \mathrm{d}\tau \tag{B.4}$$

for $f_i(t)$, given that the involved integrals can be calculated explicitly.

Positivity and boundedness of solutions.   Especially for modeling biological systems, having a non-negative solution can be a necessity for reasonableness. Often, the model variables represent densities, concentrations or count individuals, i.e. negative values do not make sense in this context. Hence, it is desirable to check a model for positivity of the solution and conclude parameter constraints where necessary. If the model solution can be derived analytically, positivity can be checked directly. Otherwise, each variable has to be examined respectively. We can check the positivity of a solution f_i $(1 \leq i \leq n)$ by investigating the sign of r_i under the assumption of a non-negative initial condition and that $f_i = 0$ and $f_{j \neq i} \geq 0$. If these circumstances result in $r_i \geq 0$, positivity of f_i can be concluded, as this means that f_i will not decline any further once it reaches zero. If positivity of a variable is preserved, it automatically implies zero as a respective lower bound for the solution. Investigating boundedness can give useful insight into the meaningfulness of the model and the observed behavior. Bounds can be derived e.g. by analyzing the analytical solution or the so-called steady state solution(s).

Steady states and their stability.   A *steady state (solution)*[26] is a solution where the described system does not change in time – you could say all system variables do not show any net reaction. Hence, mathematically, this means that the reaction term of each variable vanishes: $r_i = 0$ $(i = 1, \dots, n)$. For autonomous systems, this gives the ansatz to determine the steady states, i.e. the solution set $\bar{f} = \{(\bar{f}_1, \dots, \bar{f}_n)^T \,|\, r_{i=1,\dots,n}(\bar{f}_1, \dots, \bar{f}_n) = 0\}$. In practice, the existence of a steady state might be coupled to parameter constraints.

The *stability* of a steady state $\bar{f}$ can give information about the long-time behavior of the underlying biological/physical system. It is called *(asymptotically) stable* if the state of the system converges towards the steady state when starting sufficiently close to it, i.e. if

$$\exists \epsilon > 0 : \quad \lim_{t \to \infty} f(t) = \bar{f} \quad \forall \, |f(t_0) - \bar{f}| < \epsilon \,,$$

for $f(t) = \big(f_1(t), \dots, f_n(t)\big)^T$, and *unstable* otherwise. For a single ODE $\dot{f}_i = r_i(f_i)$, stability can be checked with:

$$\frac{\mathrm{d}}{\mathrm{d}f_i} r_i \big|_{f_i = \bar{f}_i} \begin{cases} < 0 & \Rightarrow \text{stable}, \\ > 0 & \Rightarrow \text{unstable}, \\ = 0 & \Rightarrow \text{unclear stability}. \end{cases}$$

If stability by linearization is unclear, another method is needed (e.g. by investigating the change of a time-dependent perturbation from the steady state).

For a system of ODEs, we can use the *theorem of Hartman and Grobman* [129, 130] to determine the stability of a steady state $\bar{f}$ from the eigenvalues of the Jacobian matrix

$$J \big|_{f = \bar{f}} = \begin{pmatrix} \frac{\partial}{\partial_{f_1}} 1 & \cdots & \frac{\partial}{\partial_{f_n}} r_1 \\ \vdots & \ddots & \vdots \\ \frac{\partial}{\partial_{f_1}} r_n & \cdots & \frac{\partial}{\partial_{f_n}} r_n \end{pmatrix} \Bigg|_{f = \bar{f}}$$

which linearizes the system. Then, the steady state $\bar{f}$ is stable if the real parts of all eigenvalues of $J \big|_{f = \bar{f}}$ are negative and unstable otherwise. Note however, that this theorem is only applicable if all eigenvalues of the Jacobian matrix have a non-zero real part.

---

[26]other common names are: stationary state/solution, equilibrium (state)

Quasi-steady state approximation.   Another, related principle is the *quasi-steady state approximation*. It describes the assumption that the dynamics described by the mathematical model follow two different time scales: a fast and a slow one. Then, variables whose dynamics happen on the fast time-scale are approximated by their steady states. This allows to reduce the model to a system only considering the "slow system". A classical example are the *Michaelis-Menten kinetics* [108, Ch. 6.1], which model a basic enzyme dynamics (fast: complex formation, slow: reaction).

B.III   Exemplary application: Modeling population dynamics

Let $P = P(t)$ denote the size of a population (e.g. cells, bacteria, animal species, ...) at time $t \geq 0$. Then, the derivative $\dot{P}(t)$ describes the change of P over time. It is reasonable to assume that the population growth is directly proportional to its current size, as a larger population means more reproducing individuals. Since "growth" of a quantity mathematically translates to a positive derivative, this can be modeled e.g. by the differential equation

$$\dot{P}(t) = a \cdot P(t),$$

where the parameter $a > 0$ can be interpreted as the (constant) growth rate of the population. Analogously, a larger population contains a higher number of "old" individuals. Hence, for a limited life expectancy the negative change of the population size can be included by

$$\dot{P}(t) = a \cdot P(t) - b \cdot P(t) = \underbrace{(a - b) \cdot P(t)}_{\text{reaction term } r(P)} \tag{B.5}$$

with death rate $b > 0$. This ODE is an example of a linear, homogeneous, autonomous differential equation.

Model solution.   Given an initial population size $P(t = 0) = P_0 \geq 0$, the initial value problem for (B.5) can be solved analytically e.g. by separation of variables:

$$\frac{\mathrm{d}P}{\mathrm{d}t} = (a - b) \cdot P(t) \quad \overset{\text{(B.4)}}{\Rightarrow} \int_{P_0}^{P(t)} \frac{1}{p} \, \mathrm{d}p = \int_0^t (a - b) \, \mathrm{d}\tau \quad \Rightarrow P(t) = P_0 \, e^{(a-b)t} \text{ for } t \geq 0. \tag{B.6}$$

The solution shows that the relation between growth and death rate determines if we observe an increasing ($a > b \Rightarrow P(t) \geq P_0$) or declining ($a < b \Rightarrow P(t) \leq P_0$) population size. Due to the form of this solution, equation (B.5) is also called an exponential growth/decay model.

Positivity and boundedness of the solution.   With having the analytical solution (B.6), positivity of P can be followed directly by $P_0 \geq 0$ and the non-negativity of the exponential function. The same result can be concluded by investigating the respective ODE (B.5) as described in Section B.II: $P = 0 \Rightarrow r(P) = 0$. Positivity of the solution implies the lower bound $P \geq 0$. For a declining population ($a < b$) the initial population size is an upper bound $P \leq P_0$, while for an increasing population ($a > b$) we see from (B.6) that P can be arbitrarily large for a sufficiently large t, i.e. there is no upper bound for the population size P.

Steady states.   The long-term behavior of the biological system can be investigated with the steady states. Before we actually calculate these, we give thought to which behavior we would expect intuitively. If the population grows faster than it dies, we observe unlimited population growth. In contrast, if the reproduction cannot compensate the occurring death, the population will go extinct eventually. Lastly, if growth and death are balanced, the population size will remain constant at its initial state. In summary, we would expect:

$$
P(t) \xrightarrow{t \to \infty}
\begin{cases}
\infty & \text{for } a > b, \\
0 & \text{for } a < b, \\
P_0 & \text{for } a = b.
\end{cases}
$$

Now for the mathematical analysis: For $a = b$ the last result follows directly by insertion into the analytical solution (B.6): $P(t) = P_0 \cdot e^0 = P_0 \, \forall t \geq 0$. For $a \neq b$ we set $\dot{P} = r(\bar{P}) = 0$ in equation (B.5), yielding only the *trivial* steady state $\bar{P} = 0$ of the system. Differentiation of the reaction term r and subsequent insertion of the steady state $\bar{P}$ shows how its stability depends on the relation between the rates a and b:

$$
\frac{\mathrm{d}}{\mathrm{d}P} \, r(P) \bigg|_{\bar{P}=0} = (a - b)\big|_{\bar{P}=0}
\begin{cases}
> 0 & \text{for } a > b \ \Rightarrow \ \bar{P} = 0 \text{ unstable,} \\
< 0 & \text{for } a < b \ \Rightarrow \ \bar{P} = 0 \text{ stable.}
\end{cases}
$$

All together, the obtained steady state and its stability confirm the intuitive long-term behavior.

From exponential to logistic growth.   Although exponential growth is a reasonable choice to describe an increasing population, in reality the population size might be limited to a capacity (e.g. due to limitations in space or resources). To capture this in the modeling, we can modify the exponential growth term in (B.5) by including a damping factor:

$$
\dot{P}(t) = \underbrace{a \cdot P(t)}_{\substack{\text{exponential} \\ \text{growth}}} \cdot \underbrace{\left(1 - \frac{P(t)}{K_P} \right)}_{\text{damping factor}} - b \cdot P(t) \,,
$$

where K_P is the capacity of the biological system. For $P \in (0, K_P)$ the ratio P/K_P ranges between zero and one. In particular, the closer the population size P is to the capacity K_P, the closer the ratio P/K_P gets to one and hence the stronger the damping factor $(1 - P/K_P)$ slows down the exponential growth. To tune the strength of damping with respect to the "distance" between the current population size P and the capacity K_P, we can introduce another parameter $\nu > 0$ by

$$
\dot{P}(t) = \underbrace{a \cdot P(t) \cdot \left(1 - \left(\frac{P(t)}{K_P} \right)^{\nu} \right)}_{\text{general logistic growth}} - b \cdot P(t) \,. \tag{B.7}
$$

The larger the parameter ν, the closer the population size can get to the capacity before the exponential growth is significantly damped. Without the death term $b \cdot P(t)$, equation (B.7) describes the so-called *general logistic growth*. Some special cases for ν yield further widely used growth models: if $\nu = 1$ resp. $\nu \searrow 0$ we refer to *logistic growth* resp. *Gompertz growth* [131].

Appendix C Properties of the chemoresistance models

In this section, we investigate the mathematical properties of the chemoresistance models $\mathcal{M}_{DS}^{\mathrm{CYP}}$ and $\mathcal{M}_{DS}^{0}$ in terms of positivity and boundedness of the solutions as well as the steady states and their stability.

Positivity of the solutions. Positivity of V and η was already reasoned in Section 3.1, which applies to both models. For the variables D and S we only need to check the solutions during the treatment phase, since afterwards they are zero, hence non-negative. In model $\mathcal{M}_{DS}^{0}$ the drug concentrations are constant and non-negative by definition: $D = D_0 \geq 0$ and $S = S_0 \geq 0$. For $\mathcal{M}_{DS}^{\mathrm{CYP}}$ positivity follows directly by

$$\dot{D} = -\gamma \cdot V \cdot D \overset{D=0}{=} 0 \quad \text{and} \quad \dot{S} = -\gamma \cdot V \cdot S \overset{S=0}{=} 0 \qquad \text{for } V \geq 0\,.$$

Boundedness of the solutions. Positivity of the solutions means boundedness from below by zero, which is fulfilled for all variables in both models. The population dynamics are given by exponential growth, i.e. V is unbounded from above in the biological setting modeled by $\mathcal{M}_{DS}^{\mathrm{CYP}}$ and $\mathcal{M}_{DS}^{0}$. The ESL η is bounded from above by one due to the definition of its ODE (recall Section 3.1). Since $\dot{D}, \dot{S} \leq 0 \; \forall t \geq t_0$, their solutions are bounded from above by the respective initial value D_0 and S_0.

Steady states and their stability. Due to the unlimited exponential cell growth in both models $\mathcal{M}_{DS}^{\mathrm{CYP}}$ and $\mathcal{M}_{DS}^{0}$ given by the ODE

$$\dot{V} = \big(\beta - \lambda - (\beta + \lambda_{\mathrm{ind}})\eta\big) \cdot V\,, \tag{C.1}$$

there are only two possibilities to obtain

$$\dot{V}\big|_{V=\bar{V},\eta=\bar{\eta}} = 0\,, \quad \text{which are} \quad \bar{V} = 0 \quad \text{or} \quad \bar{\eta} = \tfrac{\beta-\lambda}{\beta+\lambda_{\mathrm{ind}}}\,.$$

We are interested in potential steady states of the models after the treatment, i.e. for $t \geq t_{\mathrm{treat}}$. Since all remaining drugs are removed after the treatment phase, the ESL stays constant at the value $\eta = \eta(t_{\mathrm{treat}})$, i.e. we have $\bar{D}, \bar{S} = 0$ and $\bar{\eta} = \eta(t_{\mathrm{treat}})$.

If this stress level is sufficiently large, i.e. $\eta(t_{\mathrm{treat}}) > \tfrac{\beta-\lambda}{\beta+\lambda_{\mathrm{ind}}}$ (recall (3.10)), the tumor cells go extinct, yielding the stable steady state

$$\big(\bar{V}, \bar{D}, \bar{S}, \bar{\eta}\big)^T = \big(0, 0, 0, \eta(t_{\mathrm{treat}})\big)^T, \qquad \text{for } \eta(t_{\mathrm{treat}}) > \tfrac{\beta-\lambda}{\beta+\lambda_{\mathrm{ind}}}\,.$$

The stability follows from

$$\frac{\mathrm{d}}{\mathrm{d}V}\Big(\big(\beta - \lambda - (\beta + \lambda_{\mathrm{ind}})\eta\big) \cdot V\Big)\Big|_{V=\bar{V},\eta=\bar{\eta}} = \beta - \lambda - \big(\beta + \lambda_{\mathrm{ind}}\big)\underbrace{\eta(t_{\mathrm{treat}})}_{> \frac{\beta-\lambda}{\beta+\lambda_{\mathrm{ind}}}} < 0\,,$$

as the model system can be reduced to only ODE (C.1) after the treatment phase. If by the end of the treatment the ESL does not exceed the mentioned threshold, i.e. $\eta(t_{\mathrm{treat}}) < \tfrac{\beta-\lambda}{\beta+\lambda_{\mathrm{ind}}}$, there exists no steady state, since the induced stress was not enough and the population continues to grow.

If the ESL reaches the value $\frac{\beta-\lambda}{\beta+\lambda_{\text{ind}}}$ exactly at the time t_{treat} where the drugs are removed, it stays constant at this level resulting in a stationary population size $V = V(t_{\text{treat}})$. This gives the steady state

$$\left(\bar{V},\,\bar{D},\,\bar{S},\,\bar{\eta}\right)^T = \left(V(t_{\text{treat}}),\,0,\,0,\,\frac{\beta-\lambda}{\beta+\lambda_{\text{ind}}}\right)^T.$$

In a real life setting, this scenario is not realistic and further investigation of the stability of this steady state is of minor interest.

Towards solving the chemoresistance models. We recall the models, with $T = [t_0 = 0, t_{\text{treat}}]$ denoting the treatment phase:

$$\mathcal{M}_{DS}^{\text{CYP}} : \begin{cases} \dot{V} = \left(\beta - \lambda - \left(\beta + \lambda_{\text{ind}}\right)\eta\right) \cdot V, \\[2mm] \dot{\eta} = \left(\alpha_D^- \delta_{D,HC}^-\big(D(t), S(t)\big) + \alpha_S^- \delta_{S,HC}^-\big(S(t)\big)\right)(1 - \eta), \\[2mm] D(t) = D_0 \exp\left(-\gamma_{D,HC} \cdot t\right) \cdot \mathbb{1}_T(t), \\[2mm] S(t) = S_0 \exp\left(-\gamma_{S,HC} \cdot t\right) \cdot \mathbb{1}_T(t), \end{cases}$$

$$\mathcal{M}_{DS}^{0} : \begin{cases} \dot{V} = \left(\beta - \lambda - \left(\beta + \lambda_{\text{ind}}\right)\eta\right) \cdot V, \\[2mm] \dot{\eta} = \left(\alpha_D^- \delta_{D,HC}^-\big(D_0, S_0\big) + \alpha_S^- \delta_{S,HC}^-\big(S_0\big)\right)(1 - \eta)\,\mathbb{1}_T(t), \end{cases}$$

with respectively $V(t_0 = 0) = V_0$ and $\eta(t_0 = 0) = \eta_{0,HC} \leq \frac{\beta-\lambda}{\beta+\lambda_{\text{ind}}} \in (0,1)$. Both models have the first ODE in common, on which we can apply separation of variables (B.4):

$$\int_{V_0}^{V(t)} \frac{1}{v}\,\mathrm{d}v = \int_{t_0=0}^{t} \beta - \lambda - \left(\beta + \lambda_{\text{ind}}\right)\eta(\tau)\,\mathrm{d}\tau$$

$$\Rightarrow \quad \ln\big(V(t)\big) - \ln\big(V_0\big) = (\beta - \lambda)t - \left(\beta + \lambda_{\text{ind}}\right)\int_0^t \eta(\tau)\,\mathrm{d}\tau$$

$$\Rightarrow \quad V(t) = V_0 \exp\left((\beta - \lambda)t - \left(\beta + \lambda_{\text{ind}}\right)\int_0^t \eta(\tau)\,\mathrm{d}\tau\right),$$

for $t \in [0, t_{\text{end}}]$. If $t \in [t_{\text{treat}}, t_{\text{end}}]$, we have

$$\int_0^t \eta(\tau)\,\mathrm{d}\tau = \int_0^{t_{\text{treat}}} \eta(\tau)\,\mathrm{d}\tau + \int_{t_{\text{treat}}}^{t} \eta(t_{\text{treat}})\,\mathrm{d}\tau = \int_0^{t_{\text{treat}}} \eta(\tau)\,\mathrm{d}\tau + \eta(t_{\text{treat}})(t - t_{\text{treat}}),$$

as then $\dot{\eta} = 0 \Rightarrow \eta(t) = \eta(t_{\text{treat}})\ \forall t \in [t_{\text{treat}}, t_{\text{end}}]$. An analogous approach for the second ODE (which differs for both models only by the time-dependence of $\delta_{D,HC}^-$ and $\delta_{S,HC}^-$) yields:

$$\int_{\eta_{0,HC}}^{\eta(t)} \frac{1}{1 - \zeta}\,\mathrm{d}\zeta = \int_0^t \alpha_D^- \delta_{D,HC}^- + \alpha_S^- \delta_{S,HC}^-\,\mathrm{d}\tau$$

$$\Rightarrow\ \ln\big(1 - \eta_{0,HC}\big) - \ln\big(1 - \eta(t)\big) = \begin{cases} \int_0^t \alpha_D^- \delta_{D,HC}^-\big(D(\tau), S(\tau)\big) + \alpha_S^- \delta_{S,HC}^-\big(S(\tau)\big)\,\mathrm{d}\tau & \text{for } \mathcal{M}_{DS}^{\text{CYP}}, \\[3mm] \int_0^t \alpha_D^- \delta_{D,HC}^-\big(D_0, S_0\big) + \alpha_S^- \delta_{S,HC}^-\big(S_0\big)\,\mathrm{d}\tau & \text{for } \mathcal{M}_{DS}^0, \end{cases}$$

eventually resulting in

$$\eta(t) = \begin{cases} 1 - (1 - \eta_{0,HC})\exp\left(-\int_0^t \alpha_D^- \delta_{D,HC}^-\big(D(\tau), S(\tau)\big) + \alpha_S^- \delta_{S,HC}^-\big(S(\tau)\big)\,\mathrm{d}\tau\right) & \text{for } \mathcal{M}_{DS}^{\text{CYP}}, \\[3mm] 1 - (1 - \eta_{0,HC})\exp\left(-\left(\alpha_D^- \delta_{D,HC}^-\big(D_0, S_0\big) + \alpha_S^- \delta_{S,HC}^-\big(S_0\big)\right)t\right) & \text{for } \mathcal{M}_{DS}^0, \end{cases}$$

for $t \in [t_{\text{treat}}, t_{\text{end}}]$ and $\eta(t) = \eta(t_{\text{treat}})\ \forall t \in [t_{\text{treat}}, t_{\text{end}}]$.

Appendix D   Supplementary material: Model calibration and post processing

We provide additional material regarding the model calibrations and the post processing of the results. In particular, we give details on the uncertainty modeling for percentage viability measurements (Appendix D.I) as well as on systematic resampling (Appendix D.II). Furthermore, we summarize the prior distributions for the applied model calibrations (Appendix D.III) and explain how we obtain a KDE for a marginal posterior distribution on the bounded support of its respective prior (Appendix D.IV).

D.I   Uncertainty modeling: Ratio distribution of two Gamma distributions

We consider two uncertainty factors ε_1 and ε_2 which are respectively Gamma distributed according to (4.3), i.e.

$$\varepsilon_1 \sim \Gamma\left(\frac{1}{\sigma_1^2}, \frac{1}{\sigma_1^2}\right) = \Gamma(a_1, a_1) \qquad \text{and} \qquad \varepsilon_2 \sim \Gamma\left(\frac{1}{\sigma_2^2}, \frac{1}{\sigma_2^2}\right) = \Gamma(a_2, a_2) \,,$$

with variances $\sigma_1^2, \sigma_2^2 \in (0, 1)$ and the short notations $a_1 = 1/\sigma_1^2$ resp. $a_2 = 1/\sigma_2^2$. We show in this section that the ratio between two such independent random variables is distributed according to a generalized Beta prime distribution via

$$\frac{\varepsilon_1}{\varepsilon_2} \sim \beta'\left(a_1, a_2, 1, \frac{a_2}{a_1}\right), \text{ with PDF } \quad f^{a_1,a_2}_{(\varepsilon_1/\varepsilon_2)}(y) = \frac{\left(\frac{y}{a_2/a_1}\right)^{a_1-1}\left(1 + \frac{y}{a_2/a_1}\right)^{-a_1-a_2}}{B(a_1, a_2) \cdot a_2/a_1} \,, \qquad \text{(D.1)}$$

where $B(\cdot\,,\,\cdot)$ denotes the Beta function. Recall the PDF for a random variable $\varepsilon \sim \Gamma(a, a)$:

$$f^{a,a}_\varepsilon(x) = \frac{a^a}{\Gamma(a)}\, x^{a-1} e^{-ax} \,,$$

with $x, a > 0$ and the Gamma function

$$\Gamma(a) = \int_0^\infty u^{a-1} e^{-u}\, \mathrm{d}u \,. \qquad \text{(D.2)}$$

Since ε_1 and ε_2 are independent, their joint PDF is given by:

$$f^{a_1,a_2}_{\varepsilon_1,\varepsilon_2}(x_1, x_2) = f^{a_1,a_1}_{\varepsilon_1}(x_1) \cdot f^{a_2,a_2}_{\varepsilon_2}(x_2) = \frac{a_1^{a_1} \cdot a_2^{a_2}}{\Gamma(a_1) \cdot \Gamma(a_2)}\, x_1^{a_1-1} \cdot x_2^{a_2-1}\, e^{-a_1 x_1 - a_2 x_2} \,,$$

with $x_1, x_2 > 0$. The PDF of the ratio $\varepsilon_1/\varepsilon_2$ can be calculated with the so-called ratio distribution (RD) of two independent random variables [132]. In particular, for $y = \frac{x_1}{x_2} \Rightarrow x_1 = y x_2$, it follows:

$$
\begin{aligned}
f^{a_1,a_2}_{(\varepsilon_1/\varepsilon_2)}(y) &\stackrel{\text{RD}}{=} \int_{-\infty}^{+\infty} f^{a_1,a_2}_{\varepsilon_1,\varepsilon_2}(y x_2, x_2) \cdot |x_2|\, \mathrm{d}x_2 \\
&= \int_0^\infty \frac{a_1^{a_1} \cdot a_2^{a_2}}{\Gamma(a_1) \cdot \Gamma(a_2)}\, (y x_2)^{a_1-1} \cdot x_2^{a_2-1}\, e^{-a_1 y x_2 - a_2 x_2} \cdot x_2\, \mathrm{d}x_2 \\
&= \frac{a_1^{a_1} \cdot a_2^{a_2}}{\Gamma(a_1) \cdot \Gamma(a_2)}\, y^{a_1-1} \int_0^\infty x_2^{a_1+a_2-1}\, e^{-x_2(a_1 y + a_2)}\, \mathrm{d}x_2 \,.
\end{aligned}
$$

By the substitution $u = x_2(a_1 y + a_2) \Rightarrow x_2 = \frac{u}{a_1 y + a_2}$, we get:

$$
\begin{aligned}
f_{(\varepsilon_1/\varepsilon_2)}^{a_1,a_2}(y) &= \frac{a_1^{a_1} \cdot a_2^{a_2}}{\Gamma(a_1) \cdot \Gamma(a_2)}\, y^{a_1-1} \int_0^\infty \frac{u^{a_1+a_2-1}}{(a_1 y + a_2)^{a_1+a_2-1}}\, e^{-u} \cdot \frac{1}{a_1 y + a_2}\, \mathrm{d}u \\
&= \frac{a_1^{a_1} \cdot a_2^{a_2}}{\Gamma(a_1) \cdot \Gamma(a_2)}\, y^{a_1-1} (a_1 y + a_2)^{-a_1-a_2} \underbrace{\int_0^\infty u^{a_1+a_2-1}\, e^{-u}\, \mathrm{d}u}_{\overset{(D.2)}{=}\ \Gamma(a_1+a_2)} \\
&= \frac{a_1^{a_1} \cdot a_2^{a_2}}{B(a_1,a_2)}\, y^{a_1-1}\, a_2^{-a_1-a_2} \left(\frac{a_1}{a_2} \cdot y + 1 \right)^{-a_1-a_2},
\end{aligned}
$$

where we used the relation $B(a_1,a_2) = \frac{\Gamma(a_1+a_2)}{\Gamma(a_1) \cdot \Gamma(a_2)}$ in the last step. Eventually, we achieve the desired PDF from (D.1) by

$$
f_{(\varepsilon_1/\varepsilon_2)}^{a_1,a_2}(y) = \frac{y^{a_1-1}}{B(a_1,a_2)} \underbrace{a_1^{a_1}\, a_2^{a_2}\, a_2^{-a_1-a_2}}_{=\ \frac{(a_1/a_2)^{a_1-1}}{(a_1/a_2)^{-1}}} \left(\frac{a_1}{a_2} \cdot y + 1 \right)^{-a_1-a_2} = \frac{\left(\frac{y}{a_2/a_1} \right)^{a_1-1} \left(1 + \frac{y}{a_2/a_1} \right)^{-a_1-a_2}}{B(a_1,a_2) \cdot a_2/a_1},
$$

i.e. the ratio of the uncertainty factors $\varepsilon_1 \sim \Gamma(a_1, a_1)$ and $\varepsilon_2 \sim \Gamma(a_2, a_2)$, with $a_1, a_2 > 1$, is Beta prime distributed according to $\frac{\varepsilon_1}{\varepsilon_2} \sim \beta'\big(a_1, a_2, 1, \frac{a_2}{a_1}\big)$.

D.II   Methodological details for SMC: Systematic resampling

The following Algorithm D.1 gives the steps of *systematic resampling* according to [80]. As explained in Subsection 4.3.2, this method can be used alternatively to *random resampling* to appropriately reweight the particles during SMC.

Algorithm D.1 – Systematic resampling (SR)

1: sample $r \sim \mathcal{U}(0, 1/P)$
2: set $\omega = W_1^k$, $s = 1$, $\mathfrak{R} = \emptyset$
3: **for** $p = 1, \dots, P$ **do**
4:      set $u = r + \frac{p-1}{P}$
5:      **while** $u > \omega$ **do**
6:          set $s = s + 1$ and $\omega = \omega + W_s^k$
7:      **end while**
8:      include particle θ_s to $\mathfrak{R}$, i.e. $\mathfrak{R} = \mathfrak{R} \cup \{\theta_s\}$
9: **end for**

D.III   Applying SMC: Prior distributions for model calibrations

The following Tables D.1 resp. D.2 summarize the prior distributions to perform the calibrations for models $\mathcal{M}_N^\eta$ and $\mathcal{M}_N$ resp. $\mathcal{M}_{DS}^0$ and $\mathcal{M}_{DS}^{\mathrm{CYP}}$. The reasoning behind these distributions is explained in Subsections 5.3.1 resp. 5.3.2.

Table D.1: Overview of the *a priori* information used to calibrate the models $\mathcal{M}_N^\eta$ and $\mathcal{M}_N$. Note that α_N and η_0 do only appear in model $\mathcal{M}_N^\eta$. The following notations are used: "a, b" (uniform prior on $[a, b]$), "$= a$" (not calibrated, fixed to a).

hyperparameters				cell dynamics					nutrients' influence		
σ_0^2	σ_N^2	n_N	c_n	β	c_β	c_λ	V_{cap}	b	N_{thr}	α_N	η_0
$0, 0.5$	$0, 0.5$	$0, 0.5$	$0, 1$	$0, 1$	$0, 1$	$0, 1$	$1, 3$	$1, 12$	$0, 1$	$0, 12$	$= 0$

Table D.2: Overview of the *a priori* information used to calibrate model $\mathcal{M}_{DS}^0$ resp. $\mathcal{M}_{DS}^{CYP}$ for different combinations of $H_0 \in \{0,1\}$ and $C_0 \in \{0,1\}$. The following notations are used: "N/A" (not calibrated), "a, b" (uniform prior on $[a,b]$), "a, h, b" (triangular prior on $[a,b]$ with mode h), "$= a$" (not calibrated, fixed to a), "$=$ MAP" (not calibrated, fixed to MAP estimate from calibration for $H_0, C_0 = 0$, i.e. HC0).

(a) Priors for calibration of model $\mathcal{M}_{DS}^0$ using Hep3B2 data.

environment	cell dynamics		ESL dynamics							
	$(\beta-\lambda)$	$(\beta+\lambda_{\text{ind}})$	$\eta_{0,HC}$	α_D^-	$\widehat{D}_{\text{norm},HC}$	$\widehat{m}_1$	$\alpha_S^-\delta_S^-(1)$	c_δ	$d_S(0.5)$	c_d
HC0	N/A	0,3	$= 0$	0,20	$-4,0,4$	0,1.7	0,2	0,0,1	0,1	0,1
H1/C1/HC1	$=$ MAP		0,0,1							

(b) Priors for calibration of model $\mathcal{M}_{DS}^{CYP}$ using HepG2 or C3Asub28 data.

environment	cell dynamics		ESL dynamics									drug dynamics	
	$(\beta-\lambda)$	$(\beta+\lambda_{\text{ind}})$	$\eta_{0,HC}$	α_D^-	$\widehat{D}_{\text{norm},HC}$	m_1	α_S^-	$S_{\text{thr},HC}$	$\widehat{m}_2$	S_{supp}	$\widehat{m}_3$	γ_D	γ_S
HC0	N/A	0,3	$= 0$	0,20	$-4,0,4$	0,6	0,10	0,3	0,1.7	0,1	0,1.7	0,20	0,20
H1/C1/HC1	$=$ MAP		0,0,1										

D.IV   Post processing of the calibration results: Truncated KDE

In this section, we explain how we truncate a kernel density estimation (KDE), i.e. a smoothed approximation of the PDF, based on the particle representation of a marginal posterior distribution with bounded support. The boundedness of the posterior support is carried over from the prior (recall that we used either uniform or triangular priors), as the posterior measure $\mu^{\mathcal{I}}$ is absolutely continuous with respect to the prior μ_0 [81], i.e. $\operatorname{supp}(\pi^{\mathcal{I}}) \subseteq \operatorname{supp}(\pi_0)$.

Native KDE.   Suppose we want to approximate the PDF of the marginal posterior of the j-th parameter ($j = 1, \ldots, d \in \mathbb{N}$), for which we assumed a prior distribution whose support is bounded on an interval $[a, b]$, $a < b$. We use a KDE with Gaussian kernels and Scott's bandwidth selection method [93]. In practice, this can be calculated by applying the Python function

$$\texttt{scipy.stats.gaussian\_kde(}\underbrace{\texttt{particles\_j}}_{\{(\theta_p)_j\}_{p=1}^P}\texttt{, weights}=\underbrace{\texttt{w\_particles}}_{\{W_p\}_{p=1}^P}\texttt{)},$$

where the arguments are the j-th component of all particles with the corresponding weights. If $a \ll (\theta_p)_j \ll b \;\forall p \in \{1, \ldots, P\}$, i.e. the collection of marginalized particles is situated "far enough" (which depends on the bandwidth) away from the bounds, the support of this KDE is virtually included[27] in $[a, b]$. Therefore, in this case, there is no need to truncate the KDE to obtain the desired boundedness.

However, the above scenario might not always apply in practice, especially if the bounds of the prior are motivated by mathematical modeling. For instance, if a parameter $c \in [0, 1]$ quantifies some kind of response, the mathematical bounds can be interpreted as "no response" ($c \equiv 0$) and "maximal response" ($c \equiv 1$). Then, depending on the underlying data, it can actually happen that the corresponding marginal particles accumulate at one of these bounds. In general, if a considerable part of the particles is close to a border, the support of the KDE will overshoot this border due to its construction by [133], that is

$$\mathrm{KDE}_h(\theta) = \frac{1}{Ph} \sum_{p=1}^P \kappa\left(\frac{\theta - (\theta_p)_j}{h}\right),$$

where $h > 0$ is the bandwidth, P the sample size and κ the kernel density, i.e. in our case the PDF of a standard normal distribution. We see that with the latter, a particle close to the border b (w.l.o.g.), i.e. $(\theta_p)_j \lesssim b$, contributes to the estimator in such a way that $\mathrm{KDE}_h(\theta) > 0$ also for $\theta \gtrsim b$. This contribution accumulates with the number of particles which are situated close to b. Hence, in such a scenario, the above KDE is not feasible to obtain an approximation of the marginal PDF with bounded support. To preserve the boundedness of the marginal posterior particles, we present an adapted version of the native KDE in the following.

---

[27] To be precise, the actual support of the KDE is unbounded due to the Gaussian kernels. However, suppose $\theta_{\min,j}$ resp. $\theta_{\max,j}$ being the smallest/largest value of $\{(\theta_p)_j\}_{p=1}^P$, then the value of the KDE will approach zero if evaluated at points sufficiently smaller/larger than $\theta_{\min,j}$ resp. $\theta_{\max,j}$.

Truncated KDE.   Figure D.1 illustrates how we appropriately limit the native KDE to the bounded support of the prior distribution – we will refer to this as the *truncated KDE* (trKDE). Note that the latter needs to sustain the features of a PDF, especially having an integral of one.
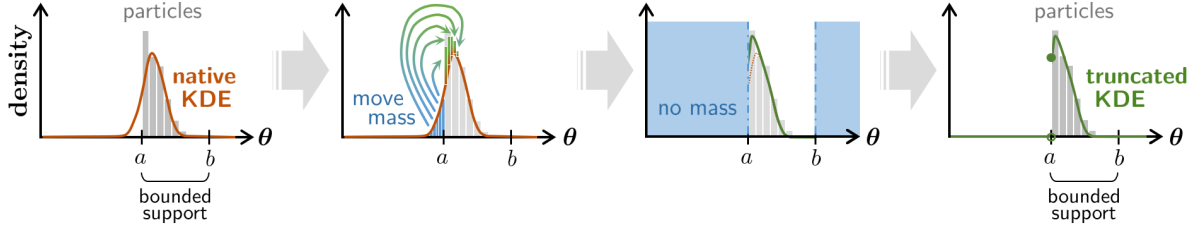
Figure D.1: Outline of how the truncated KDE is obtained from the native KDE, based on the weighted particle approximation of a marginal posterior.

Without the truncation, the probability mass of the particle approximation close to a boundary gets spread outside of the bounded support of the prior (Figure D.1: first plot). In practice, we observed that the distance of any external (i.e. outside of $[a, b]$), significantly non-zero mass of the KDE has a distance from the boundaries which is not larger than the interval length $b - a$. Hence, we can move all external mass into the interval $[a, b]$ by defining the truncated KDE as

$$\text{trKDE}_h(\theta) = \Big(\text{KDE}_h(a + \tau_a) + \underbrace{\text{KDE}_h(a - \tau_a)}_{\text{external mass}} + \text{KDE}_h(b - \tau_b) + \underbrace{\text{KDE}_h(b + \tau_b)}_{\text{external mass}} \Big) \cdot \mathbb{1}_{[a,b]}(\theta) \,,$$

with $\tau_a, \tau_b \in [0, b - a]$ being the distance of $\theta \in [a, b]$ from a resp. b and $\mathbb{1}_{[a,b]}$ denoting the indicator function on $[a, b]$. In particular, we basically "shift" external mass with distance $\tau_* \ (* \in \{a, b\})$ from the respective boundary to the point with the same distance, but inside the interval $[a, b]$ (Figure D.1: second plot). Therefore, we can set $\text{trKDE}_h(\theta) = 0 \ \forall \theta \notin [a, b]$ without losing any mass (Figure D.1: third plot), i.e. preserving an integral of one. This results in an appropriate approximation of the marginal posterior PDF given by the particles and truncated on $[a, b]$ (Figure D.1: fourth plot).

Appendix E   Complementary calibration results

In this part of the appendix, we present further investigations of the results regarding the model calibrations for both applications (nutrient deprivation models: Section E.I, chemoresistance models for cell line Hep3B2/HepG2: Sections E.II resp. E.III), complementary to Chapter 6.

E.I   Application 1: Nutrient deprivation models

This section[28] gives additional material regarding the calibration results for comparing the nutrient deprivation models $\mathcal{M}_N^\eta$ and $\mathcal{M}_N$, which are discussed in Subsection 6.2.2. We summarize the obtained estimates for the hyperparameters (Subsection E.I.1) as well as provide more details on the fit of model solution and data in terms of the uncertainty range (Subsection E.I.2) and validation metric (Subsection E.I.3).

E.I.1   Estimates of the hyperparameters

Table E.3 lists the marginal means and variances of the posteriors for the proportionality constants and reparametrization parameters. We see similar results for both models. In fact, observable differences between the parameter estimates, i.e. the mean values in Table E.3a, of both models are found to be statistically insignificant ($p_{\text{sig}} > 0.05$) by applying a two-tailed Student t-test on the $q = 12$ estimates assuming unequal variances.

Table E.3: Comparison of further estimated parameters of models $\mathcal{M}_N^\eta$ and $\mathcal{M}_N$. Numerical deviations from performing the SMC algorithm $q = 12$ times are given as 95% confidence interval ($\bar{x} \pm 1.96 \cdot \sigma_x q^{-1/2}$ with $\bar{x}$, σ_x mean resp. standard deviation of observations).

(a) Marginal means $\mathbb{E}(\,\cdot\,)$ of the posterior.

	n_N	n_0	c_n	c_β	c_λ
$\mathcal{M}_N^\eta$	0.243 ± 0.001	0.182 ± 0.006	0.752 ± 0.027	0.240 ± 0.013	0.554 ± 0.046
$\mathcal{M}_N$	0.244 ± 0.002	0.190 ± 0.006	0.780 ± 0.024	0.236 ± 0.022	0.576 ± 0.085

(b) Marginal variances $\text{Var}(\,\cdot\,)$ of the posterior.

	n_N	n_0	c_n	c_β	c_λ
$\mathcal{M}_N^\eta$	0.002 ± 0.001	0.007 ± 0.004	0.032 ± 0.016	0.016 ± 0.010	0.069 ± 0.035
$\mathcal{M}_N$	0.002 ± 0.001	0.008 ± 0.005	0.034 ± 0.020	0.011 ± 0.007	0.053 ± 0.029

---

[28]Note that content and formulations of this section are taken from our publication [63] and some notations, especially regarding the numerical deviations, might differ to maintain consistency within the thesis.

E.I.2   Uncertainty range of the estimated solution

To investigate if the observable drop in the measured viability on the third day in Figure 19 influences the quality of the fit, we consider the underlying measurement uncertainty. Depending on the uncertainty variance σ^2, we can calculate the percentiles $\mathcal{P}_{0.05}$ and $\mathcal{P}_{0.95}$ of the Gamma distributed uncertainty factor ε:

$$\bar{\sigma}_N^2 = 0.0355 \quad \Rightarrow \quad \mathcal{P}_{0.05} = 0.712\,,\ \mathcal{P}_{0.95} = 1.329\,,$$
$$\bar{\sigma}_0^2 = 0.2410 \quad \Rightarrow \quad \mathcal{P}_{0.05} = 0.350\,,\ \mathcal{P}_{0.95} = 1.920\,.$$

These determine the 90% uncertainty range (4.5) for the calibration data D1–D4 resp. D0, i.e. give an interval around the solution $V(t)$, where the model expects 90% of the measurements. We want to know how many measurements are actually situated where they are expected.

For each data set, we count the scaled measurements I/n, which are situated below, within or above the 90% uncertainty range of the corresponding average solution V. A visual overview of the calculated percentages can be seen in Figure E.2. In each subplot (left/right: model $\mathcal{M}_N$ resp. $\mathcal{M}_N^\eta$), there are three different markers per data set (vertical axis), showing how many data points (horizontal axis) are situated below/within/above the 90% range. For instance, regarding data set D4 (topmost on vertical axis), in both plots the black bullet marker shows that approx. 87% of the measurements actually lie within the 90% range, whereas the dark/light blue triangle marker shows that about 4%/9% of them are above/below the 90% range.
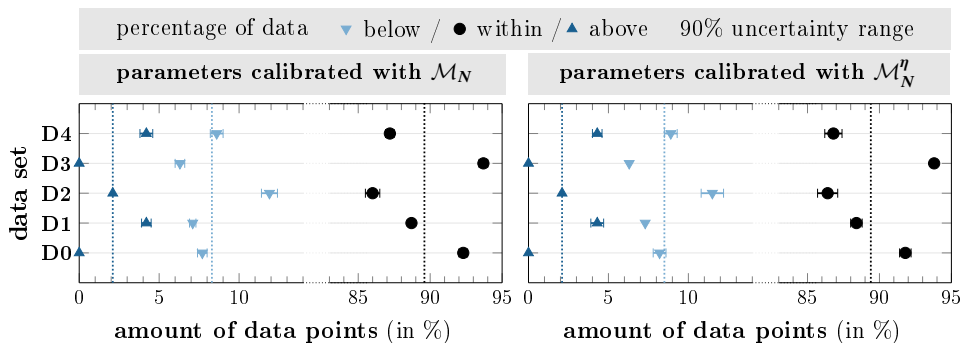
Figure E.2: Percentage of data points which are situated below/within/above the 90% range $[V \cdot \mathcal{P}_{0.05}\,,\ V \cdot \mathcal{P}_{0.95}]$ around the solution V. The dotted lines in the corresponding color give the average over all data sets D0–D4. Error bars show the numerical deviations from performing the SMC algorithm $q = 12$ times by the 95% confidence interval ($\bar{x} \pm 1.96 \cdot \sigma_x q^{-1/2}$ with $\bar{x}$, σ_x mean resp. standard deviation of observations).

We see that averaging over the data sets (dotted vertical lines), for both models roughly 90% (black line) of the scaled data is actually situated within the 90% uncertainty range. Regarding the remaining data points, we observe that the model solutions tend to be larger than the measurements, since about 8.3–8.5% (light blue line) of the data points lie below the 90% range, whereas only about 2.1% (dark blue line) are above.

To investigate this observation, we take a closer look at the data below the 90% range by checking if the discrepancy focuses on specific measurements, see Table E.4. On the third day, the measurements show an extraordinarily large amount of data below the 90% uncertainty range, where only 5% would be expected. This supports the hypothesis that the measurements on that day might be outliers.

Table E.4: Average (over the $q = 12$ SMC runs) percentage of data points in D0–D4 which are below the 90% uncertainty range for different initial cell densities V_0 (rows) and days t (columns). Numerical deviations between the runs are given by the 95% confidence interval ($\bar{x} \pm 1.96 \cdot \sigma_x q^{-1/2}$ with $\bar{x}$, σ_x mean resp. standard deviation of observations). If there are no deviations, we omit the confidence intervals and decimal places (which are zero) for better readability.

| | V_0 | Day of measurement | | | | | | | |
		0	**1**	**2**	**3**	**4**	**5**	**6**	**7**
$\mathcal{M}_N^\eta$	**1.00**	0	0	0.8 ± 1.1	5	3.3 ± 1.4	0	5	5
	0.50	5	0	7.9 ± 1.5	35	0	0	0	0
	0.25	14.2 ± 1.1	5	32.1 ± 1.5	72.9 ± 1.5	5.4 ± 0.8	0	1.3 ± 1.3	5
$\mathcal{M}_N$	**1.00**	0	0.8 ± 1.1	0	0	0	0	0	0
	0.50	5.8 ± 1.1	0	5.8 ± 1.1	35	0	0	0	0
	0.25	13.8 ± 1.8	5	30.8 ± 1.1	73.8 ± 1.3	5.4 ± 0.8	0	1.3 ± 1.3	4.2 ± 1.1

Furthermore, we observe that the percentages are higher the smaller V_0 is: approx. 35% resp. 68–78% of the measurements are below the 90% range for $V_0 = 0.50$ resp. $V_0 = 0.25$. This negative correlation is expectable, since the width of the range $\left[V \cdot \mathcal{P}_{0.05} \, , \, V \cdot \mathcal{P}_{0.95} \right]$ decreases with smaller V (recall right side of Figure 5). This also explains that, within the measurements of a particular day, more data points tend to be below the 90% range for smaller V_0.

E.I.3   Quality of fit to the data

As the validation metric (6.1) measures the mismatch between data and model prediction, we use the following scale to compare the quality of fit between both nutrient deprivation models:

$$d_{\mathrm{comp}} = \frac{d_{\mathrm{valid}}\left(F^{\mathrm{data}}, F^{\mathrm{sol}}_{\mathcal{M}_N^\eta} \right)}{d_{\mathrm{valid}}\left(F^{\mathrm{data}}, F^{\mathrm{sol}}_{\mathcal{M}_N} \right)} \quad \begin{cases} \ll 1 & \text{indicates: better fit for } \mathcal{M}_N^\eta \,, \\ \approx 1 & \text{indicates: } \mathcal{M}_N \text{ and } \mathcal{M}_N^\eta \text{ fit equally well}\,, \\ \gg 1 & \text{indicates: better fit for } \mathcal{M}_N \,. \end{cases}$$

Table E.5 summarizes d_{comp} for each data set and initial cell density V_0. For data set DV (validation data set), the solution of the reduced model $\mathcal{M}_{\mathrm{opt}}$ was used by inserting the average estimated parameters resulting from the calibration of $\mathcal{M}_N^\eta$ resp. $\mathcal{M}_N$.

Table E.5: Ratio d_{comp} of the validation metrics using model $\mathcal{M}_N^\eta$ resp. $\mathcal{M}_N$ averaged over all time points considering measurements regarding various V_0 (columns) and data sets, i.e. different N_0 (rows). The values in the last row/column are averaged over all data sets/initial cell densities before taking the mean over the SMC runs. Numerical deviations between the runs are given by the 95% confidence interval ($\bar{x} \pm 1.96 \cdot \sigma_x q^{-1/2}$ with $\bar{x}$, σ_x mean resp. standard deviation of observations).

| | Initial cell density V_0 | | | | | |
Data set	**1.00**	**0.50**	**0.25**	**0.10**	**0.05**	**all (avg.)**
DV	1.05 ± 0.16	1.04 ± 0.09	1.07 ± 0.05	1.01 ± 0.07	1.03 ± 0.04	1.04 ± 0.08
D4	1.04 ± 0.04	1.01 ± 0.03	1.00 ± 0.03	-	-	1.02 ± 0.01
D3	1.01 ± 0.02	0.99 ± 0.05	0.99 ± 0.04	-	-	1.00 ± 0.03
D2	1.02 ± 0.01	1.02 ± 0.06	1.03 ± 0.04	-	-	1.02 ± 0.02
D1	1.00 ± 0.02	1.01 ± 0.04	1.01 ± 0.01	-	-	1.01 ± 0.02
D0	0.94 ± 0.04	1.06 ± 0.05	1.03 ± 0.02	-	-	1.01 ± 0.03
all (avg.)	1.01 ± 0.03	1.02 ± 0.04	1.02 ± 0.01	1.01 ± 0.07	1.03 ± 0.04	1.02 ± 0.02

All values are close to one and the differences between them are in the scale of numerical variations of the SMC algorithm. Hence, the investigation of the validation metric does not show any clear preference of a particular model.

E.II   Application 2: Chemoresistance of Hep3B2

This section provides complementary details to Subsection 6.3.1 regarding the calibration results of the reduced chemoresistance model $\mathcal{M}_{DS}^0$ with the data for cell line Hep3B2. In particular, we present the marginal estimates (Subsection E.II.1), investigate the parameter correlations (Subsection E.II.2) and compare the marginal distributions of specific parameters (Subsection E.II.3).

E.II.1   Marginal estimates

Figure E.3 compares the marginal distributions of the model parameters based on the particle approximation collecting all SMC runs. Note that the parameters $D_{\mathrm{norm},HC}$ and m_1 were calibrated in log scale to improve the coverage of the high probability region with the prior sample (recall Subsection 5.3.2), but their marginal distributions and corresponding MAPs are determined by calculating the KDE in linear scale.
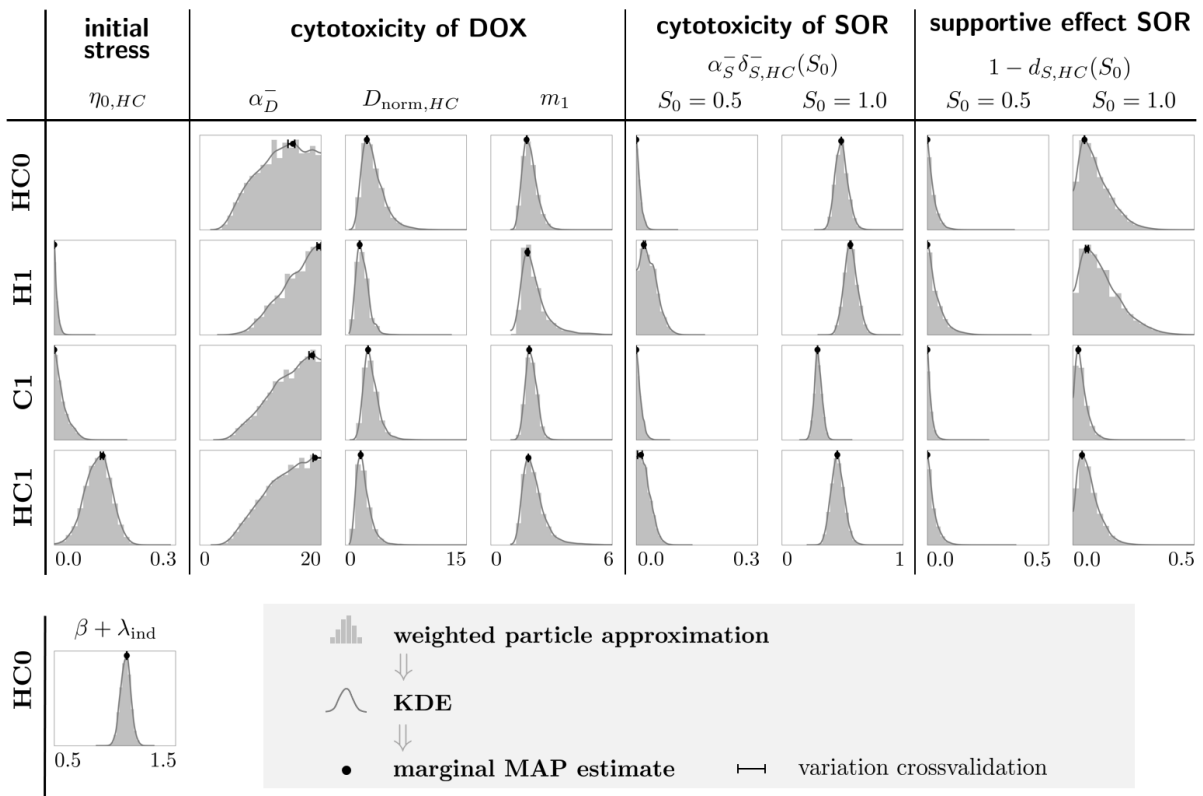
Figure E.3: Marginal posteriors of Hep3B2 calibrations. The numerical deviations for cross-validating the MAP estimates according to Subsection 6.1.3 are shown as error bars, which might not be visible due to high robustness of the respective estimate. Recall that $\beta + \lambda_{\mathrm{ind}}$ resp. $\eta_{0,HC}$ are only calibrated for HC0 resp. H1/C1/HC1 ($\beta + \lambda_{\mathrm{ind}}$ is fixed to its MAP for H1/C1/HC1 and $\eta_{0,HC} = 0$ for HC0 per definition).

E.II.2   Parameter correlations

We check the (linear) parameter correlations of the particle approximation collecting all SMC runs as described in Subsection 6.1.4. To capture numerical variations, we repeated the calculation of the correlation coefficients 1000 times for respectively different set of 5000 samples. Since this resulted in robust coefficients[29], we give the average values of r in the following Figures E.4 an E.5 . Note that in all subplots of both figures the axis limits are not consistent and especially not labeled as this is not the focus of this investigation. Figure E.4 depicts the correlations between the DOX susceptibility threshold $D_{\mathrm{norm},HC}$ and the remaining parameters of the ODE for the ESL η.
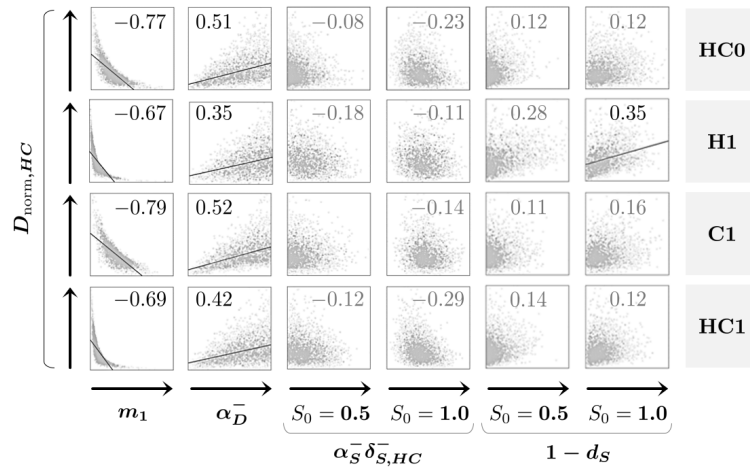
Figure E.4: Scatter plots with 5000 samples drawn from the 2D distributions of pairwise parameter combination of $D_{\mathrm{norm},HC}$ with the remaining calibrated parameters (columns) resulting from model calibrations with Hep3B2 data. Only statistically significant ($p_{\mathrm{sig}} < 0.05$) correlation coefficients r are given and a regression line is depicted if at least a moderate linear correlation ($|r| > 0.3$) is observable.

Recalling the categorization of the correlation coefficient r from (6.4), we observe a strong negative correlation with m_1 (potentially nonlinear as the L-shaped point cloud suggests) and a moderate positive one with α_D^- for all environmental conditions. Furthermore, there are less obvious indications from the shape of the point clouds that there is a relevant positive correlation with $1 - d_S$. Note that for $1 - d_S$ the correlation results could be distorted due to the proximity of the respective marginal posteriors to the lower bound of zero (see Figure 28). In summary, all parameters involved in the DOX stress response $\alpha_D^- \delta_{D,HC}^-$ show considerable correlations.

For the sake of completeness, Figure E.5 shows analogous plots for the remaining parameter estimations. Note that we do not show the correlations of pairwise combinations of α_D^-, $\alpha_S^- \delta_{S,HC}^-$ and $1 - d_S$ since they are mostly found to be statistically insignificant and/or very weak. The only exception is a moderate positive correlation between $1 - d_S(0.5)$ and $1 - d_S(1.0)$ which is an expected result as we used the parametrization $d_S(1.0) = c_d \cdot d_S(0.5)$ and calibrated $c_d \in (0, 1]$ instead of $d_S(1.0)$.

---

[29]The standard deviation of the numerical dispersion is in the magnitude of 10^{-2}, i.e. the deviations are of minor interest, as the interpretation guidelines in (6.4) are not rigid.
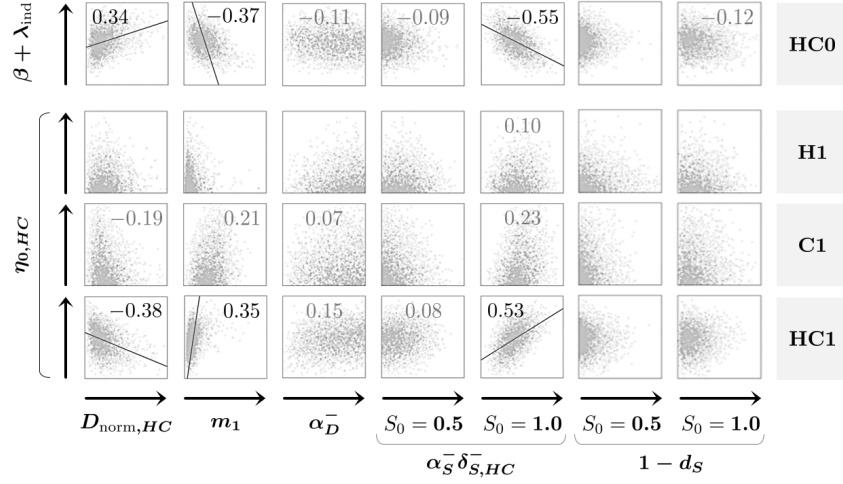
(a) Illustration of the correlations between $\beta + \lambda_{\text{ind}}$ (top row) resp. $\eta_{0,HC}$ (rows 2–4) with the remaining calibrated parameters (columns).
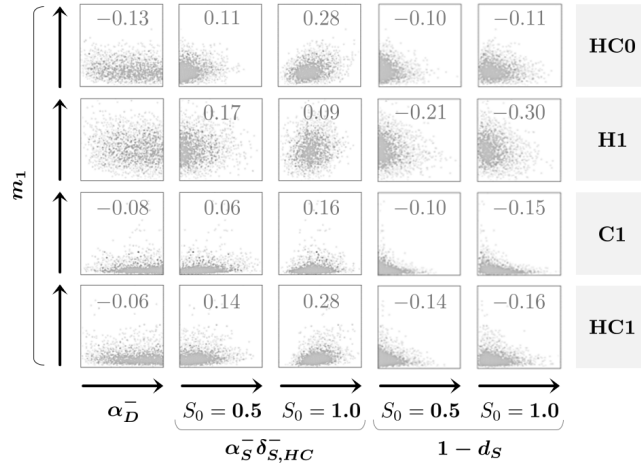
(b) Illustration of the correlations between m_1 with the remaining calibrated parameters (columns).

Figure E.5: Scatter plots with 5000 samples drawn from the 2D distributions of pairwise parameter combinations resulting from model calibrations with Hep3B2 data. Only statistically significant ($p_{\text{sig}} < 0.05$) correlation coefficients r are given and a regression line is depicted if at least a moderate linear correlation ($|r| > 0.3$) is observable.

E.II.3   Comparison of the marginal parameter estimates

We provide further results from investigating the marginalized estimates (which neglects correlations) of particular parameters. We focus on comparing the respective marginal distributions in different environments with the significance check as proposed in Subsection 6.1.3 and Figure 15.

Marginal posterior comparison: Initial stress level.   Figure E.6 illustrates the statistical significance of the differences between the marginal distributions of $\eta_{0,HC}$ from Figure 23. We see clear significance for all cases.
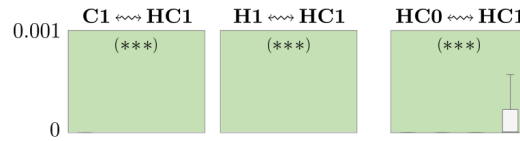
Figure E.6: Resulting p-values of the significance check (sample sizes per subplot from left to right: 500, 100, 50, 30) comparing the marginal distributions of $\eta_{0,HC}$ for Hep3B2 in different environmental settings. Vertical axis limits: 0–0.001. Note that some boxplots are not visible due to vanishing p-values.

Marginal posterior comparison: Cytotoxic efficacy of SOR. Figure E.7 statistically compares the marginal distributions of $\alpha_S^- \delta_{S,HC}^-(S_0)$ from Figure 25. We see clear significance for the marginals for almost all scenarios, except for the cases of tissue stiffening with $S_0 = 0.5$ (potentially insignificant for sole cirrhosis resp. potentially significant for cirrhosis in hypoxic conditions) and combined hypoxia and cirrhosis with $S_0 = 1.0$ (potentially insignificant).
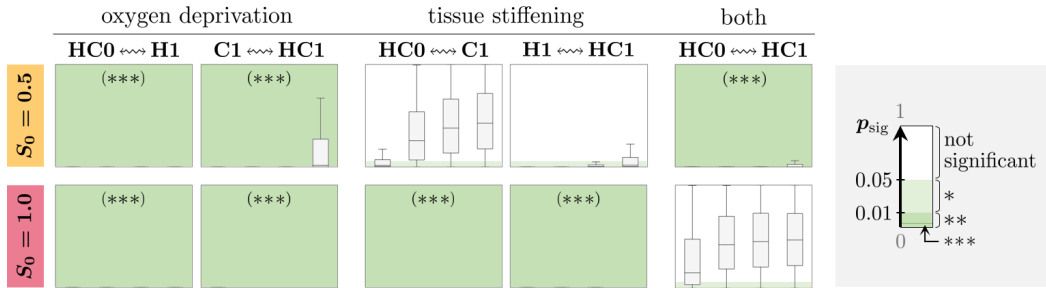
Figure E.7: Resulting p-values of the significance check (sample sizes per subplot from left to right: 500, 100, 50, 30) comparing the marginal distributions of $\alpha_S^- \delta_{S,HC}^-(S_0)$ for Hep3B2 in different environmental settings. Vertical axis limits are given by the receptive mark in the subplot: $0-1/0.001$ (no mark / ***). Note that some boxplots are not visible due to vanishing p-values.

Marginalized investigation: Estimates of DOX susceptibility. We investigate the marginals of the DOX susceptibility threshold $D_{\mathrm{norm},HC}(H_0, C_0) = D_{\mathrm{norm}} \cdot d_H(H_0) \cdot d_C(C_0)$ for $H_0, C_0 \in \{0, 1\}$, i.e. without considering correlations to other parameters. Figure E.8 compares the respective marginal posteriors and MAPs of $D_{\mathrm{norm},HC}$ for different environments.
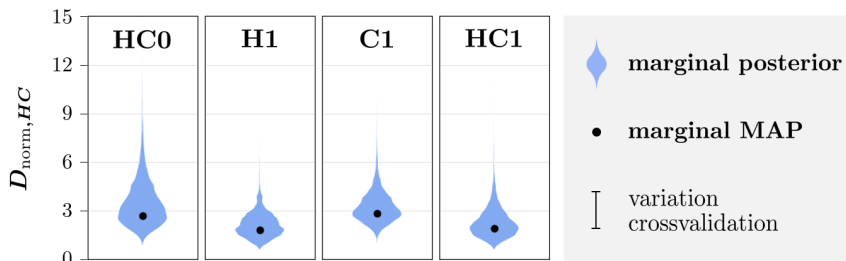
Figure E.8: Comparison of marginal posteriors (violin plots) and corresponding MAPs of $D_{\mathrm{norm},HC}$ for Hep3B2. Due to minor numerical variations, the cross-validated 95% confidence intervals (error bars) are not visible.

The marginal MAPs of $D_{\mathrm{norm},HC}$ show the following environmental effects:

$$\begin{aligned}
\text{sole hypoxia (HC0} \rightsquigarrow \text{H1):} \quad & 2.659 \searrow 1.778 \quad (-33.1\%)\,, \\
\text{hypoxia in cirrhosis (C1} \rightsquigarrow \text{HC1):} \quad & 2.805 \searrow 1.903 \quad (-32.2\%)\,, \\
\text{sole cirrhosis (HC0} \rightsquigarrow \text{C1):} \quad & 2.659 \nearrow 2.805 \quad (+5.5\%)\,, \\
\text{cirrhosis in hypoxia (H1} \rightsquigarrow \text{HC1):} \quad & 1.778 \nearrow 1.903 \quad (+7.0\%)\,.
\end{aligned}$$

Since a smaller value for $D_{\mathrm{norm},HC}$ translates to an enhanced susceptibility, we observe hypoxia resp. cirrhosis to increase/decrease the DOX susceptibility. Furthermore, we do not see a large difference between the effect of sole hypoxia/cirrhosis and a respective combination of both. This suggest no synergistic effect between hypoxia and stiffness on the susceptibility. In general, the relative decrease of D_{norm} due to hypoxia (approx. -31%) appears to outweigh the increase by cirrhosis (approx. $+6\%$). This is consistent with the observation

$$\text{HC0} \rightsquigarrow \text{HC1}: \quad 2.659 \searrow 1.903 \quad (-28.4\%)\,.$$

Comparing the marginal posteriors of $D_{\mathrm{norm},HC}$ for different environmental settings shows a clear statistical significance of the increasing effect of hypoxia on the DOX susceptibility, in contrast to the influence of ECM stiffness (see Figure E.9). This could indicate that the DOX susceptibility is actually not effected by cirrhosis, however this cannot be concluded distinctively. Figure E.9 shows that the significance results for observed differences between the fitted estimates of $D_{\mathrm{norm},HC}$ are mostly very similar to the ones for the marginals. The only exception is visible for comparing H1 with HC1, which appears to be clearly significant for the fitted estimates in contrast to the marginals. This weakens the indications obtained with the marginals that the DOX susceptibility is generally not influenced by cirrhosis.
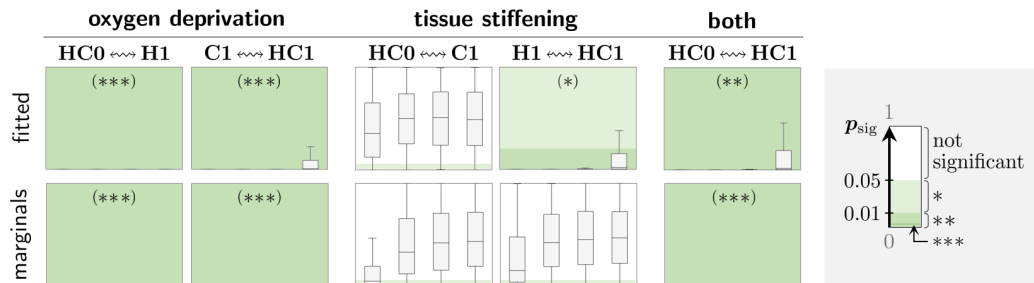
Figure E.9: Resulting p-values of the significance check comparing the marginal distributions resp. fitted estimates of $D_{\mathrm{norm},HC}$ (in Figure E.8) for Hep3B2 in different environmental settings (sample sizes per subplot from left to right: 500, 100, 50, 30). Vertical axis limits are given by the receptive mark in the subplot: $0-1/0.05/0.01/0.001$ (no mark $/ * / ** / ***$). Note that some boxplots are not visible due to vanishing p-values.

Marginal posterior comparison: DOX impact.   Figure E.10 depicts the statistical significance of the differences between the marginal distributions of α_D^- from Figure 26. We observe potentially insignificant differences between the marginals for all cases. For the fitted values however, the differences appear to be clearly significant for sole hypoxia resp. cirrhosis (columns 1 and 3) and a combination of both (column 5). In general, this could hint on a significant influence of hypoxia/stiffening on the DOX impact rate.
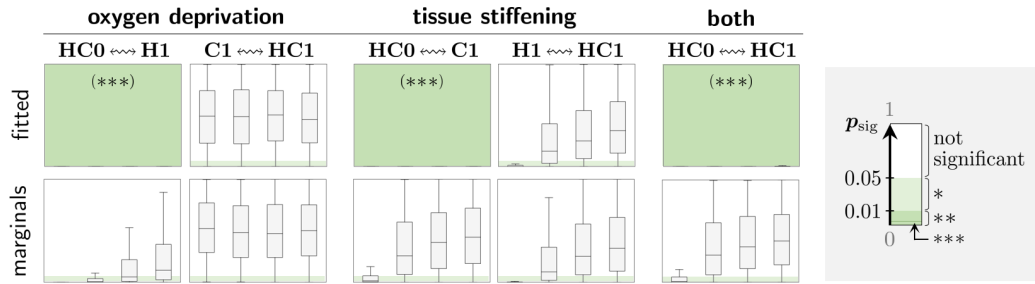
Figure E.10: Resulting p-values of the significance check comparing the marginal distributions resp. fitted estimates of α_D^- for Hep3B2 in different environmental settings (sample sizes per subplot from left to right: 500, 100, 50, 30). Vertical axis limits are given by the receptive mark in the subplot: $0-1/0.001$ (no mark / ∗∗∗). Note that some boxplots are not visible due to vanishing p-values.

Marginal posterior comparison: Supportive effect of SOR.   Figure E.11 shows the statistical comparison of the marginal distributions for $1 - d_S(S_0)$ from Figure 28. For $S_0 = 0.5$, we see potentially insignificant differences between the marginals when comparing HC0 with HC1 (column 5) and an unclear significance for the remaining cases (columns 1–4). For $S_0 = 1.0$, the observed differences appear to be clearly (columns 2–4) or potentially (columns 1 and 5) significant.
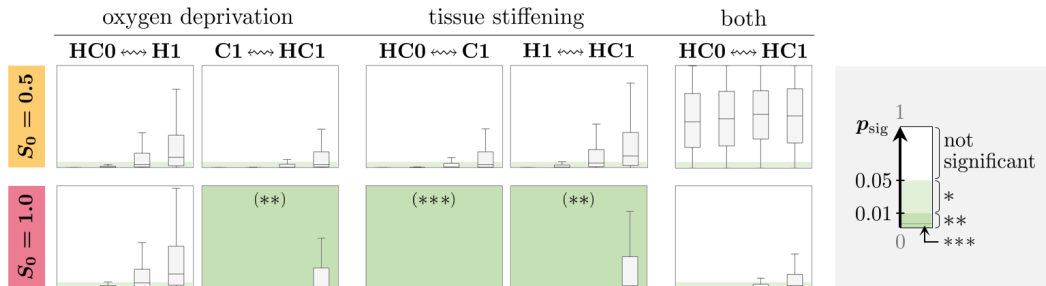
Figure E.11: Resulting p-values of the significance check comparing the marginal distributions of $1 - d_S(S_0)$ for Hep3B2 in different environmental settings (sample sizes per subplot from left to right: 500, 100, 50, 30). Vertical axis limits are given by the receptive mark in the subplot: $0-1/0.01/0.001$ (no mark / ∗∗ / ∗∗∗). Note that some boxplots are not visible due to vanishing p-values.

E.III   Application 2: Chemoresistance of HepG2

This section provides complementary details to Subsection 6.3.2 regarding the calibration results of the adjusted reduced chemoresistance model $\mathcal{M}_{DS}^{0,\star}$ with the data for cell line HepG2. We start with some additional information regarding the obtained parameter estimates (Subsection E.III.1). Next, we check the statistical significance of observed differences between parameter estimates for HC0 and H1 (Subsection E.III.2). Eventually, we take a look at the parameter correlations in the particle sample (Subsection E.III.3).

E.III.1   Marginal estimates

Figure E.12 compares the marginal distributions of the model parameters based on the particle approximation collecting all SMC runs. Note that the parameters $D_{\mathrm{norm},HC}$ and $1/c_{\mathrm{damp}}$ were calibrated in log scale to improve the coverage of the high probability region with the prior sample (recall Subsection 5.3.2), but their marginal distributions and corresponding MAPs are determined by calculating the KDE in linear scale.
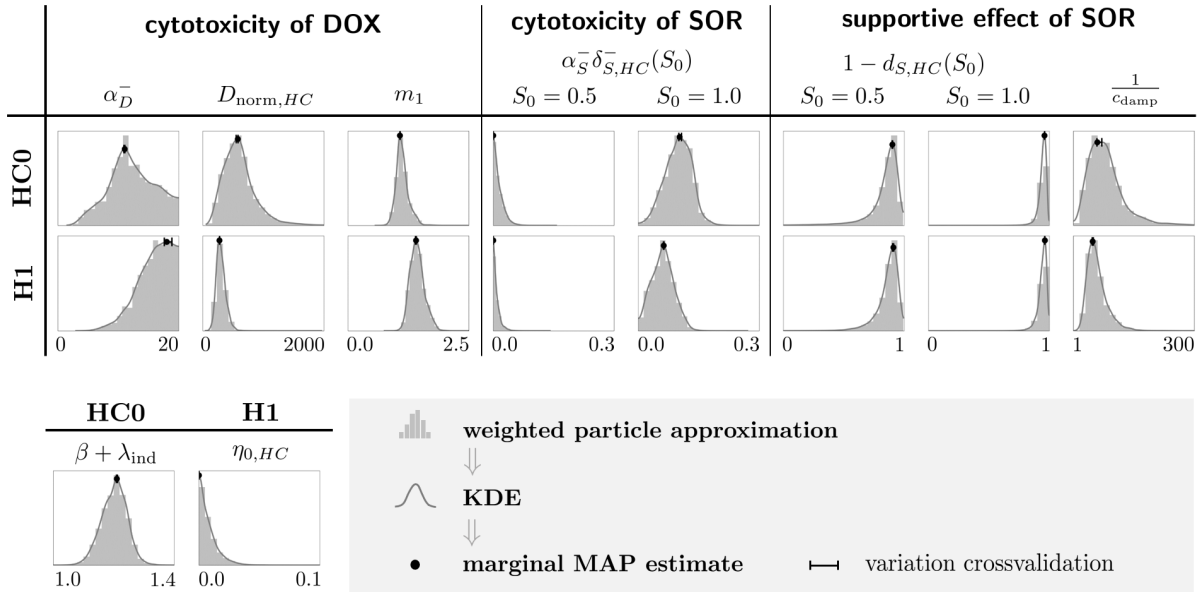
Figure E.12: Marginal posteriors of HepG2 calibrations. The numerical deviations for cross-validating the MAP estimates according to Subsection 6.1.3 are shown as error bars, which might not be visible due to high robustness of the respective estimate. Recall that $\beta + \lambda_{\mathrm{ind}}$ resp. $\eta_{0,HC}$ are only calibrated for HC0 resp. H1 ($\beta + \lambda_{\mathrm{ind}}$ is fixed to its MAP for H1 and $\eta_{0,HC} = 0$ for HC0 per definition).

Furthermore, Subsection 6.3.2 presented alternative estimates for parameters regarding the stress response to DOX. They were obtained by a weighted least square fit to take the corresponding parameter correlations (see later Subsection E.III.3) into account. Table E.6 provides the corresponding 95% confidence intervals of these fits.

Table E.6: 95% confidence intervals ($\pm\, 1.96 \cdot$ standard deviation) resulting from the least square fits in Figure 34 and Table 8.

	HC0	H1
$\boldsymbol{\alpha_D^-}$	$10.694 \pm\ \ 4.589$	$17.413 \pm\ \ 3.391$
$\boldsymbol{D}_{\mathrm{norm},\boldsymbol{HC}}$	501.122 ± 305.410	318.290 ± 103.267
$\boldsymbol{m_1}$	$1.128 \pm\ \ 0.129$	$1.433 \pm\ \ 0.147$
$\boldsymbol{1 - d_S(0.5)}$	$0.879 \pm\ \ 0.069$	$0.873 \pm\ \ 0.084$
$\boldsymbol{1 - d_S(1.0)}$	$0.948 \pm\ \ 0.032$	$0.942 \pm\ \ 0.043$
$\dfrac{1}{\boldsymbol{c}_{\mathrm{damp}}}$	22.542 ± 12.446	$18.864 \pm\ \ 8.756$
	$22.467 \pm\ \ 9.174$	$19.128 \pm\ \ 6.296$

Recall that it was not possible to achieve reasonable parameter estimates with the complete model $\mathcal{M}_{DS}^{\mathrm{CYP}}$ to appropriately reconstruct the HepG2 (HC0/H1) data from [22]. Nevertheless, for some parameters, these calibrations yield fairly concentrated marginal distributions. One of them is the DOX metabolization rate $\gamma_{D,HC}$, which results in estimates $\gamma_{D,HC} \approx 5$ for both HC0 and H1 (see Figure E.13). This value is close to the estimates constructed in Subsection 6.3.2. However, we cannot be entirely sure that these marginals are reliable since the underlying model/algorithmic assumptions are currently not at a stage to get reasonable results as a whole. Hence, there is no interest in presenting further results from these calibrations at the moment.
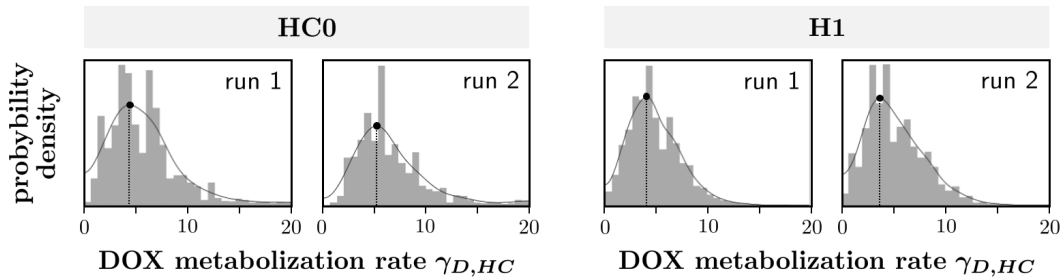
Figure E.13: Marginal distributions and corresponding MAPs estimates (markers and dotted line) of the DOX metabolization rate $\gamma_{D,HC}$ from two test runs for calibrating model $\mathcal{M}_{DS}^{\mathrm{CYP}}$ to HepG2 (HC0/H1) data. The solid line shows the KDEs and the scaling of vertical axis is not consistent for all subplots.

E.III.2   Significance checks

This subsection compares parameter estimates (HC0 vs. H1) according to Subsection 6.1.3 and Figure 15. Figure E.14 shows the statistical comparison of the marginal distributions of $\alpha_S^- \delta_{S,HC}^-(S_0)$, $1 - d_S(S_0)$ and $1/c_{\mathrm{damp}}$ from Figure E.12 as well as of their least square fits from Table E.6. We see clear significance for the marginals of $\alpha_S^- \delta_{S,HC}^-(S_0)$ for $S_0 = 1.0$ in contrast to $S_0 = 0.5$. The differences between corresponding estimates for $1 - d_S(S_0)$ (fit and marginals) are potentially statistically insignificant. For $1/c_{\mathrm{damp}}$, significance is only clear for the fit with $S_0 = 1.0$, however the remaining plots indicate a similar tendency.
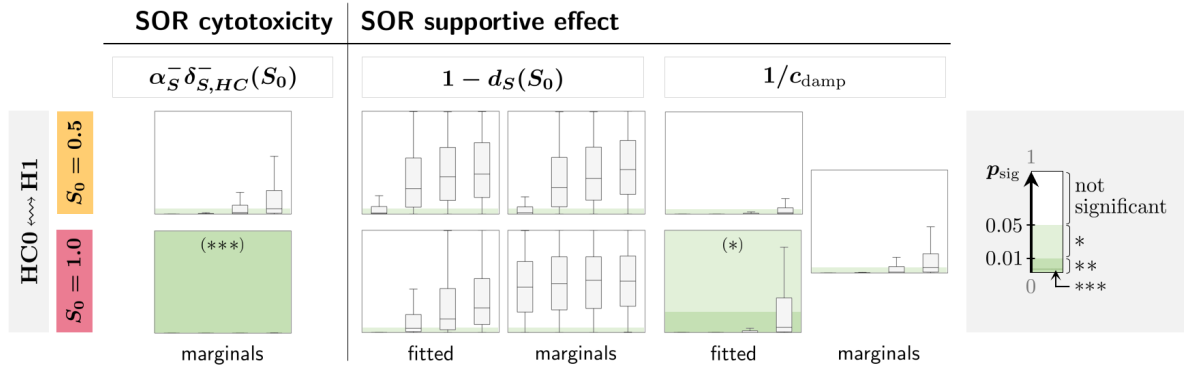
Figure E.14: Resulting p-values of the significance check comparing the marginal distributions of the SOR-related parameters (HepG2) for HC0 and H1 (sample sizes per subplot from left to right: 500, 100, 50, 30). Vertical axis limits are given by the receptive mark in the subplot: $0-1/0.05/0.001$ (no mark $/*/***$). Note that some boxplots are not visible due to vanishing p-values.

Analogously, Figure E.14 statistically compares the marginal distributions of α_D^-, $D_{\mathrm{norm},HC}$ and m_1 from Figure E.12 as well as their least square fits from Table E.6. For all parameter estimates (fitted and marginals), we observe a clear statistical significance of observed differences.
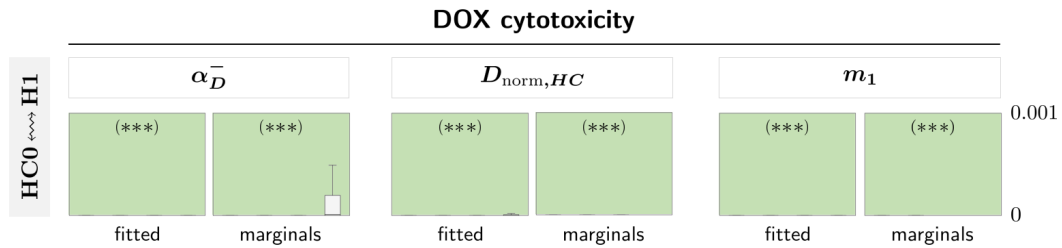
Figure E.15: Resulting p-values of the significance check comparing the fitted resp. marginal estimates of the parameters regarding the unsupported stress response to DOX (HepG2) for HC0 and H1 (sample sizes per subplot from left to right: 500, 100, 50, 30). Vertical axis limits: $0-0.001$. Note that most of the boxplots are not visible due to vanishing p-values.

Lastly, Figure E.16 shows the potential statistical insignificance of the observed differences for the DOX metabolization rate $\gamma_{D,HC}$, which were reconstructed with the approach in (6.7) in Subsection 6.3.2.
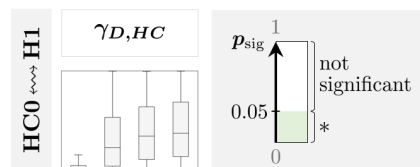
Figure E.16: Resulting p-values of the significance check comparing estimates of $\gamma_{D,HC}$ (HepG2) for HC0 and H1 (sample sizes per subplot from left to right: 500, 100, 50, 30). Vertical axis limits: $0-1$.

E.III.3   Parameter correlations

We check the (linear) parameter correlations of the particle approximation collecting all SMC runs analogously to the previous Subsection E.II.2. Again, we get sufficiently robust coefficients (standard deviation in the magnitude of 10^{-2}). Hence, we present the average values of r in the following. Figure E.17 depicts the selection of considerable correlations (i.e. $p_{\text{sig}} < 0.05$ and $|r| > 0.1$) between the parameters.
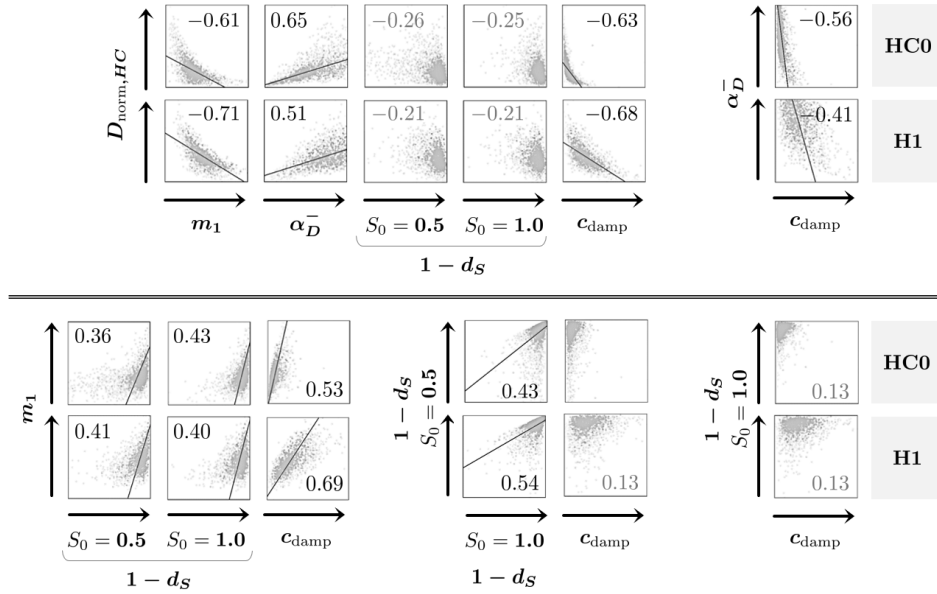
(a) Illustration of considerable correlations between parameters regarding the stress response to DOX.
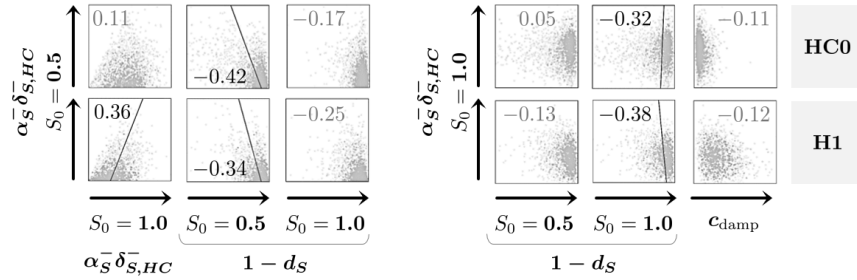
(b) Illustration of further considerable correlations (for the sake of completeness).

Figure E.17: Scatter plots with 5000 samples drawn from the 2D distributions of pairwise parameter combinations resulting from model calibrations with HepG2 data. Only statistically significant ($p_{\text{sig}} < 0.05$) correlation coefficients r are given and a regression line is depicted if at least a moderate linear correlation ($|r| > 0.3$) is observable.

As expected, we see relevant correlations between all parameters regarding the stress response to DOX (Subfigure E.17a), which is similar to Hep3B2 (recall Figure E.4). As HepG2 exhibits a considerable supportive influence of SOR contrary to Hep3B2, the correlations of $D_{\text{norm},HC}$, α_D^- and m_1 to the supportive parameters ($1 - d_S$ and c_{damp}) are more distinct. We observe L-shaped point clouds indicating non-linear correlations between $D_{\text{norm},HC}$ and m_1 resp. c_{damp}.

List of Figures

List of Tables

References

[1] B. R. Kirkwood and J. A. Sterne. *Essential medical statistics*. 2nd ed. John Wiley & Sons, 2010. ISBN: 9781444392845.

[2] R. P. Araujo and D. L. S. McElwain. "A history of the study of solid tumour growth: the contribution of mathematical modelling". *Bulletin of Mathematical Biology* 66.5 (2004), pp. 1039–1091. ISSN: 0092-8240. DOI: 10.1016/j.bulm.2003.11.002.

[3] F. Michor, J. Liphardt, M. Ferrari and J. Widom. "What does physics have to do with cancer?" *Nature Reviews Cancer* 11.9 (2011), pp. 657–670. ISSN: 1474-1768. DOI: 10.1038/nrc3092.

[4] L. Preziosi. *Cancer modelling and simulation*. Chapman & Hall/CRC mathematical biology and medicine series. Chapman & Hall/CRC, 2003. ISBN: 9781135440534. DOI: 10.1201/9780203494899.

[5] H. M. Byrne, T. Alarcon, M. R. Owen, S. D. Webb and P. K. Maini. "Modelling aspects of cancer dynamics: a review". *Philosophical transactions. Series A, Mathematical, physical, and engineering sciences* 364.1843 (2006), pp. 1563–1578. ISSN: 1364-503X. DOI: 10.1098/rsta.2006.1786.

[6] K. Brindle. "New approaches for imaging tumour responses to treatment". *Nature Reviews Cancer* 8.2 (2008), pp. 94–107. ISSN: 1474-1768. DOI: 10.1038/nrc2289.

[7] D. A. Hormuth, A. M. Jarrett, E. A. B. F. Lima, M. T. McKenna, D. T. Fuentes and T. E. Yankeelov. "Mechanism-Based Modeling of Tumor Growth and Treatment Response Constrained by Multiparametric Imaging Data". *JCO Clinical Cancer Informatics* 3.3 (2019), pp. 1–10. ISSN: 2473-4276. DOI: 10.1200/CCI.18.00055.

[8] T. E. Yankeelov, R. G. Abramson and C. C. Quarles. "Quantitative multimodality imaging in cancer research and therapy". *Nature Reviews Clinical Oncology* 11.11 (2014), pp. 670–680. ISSN: 1759-4782. DOI: 10.1038/nrclinonc.2014.134.

[9] C. S. Szot, C. F. Buchanan, J. W. Freeman and M. N. Rylander. "3D in vitro bioengineered tumors based on collagen I hydrogels". *Biomaterials* 32.31 (2011), pp. 7905–7912. ISSN: 0142-9612. DOI: 10.1016/j.biomaterials.2011.07.001.

[10] A. Ozkan, N. Ghousifam, P. J. Hoopes, T. E. Yankeelov and M. N. Rylander. "In vitro vascularized liver and tumor tissue microenvironments on a chip for dynamic determination of nanoparticle transport and toxicity". *Biotechnology and Bioengineering* 116.5 (2019), pp. 1201–1219. ISSN: 1097-0290. DOI: 10.1002/bit.26919.

[11] H. Byrne and L. Preziosi. "Modelling solid tumour growth using the theory of mixtures". *Mathematical Medicine and Biology* 20.4 (2003), pp. 341–366. ISSN: 1477-8599. DOI: 10.1093/imammb/20.4.341.

[12] H. Enderling and M. A.J. Chaplain. "Mathematical modeling of tumor growth and treatment". *Current pharmaceutical design* 20.30 (2014), pp. 4934–4940. ISSN: 1617-7940.

[13] H. Cho, A. L. Lewis, K. M. Storey, R. Jennings, B. Shtylla, A. M. Reynolds and H. M. Byrne. "A Framework for Performing Data-Driven Modeling of Tumor Growth with Radiotherapy Treatment". In: *Using Mathematics to Understand Biological Complexity*. Springer, Cham, 2021, pp. 179–216. DOI: 10.1007/978-3-030-57129-0_8.

[14] P. Schlicke, C. Kuttler and C. Schumann. "How mathematical modeling could contribute to the quantification of metastatic tumor burden under therapy: insights in immunotherapeutic treatment of non-small cell lung cancer". *Theoretical Biology and Medical Modelling* 18.1 (2021). ISSN: 1742-4682. DOI: 10.1186/s12976-021-00142-1.

[15] T. E. Yankeelov, N. Atuegwu, D. Hormuth, J. A. Weis, S. L. Barnes, M. I. Miga, E. C. Rericha and V. Quaranta. "Clinically relevant modeling of tumor growth and treatment response". *Science translational medicine* 5.187 (2013), 187ps9. DOI: 10.1126/scitranslmed.3005686.

[16] D. Ambrosi and L. Preziosi. "Cell adhesion mechanisms and stress relaxation in the mechanics of tumours". *Biomechanics and Modeling in Mechanobiology* 8.5 (2009), pp. 397–413. ISSN: 1617-7940. DOI: 10.1007/s10237-008-0145-y.

[17] R. K. Jain, R. T. Tong and L. L. Munn. "Effect of vascular normalization by antiangiogenic therapy on interstitial hypertension, peritumor edema, and lymphatic metastasis: insights from a mathematical model". *Cancer Research* 67.6 (2007), pp. 2729–2735. ISSN: 0008-5472. DOI: 10.1158/0008-5472.CAN-06-4102.

[18] A. Pathak and S. Kumar. "Independent regulation of tumor cell migration by matrix stiffness and confinement". *Proceedings of the National Academy of Sciences of the United States of America* 109.26 (2012), pp. 10334–10339. DOI: 10.1073/pnas.1118073109.

[19] R. K. Jain, J. D. Martin and T. Stylianopoulos. "The role of mechanical forces in tumor growth and therapy". *Annual review of biomedical engineering* 16 (2014), pp. 321–346. DOI: 10.1146/annurev-bioeng-071813-105259.

[20] Y. Kim, M. A. Stolarska and H. G. Othmer. "The role of the microenvironment in tumor growth and invasion". *Progress in Biophysics and Molecular Biology* 106.2 (2011), pp. 353–379. ISSN: 0079-6107. DOI: 10.1016/j.pbiomolbio.2011.06.006.

[21] E. A. B. F. Lima, N. Ghousifam, A. Ozkan, J. T. Oden, A. Shahmoradi, M. N. Rylander, B. Wohlmuth and T. E. Yankeelov. "Calibration of Multi-Parameter Models of Avascular Tumor Growth Using Time Resolved Microscopy Data". *Scientific reports* 8.1 (2018). DOI: 10.1038/s41598-018-32347-9.

[22] A. Özkan, D. L. Stolley, E. N. K. Cressman, M. McMillin, S. DeMorrow, T. E. Yankeelov and M. N. Rylander. "Tumor Microenvironment Alters Chemoresistance of Hepatocellular Carcinoma Through CYP3A4 Metabolic Activity". *Frontiers in oncology* 11 (2021). ISSN: 2234-943X. DOI: 10.3389/fonc.2021.662135.

[23] J. P. Kaipio and E. Somersalo. *Statistical and Computational Inverse Problems*. Vol. 160. Applied Mathematical Sciences. Springer, 2005. ISBN: 978-0-387-27132-3. DOI: 10.1007/b138659.

[24] M. Dashti and A. M. Stuart. "The Bayesian Approach to Inverse Problems". In: *Handbook of Uncertainty Quantification*. Springer, Cham, 2017, pp. 311–428. DOI: 10.1007/978-3-319-12385-1_7.

[25] A. M. Stuart. "Inverse problems: A Bayesian perspective". *Acta Numerica* 19 (2010), pp. 451–559. ISSN: 1474-0508. DOI: 10.1017/S0962492910000061.

[26] N. Chopin. "A sequential particle filter method for static models". *Biometrika* 89.3 (2002), pp. 539–552. ISSN: 1464-3510. DOI: 10.1093/biomet/89.3.539.

[27] P. Del Moral, A. Doucet and A. Jasra. "Sequential Monte Carlo samplers". *Journal of the Royal Statistical Society: Series B (Statistical Methodology)* 68.3 (2006), pp. 411–436. ISSN: 1369-7412. DOI: 10.1111/j.1467-9868.2006.00553.x.

[28] J. Nocedal and S. J. Wright. *Numerical optimization*. Springer, 1999. ISBN: 978-0-387-40065-5. DOI: 10.1007/978-0-387-40065-5.

[29]   J. Collis, A. J. Connor, M. Paczkowski, P. Kannan, J. Pitt-Francis, H. M. Byrne and M. E. Hubbard. "Bayesian Calibration, Validation and Uncertainty Quantification for Predictive Modelling of Tumour Growth: A Tutorial". *Bulletin of Mathematical Biology* 79.4 (2017), pp. 939–974. ISSN: 1522-9602. DOI: `10.1007/s11538-017-0258-5`.

[30]   J. Dick, R. N. Gantner, Q. T. Le Gia and C. Schwab. "Higher order quasi-Monte Carlo integration for Bayesian PDE inversion". *Computers & Mathematics with Applications* 77.1 (2019), pp. 144–172. ISSN: 0898-1221. DOI: `10.1016/j.camwa.2018.09.019`.

[31]   C. Schillings and C. Schwab. "Sparse, adaptive Smolyak quadratures for Bayesian inverse problems". *Inverse Problems* 29.6 (2013). DOI: `10.1088/0266-5611/29/6/065011`.

[32]   I.-G. Farcas, J. Latz, E. Ullmann, T. Neckel and H.-J. Bungartz. "Multilevel adaptive sparse Leja approximations for Bayesian inverse problems". *SIAM Journal on Scientific Computing* 42.1 (2020), A424–A451. ISSN: 1095-7197. DOI: `10.1137/19M1260293`.

[33]   C. P. Robert and G. Casella. *Monte Carlo Statistical Methods*. Springer New York, 2004. ISBN: 978-1-4757-4145-2. DOI: `10.1007/978-1-4757-4145-2`.

[34]   J. T. Oden, E. A. B. F. Lima, R. C. Almeida, Y. Feng, M. N. Rylander, D. Fuentes, D. Faghihi, M. M. Rahman, M. DeWitt, M. Gadde and J. C. Zhou. "Toward Predictive Multiscale Modeling of Vascular Tumor Growth". *Archives of Computational Methods in Engineering* 23.4 (2016), pp. 735–779. ISSN: 1886-1784. DOI: `10.1007/s11831-015-9156-x`.

[35]   C. Falcó, D. J. Cohen, J. A. Carrillo and R. E. Baker. *Quantifying tissue growth, shape and collision via continuum models and Bayesian inference*. DOI: `10.48550/arXiv.2302.02968`.

[36]   R. M. Neal. "Annealed importance sampling". *Statistics and Computing* 11.2 (2001), pp. 125–139. ISSN: 0960-3174. DOI: `10.1023/A:1008923215028`.

[37]   F. Liang and W. H. Wong. "Real-Parameter Evolutionary Monte Carlo With Applications to Bayesian Mixture Models". *Journal of the American Statistical Association* 96.454 (2001), pp. 653–666. ISSN: 1537-274X. DOI: `10.1198/016214501753168325`.

[38]   A. Jasra, D. A. Stephens and C. C. Holmes. "On population-based simulation for static inference". *Statistics and Computing* 17.3 (2007), pp. 263–279. ISSN: 1573-1375. DOI: `10.1007/s11222-007-9028-9`.

[39]   J. Ching and Y.-C. Chen. "Transitional Markov Chain Monte Carlo Method for Bayesian Model Updating, Model Class Selection, and Model Averaging". *Journal of Engineering Mechanics* 133.7 (2007), pp. 816–832. ISSN: 0733-9399. DOI: `10.1061/(ASCE)0733-9399(2007)133:7(816)`.

[40]   A. Beskos, A. Jasra, E. A. Muzaffer and A. M. Stuart. "Sequential Monte Carlo methods for Bayesian elliptic inverse problems". *Statistics and Computing* 25.4 (2015), pp. 727–737. ISSN: 0960-3174. DOI: `10.1007/s11222-015-9556-7`.

[41]   Y. Zhou, A. M. Johansen and J. A. Aston. "Toward Automatic Model Comparison: An Adaptive Sequential Monte Carlo Approach". *Journal of Computational and Graphical Statistics* 25.3 (2016), pp. 701–726. ISSN: 1537-2715. DOI: `10.1080/10618600.2015.1060885`.

[42]   G. Evensen. "The Ensemble Kalman Filter: theoretical formulation and practical implementation". *Ocean Dynamics* 53.4 (2003), pp. 343–367. ISSN: 1616-7228. DOI: `10.1007/s10236-003-0036-9`.

[43] C. Schillings and A. M. Stuart. "Analysis of the Ensemble Kalman Filter for Inverse Problems". *SIAM Journal on Numerical Analysis* 55.3 (2017), pp. 1264–1290. ISSN: 0036-1429. DOI: `10.1137/16M105959X`.

[44] O. G. Ernst, B. Sprungk and H.-J. Starkloff. "Analysis of the ensemble and polynomial chaos Kalman filters in Bayesian inverse problems". *SIAM/ASA Journal on Uncertainty Quantification* 3.1 (2015), pp. 823–851. DOI: `10.1137/140981319`.

[45] D. Blömker, C. Schillings, P. Wacker and S. Weissmann. "Well posedness and convergence analysis of the ensemble Kalman inversion". *Inverse Problems* 35.8 (2019). ISSN: 1361-6420. DOI: `10.1088/1361-6420/ab149c`.

[46] S. Weissmann. "Gradient flow structure and convergence analysis of the ensemble Kalman inversion for nonlinear forward models". *Inverse Problems* 38.10 (2022). DOI: `10.1088/1361-6420/ac8bed`.

[47] Y. Marzouk, T. Moselhy, M. Parno and A. Spantini. "Sampling via Measure Transport: An Introduction". In: *Handbook of Uncertainty Quantification*. Ed. by R. Ghanem, D. Higdon and H. Owhadi. Springer International Publishing, 2016, pp. 1–41. ISBN: 9783319112596. DOI: `10.1007/978-3-319-11259-6_23-1`.

[48] D. J. Warne, R. E. Baker and M. J. Simpson. "A practical guide to pseudo-marginal methods for computational inference in systems biology". *Journal of Theoretical Biology* 496 (2020). ISSN: 0022-5193. DOI: `10.1016/j.jtbi.2020.110255`.

[49] S. T. Johnston, J. V. Ross, B. J. Binder, D. L. Sean McElwain, P. Haridas and M. J. Simpson. "Quantifying the effect of experimental design choices for in vitro scratch assays". *Journal of Theoretical Biology* 400 (2016), pp. 19–31. ISSN: 0022-5193. DOI: `10.1016/j.jtbi.2016.04.012`.

[50] D. J. Warne, R. E. Baker and M. J. Simpson. "Using Experimental Data and Information Criteria to Guide Model Selection for Reaction-Diffusion Problems in Mathematical Biology". *Bulletin of Mathematical Biology* 81.6 (2019), pp. 1760–1804. ISSN: 1522-9602. DOI: `10.1007/s11538-019-00589-x`.

[51] D. J. Wilkinson. "Parameter Inference for Stochastic Kinetic Models of Bacterial Gene Regulation: A Bayesian Approach to Systems Biology". In: *Bayesian Statistics 9*. Oxford University Press, 2011, pp. 679–706. DOI: `10.1093/acprof:oso/9780199694587.003.0023`.

[52] A. P. Browning, S. W. McCue, R. N. Binny, M. J. Plank, E. T. Shah and M. J. Simpson. "Inferring parameters for a lattice-free model of cell migration and proliferation using experimental data". *Journal of Theoretical Biology* 437 (2018), pp. 251–260. ISSN: 0022-5193. DOI: `10.1016/j.jtbi.2017.10.032`.

[53] J. Hardin and G. Bertoni. *Becker's world of the cell*. Global edition. Pearson, 2018. ISBN: 9781292177779.

[54] Y. Ionov, M. A. Peinado, S. Malkhosyan, D. Shibata and M. Perucho. "Ubiquitous somatic mutations in simple repeated sequences reveal a new mechanism for colonic carcinogenesis". *Nature* 363.6429 (1993), pp. 558–561. ISSN: 1476-4687. DOI: `10.1038/363558a0`.

[55] F. Spill, D. S. Reynolds, R. D. Kamm and M. H. Zaman. "Impact of the physical microenvironment on tumor progression and metastasis". *Current Opinion in Biotechnology* 40 (2016), pp. 41–48. ISSN: 0958-1669. DOI: `10.1016/j.copbio.2016.02.007`.

[56] A. L. Correia and M. J. Bissell. "The tumor microenvironment is a dominant force in multidrug resistance". *Drug resistance updates : reviews and commentaries in antimicrobial and anticancer chemotherapy* 15.1-2 (2012), pp. 39–49. DOI: 10.1016/j.drup.2012.01.006.

[57] R. R. Gonzalez-Perez and B. R. Rueda. *Tumor angiogenesis regulators*. CRC Press, 2013. ISBN: 9781466580978.

[58] T. D. Tlsty and L. M. Coussens. "Tumor stroma and regulation of cancer development". *Annual review of pathology* 1 (2006), pp. 119–150. ISSN: 1553-4006. DOI: 10.1146/annurev.pathol.1.110304.100224.

[59] C. Gaggioli, S. Hooper, C. Hidalgo-Carcedo, R. Grosse, J. F. Marshall, K. Harrington and E. Sahai. "Fibroblast-led collective invasion of carcinoma cells with differing roles for RhoGTPases in leading and following cells". *Nature cell biology* 9.12 (2007), pp. 1392–1400. ISSN: 1465-7392. DOI: 10.1038/ncb1658.

[60] D. M. Gilkes, G. L. Semenza and D. Wirtz. "Hypoxia and the extracellular matrix: drivers of tumour metastasis". *Nature Reviews Cancer* 14.6 (2014), pp. 430–439. ISSN: 1474-1768. DOI: 10.1038/nrc3726.

[61] *CellTiter-Blue® Cell Viability Assay Technical Bulletin.* URL: https://www.promega.de/products/cell-health-assays/cell-viability-and-cytotoxicity-assays/celltiter_blue-cell-viability-assay/?catNum=G8080.

[62] E. E. Antoine, P. P. Vlachos and M. N. Rylander. "Tunable collagen I hydrogels for engineered physiological tissue micro-environments". *PLOS ONE* 10.3 (2015), e0122500. ISSN: 1932-6203. DOI: 10.1371/journal.pone.0122500.

[63] S. Schönfeld, A. Ozkan, L. Scarabosio, M. N. Rylander and C. Kuttler. "Environmental stress level to model tumor cell growth and survival". *Mathematical Biosciences and Engineering* 19.6 (2022), pp. 5509–5545. ISSN: 1551-0018. DOI: 10.3934/mbe.2022258.

[64] J. E. Ferrell. "How regulated protein translocation can produce switch-like responses". *Trends in Biochemical Sciences* 23.12 (1998), pp. 461–465. ISSN: 09680004. DOI: 10.1016/S0968-0004(98)01316-4.

[65] L. Claret, P. Girard, P. M. Hoff, E. van Cutsem, K. P. Zuideveld, K. Jorga, J. Fagerberg and R. Bruno. "Model-based prediction of phase III overall survival in colorectal cancer on the basis of phase II tumor dynamics". *Journal of clinical oncology : official journal of the American Society of Clinical Oncology* 27.25 (2009), pp. 4103–4108. DOI: 10.1200/JCO.2008.21.0807.

[66] S. L. Gerson, P. F. Caimi, B. M. William and R. J. Creger. "Chapter 57 - Pharmacology and Molecular Mechanisms of Antineoplastic Agents for Hematologic Malignancies". In: *Hematology (Seventh Edition).* Ed. by R. Hoffman, E. J. Benz, L. E. Silberstein, H. E. Heslop, J. I. Weitz, J. Anastasi, M. E. Salama and S. A. Abutalib. Elsevier, 2018, pp. 849–912. ISBN: 978-0-323-35762-3. DOI: 10.1016/B978-0-323-35762-3.00057-3.

[67] *Sorafenib (Nexavar): summary of product characteristics.* URL: https://www.ema.europa.eu/documents/product-information/nexavar-epar-product-information_en.pdf.

[68] L. Petzold. "Automatic Selection of Methods for Solving Stiff and Nonstiff Systems of Ordinary Differential Equations". *SIAM Journal on Scientific and Statistical Computing* 4.1 (1983), pp. 136–148. ISSN: 0196-5204. DOI: 10.1137/0904010.

[69] A. C. Hindmarsh. "ODEPACK, a systemized collection of ODE solvers". *Scientific computing* (1983).

[70] R. C. Smith. *Uncertainty quantification: theory, implementation, and applications*. Vol. 12. Siam, 2014. ISBN: 978-1611973211.

[71] T. J. Sullivan. *Introduction to uncertainty quantification*. Vol. 63. Springer, 2015. ISBN: 978-3-319-23395-6. DOI: 10.1007/978-3-319-23395-6.

[72] A. Klenke. *Probability theory: a comprehensive course*. Springer Science & Business Media, 2013. ISBN: 978-1-4471-5361-0. DOI: 10.1007/978-1-4471-5361-0.

[73] R. Sásik, E. Calvo and J. Corbeil. "Statistical analysis of high-density oligonucleotide arrays: a multiplicative noise model". *Bioinformatics* 18.12 (2002), pp. 1633–1640. ISSN: 1460-2059. DOI: 10.1093/bioinformatics/18.12.1633.

[74] G. Aubert and J.-F. Aujol. "A Variational Approach to Removing Multiplicative Noise". *SIAM Journal on Applied Mathematics* 68.4 (2008), pp. 925–946. ISSN: 0036-1399. DOI: 10.1137/060671814.

[75] Y.-M. Huang, M. K. Ng and Y.-W. Wen. "A New Total Variation Method for Multiplicative Noise Removal". *SIAM Journal on Imaging Sciences* 2.1 (2009), pp. 20–40. ISSN: 1936-4954. DOI: 10.1137/080712593.

[76] G. Steidl and T. Teuber. "Removing Multiplicative Noise by Douglas-Rachford Splitting Methods". *Journal of Mathematical Imaging and Vision* 36.2 (2010), pp. 168–184. ISSN: 0924-9907. DOI: 10.1007/s10851-009-0179-5.

[77] M. C. Kennedy and A. O'Hagan. "Bayesian Calibration of Computer Models". *Journal of the Royal Statistical Society: Series B (Statistical Methodology)* 63.3 (2001), pp. 425–464. ISSN: 1467-9868. DOI: 10.1111/1467-9868.00294.

[78] J. Brynjarsdottir and A. O'Hagan. "Learning about physical parameters: the importance of model discrepancy". *Inverse Problems* 30.11 (2014). ISSN: 1361-6420. DOI: 10.1088/0266-5611/30/11/114007.

[79] N. Kantas, A. Beskos and A. Jasra. "Sequential Monte Carlo Methods for High-Dimensional Inverse Problems: A Case Study for the Navier–Stokes Equations". *SIAM/ASA Journal on Uncertainty Quantification* 2.1 (2014), pp. 464–489. ISSN: 2166-2525. DOI: 10.1137/130930364.

[80] A. Doucet, A. M. Johansen et al. "A tutorial on particle filtering and smoothing: Fifteen years later". *Handbook of nonlinear filtering* 12.656-704 (2009).

[81] M. Bulté, J. Latz and E. Ullmann. "A Practical Example for the Non-linear Bayesian Filtering of Model Parameters". In: *Quantification of Uncertainty: Improving Efficiency and Technology*. Springer, Cham, 2020, pp. 241–272. DOI: 10.1007/978-3-030-48721-8_11.

[82] R. Douc and O. Cappe. "Comparison of resampling schemes for particle filtering". In: *ISPA 2005. Proceedings of the 4th International Symposium on Image and Signal Processing and Analysis, 2005*. 2005, pp. 64–69. ISBN: 1845-5921. DOI: 10.1109/ISPA.2005.195385.

[83] M. Gerber, N. Chopin and N. Whiteley. "Negative association, ordering and convergence of resampling methods". *The Annals of Statistics* 47.4 (2019), pp. 2236–2260. ISSN: 0090-5364. DOI: 10.1214/18-aos1746.

[84] S. Thrun. "Probalistic Robotics". *Kybernetes* 35.7/8 (2006), pp. 1299–1300. DOI: 10.1108/03684920610675292.

[85] J. S. Liu and J. S. Liu. *Monte Carlo strategies in scientific computing*. Vol. 75. Springer, 2008. ISBN: 978-0-387-76371-2. DOI: `10.1007/978-0-387-76371-2`.

[86] H. Haario, E. Saksman and J. Tamminen. "An Adaptive Metropolis Algorithm". *Bernoulli* 7.2 (2001), pp. 223–242. ISSN: 1350-7265. DOI: `10.2307/3318737`.

[87] A. Beskos, G. Roberts and A. Stuart. "Optimal scalings for local Metropolis–Hastings chains on nonproduct targets in high dimensions". *The Annals of Applied Probability* 19.3 (2009), pp. 863–898. ISSN: 1050-5164. DOI: `10.1214/08-AAP563`.

[88] "Build models that drive breakthroughs". *Technology Networks* (14.11.2018). URL: `https://www.technologynetworks.com/cancer-research/ebooks/build-models-that-drive-breakthroughs-311843`.

[89] K. Wrzesinski, A. Rogowska-Wrzesinska, R. Kanlaya, K. Borkowski, V. Schwämmle, J. Dai, K. E. Joensen, K. Wojdyla, V. B. Carvalho and S. J. Fey. "The cultural divide: exponential growth in classical 2D and metabolic equilibrium in 3D environments". *PLOS ONE* 9.9 (2014). ISSN: 1932-6203. DOI: `10.1371/journal.pone.0106973`.

[90] A. Özkan, D. L. Stolley, E. N. K. Cressman, M. McMillin, T. E. Yankeelov and M. N. Rylander. "Cirrhosis and Inflammation Regulates CYP3A4 Mediated Chemoresistance in Vascularized Hepatocellular Carcinoma-on-a-chip" (2022). DOI: `10.1101/2022.05.04.490682`.

[91] S. Ferson, W. L. Oberkampf and L. Ginzburg. "Model validation and predictive capability for the thermal challenge problem". *Computer Methods in Applied Mechanics and Engineering* 197.29-32 (2008), pp. 2408–2430. ISSN: 0045-7825. DOI: `10.1016/j.cma.2007.07.030`.

[92] R. E. Kass and A. E. Raftery. "Bayes Factors". *Journal of the American Statistical Association* 90.430 (1995), pp. 773–795. ISSN: 1537-274X. DOI: `10.1080/01621459.1995.10476572`.

[93] D. W. Scott. *Multivariate density estimation: Theory, practice, and visualization*. 2nd ed. John Wiley & Sons, 2015. ISBN: 9781118575574. DOI: `10.1002/9781118575574`.

[94] B. L. Welch. "The generalisation of student's problems when several different population variances are involved". *Biometrika* 34.1-2 (1947), pp. 28–35. ISSN: 1464-3510. DOI: `10.1093/biomet/34.1-2.28`.

[95] S. William. "The probable error of a mean". *Biometrika* 6.1 (1908), pp. 1–25. DOI: `10.2307/2331554`.

[96] F. Wilcoxon. "Individual Comparisons by Ranking Methods". *Biometrics Bulletin* 1.6 (1945), pp. 80–83. ISSN: 00994987. DOI: `10.2307/3001968`.

[97] H. B. Mann and D. R. Whitney. "On a Test of Whether one of Two Random Variables is Stochastically Larger than the Other". *The Annals of Mathematical Statistics* 18.1 (1947), pp. 50–60. ISSN: 0003-4851. DOI: `10.1214/aoms/1177730491`.

[98] E. Brunner and U. Munzel. "The Nonparametric Behrens-Fisher Problem: Asymptotic Theory and a Small-Sample Approximation". *Biometrical Journal* 42.1 (2000), pp. 17–25. ISSN: 0323-3847. DOI: `10.1002/(SICI)1521-4036(200001)42:1{\textless}17::AID-BIMJ17{\textgreater}3.0.CO;2-U`.

[99] K. Pearson. "VII. Note on regression and inheritance in the case of two parents". *Proceedings of the Royal Society of London* 58.347-352 (1895), pp. 240–242. ISSN: 0370-1662. DOI: `10.1098/rspl.1895.0041`.

[100] H. Akoglu. "User's guide to correlation coefficients". *Turkish Journal of Emergency Medicine* 18.3 (2018), pp. 91–93. DOI: 10.1016/j.tjem.2018.08.001.

[101] B. Ratner. "The correlation coefficient: Its values range between $+1/-1$, or do they?" *Journal of Targeting, Measurement and Analysis for Marketing* 17.2 (2009), pp. 139–142. ISSN: 1479-1862. DOI: 10.1057/jt.2009.5.

[102] C. Spearman. "The Proof and Measurement of Association Between Two Things". In: *Studies in individual differences: The search for intelligence*. Appleton-Century-Crofts, 1961, pp. 45–58. DOI: 10.1037/11491-005.

[103] M. G. Kendall. "A New Measure of Rank Correlation". *Biometrika* 30.1/2 (1938), pp. 81–93. ISSN: 1464-3510. DOI: 10.2307/2332226.

[104] O. J. Schmitz. *Ecology and ecosystem conservation*. Island Press, 2013. ISBN: 978-1-59726-048-0.

[105] C. Lewis-Beck and M. S. Lewis-Beck. *Applied regression: An introduction*. Second edition. Vol. 22. Quantitative applications in the social sciences. SAGE, 2015. ISBN: 9781483381466.

[106] G.-H. Qiu, X. Xie, F. Xu, X. Shi, Y. Wang and L. Deng. "Distinctive pharmacological differences between liver cancer cell lines HepG2 and Hep3B". *Cytotechnology* 67.1 (2015), pp. 1–12. ISSN: 0920-9069. DOI: 10.1007/s10616-014-9761-9.

[107] *P450-Glo™ Assays Technical Bulletin*. URL: https://www.promega.de/products/cell-health-assays/adme-assays/p450-glo-cyp3a4-assay-and-screening-system/?catNum=V9001.

[108] J. D. Murray. *Mathematical biology: I. An introduction*. Third edition. Vol. 17. Interdisciplinary Applied Mathematics. Springer, 2002. ISBN: 0-387-95223-3. DOI: 10.1007/b98868.

[109] C. C. Aggarwal. *Neural Networks and Deep Learning: A Textbook*. Springer International Publishing, 2018. ISBN: 9783319944630. DOI: 10.1007/978-3-319-94463-0.

[110] M. A. Nielsen. *Neural Networks and Deep Learning*. Determination Press, 2015. URL: http://neuralnetworksanddeeplearning.com/.

[111] C. E. Rasmussen and C. K. Williams. *Gaussian processes for machine learning*. Vol. 1. Springer, 2006. ISBN: 978-0-262-18253-9.

[112] X. Ma and N. Zabaras. "An adaptive hierarchical sparse grid collocation algorithm for the solution of stochastic differential equations". *Journal of Computational Physics* 228.8 (2009), pp. 3084–3113. ISSN: 0021-9991. DOI: 10.1016/j.jcp.2009.01.006.

[113] I. Babuška, F. Nobile and R. Tempone. "A stochastic collocation method for elliptic partial differential equations with random input data". *SIAM review* 52.2 (2010), pp. 317–355. DOI: 10.1137/100786356.

[114] A.-L. Haji-Ali, F. Nobile, L. Tamellini and R. Tempone. "Multi-index stochastic collocation for random PDEs". *Computer Methods in Applied Mechanics and Engineering* 306 (2016), pp. 95–122. DOI: 10.1016/j.cma.2016.03.029.

[115] D. Xiu and G. E. Karniadakis. "The Wiener–Askey polynomial chaos for stochastic differential equations". *SIAM journal on scientific computing* 24.2 (2002), pp. 619–644. DOI: 10.1137/S1064827501387826.

[116] R. G. Ghanem and P. D. Spanos. *Stochastic finite elements: a spectral approach*. Courier Corporation, 2003. ISBN: 0-486-42818-4.

[117] J. S. Hesthaven, C. Pagliantini and G. Rozza. "Reduced basis methods for time-dependent problems". *Acta Numerica* 31 (2022), pp. 265–345. DOI: 10.1017/S0962492922000058.

[118] K. Lee and K. T. Carlberg. "Model reduction of dynamical systems on nonlinear manifolds using deep convolutional autoencoders". *Journal of Computational Physics* 404 (2020). DOI: 10.1016/j.jcp.2019.108973.

[119] S. Fresca, L. Dede' and A. Manzoni. "A comprehensive deep learning-based approach to reduced order modeling of nonlinear time-dependent parametrized PDEs". *Journal of Scientific Computing* 87 (2021). ISSN: 1573-7691. DOI: 10.1007/s10915-021-01462-7.

[120] R. K. Tripathy and I. Bilionis. "Deep UQ: Learning deep neural network surrogate models for high dimensional uncertainty quantification". *Journal of computational physics* 375 (2018), pp. 565–588. ISSN: 0021-9991. DOI: 10.1016/j.jcp.2018.08.036.

[121] M. Geist, P. Petersen, M. Raslan, R. Schneider and G. Kutyniok. "Numerical solution of the parametric diffusion equation by deep neural networks". *Journal of Scientific Computing* 88.1 (2021). ISSN: 1573-7691. DOI: 10.1007/s10915-021-01532-w.

[122] K. O. Lye, S. Mishra and D. Ray. "Deep learning observables in computational fluid dynamics". *Journal of Computational Physics* 410 (2020). ISSN: 0021-9991. DOI: 10.1016/j.jcp.2020.109339.

[123] R. D. Reed and R. J. Marks. *Neural smithing: Supervised learning in feedforward artificial neural networks*. The MIT Press, 1999. ISBN: 9780262181907.

[124] T. Cui, Y. M. Marzouk and K. E. Willcox. "Data-driven model reduction for the Bayesian solution of inverse problems". *International Journal for Numerical Methods in Engineering* 102.5 (2015), pp. 966–990. DOI: 10.1002/nme.4748.

[125] C. Lieberman, K. Willcox and O. Ghattas. "Parameter and state model reduction for large-scale statistical inverse problems". *SIAM Journal on Scientific Computing* 32.5 (2010), pp. 2523–2542. DOI: 10.1137/090775622.

[126] W. A. Adkins and M. G. Davidson. *Ordinary differential equations*. Springer Science & Business Media, 2012. ISBN: 978-1-4614-3618-8. DOI: 10.1007/978-1-4614-3618-8.

[127] L. C. Evans. *Partial differential equations*. Vol. 19. American Mathematical Society, 2010. ISBN: 978-0-8218-4974-3.

[128] E. Hairer, S. P. Nørsett and G. Wanner. *Solving Ordinary Differential Equations I: Non-stiff Problems*. 2. Aufl. Vol. 8. Springer Series in Computational Mathematics. Springer, 1993. ISBN: 978-3-540-56670-0. DOI: 10.1007/978-3-540-78862-1.

[129] P. Hartman. "A lemma in the theory of structural stability of differential equations". *Proceedings of the American Mathematical Society* 11.4 (1960), pp. 610–620. ISSN: 0002-9939. DOI: 10.1090/S0002-9939-1960-0121542-7.

[130] D. M. Grobman. "Homeomorphism of systems of differential equations (in Russian)". *Doklady Akademii Nauk SSSR* 128 (1959), pp. 880–881.

[131] B. Gompertz. "XXIV. On the nature of the function expressive of the law of human mortality, and on a new mode of determining the value of life contingencies. In a letter to Francis Baily, Esq. F. R. S. &c". *Philosophical Transactions of the Royal Society of London* 115 (1825), pp. 513–583. ISSN: 0261-0523. DOI: 10.1098/rstl.1825.0026.

[132] J. H. Curtiss. "On the Distribution of the Quotient of Two Chance Variables". *The Annals of Mathematical Statistics* 12.4 (1941), pp. 409–421. ISSN: 0003-4851. DOI: 10.1214/aoms/1177731679.

[133] E. Parzen. "On Estimation of a Probability Density Function and Mode". *The Annals of Mathematical Statistics* 33.3 (1962), pp. 1065–1076. ISSN: 0003-4851. DOI: 10.1214/aoms/1177704472.